Max-Planck-Institut für Meteorologie

EXAMENSARBEIT Nr. 56

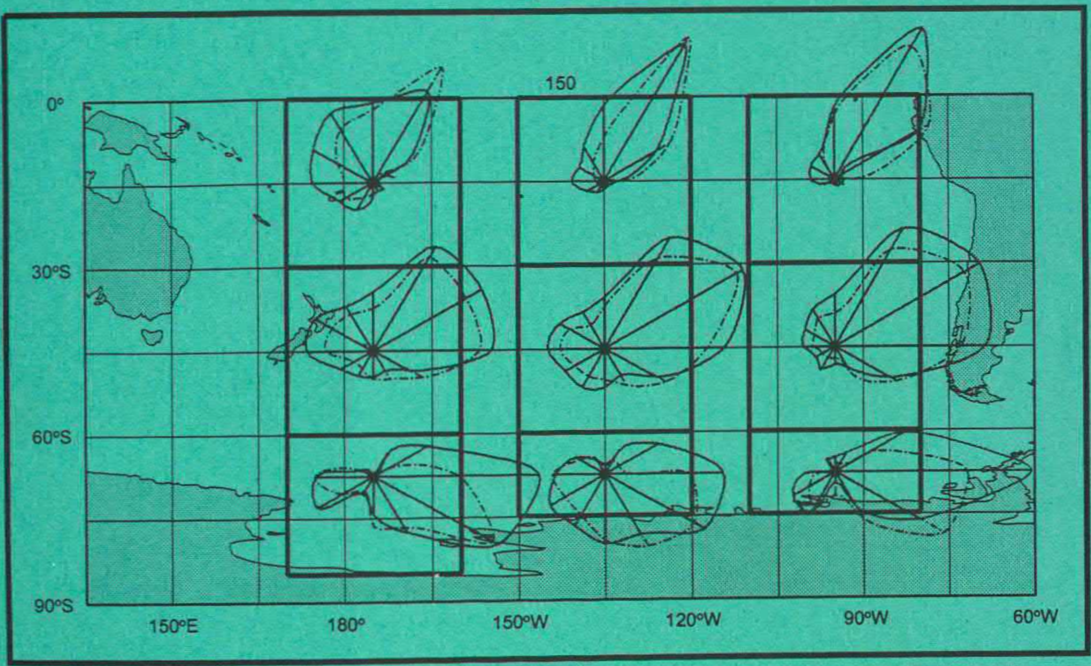

USE OF OCEAN WAVE SPECTRA RETRIEVED FROM ERS-1 SAR WAVE MODE DATA FOR GLOBAL WAVE MODELLING

von

Patrick Heimbach

Dissertation zur Erlangung des Doktorgrades

Autor:

Patrick Heimbach

Max-Planck-Institut
für Meteorologie

MAX-PLANCK-INSTITUT
FÜR METEOROLOGIE
BUNDESSTRASSE 55
D - 20146 HAMBURG
GERMANY

Tel.: +49-(0)40-4 11 73-0
Telefax: +49-(0)40-4 11 73-298
E-Mail: <name> @ dkrz.de

Use of ocean wave spectra retrieved from ERS-1 SAR wave mode data for global wave modelling

Dissertation
zur Erlangung des Doktorgrades der Naturwissenschaften
im Fachbereich Geowissenschaften
der Universität Hamburg

vorgelegt von

Patrick Heimbach
aus Düsseldorf

Hamburg
1998

ISSN 0938-5177

Als Dissertation angenommen vom Fachbereich Geowissenschaften der Universität Hamburg

auf Grund der Gutachten von Prof. Dr. Klaus Hasselmann
und Prof. Dr. Werner Alpers

Hamburg, den 30. Juni 1998

Prof. Dr. G. Miehlich
Dekan
des Fachbereiches Geowissenschaften

Meiner Mutter gewidmet.

Вот мой секрет, он очень прост:
зорко одно лишь сердце.
Самого главного глазами не увидишь.
— Антуан де Сент-Экзюпери, *Маленький принц* (1943)

ABSTRACT

Since the launch of the first European remote sensing satellite ERS-1 in 1991 detailed spectral information on the sea state have for the first time become available globally, continuously and in near–real time through the synthetic aperture radar's (SAR) imagette sampling mode (so-called 'SAR wave mode', SWM). These unprecedented data allow for the first time a global spectral validation of the wave forecast model WAM, which is run operationally at the European Centre for Medium-Range Weather Forecasts (ECMWF) and at many other weather centres. The WAM computes the two-dimensional wave spectrum at each point on a spherical grid from first principles by solving a spectral energy balance equation with source terms incorporating the physics of wind input, resonant nonlinear wave-wave interactions, and dissipation. It is driven by surface wind vector fields which are generally provided by an atmospheric model.

The ocean wave spectra were retrieved from SWM imagette spectra by means of the recently developed WASAR algorithm. This algorithm is based on the inversion of the closed nonlinear wave–to–SAR spectral transform, and on an iterative improvement of the first guess input spectrum. The first guess spectra were computed with the operational WAM model of the ECMWF.

This work features a global set of three years of ERS-1 SWM data collected between January 1993 and December 1995. The work is divided into four main parts.

1. Prior to application, an extensive assessment of quality and performance–related aspects of the SWM data and the extraction procedure of ocean wave spectra was performed. The combined quality analysis of the SWM product and the fidelity analysis of the WASAR algorithm showed that about three quarters of the SWM data could be meaningfully retrieved. A single or second iteration of the input spectrum yielded an appreciable improvement of the retrievals. It is, therefore, recommended to be applied also for operational applications, representing a necessary trade-off between accuracy and computing time. In order to assess the dependence of the retrieval with respect to the first guess input spectrum, sensitivity experiments were conducted, in which the first guess was modified in different ways (changes in energy, frequency and direction). A statistical assessment of the modified retrieval runs showed only weak residual dependence of the retrieval on the first guess input spectrum.

2. Complementary to the quality and performance analyses, a global validation of SWM–retrieved significant wave heights H_s^{swm} was performed for the period 1994, using independent, collocated data from the ERS-1 (H_s^{ers}) and the TOPEX (H_s^{top}) altimeters. A good overall agreement was found, with a slight low bias of H_s^{swm} with respect to both H_s^{ers} and H_s^{top}. Taking advantage of the spectral information provided by one partner of the collocated pairs, stratification of the full H_s sample with respect to spectral properties could be made. The slight underestimation of H_s^{swm} could be attributed to the underestimation of high windseas by the SWM. The altimeter and SWM–retrieved swell wave heights were in very good agreement. The windsea underestimation could not be unambiguously attributed to a single cause.

3. The third part of this work is devoted to detailed global and regional intercomparisons of monthly and seasonal mean WAM and SWM–retrieved spectral parameters. The time series of SWM-retrieved and WAM-derived monthly mean significant wave heights H_s in various ocean basins show good overall agreement, but with a small systematic underestimation of H_s by the WAM model. A decomposition of the wave spectra into windsea and swell reveals an average 10 % overprediction of the windsea by the WAM model, while swell is underpredicted by 20 to 30 %. The positive windsea bias exhibits no clear wave height dependence, while the negative swell bias decreases with swell wave height. This could be due to a too strong damping source term in the WAM model at low frequencies. The windsea overestimation is attributed to erroneous wind forcing. This is in accordance with both wave assimilation studies, and with comparisons between ERS-1 scatterometer and ECMWF surface wind fields. Detailed spatial and temporal intercomparisons are presented for retrieved and modelled windsea and swell wave heights, wave lengths and propagation directions. Evidence is found that the wave field carries a signature of a misalignment between the wind vector and the wind stress, the latter being rotated towards the direction of the swell part of the wave spectrum. In addition to identifying large scale wave model or wind field deficiencies, the regional investigations point to the existence of smaller scale phenomena which may not be adequately reproduced by the WAM model at the present resolution of the wind forcing. Finally, an intercomparison is made of the observed and modelled azimuthal cut-off length scales. The adjustment of the retrieval algorithm to reproduce the observed cut-off length scale is found to be very effective. Computed ratios of the observed azimuthal cut-off wavenumber to the mean azimuthal wavenumber component indicate that about 75 % of the swell can be directly resolved by the SAR, whereas about 70 % of the windsea spectra lie at least partially beyond the cut-off. A global map of seasonal mean cut-off length scales indicates that stronger cut-offs generally occur in regions of strong wind activity and, as expected from the fetch laws, in closed regional ocean basins. A linear relationship between the cut-off and the wind speed without consideration of the stage of development was unable to explain the observed relationship.

4. In the fourth part, the use of ERS-1 SWM–retrievals for dynamical investigations of the WAM model was demonstrated through a case study. The classical experiment conducted by *Snodgrass et al.* [1966] in the Pacific was repeated, based however upon an entirely different measurement technique: swell evolving from an individual storm event in the South Pacific was tracked along its propagation through the Pacific over a ten day period by means of ERS-1 SAR data. Wave height tracking was found to be difficult. The most likely reason is the effect of shadowing by islands, part of which is not resolved by the WAM. A method was proposed to validate the SWM–retrieved wavelength, using independent information but without reference to other than the SWM data. The SWM–retrieved wavelength was successfully validated, and was found to deviate significantly from the WAM simulation. A too weak wind forcing was suggested to have caused the discrepancy. This was confirmed by ERS-1 scatterometer winds that were measured simultaneously to the SWM spectra. Whereas the scatterometer measurement had to rely on a close overflight of the space–time localized storm event itself, the SAR could still detect the storm's impact on the wave field for several days in various regions. Finally, spectral wave age was found to be a useful quantity for dynamical analyses of wave propagation by the WAM model.

In summary, the benefit of ERS-1 SAR wave mode spectral data for improving global wave modelling was clearly demonstrated. Ocean wave spectra were reliably retrieved from SAR imagette spectra. Signatures were revealed in the wave field of erroneous winds produced by the atmospheric model, and of remaining deficiencies in the representation of the momentum transfer at the air–sea interface. These studies corroborate the potential of spectral wave data for monitoring global wave spectral climatology, and the benefit of combined use of different spaceborne remote sensing instruments for instrument and model validation. More insights into the dynamics at the wavy air–sea interface can be expected with the data already provided by ERS-1/2 and anticipated from ENVISAT.

ZUSAMMENFASSUNG

Seit dem Start des europäischen Fernerkundungssatelliten ERS-1 im Jahre 1991 stehen erstmals global, kontinuierlich und in Quasi-Echtzeit detaillierte spektrale Informationen des Seegangs zur Verfügung. Die mit dem Radar mit synthetischer Apertur (SAR) an Bord des ERS-1, im sog. Wellenmodus (engl.: SAR wave mode, SWM) betrieben, gewonnenen Daten erlauben erstmals eine globale Validierung spektraler Eigenschaften des u.a. am Europäischen Zentrum für Mittelfristige Wettervorhersage (EZMW, engl: ECMWF) operationell betriebenen Seegangsmodells WAM. Das WAM-Modell berechnet das zweidimensionale Seegangsspektrum in jedem Punkt eines sphärischen Gitters durch Lösung der spektralen Energiebilanzgleichung mit den Quellfunktionen für die Windanfachung, die nichtlinearen Wellen-Wellen-Wechselwirkungen sowie die Dissipation. Es wird durch Vektorfelder der Winde in 10 m Höhe, welche generell Modellanalysen entstammen, angetrieben.

Notwendige Vorarbeit für eine korrekte Nutzung der Daten war die Ableitung von Seegangsspektren aus den gemessenen SWM Bildspektren mit Hilfe des jüngst entwickelten WASAR-Algorithmus. Dieser Algorithmus basiert auf der Invertierung einer geschlossenen nichtlinearen spektralen Integraltransformation sowie auf einem Verfahren zur iterativen Verbesserung des hierzu notwendigen Eingangsspektrums erster Schätzung (engl.: first guess input spectrum). Die Eingangsspektren wurden mit dem operationellen WAM-Modell am EZMW berechnet.

Im Zentrum dieser Arbeit steht ein drei Jahre umfassender, globaler Satz von ERS-1 SWM-Daten zwischen Januar 1993 und Dezember 1995. Die Analyse dieser Daten geschieht in vier Teilen:

1. Vor der Nutzung der Daten stand eine umfangreiche Untersuchung verschiedener Aspekte der Datenqualität und der Algorithmengüte. Eine kombinierte Analyse der Qualität des von der Europäischen Raumfahrtbehörde ESA in Quasi-Echtzeit verteilten SWM-Produktes sowie der Güte des WASAR-Algorithmus ergab, daß insgesamt aus ca. drei viertel der SWM-Daten zuverlässige Seegangsspektren abgeleitet werden konnten. Die ein- bzw. zweifache Iteration des Eingangsspektrums führte zu einer deutlichen Verbesserung der Güte des Algorithmus. Für operationelle Anwendungen, bei denen ein Kompromiß zwischen Rechenzeit und Genauigkeit gefunden werden muß, empfiehlt sich daher eine zweifache Iteration des Eingangsspektrums. Um die Abhängigkeit des WASAR-Algorithmus vom gewählten Eingangsspektrum abzuschätzen, wurden Sensitivitätsexperimente durchgeführt, in welchen das Eingangsspektrum auf verschiedene Arten verändert wurde (Änderungen der spektralen Energie, der Frequenz sowie der Richtung). Die Auswertung eines größeren Ensembles WASAR-abgeleiteter Seegangsspektren ergab nur eine schwache Änderung der aus modifizierten Eingangsspektren abgeleiteten gegenüber den aus unmodifizierten Eingangsspektren abgeleiteten Seegangsspektren.

2. Komplementär zu den Analysen von Datenqualität und Algorithmengüte wurden alle aus SWM-Daten abgeleiteten signifikanten Wellenhöhen H_s^{swm}, die global für das Jahr 1994 zu Verfügung standen, mit unabhängigen, kollokierten Daten validiert. Letztere wurden mit den satellitengestützten ERS-1 (H_s^{ers}) und TOPEX (H_s^{top}) Altimetern gewonnen. Es ergab sich eine generell gute Übereinstimmung, wenngleich eine geringfügige Unterschätzung der mittleren H_s^{swm} im Vergleich zu H_s^{ers}

und H_s^{top} sichtbar war. Die Ausnutzung der spektralen Information, die für einen der Partner der kollokierten Datenpaare bekannt war, erlaubte eine Aufteilung des Gesamtdatensatzes in Untermengen, bestehend aus Fällen reiner Dünung sowie Fällen reiner Windsee. Auf diese Weise gelang es, spektrale Unterschiede in die Validierung von Wellenhöhen miteinzubeziehen. Die geringfügige Unterschätzung der mittleren H_s^{swm} ließ sich auf eine Unterschätzung der aus SWM-Daten abgeleiteten Wellenhöhe der Windsee zurückführen. Die Wellenhöhe der von SWM und Altimetern gemessenen Dünung zeigte hingegen eine sehr gute Übereinstimmung. Die Unterschätzung der Windsee konnte nicht auf eine einzelne Ursache zurückgeführt werden.

3. Im Zentrum des dritten Teils der Arbeit stehen globale und regionale Vergleiche monatlicher und saisonal gemittelter spektraler Parameter zwischen ERS-1 SWM-Daten und kollokierten WAM-Simulationen. Zeitserien von aus ERS-1 SWM-abgeleiteten (H_s^{swm}) und WAM-simulierten (H_s^{wam}) signifikanten Wellenhöhen in verschiedenen Ozeanbecken stimmen generell gut überein, jedoch mit eine leichten, systematischen Unterschätzung durch das WAM-Modell. Eine Zerlegung der vollen Seegangsspektren in Windsee- und Dünungsanteile als erster Schritt spektraler Untersuchungen offenbart eine ca. 10-prozentige Überschätzung der Modellwindsee, im Gegensatz zu einer 20 bis 30-prozentigen Unterschätzung der Modelldünung. Während die positive Differenz der Windseewellenhöhen keine klare Abhängigkeit von der Wellenhöhe selbst aufweist, nimmt die Differenz der Dünungswellenhöhen mit zunehmender Wellenhöhe selbst ab. Dies wird wahrscheinlich durch eine zu starke Dämpfung der niedrigen Frequenzen im WAM-Modell verursacht. Die Überschätzung der Modellwindsee läßt sich auf fehlerhafte Windantriebsfelder zurückführen. Dieses Resultat paßt sowohl zu neuen Assimilationsstudien von Seegangsspektren, aus denen Windfeldkorrekturen bestimmt wurden, als auch zu Vergleichen der EZMW-Windfelder mit ERS-1 Scatterometerbeobachtungen. Im weiteren Verlauf der Arbeit werden räumliche und zeitliche Vergleiche von SWM-abgeleiteten und WAM-simulierten Windsee- und Dünungswellenhöhen, Wellenlängen sowie Ausbreitungsrichtungen durchgeführt. Die Vergleiche enthalten u.a. Hinweise darauf, daß das gemessene Seegangsfeld eine Signatur einer Abweichung zwischen Windrichtung und Windschubspannung in Form einer Drehung der Windschubspannung in Richtung bestimmter Dünungssysteme trägt. Über die Identifikation großskaliger Abweichungen zwischen Modell und Beobachtung hinaus, deuten regionale Untersuchungen auf kleinerskalige Phänomene hin, die von dem WAM-Modell entweder aufgrund seiner Auflösung oder der Auflösung der Antriebswindfelder nicht simuliert werden konnten. Den Abschluß des dritten Teils bilden Vergleiche zwischen beobachteter und simulierter Abschneidungslängenskala in Azimuthrichtung von SAR-Spektren (engl.: azimuthal cut-off length scales). Die Anpassung der simulierten an diese jedem SAR-Bildspektrum inhärenten Längenskala durch den WASAR-Algorithmus erwieß sich als sehr effektiv. Die Bestimmung des Verhältnisses zwischen beobachteter azimuthaler Abschneidungswellenzahl und Komponente der mittleren Wellenzahl spektraler Teilsysteme (engl.: spectral partitionings) in Azimuthrichtung für ein größeres Ensemble von Daten zeigte, daß etwa 75 Prozent der Dünung explizit vom SAR aufgelöst werden konnte, wohingegen ca. 70 Prozent der Windsee mindestens partiell unterhalb der durch die azimuthale Abschneidung begrenzten Auflösung liegt. Eine globale Verteilung der saisonal gemittelten azimuthalen Abschneidungswellenlänge λ_c wies höhere Wellenlängen generell in Starkwindgebieten sowie in geschlossenen regionalen Becken, in denen das Wachstum des Seegangs durch eine limitierte Windwirklänge (engl.: fetch-limited) eingeschränkt ist, auf. Ein linearer Zusammenhang zwischen λ_c und der Windgeschwindigkeit in 10 m Höhe u_{10} erwies sich jedoch ohne weitere Berücksichtigung von Windwirklänge und Entwicklungsstadium als ungenügend.

4. Im vierten Abschnitt der Arbeit wird die Anwendung der ERS-1 SWM-Daten für dynamische Untersuchungen des WAM-Modells anhand eines Fallbeispiels untersucht. Das klassische Experiment zur großskaligen Dünungspropagation, welches *Snodgrass et al.* [1966] im Pazifik durchgeführt hat-ten, wurde anhand satellitengestützter Meßinstrumente wiederholt: die von einem einzelnen Sturmereignis im Südpazifik ausgestrahlte Dünung wurde bei ihrer Ausbreitung durch den Pazifik anhand von ERS-1 SAR-Daten über einen Zeitraum von zehn Tagen hinweg verfolgt. Eine quantitvative Verfolgung von Wellenhöhen erwies sich dagegen als schwierig. Als Hauptursache hierfür ist der Abschattungseffekt zahlreicher Inseln im Pazifik zu sehen, die nur teilweise vom WAM-Modell aufgelöst sind. Eine Methode zur Validierung der SWM-abgeleiteten Wellenlänge wurde vorgeschlagen, die zwar unabhängig von der genauen lokalen Messung ist, aber dennoch keinerlei anderer als der SWM–Daten bedarf. Hiermit wurden die in diesem Fallbeispiel SWM-abgeleiteten Wellenlängen erfolgreich validiert. Weiterhin zeigte sich eine deutliche Abweichung zwischen gemessenen und beobachteten Wellenlängen. Als Ursache für diese Abweichungen wurden wiederum fehlerhafte Windantriebsfelder vermutet. Dies konnte anhand von ERS-1 Scatterometerwinden, die gleichzeitig mit den SWM-Daten gemessen wurden, verifiziert werden. Während die Verifikation darauf angewiesen war, daß der Satellit den Sturm tatsächlich zur richtigen Zeit an der richtigen Stelle überflog, konnten die Seegangsmessungen mittels SWM den Einfluß, den der Sturm dem Wellenfeld eingeprägt hatte, noch mehrere Tage später an verschiedenen Orten nachweisen. Schließlich wurde gezeigt, daß eine weitere Modellgröße, das spektrale Wellenalter, nützlich für dynamische Untersuchungen der Seegangsausbreitung sein kann.

Zusammenfassend konnte der Nutzen der globalen, kontinuierlichen Messung von ERS-1 SWM-Spektren für eine Verbesserung des globalen Seegangsmodells WAM demonstriert werden. Die hierzu notwendige Ableitung von Ozeanwellenspektren aus den gemessenen SAR-Bildspektren erwies sich als erfolgreich. Weiterhin wurden Signaturen im beobachteten Seegangsfeld gefunden, die zum einen fehlerhafte Windanfachungen belegen und zum anderen auf eine ungenügende Darstellung des Impulsaustausches zwischen Atmosphäre und Ozean hindeutet. Diese Arbeit bestärkt das Potential satellitengestützter spektraler Seegangsbeobachtungen für die Errichtung spektraler Klimatologien. Sie untermauert zudem den Nutzen des kombinierten Einsatzes verschiedener Meßinstrumente für Instrumenten- und Modellvalidierungen. Weitere Erkenntnisse über die Dynamik der Austauschprozesse an der Grenzschicht zwischen Atmosphäre und Ozean, die durch das Seegangsfeld entscheidend beeinflußt wird, sind anhand der bereits existierenden Daten von ERS-1/2 sowie der in naher Zukunft von ENVISAT zu Verfügung stehenden Messungen zu erwarten.

Contents

List of Tables

List of Figures

Note to readers

A new information medium, the World Wide Web (WWW), has grown rapidly over the past few years. While the information density still varies considerably from site to site, occasionally witnessing poor information-to-click ratios, the majority of homepages, particularly within the remote sensing as well as the numerical wheather prediction and climate modelling community, provide useful in-depth and up-to-date information. Furthermore, many services are currently preparing WWW access to their data bases, enabling easy dissemination of available data to the user community. Taking this development into account, we have added WWW links to important sites at the end of the bibliography. References in the text are indicated as [WWW]. Note, that this list is certainly far from complete.

For German readers not familiar with certain aspects covered in this work, an English/German dictionary of some technical terms has been added in Appendix E. Abbreviations and acronyms used in the present work are listed in Appendix D.

1 INTRODUCTION

1.1 Scientific background

One of the major drivers of the first European Remote Sensing Satellite *ERS-1* [WWW], launched on 17 July 1991, was applications in wave research and wave forecasting. Through the wave mode of the synthetic aperture radar (SAR) ERS-1 provided for the first time detailed spectral information on the sea state globally, continuously and in quasi-real time, far beyond the capabilities of other wave observation systems. These unprecedented data allow for the first time a global spectral validation of the state-of-the-art wave model WAM.

The potential of forthcoming ERS-1 wave data has been a strong motivation for significant advances in wave modelling (an extensive historical account as well as comprehensive overview of the field is given in *Komen et al.* [1994]; among earlier monographes are *Kinsman* [1965] and *Phillips* [1977]). Wave modelling has to account for the different processes of wave generation by the wind, nonlinear interactions, wave propagation and dissipation. First important developments were made in the mid-fifties when it was recognized that promising advances could only be achieved through a statistcal description of the wave field. *Pierson et al.* [1955] introduced the concept of the wave spectrum, for which a transport or energy balance equation was subsequently proposed by *Gelci et al.* [1957]. A significant step was the derivation of a general expression for the source function in the energy balance equation consisting of three terms which incorporate the basic physical processes of wave generation by the wind, nonlinear conservative spectral energy transfer, and white capping dissipation, governing the dynamics of surface waves [*Hasselmann, K.* 1960]. By the mid-sixties explicit representations were available for the wind input source term [*Phillips* 1957]; [*Miles* 1957], as well as for conservative nonlinear interactions among different wave components [*Hasselmann, K.* 1961, 1963a,b], forming the basis of first generation spectral wave prediction models. However, in first generation models nonlinear effects were largely simplified or neglected altogether, thus avoiding an explicit modelling of the complete energy balance and resulting in a decoupled representation of the wave dynamics. Although of some success, these wave models were not able to account for some essential observed properties of growing windsea spectra. Gradually it was recognized that the nonlinear interactions played a central role for wave growth. This was confirmed through extensive field measurements under fetch-limited conditions by *Mitsuyasu et al.* [1971], and by *Hasselmann, K. et al.* [1973] in the Joint North Sea Wave Project (JONSWAP).

A significantly revised view of the spectral energy balance emerged, which found its way into wave modelling through the development of more sophisticated, second generation models (see the detailed review of the Sea Wave Modeling Project by the *SWAMP Group* [1985]). The representation of the nonlinear source term in second generation models is still based on a parametrization which is gauged on a family of spectral distributions. This effectively leads to a parametrical description of the windsea in terms of a few spectral parameters. This, and the limitation of the interactions to a set of idealized reference distributions, prevent an accurate description of the transition regime between windsea and swell in ceasing or turning wind conditions, and of complex sea states encountered in the open ocean.

Therefore, today's global third generation wave models like the WAM [*WAMDI Group* 1988] integrate the basic energy balance equation from first principles without introducing prior assumptions on the spectral shape. The physical processes are fully incorporated into the three source terms. Despite the WAM's success, confirmed through many validation and application studies, uncertainties remain in all three source terms. The least well known is the dissipation source term which is supposed to be dominated by wave breaking. The lack of knowledge of the absolute magnitude of dissipation, nevertheless, can be largely compensated through an adequate adjustment of the wind input source term, particularly in the equilibrium range of the spectrum. Although the parametrization of the wind input to the waves in the WAM is based on a two-way interaction between the wind and the waves, the exact approach of a sea state dependent parametrization is still subject to discussion. Finally, the representation of the nonlinear interactions rests upon a discrete interaction approximation as exact transfer computations are still too cpu time consuming. Uncertainties remain as to the reliability of the implemented approximation under complex situations of turning winds and windsea–swell transitions.

The development of improved ocean wave models for operational wave forecasts and the computation of wave climatologies from past wind field data is of considerable economic benefit for numerous activities, such as ship routing [*Lehner et al.* 1996], fisheries, off-shore operations and coastal protection (see e.g. *ESA* [1996]). Such improvements have to rely on increasingly detailed wave measurements which, on a global scale, can only be provided through satellite remote sensing.

An optimal way to combine satellite data with model predictions is through the use of data assimilation techniques (see e.g. *Komen et al.* [1994] and references therein). Operational assimilation of wave data from spaceborne instruments has so far been restricted to significant wave height, obtained from the ERS-1 altimeter [*Lionello et al.* 1992, 1995]; [*Janssen et al.* 1996]. Although assimilation was found to be beneficial, assimilation of a single parameter such as H_s alone limited the improvement in forecast as the assimilation acts upon the total spectrum rather than discriminating between different wave systems (such as windsea and swell) which ought to be adjusted separately and in a different manner (see e.g. *Voorrips et al.* [1996]). Therefore, improved assimilation schemes have recently been developed which are able to assimilate individual spectral components of the wave field on the basis of SWM spectral retrievals. These can be broadly classified into local, optimal interpolation schemes [*Hasselmann, S. et al.* 1994]; [*Hasselmann, S. et al.* 1997]; [*Breivik et al.* 1997]; [*Voorrips and de Valk* 1997], and non-local schemes using a Green's or impulse response function approach [*Bauer et al.* 1996a] (see also *Bauer et al.* [1996b, 1997] for a direct comparison of both schemes). Although spectral assimilation schemes have not yet been implemented operationally at ECMWF, their benefit was clearly revealed in the above studies.

Owing to the sensitivity of the surface wave field to the wind, and to the advection of the transferred momentum by the waves, the wave field remembers the wind's impact for up to several days. When assessing the performance of a wave model, effects of an erroneous forcing wind field thus have to be taken into account as a possible error source besides pure model deficiencies Various studies have repeatedly attributed deviations between model simulations and observation to erroneous winds rather than to inaccurate representation of physical processes in the model [*Komen et al.* 1994]; [*Graber et al.* 1995]. Therefore, assimilation of spectral wave data not only leads to improved wave fields but also to wind field corrections. In this way, accurate wave models combined with spectral wave measurements enables the validation of the surface winds of atmospheric general circulation models (GCMs).

Beyond practical applications, an understanding of the dynamics of waves is essential also for an improved understanding of the mechanisms that govern the transfer of momentum, sensible and latent

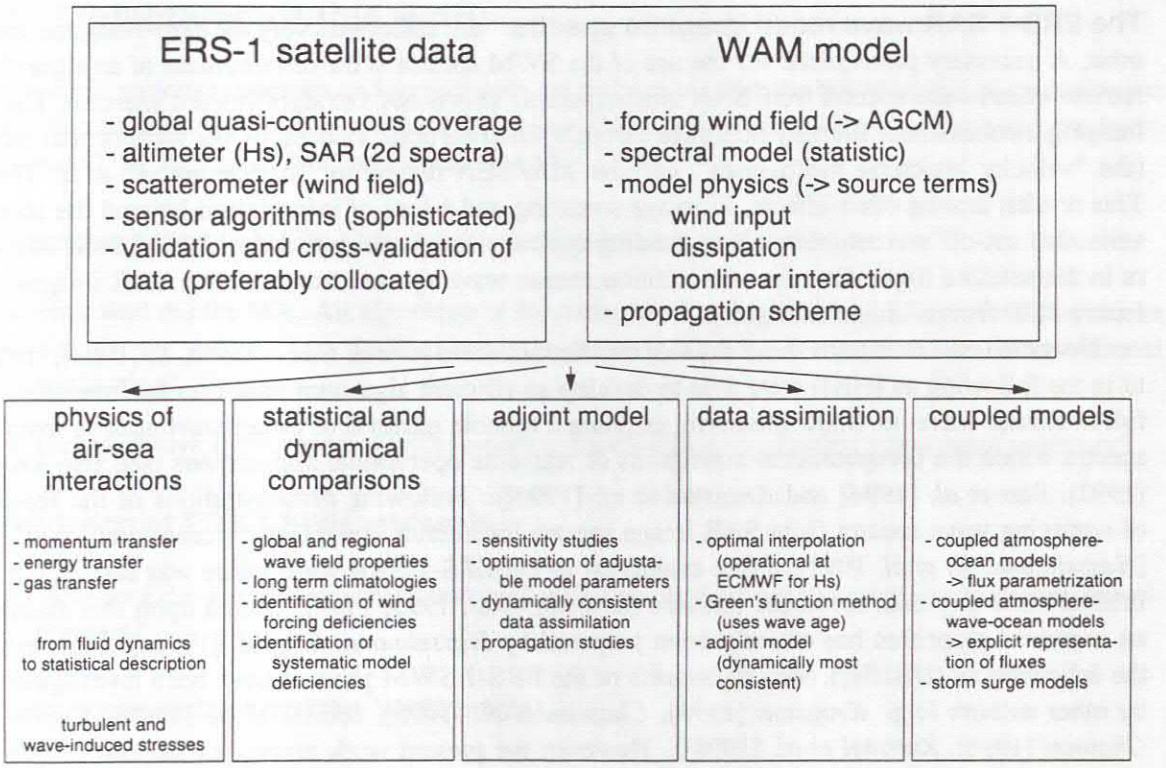

Figure 1.1: Aspects of combined modelling and observation of ocean waves.

heat and gases such as CO_2 across the air-sea interface – an area of research that is rapidly gaining significance through the development of sophisticated global coupled ocean–atmosphere–carbon cycle climate models (*Hasselmann, K.* [1991]; *Komen et al.* [1994]; *Weber et al.* [1993]; *Mastenbroek et al.* [1993]; *Jähne and Monahan* [1995]; *Janssen and Viterbo* [1996]; *Weisse and Alvarez* [1997]).

An important branch of research of air–sea interactions focuses on an accurate representation of the wind stress from air-sea bulk transfer coefficients, especially the relationship between the wind stress, wind profile and sea state (cf. Section 2.4) which is important for studies of the wind-driven ocean circulation. The dependence of wind stress on sea-state is still an open question (cf. Section 2.5). In addition, recent results indicate that the wind stress vector may not be aligned with the wind in the presence of long swell (Section 2.6). Spectral wave data are indispensable to resolve these questions.

Various groups have begun recently to investigate long-term wave climatologies with the aim to assess possible changes of wave climate due to long-term natural variability such as the North Atlantic Oscillation (NAO), anthropogenic greenhouse warming, or other climate changes (see e.g. *Bacon and Carter* [1991]; *von Storch et al.* [1993]; *WASA Group* [1995, 1998]; *Bouws et al.* [1996]; *Kushnir et al.* [1997]; *Bauer et al.* [1998]). Continuous global wave field observations would be valuable for such studies as the integration of wind effects by the waves cannot be recovered from impacts on wave height alone but translates into more complex spectral properties.

The manifold aspects of the intimate relationship between wave modelling and detailed global continuous observation of spectral properties of the wave field, and their combined use for various applications are summarized in a schematic overview (Figure 1.1). The ERS-1 SAR wave mode data and the WAM model form the cornerstones of the present work.

The ERS-1 SAR wave mode imagette spectra are collected every 200 km along the satellite orbit. A necessary prerequisite for the use of the SWM spectra is the development of an algorithm to retrieve ocean wave spectra from SAR image spectra. This is not a straightforward exercise. The SAR imaging mechanism is strongly nonlinear through the distortions induced by the wave orbital motions (the "velocity bunching mechanism", cf. the MARSEN review in *Hasselmann, K. et al.* [1985]). This results, among other effects, in image smearing and a loss of information beyond the so-called azimuthal cut-off wavenumber, corresponding typically to wavelengths shorter than about 100 – 200 m in the satellite flight direction. In addition, ocean wave spectra from satellite SAR images suffer from a 180° frozen-image ambiguity.

Nevertheless, even with these limitations, *Hasselmann, K. and Hasselmann, S.* [1991], (referred to in the following as [HH]) were able to develop an efficient algorithm based on the inversion of the full nonlinear wave–to–SAR transform, enabling a reliable retrieval of ocean wave spectra from SAR spectra within the computational constraints of real-time operational applications (see also *Krogstad* [1992], *Bao et al.* [1994] and *Krogstad et al.* [1994]). Following demonstrations of the feasibility of retrieving wave spectra from SAR image spectra for aircraft and the first ocean satellite SEASAT [*Hasselmann, K. et al.* 1991], a first evaluation of the ERS-1 SAR wave mode was carried out for a limited three–day data set in the Atlantic [*Brüning et al.* 1993, 1994]. Based upon this evaluation, an improved algorithm has recently been proposed by *Hasselmann, S. et al.* [1996a], (referred to in the following as [HBHH]). Various aspects of the ERS-1 SWM product have been investigated also by other authors (e.g. *Krogstad* [1994], *Chapron et al.* [1995], *Breivik et al.* [1995], *Kerbaol and Chapron* [1996], *Kerbaol et al.* [1998]). However, the present work represents the first attempt at a global assessment of detailed wave spectral properties of several years of ERS-1 SWM data.

The WAM model constitutes the second major ingredient of this work. It is used to provide the first guess for the wave spectral retrievals, and we shall use the WAM model predictions again in intercomparing the modeled and retrieved wave spectra. The approach is not as circular as this may appear, since it has been demonstrated in [HBHH], and is further verified in this work, that the improved retrieval algorithm used here is insensitive to the initial input spectrum. The first guess information is used essentially only to remove the 180° ambiguity and augment the retrieved spectrum beyond the azimuthal cut-off.

The WAM model now runs routinely at most operational forecasting centres and has been implemented at more than 100 research institutions. It has been extensively validated locally through case studies and field data, including fetch-limited wave growth conditions and extreme storm conditions, and on a statistical basis against buoy data (for an extensive overview see *Komen et al.* [1994]).

Global validation of the WAM model using spaceborne data has so far been limited to H_s data derived from satellite altimeters. A comprehensive compilation of WAM validation studies using spaceborne altimeter data from SEASAT (1978), GEOSAT (1985–1989), ERS-1 (1991–1996) and TOPEX/POSEIDON (since 1992) as well as a direct global intercomparison between ERS-1 and TOPEX altimeter significant wave heights is given in *Bauer and Staabs* [1998].

Because of their limitation to significant wave heights, altimeter data, although providing continuous global coverage, are of limited value when trying to detect detailed deficiencies in the spectral properties of a wave model. Spaceborne SARs, operated in low bit rate sampling mode, are at present the only instruments able to provide the required detailed two-dimensional spectral data with continuous global coverage.

1.2 Objectives of this work

In this work, various properties and applications in conjunction with the WAM model of spectral wave data collected from spaceborne synthetic aperture radars operated in intermittent sampling mode are investigated. In particular, four main issues are addressed:

1. Assessment of satellite data quality and retrieval performance

- How well did the WASAR algorithm of *Hasselmann, S. et al.* [1996a, 1998] perform to retrieve ocean wave spectra from SAR wave mode spectra? What are the implications for operational application?
- How sensitive is the retrieval with respect to modifications in the first guess input spectrum?

2. Validation of ERS-1 SWM retrievals

- How do ERS-1 SWM retrievals compare with independent measurement from spaceborne altimeters?

3. Satistical validation of the WAM model

- An assessment is given of typical windsea and swell conditions as observed and modelled in various parts of the oceans, stratified with respect to various spectral properties.
- Systematic model deficiencies are identified that were previously unrecognized due to the lack of observational spectral data of global coverage.
- Mechanisms which might explain the discrepancies between model and observation are identified. Among the main candidates to be considered are:
  - Errors in the driving wind field
  - Insufficient representation of certain aspects of the nonlinear wave–wave interactions
  - Insufficient representation of the propagation and dissipation of swell
  - Influence of the assimilation of ERS-1 altimeter–derived H_s

4. Analysis of the dynamics of wave propagation

- Complementary to statistical intercomparisons, individual events are investigated to resolve dynamical details. In particular, the propagation across the ocean of swell from individual storm events is analyzed. Such investigations were proposed e.g. by *Sverdrup and Munk* [1947]. Corresponding in–situ measurements were carried out in a large scale experiment by *Snodgrass et al.* [1966], but were limited to stations along a single reference great circle. After a long period of stagnation, the ERS-1 SWM retrievals with their continuous global coverage enable the issue to be re-addressed.
- Investigate the discrepancies between model and observation, as revealed in the statistical intercomparison, for individual events.

1.3 Data and models used

ERS-1 SAR wave mode spectra The spectral wave data were collected by the ERS-1 SAR operated in the low bit rate intermittent sampling mode (SAR wave mode, SWM; cf. Section 4.2.5). They are disseminated by the European Space Agency [*ESA* WWW] as part of the fast delivery product (FDP) via the Global Telecommunication System (GTS) to the major forecasting services in near real–time. To retrieve ocean wave spectra from SAR image spectra as proposed by [HBHH], the *WASAR* [WWW] algorithm was implemented, essentially through merging and extending pre-existing components [*Hasselmann, S. et al.* 1998] (cf. Section 4.5). For the present work, three years of wave spectra were retrieved from SWM data between January 1993 and December 1995, and archived together with collocated WAM model spectra.

WAM model spectra The model investigated is the state-of-the-art, third generation wave model *WAM* [WWW] in its present cycle 4 [*WAMDI Group* 1988]; [*Günther et al.* 1992]; [*Komen et al.* 1994] (cf. Chapter 3). Two sets of model data are at our disposal:

- The main set was produced operationally at the European Centre for Medium-Range Weather Forecasts *ECMWF* [WWW], Reading (UK). The operational runs were performed every six hours, corresponding to one assimilation time step of ERS-1 altimeter data. The model spectra were collocated to the ERS-1 SWM spectra available in near real–time. This collocated set for the three years of data, together with the ECMWF analyzed surface wind vector at all ERS-1 SWM locations, consitutes the main data set of this study.

- A global run of the WAM model was conducted at MPI for austral winter JJA 1995. The model set-up and wind forcing was identical to the ECMWF set-up, but without the assimilation of altimeter data. The model was furthermore extended by a module kindly provided by E. Bauer to compute detailed wave age spectra at all model grid points [*Bauer et al.* 1996a]. The reason for re-running the wave model was twofold:
  - The impact of the assimilation of ERS-1 altimeter wave heights on the ECMWF wave products and their global statistical properties needed to be assessed.
  - The spectral wave age is a useful quantity for dynamical investigations related to wave propagation over large distances. In the context of ocean swell propagation, spectral wave age enables one to trace back swell to its origin in space and time.

Other data This study profited from the availability of satellite data from different sensors and different satellites for verifying hypotheses that were raised in the course of the work.

- The validation of H_s retrieved from SWM data during the year 1994 (Chapter 6) was based on altimeter data collected by the TOPEX and the ERS-1 altimeter (cf. Section 4.2.3). The ERS-1 altimeter data were also part of the ESA FDP, and obtained via ECMWF. The TOPEX data were provided as offline product by *AVISO* [WWW], Toulouse (France).

- Hypotheses raised in Chapter 9 on erroneous wind fields of individual storm cases were tested through the use of wind vectors retrieved from the ERS-1 scatterometer (WNS, cf. Section 4.2.4). The WNS data are offline products processed at the French ERS Processing and Archiving Facility (F-PAF) *CERSAT* [WWW] and distributed on CD-ROM.

1.4 Outline of the performed analyses

To retrieve ocean wave spectra from the ERS-1 SWM data, the *WASAR* [WWW] algorithm [*Hasselmann, S. et al.* 1996a, 1998] was implemented, essentially through merging and extending pre-existing components (Section 4.5). The retrievals were performed for a set of three years of ERS-1 SWM data. The SWM-retrieved and collocated model wave spectra and wind vectors were archived in the data storage facility of the German Climate Computing Centre *DKRZ* [WWW].

Prior to application, the SWM data and their wave spectral retrievals were subject to various analyses (Chapter 5; see also *Heimbach et al.* [1998]). The SWM data quality, their operational availability and the WASAR algorithm performance were assessed (Section 5.1). Given the complexity of the retrieval algorithm, operational aspects were considered regarding the iterative improvement of the input spectrum (Section 5.2). An important motivation for extending the original inversion algorithm of [HH] was to improve the algorithm's robustness with respect to changes of the first guess input spectrum. Therefore, the sensitivity of the WASAR algorithm with respect to the first guess is assessed in some detail (Section 5.3).

Complementary to the quality and performance analyses, a global validation of SWM–retrieved significant wave heights was performed, using independent data from the ERS-1 and the TOPEX altimeters (Chapter 6; see also *Bauer and Heimbach* [1998]). Although limited in scope to one single parameter of the full wave spectrum, such an assessment is essential to increase confidence in the SWM retrievals, and to detect remaining deficiencies. Taking advantage of the spectral information provided by one partner of the collocated pairs, stratification of the full H_s sample with respect to spectral properties, e.g. of windsea and swell, could nevertheless be made (Section 6.3).

An important part of this work is devoted to global and regional intercomparisons of integral and spectral properties between the SWM retrievals and WAM model data (Chapter 7; see also *Heimbach et al.* [1998]). The aim is to assess significant deviations between model and observations, in particular those which are manifested on larger ocean basin scales, and those which are expressed through the detailed spectral properties. Statistical properties of collocated bivariate sets of monthly WAM and SWM–derived total, windsea, and swell wave heights are investigated in different ocean basins (Sections 7.1 and 7.2). Stratification with respect to windsea and swell is the first step of a decomposition of the spectra into their main wave components. Global and regional distributions of seasonal mean windsea and swell properties are computed for different seasons (Section 7.3 to 7.6). A variety of phenomena are revealed, part of which can be attributed to wind field or model deficiencies, and part of which call for more detailed investigation.

Besides the quantities inferred from the ocean wave spectra, an additional parameter, the r.m.s. orbital velocity retrieved from the SWM spectra, is investigated (Chapter 8). This is inferred from the azimuthal cut-off length scale inherent in SAR image spectra of ocean waves. It is essentially determined by the high frequency part of the spectrum, and thus represents an estimate of the part of the wave spectrum which in general cannot be resolved by the SAR. Interesting questions are: how well do retrieved wave spectra simulate the observed cut-off; which fraction, on average, of windsea and swell is actually resolved by spaceborne SARs despite the cut-off; how does the global distribution of the cut-off look like; and to what degree can it be related to the local wind?

The last part of this work features a case study in which swell generated from a single storm event in the South Pacific is tracked by the ERS-1 along its propagation over a ten day period (Chapter 9). The study demonstrates the applicability of SWM spectral retrievals for detailed investigation of the WAM model and reveals some interesting dynamical aspects. A further quantity, the full two-dimensional spectral wave age, is found to be helpful for dynamical analyses. A method is developed for validating the SWM–retrieved wavelength of swell from a common source. Finally, ERS-1 scatterometer data are invoked to confirm the hypothesis of an erroneous wind forcing, inferred from wave mode vs. wave observation deficiencies. These findings fit well into the statistical analyses presented earlier (cf. Section 7.4).

As an introduction to the field of wave modelling, Chapter 2 gives an overview of the current status of wave modelling and momentum transfer across the wavy air-sea interface in the presence of waves. The first part (Section 2.1 – 2.3) is meant as an introduction to the fundamental concepts of wave modelling, including weak nonlinear interaction theory of statistical wave fields, and their evolution described in terms of the energy balance equation with non-vanishing source terms. The second part (Section 2.4 – 2.5) reviews recent attempts to improve the coupling coefficients which parametrize the air flow over waves, and enter the growth rate coefficient of the wind input source term. Finally, new observational findings on the misalignment between wind speed and wind stress are reviewed (Section 2.6). There is some evidence that these effects can account for some of the differences between WAM and SWM–retrieved directional properties discussed in Section 7.4.

2 SURFACE WAVES IN THE OCEAN

2.1 Wave solutions of the Navier–Stokes equations

The coupled atmosphere–ocean represents a complex dynamical system which exhibits many forms of fluid motions within and at the interface of the two sub-systems. These motions can be classified into *laminar* (or organised) flows, *turbulent* flows and *wave* motions.

Turbulent vs. wave motions The basic difference between waves and turbulence is the dominance of a conservative restoring force in the case of waves, which increases linearly as the fluid elements depart from their equilibria. The presence of this linear restoring force establishes a functional relationship between the wave frequency ω and wavenumber $\boldsymbol{k}$, called *dispersion relation* $\omega = f(\boldsymbol{k})$, which is absent in turbulent flows. Thus, wavelike disturbances propagate through the background medium at a specific group velocity $\boldsymbol{v_g} = \partial\omega/\partial\boldsymbol{k}$, whereas turbulent disturbances are advected with the mean flow and are subject to nonlinear diffusion.

Directly related to the existence of a dispersion relation is the degree of nonlinearity of the motions arising through the momentum advection term in the Navier–Stokes equations. The dispersion relation, which is ideally fulfilled under linear conditions, can still be maintained under weakly nonlinear conditions, but will eventually break up as the motions become strongly nonlinear and the transition from waves to turbulence occurs. In the spectral domain this translates into weak nonlinear interactions among different wave components for wavelike motions, whereas in turbulent flows, all Fourier components are coupled and interact strongly. For near-linear nondissipative waves, interactions between different Fourier components can exchange energy if certain resonance conditions are satisfied over time scales that are long compared to the individual wave periods. For shorter time scales the amplitude A_k can be considered as constant. In terms of their wavenumber k such waves, called *small amplitude waves*, fullfil the relation $A_k k \ll 1$.

Many types of wave motions are encountered in the ocean which can directly be attributed to their characteristic forcing and restoring forces. Mathematically, all these can be recovered from the same fundamental system of Navier–Stokes equations by considering the contributions of the various terms under specific approximations. Although we shall focus only on surface gravity waves, we briefly sketch the derivation of the main types of waves in the ocean from the basic governing equations [*Lighthill* 1978]; [*LeBlond and Mysak* 1978].

Approximations to the Navier–Stokes equations Motions in the ocean or atmosphere are characterised by a set of variables of density ρ, momentum $\rho\boldsymbol{u}$, pressure p, temperature T and salinity S (for the ocean) or specific humidity q (for the atmosphere). The equations governing the motion consist of a system of conservation laws for ρ, $\boldsymbol{u}$, p, T, together with a thermodynamic equation of state for S or q. In the present context of oceanic gravity waves and momentum transfer across the air–sea interface the set of equations can be reduced to the conservation of mass and momentum. Under suitable assumptions these equations form a closed set for the variables $\boldsymbol{u}$ and p.

- *Conservation of mass* is expressed in its general, full compressible form by

$$\frac{\partial}{\partial t}\rho + \boldsymbol{\nabla}\cdot(\rho\,\boldsymbol{u}) = 0 \tag{2.1}$$

As a first approximation we assume that the oceanic fluid is *incompressible* and *nondiffusive* in terms of temperature and salinity. An analysis of the conservation law of internal energy an the state equation for the density $\rho = \rho(T,p)$ (see e.g. *Pedlosky* [1987]) then reduces equation (2.1) to $\partial\rho/\partial t + \boldsymbol{u}\cdot\boldsymbol{\nabla}\rho = 0$ under the side condition of a nondivergent flow, $\boldsymbol{\nabla}\cdot\boldsymbol{u} = 0$.

- *Conservation of momentum* in combination with the above approximation,

$$\frac{\partial}{\partial t}\rho u_i + \frac{\partial}{\partial x_j}\,(\rho u_i\,u_j) \overset{\substack{\text{incompressible}\\ \text{nondiffusive}}}{=} \rho\frac{\mathrm{D}}{\mathrm{D}t}\,u_i = \sum_n (\boldsymbol{F}^n)_i$$

leads to the *Navier–Stokes equations* identical to Newton's law of motion for a fluid continuum in a rotating coordinate system

$$\rho\,\frac{\mathrm{D}}{\mathrm{D}t}\boldsymbol{u} = -\rho\boldsymbol{\nabla}\Phi - 2\rho\,\boldsymbol{\Omega}\times\boldsymbol{u} - \boldsymbol{\nabla}p + \nu\,\Delta\boldsymbol{u} + \boldsymbol{F} \tag{2.2}$$

where $\mathrm{D}\boldsymbol{u}/\mathrm{D}t = \partial\boldsymbol{u}/\partial t + (\boldsymbol{u}\cdot\boldsymbol{\nabla})\,\boldsymbol{u}$ denotes the total (or Lagrangian) derivative following the fluid element, $\rho u_i\,u_j = (\boldsymbol{\tau})_{ij}$ represents the momentum flux or momentum stress tensor, and $\boldsymbol{F}^n$ are the forces acting upon the fluid. The terms appearing in equation (2.2) represent the gravitational force, with geopotential Φ, the Coriolis force with frequency $\boldsymbol{\Omega}$ of the Earth's rotation, the pressure gradient force, the frictional force or molecular diffusion of momentum due to the kinematic viscosity ν vanishes for incompressible flows), and other forces, including tidal forces (for a more complete treatment see e.g. *Batchelor* [1967]).

From equation (2.2) the main types of waves in the ocean may be derived by noting that under specific assumptions regarding the relevant spatial and temporal scales of the motion individual terms in the equation dominate to act as forcing and restoring. For ocean surface waves several approximations to the Navier-Stokes equations can be made.

1. The motion is incompressible and nondivergent, i.e. $\boldsymbol{\nabla}\cdot\boldsymbol{u} = 0$.
2. The motion is inviscid, i.e. kinematic (or molecular) viscosity can be neglected, $\nu = 0$.
3. The motion is stationary, i.e. $\frac{\partial\boldsymbol{u}}{\partial t} = 0$, implying that $\frac{p}{\rho} + \Phi + \frac{1}{2}|\boldsymbol{u}|^2$ is a conserved quantity along each streamline (Bernoulli's theorem).
4. The motion is irrotational, i.e. the relative vorticity vanishes, $\boldsymbol{\omega} = \boldsymbol{\nabla}\times\boldsymbol{u} = 0$. Such flows are also called *potential flows* because the velocity field can be derived from a potential ϕ through $\boldsymbol{u} = -\boldsymbol{\nabla}\phi$. The continuity equation reduces to a *Laplace equation*, $\Delta\phi = 0$.
5. The density can be assumed to be constant, $\rho =$ const., buoyancy effects thus being neglected. For internal gravity waves, for which density effects play an important role, the Boussinesq approximation is generally applied, assuming a hydrostatic equilibrium $\frac{\partial}{\partial z}p_0 = -g\rho_0$ which is perturbed, introducing a buoyancy acceleration [*Turner* 1973].

6. Three further approximations relevant for large-scale flows on a rotating sphere, the *β-plane and f-plane approximation*, and the *geostrophic approximation* are not relevant for ocean surface waves. In fact, for ocean surface waves the Coriolis term can be neglected (it yields a small perturbation of the dispersion relation, slightly turning the second order Stokes drift [*Backus* 1962] and on large scales the great circle propagation path).

In order to solve the homogeneous nonlinear system of partial differential equations, boundary values must be prescribed both at the upper moving as well as at the lower rigid boundary, ζ and $-h$, respectively. The full set of equations relevant for surface gravity waves then reads in terms of the velocity potential ϕ and the surface elevation ζ

$$\begin{aligned}
\Delta\phi &= 0 \quad \text{for} \quad z < \zeta && \text{(conservation of mass,} \\
& && \text{continuity equation)} \\
\tfrac{\partial\phi}{\partial t} + g\zeta + \tfrac{1}{2}(\nabla\phi)^2 &= 0 \quad \text{for} \quad z = \zeta && \text{(conservation of momentum, dynamic} \\
& && \text{boundary condition at the free surface)} \\
\tfrac{\partial\zeta}{\partial t} - \tfrac{\partial\phi}{\partial z} + \tilde{\nabla}\zeta \cdot \tilde{\nabla}\phi &= 0 \quad \text{for} \quad z = \zeta && \text{(kinematic boundary condition} \\
& && \text{at the free surface)} \\
\tfrac{\partial\phi}{\partial z} &= 0 \quad \text{for} \quad z = -h && \text{(kinematic boundary condition} \\
& && \text{at the bottom)}
\end{aligned} \tag{2.3}$$

together with some initial conditions for ζ and ϕ (tilda ˜ denotes two-dimensional, horizontal quantities). Wave solutions are inferred from the linearized form of equation (2.3) by expressing the solutions for ζ and ϕ in terms of Fourier modes of the horizontal wavenumber vector $\boldsymbol{k} = (k_x, k_y)^t$ and the wave angular frequency ω. One obtains the dispersion relation for surface gravity waves with two limiting cases:

$$\omega^2 = gk \tanh kh \approx \begin{cases} gk & \text{for } kh \gg 1, \text{ deep-water waves} \\ gk^2 h & \text{for } kh \ll 1, \text{ shallow-water waves} \end{cases} \tag{2.4}$$

In the following we shall deal exclusively with deep-water waves encountered in the open ocean.

2.2 Statistical description of the wave field

The wave variance spectrum By the mid-fifties it was recognized that a dynamical theory of surface waves had to rely on a statistical description of the wave field in terms of the wave spectrum. The step of converting the deterministic initial value problem to a statistical problem is achieved by assuming that in the linear approximation the sea state is homogeneous and stationary. It then follows from the Central Limit Theorem that the wave field is Gaussian [*Hasselmann, K.* 1968]; *Komen et al.* [1994], which can thus be described by the two-dimensional energy spectrum.

We consider the sea surface elevation $\zeta(\boldsymbol{x}, t)$ at the location $\boldsymbol{x}$ and time t to consist of a superposition of approximately free Fourier wave components

$$\zeta(\boldsymbol{x}, t) = \sum_{\boldsymbol{k}} \{\zeta_{\boldsymbol{k}} \exp[\mathrm{i}(\boldsymbol{k} \cdot \boldsymbol{x} - \omega t)] + \text{c.c.}\} \tag{2.5}$$

Here $\boldsymbol{k} = (k_1, k_2)^t$ denotes the horizontal wavenumber vector and ω the angular frequency obeying the dispersion relation for surface gravity waves equation (2.4). If we assume the wave field to be homogeneous in space and stationary in time, the two-point covariance function

$$\mathcal{F}(\boldsymbol{\xi}, \tau) = < \zeta(\boldsymbol{x} + \boldsymbol{\xi}, t + \tau)\, \zeta(\boldsymbol{x}, t) >$$

leads to the following conditions for the Fourier coefficients:

$$\begin{aligned} < \zeta_{\boldsymbol{k}_1} \zeta_{\boldsymbol{k}_2} > &= 0 \quad \text{for all} \quad \boldsymbol{k}_1, \boldsymbol{k}_2 \\ < \zeta_{\boldsymbol{k}_1} \zeta^*_{\boldsymbol{k}_2} > &= 0 \quad \text{for} \quad \boldsymbol{k}_1 \neq \boldsymbol{k}_2 \\ < \zeta_{\boldsymbol{k}} \zeta^*_{\boldsymbol{k}} > &= F(\boldsymbol{k})\, \mathrm{d}\boldsymbol{k} \,/\, \rho g \end{aligned}$$

The brackets $< \, . \, >$ denote ensemble means (we shall assume ergodicity in the following). We have introduced the *wave variance spectrum* $F(\boldsymbol{k})$ (also called energy density spectrum) which, integrated over the wavenumber domain yields the total wave energy per unit surface area (in spatial domain):

$$E = \rho g < \zeta^2 > = \rho g \int F(\boldsymbol{k})\, \mathrm{d}\boldsymbol{k}$$

Linear dispersive waves which are homogeneous and stationary obey Gaussian statistics, i.e. the Fourier components are independent and the field statistics is fully determined by the variance spectrum. However, in the real ocean the wave motions are subject to the Navier–Stokes equations (i.e. its approximation equation (2.3)) which also contain nonlinear terms. As long as the nonlinear interactions are weak, the Gaussian property can still be maintained approximately, so that the description in terms of the wave spectrum F is still meaningful. However, the wave spectrum now becomes a locally defined quantity , $F(\boldsymbol{k}) \longrightarrow F(\boldsymbol{x}, \boldsymbol{k}, t)$, which slowly varies with $\boldsymbol{x}$ and t, and for weak-in-the-mean processes satisfies

$$\frac{1}{k_i} \frac{\partial F}{\partial x_i} \ll F, \qquad \frac{1}{\omega} \frac{\partial F}{\partial t} \ll F \tag{2.6}$$

WKB approximation, ray theory and the energy balance equation A first important step towards numerical wave modelling was the introduction of a balance equation for the wave action or spectral energy density describing the dynamics of the local wave spectrum introduced above (*Gelci et al.* [1957] and *Hasselmann, K.* [1960]; see also *Whitham* [1964]; *Bretherton and Garrett* [1969]; *Willebrand* [1975]; *Komen et al.* [1994]). Waves satisfying the relation (2.6) can be represented through WKB trains of the form

$$\zeta(\boldsymbol{x}, t) = a(\boldsymbol{x}, t)\, \mathrm{e}^{i\, S(\boldsymbol{x}, t)} + \text{c.c.} \tag{2.7}$$

with slowly varying amplitude $a(\boldsymbol{x}, t)$ and phase function or eikonal $S(\boldsymbol{x}, t)$. The local wavenumber $\boldsymbol{k}$ and frequency ω are then given by $\boldsymbol{k} = \boldsymbol{\nabla}_{\boldsymbol{x}} S$ and $\omega = -\frac{\partial}{\partial t} S$, the latter expression being formally equivalent to a Hamilton-Jacobi equation for a wave front in wave optics. In general, ω is given by a dispersion relation determined by an intrinsic frequency σ of the free wave solutions (equation (2.4)), which in the presence of a current $\boldsymbol{U}$ is modified through a Doppler shift:

$$\begin{aligned} \omega(\boldsymbol{x}, t) &= \Omega\, [\, \boldsymbol{k}(\boldsymbol{x}, t), \boldsymbol{U}(\boldsymbol{x}, t)\,] \\ &= \boldsymbol{k} \cdot \boldsymbol{U}(\boldsymbol{x}, t) + \sigma(\boldsymbol{k}, \boldsymbol{x}) \end{aligned} \tag{2.8}$$

For such wave fields the spectral wave action density $N(\boldsymbol{k}, \boldsymbol{x}, t) = F(\boldsymbol{k}, \boldsymbol{x}, t)/\sigma(\boldsymbol{k}, \boldsymbol{x})$ is a conserved quantity. The corresponding conservation law reads

$$\frac{D}{Dt} N = \frac{\partial}{\partial t} N + \dot{\boldsymbol{x}} \cdot \boldsymbol{\nabla}_{\boldsymbol{x}} N + \dot{\boldsymbol{k}} \cdot \boldsymbol{\nabla}_{\boldsymbol{k}} N = 0 \tag{2.9}$$

It can be expressed in 4-dimensional phase space $(\boldsymbol{x}, \boldsymbol{k})$ in terms of the Poisson-bracket $\{.,.\}$ for Hamiltonian vector fields in the simple form of Liouville's theorem

$$\frac{\partial}{\partial t}N + \sum_{i=1}^{2}\left(\frac{\partial\Omega}{\partial x_i}\frac{\partial N}{\partial k_i} - \frac{\partial\Omega}{\partial k_i}\frac{\partial N}{\partial x_i}\right) = \frac{\partial}{\partial t}N + \{\Omega, N\} = 0 \tag{2.10}$$

The time derivatives $\dot{\boldsymbol{x}}$ and $\dot{\boldsymbol{k}}$ satisfy Hamiltonian-type equations of motion

$$\begin{aligned} \dot{\boldsymbol{x}} &= \boldsymbol{\nabla}_{\boldsymbol{k}}\Omega \quad \text{(propagation)} \\ \dot{\boldsymbol{k}} &= -\boldsymbol{\nabla}_{\boldsymbol{x}}\Omega \quad \text{(refraction)} \end{aligned} \tag{2.11}$$

The characteristic propagation velocity $\dot{\boldsymbol{x}} = \boldsymbol{\nabla}_{\boldsymbol{k}}\Omega$ is then given by the sum of the wave group velocity $v_{gr} = \boldsymbol{\nabla}_{\boldsymbol{k}}\sigma$ and the current velocity $\boldsymbol{U}$. In the following we shall neglect the effect of currents, i.e. $\boldsymbol{U} = 0$. Equation (2.11) then forms the basis for identifying free travelling waves with particles that propagate along rays (i.e. great circles on the sphere). In the following we consider deep water waves for which $\omega(\boldsymbol{k}, \boldsymbol{x})$ is independent of $\boldsymbol{x}$ so that the refraction term in equation (2.9) vanishes.

In the presence of interactions or external forcings the evolution of the wave spectrum can be attributed to the slow evolution of the WKB wave amplitudes by averaging over the fast moving wave components (WKB averaging). Then the wave action or energy is only adiabatically conserved for the fast moving waves. For weak nonlinear Gaussian processes the conservation laws can be extended to balance equations by introducing source functions on the r.h.s. of equation (2.9). The remaining imbalance is incorporated into the source terms. The corresponding balance equation for the energy spectrum $F(\boldsymbol{k}, \boldsymbol{x}, t)$ reads

$$\frac{D}{Dt}F = S_{tot} = \sum_j S_j\,(F, \dots) \tag{2.12}$$

where $(, \dots)$ stands for additional external parameters such as the wind.

Shortly after the introduction of a balance equation by *Gelci et al.* [1957], a basic classification of the physical processes governing the evolution of wave spectra in terms of the source function was proposed by *Hasselmann, K.* [1960]. The source function S_{tot} was considered to be the sum of three terms, representing the generation of waves by the wind S_{in}, the nonlinear interactions among different wave components S_{nl}, and the dissipation due to turbulent wave breaking S_{ds}.

$$\frac{\partial}{\partial t}F + \dot{\boldsymbol{x}}\boldsymbol{\nabla}_{\boldsymbol{x}}F = S_{in} + S_{nl} + S_{ds} \tag{2.13}$$

It is the starting point of the modelling of the dynamics of surface waves.

2.3 Weak nonlinear interaction theory

The role of weakly nonlinear interactions among surface gravity waves was first discussed by *Phillips* [1960] and *Hasselmann, K.* [1960]. At the same time *Hasselmann, K.* [1961, 1963a,b, 1966] pioneered the stochastic description of weak nonlinear interactions allowing the source terms in the energy balance equations to be expressed in terms of the wave spectrum. Interactions among different wave components were treated as perturbations of the wave spectrum in terms of higher order products of wave spectral components. Similarly, this theory allowed to recover several fluid dynamical processes of wave generation by the wind proposed by *Miles* [1957] and *Phillips* [1957] through the statistical description of the interaction of the wave field with the atmospheric fluctuating fields *Hasselmann, K.* [1966, 1967, 1968]. Finally, also processes which are locally strongly nonlinear but still weak-in-the-mean, including turbulent bottom friction [*Hasselmann and Collins* 1968] and white capping dissipation *Hasselmann, K.* [1974], could be treated in this framework. As these concepts were a fundamental prerequisite for the successful development of numerical wave prediction models, the main steps are recalled in the following (different aspects are reviewed in *LeBlond and Mysak* [1978], *Phillips* [1981], *Zakharov et al.* [1992], *Hammack and Henderson* [1993] and *Komen et al.* [1994]).

2.3.1 General considerations

Essentially, all processes which contribute to the source terms are nonlinear perturbations of the Gaussian wave field, since they introduce an imbalance in the conservation equation (2.9). On the fundamental level of the Navier-Stokes equations, these are provoked by the nonlinear Reynolds terms. However, for weakly nonlinear processes, characterized by the relation (2.6), the Gaussian property of the wave field is still maintained approximately. This has two important consequences:
1. Although perturbations act primarily on the wave amplitude $a(\boldsymbol{x}, t)$ (and possibly on the eikonal), for Gaussian processes the functional describing the changes in the wave amplitudes appearing in the source function can always be reduced to a functional of the second moments of the wave amplitudes, i.e. the wave spectrum. Thus, the energy balance equation for such processes closes on itself.
2. It is worthwile to specify the degree of nonlinearity, since it turns out that most of the processes have a rather simple representation in terms of the wave spectrum. Hence, while the perturbations of the wave field are nonlinear, many of the processes are described by source functions which are quasi-linear in the wave spectrum. To be more precise, the following processes can be distinguished:

1. *Expansible processes:* Let χ be a perturbative process of the wave variable $a_{\boldsymbol{k}}$ ($a_{\boldsymbol{k}}$ is obtained through a suitable transformation of the wave amplitude to normal mode coordinates). In general, χ is a functional of all wave variables as well as external parameters $\chi = \chi(\ldots, a_{\boldsymbol{k}'}, a_{\boldsymbol{k}}, \ldots)$. If χ can be adequately expanded in a Taylor series with respect to the wave variables $a_{\boldsymbol{k}}$ then the process is called expansible. For such processes, the corresponding source function which is a functional of the form $S[<\chi(\ldots, a_{\boldsymbol{k}'}, a_{\boldsymbol{k}}, \ldots)a^*_{\boldsymbol{k}}>]$ can be written in a closed series expansion of the wave spectrum $F(\boldsymbol{k})$. Three cases can be distinguished:

    (a) *Processes independent of the wave spectrum:* For such processes the perturbation is independent of the wave field. The source function has the simple form $S = \alpha$. *Phillips* [1957] theory of wave generation belongs to this class.

    (b) *Processes quasi-linear in the wave spectrum:* The source term is linear in the wave spectrum, $S(\boldsymbol{k}) = \beta F(\boldsymbol{k})$, with a coefficient β which can still depend on integrals over products of the spectrum. The dynamics is quasi-decoupled in spectral domain (although a residual coupling might still be present through β). Such a situation is desirable from a computational point of view since the energy balance equation can be effectively integrated without coupling of different wave components. *Miles* [1957, 1959a,b] theory of wave generation belongs to this class.

    (c) *Processes nonlinear in the wave spectrum:* Higher-order perturbations of the wave field translate into higher-order products of the wave spectrum appearing in the source function. The conservative nonlinear energy transfer among different wave components derived by *Hasselmann, K.* [1961, 1963a,b] belongs to this class.

2. *Non-expansible but still weak-in-the-mean processes:* Perturbations χ, which are strongly nonlinear locally, cannot be expanded in a series in terms of the wave field $a_{\boldsymbol{k}}$ anymore. However, if such perturbations are still weak-in-the-mean (relation (2.6)), then the perturbed wave field itself still admits an expansion in terms of the unperturbed wave field. It was shown by *Hasselmann, K.* [1974] that the source function for such processes always admits to lowest order a quasi-linear representation, i.e. $S(\boldsymbol{k}) = \beta F(\boldsymbol{k})$. The quasi-linear form holds for many processes which are presumably strongly nonlinear locally, including wave damping by turbulent bottom friction [*Hasselmann and Collins* 1968] and wave dissipation due to white capping [*Hasselmann, K.* 1974]. Also *Jeffreys* [1925, 1926] theory of wave generation is assumed to admit a quasi-linear source function.

In the following we discuss the main processes governing the evolution of surface waves, i.e. the resonant nonlinear energy transfer, the wave generation by the wind, and the dissipation in terms of their source functions. The essential aspect for wave modelling is to assess to what degree the source functions which incorporate the underlying physical processes yield accurate descriptions of the spectral evolution.

2.3.2 Conservative resonant wave–wave interaction and energy transfer

In the Hamiltonian picture a quadratic Hamiltonian accounts for linear free wave theory. A perturbation Hamiltonian is then introduced which is expanded in terms of the canonical wave coordinates that can directly be related to components of the wave variance spectrum. The expansion is carried out to third order in the wave spectrum. For surface gravity waves first and second order perturbations have no secular contributions which would contribute to conservative resonant energy transfer. The second order terms only allow resonant three-wave interactions by which two waves excite a third passive wave mode. This appears to be insufficent to produce linear, resonant wave growth of surface gravity waves, since the underlying dispersion relation prevents the resonance conditions for $\boldsymbol{k}$ and ω to be fulfilled (in contrast to capillary and internal waves, for which the energy transfer is consequently stronger than for surface waves, see e.g. *Willebrand* [1975]). The third order perturbation in the wave spectrum yields a resonance condition for three interacting waves to produce a new fourth (passive) wave thereby transfering energy into a new spectral component. The contributing waves are interpreted as a wave quadruplet which fulfill the resonance interaction conditions in $\boldsymbol{k_i}$ and $\omega_i(\boldsymbol{k_i})$

$$\begin{aligned} \boldsymbol{k_1} + \boldsymbol{k_2} &= \boldsymbol{k_3} + \boldsymbol{k_4} \\ \omega_1 + \omega_2 &= \omega_3 + \omega_4 \end{aligned}$$

The Boltzmann integral for the transfer rate of spectral energy of ocean gravity waves was first derived by *Hasselmann, K.* [1961]. It has the form of a source term appearing on the r.h.s. of equation (2.12) which is nonlinear in the wave spectrum:

$$\begin{aligned} \frac{\partial}{\partial t} F(\boldsymbol{k_4}) = \int\!\!\int\!\!\int & T(\boldsymbol{k_1}, \boldsymbol{k_2}, \boldsymbol{k_3}, \boldsymbol{k_4}) \cdot \delta(\boldsymbol{k_1} + \boldsymbol{k_2} - \boldsymbol{k_3} - \boldsymbol{k_4}) \cdot \delta(\omega_1 + \omega_2 - \omega_3 - \omega_4) \\ & \cdot \Big\{ F_1 F_3 \big[F_4 - F_2 \big] + F_2 F_4 \big[F_3 - F_1 \big] \Big\} \, \mathrm{d}\boldsymbol{k_1} \mathrm{d}\boldsymbol{k_2} \mathrm{d}\boldsymbol{k_3} \end{aligned} \tag{2.14}$$

$T(\boldsymbol{k_1}, \boldsymbol{k_2}, \boldsymbol{k_3}, \boldsymbol{k_4})$ denotes the coupling coefficient, while the δ–functions take care of the resonance conditions to be fulfilled. In *Hasselmann, K.* [1963a] the analogy to collision theory of a statistical ensemble of mass particles was established by recognizing that the wave–particle analogy also holds for weak nonlinear perturbation theory. Concrete transfer computations were performed in *Hasselmann, K.* [1963b], revealing the following properties of the energy transfer:

- The transfer process will tend to reduce sharp peaks in the spectrum and redistribute energy more uniformely over all wavenumbers. However, the transfer to frequencies far below the peak is inhibited by the dependency of the transfer coefficient on ω^8
- Besides the energy flow to high wavenumbers which is dissipated at small scales, analogue to the energy cascade in turbulence spectra, there is an energy flow to small wavenumbers which leads to a gradual shift of the peak towards low wavenumbers. The transfer in both directions is a consequence of the simultaneous conservation of mean energy and mean wave action.
- There is a tendency to an equipartition of the energy among all four interacting wave components. This phenomenon is known as the principle of detailed balance in statistical mechanics.
- Most of the energy flux is due to interactions in regions of high energy density near the peak

These properties of the conservative resonant interactions have a shape-stabilizing effect on the spectrum. This, and the importance of these interactions for wave growth and generation of swell has convincingly been confirmed for a specific class of spectra subject to fetch- and duration-limited conditions in the Joint North Sea Wave Project (JONSWAP) [*Sell and Hasselmann* 1972]; [*Hasselmann, K. et al.* 1973]. However, the explicit computation of the full Boltzmann integral equation (2.14) under general conditions is a yet technically prohibitive task, given the excessive amount of computing time required. Therefore, present day third generation wave models such as the WAM [*WAMDI Group* 1988] rely on approximate expressions which cover a sufficiently large variety of sea spectral conditions. The discrete interaction approximation implemented in the WAM was developed by *Hasselmann, S. and Hasselmann, K.* [1985] and *Hasselmann, S. et al.* [1985a] (an improvement has recently been proposed by *Snyder et al.* [1993]), and tested under complex, turning and ceasing wind conditions which have to account for turning windseas and windsea-swell transitions [*Young et al.* 1987]; [*Young and van Vledder* 1993].

Nevertheless, complex sea state conditions like those described above are difficult to be measured in the open ocean. Therefore, some uncertainty remains in the representation of such conditions in the present approximation (cf. e.g. *Fradon* [1997] for recent results of the SEMAPHORE experiment). Spectral wave data are needed to address this issue in more detail.

2.3.3 Resonant wave–atmosphere interactions

In *Hasselmann, K.* [1967, 1968] the analogy with collision theory was further explored through the introduction of Feynman rules known from statistical and quantum field theory.

More important, the weak nonlinear interaction theory was extended to include resonant interactions with external fluctuating fields. The latter fields may be identified with atmospheric turbulent wind fields or eddies representing small-scale or large-scale turbulence. In contrast to wave–wave interactions the external interactions are non-conservative and already contribute to first order. The complete set of lowest–order transfer processes for resonant wave–atmosphere interactions is given by four source terms $S_j(\boldsymbol{k})$ which depend in different ways on the wave spectral components $F(\boldsymbol{k})$:

$$S_1 = \alpha, \qquad S_3 = F(\boldsymbol{k}) \int \gamma(\boldsymbol{k},\boldsymbol{k}')F(\boldsymbol{k}')\,\mathrm{d}\boldsymbol{k}'$$

$$S_2 = \beta F(\boldsymbol{k}) \qquad S_4 = -\delta F(\boldsymbol{k}) + \int \epsilon(\boldsymbol{k},\boldsymbol{k}')F(\boldsymbol{k}')\,\mathrm{d}\boldsymbol{k}'$$

The coupling at the air-sea interface and back-interactions of the wave fields on the external fields are assumed to be included in the coupling coefficients $\alpha, \ldots, \epsilon$. These source terms can be attributed to different wave generation theories, some of which were previously introduced from fluid dynamical considerations. These are:

S_1: Phillips' theory of wave generation by constant energy transfer to the wave field through turbulent atmospheric pressure fluctuations *Phillips* [1957]

S_2: Miles' critical layer theory of unstable coupling between the wave field and the mean laminar boundary layer shear flow *Miles* [1957, 1959a,b, 1960, 1961, 1962, 1967]

S_3: a nonlinear correction of Miles' theory

S_4: energy transfer due to wave–turbulence interactions (*Hasselmann, K.* [1967]).

S_5: A further term S_5, similar in form to S_2, is assumed to represent *Jeffreys* [1925, 1926] theory of wave growth. According to this *sheltering hypothesis*, air flowing over water waves is sheltered on their lee side. The wind can do work against the waves through a pressure difference leading to wave growth. This theory may not be deduced from an expansible perturbative process, but is still weak-in-the-mean to admit a quasi-linear representation.

Owing to the genral structure $\partial F/\partial t = S$ (equation (2.13)), the coupling coefficients $\alpha, \ldots, \epsilon$ can be interpreted as growth rates of the wave spectrum. We emphasize that the main mechanisms proposed to explain the growth of surface waves are recovered within a single theory. This fact can be considered as a further success of the weak nonlinear interaction approach of statistical fields. The determination of the correct wind input physics reduces to two main aspects:

1. Which form of the source function dominates the wave growth?

2. What is the exact form of the coefficients $\alpha, \ldots, \epsilon$ of the relevant source term, and on which air-sea coupling parameters does it depend?

In the following we briefly discuss the first point, deferring 2. to a more detailed overview in Sections 2.4 and 2.5.

Many observations in the past indicate that the main processes governing the wind input are quasi-linear in the wave spectrum. Phillips' theory yields a linear growth of the wave spectrum which seems to be ineffective compared to quasi-linear approaches which yield exponential growth rates [*Snyder and Cox* 1966]. Nevertheless, linear growth sitll is of some importance in the initial stage of wave generation. The processes associated to S_3 and S_4 are assumed to be weak or can be parametrized in the quasi-linear source term at the present level of accuracy. Today's third generation wave models are based on Miles' critical layer mechanism of wave growth. Laboratory measurements indicate that Jeffreys' competing sheltering hypothesis seems to yield too low pressure differences to account for the observed wave growth. However, its role in wave generation is still a matter of discussion (cf. Section 2.5). An answer to this question has to rely on an appropriate representation of the growth rate β which depends on an appropriate parametrization of the momentum transfer in terms of air-sea coupling parameters to be discussed in Section 2.5. However, the consideration of these transfer processes has to take into account the dominant role of the nonlinear energy transfer and the dissipation during wave growth. Therefore, at any stage of wave growth, the parametrization of the air-sea momentum transfer of Section 2.5 is linked to the spectral balance of Section 2.3.

2.3.4 Weak-in-the-mean dissipation

The following consideraiton is limited to open ocean conditions for which turbulent bottom friction in shallow water [*Hasselmann and Collins* 1968] may be neglected.

Wave breaking is believed to be mainly controlled by white capping dissipation on scales relevant for numerical wave modelling (see e.g. the review by *Melville* [1996] and *Komen et al.* [1994]). The source term S_{ds} of this weak-in-the-mean process was shown to be quasi-linear with a damping coefficient proportional to the square of the wave frequency ω [*Hasselmann, K.* 1974]. However, uncertainties remain as to the contribution of other processes of wave breaking which act over many scales through nonlinear short wave – long wave interactions (cf. e.g. *Hasselmann, K.* [1971]).

Due to its quasi-linearity, white capping dissipation is closely linked to the wind input. Based on the Bight of Abaco measurements by *Snyder et al.* [1981], *Komen et al.* [1984] have modified S_{ds} to allow for an equilibrium range beyond the peak of the spectrum in which the wind input and the dissipation balance. This expression was again modified by *Janssen* [1991] to remain consistent with a newly introduced wave spectrum-dependent drag coefficient in the wind input source function.

The fact that the wave growth beyond the spectral peak is mainly controlled by the net effect of the wind input and dissipation was confirmed through model tuning experiments performed by *Barzel* [1994]. The main unresolved problem thus remains the determination of the absolute magnitude of the individual processes of wave generation and dissipation.

2.3.5 Resonant wave–ocean interactions

The concept of nonlinear interactions between wave fields and external atmospheric fields can be readily adapted to describe the coupling of waves to oceanic motions such as internal waves, horizontal turbulent flows, seismic waves and physical inhomogeneities *Hasselmann, K.* [1966, 1967, 1968]. The lowest–order resonant interactions represent

- linear and nonlinear interactions with mean currents
- generation and scattering of waves by large and medium–scale turbulence
- parametric damping by small–scale turbulence

The turbulence field can be further decomposed into a horizontal part and internal modes comprising internal waves. The wave-ocean coupling is assumed to be weak compared to the processes discussed before. While its role in present day wave models can safely be neglected, it might gain importance with the advent of sophisitcated coupled atmosphere-wave-ocean models such as the ECAWOM [*Weisse and Alvarez* 1997] in which more processes will be resolved leading to improved coupling fluxes.

2.4 Momentum transfer at the air–sea interface

The growth rate β discussed in the previous section incorporates quantities parametrizing the air-sea momentum transfer. These will be seen to be the friction velocity u_* (equation (2.18)), the roughness length z_0 (equation (2.19)), and the Charnock parameter α_{ch} (equation (2.22)). Thus, the growth rate is of the form

$$\beta = \beta(u_*, z_0, \alpha_{ch}) \tag{2.15}$$

In this section we recall some aspects of deriving such air-sea interaction parameters, before reviewing how these can be generalized in the presence of waves in Section 2.5. These generalized parameters, included in the growth rate, yield a two-way interaction between the wave field and the air flow which is accounted for in the integration of the energy balance equation.

The momentum drag by the atmospheric winds on the ocean is responsible for the generation of waves, the development of the ocean mixed layer and the large scale wind-driven ocean circulation.

Near the ocean surface the atmospheric circulation is strongly affected by friction and heating causing profound modifications in the air flow. An atmospheric boundary layer (ABL) establishes, where strong wind shear due to the no-slip boundary condition at the sea surface together with convection due to surface heating lead to strong air–sea interactions through the development turbulence (cf. *Garratt* [1992]). These interactions comprise exchange of matter, energy and momentum (for a recent review of these fluxes, see *Smith et al.* [1996]). In the following we shall be restricted to momentum fluxes under neutral conditions (dynamic turbulence), the extension to sensible and latent heat fluxes (convective turbulence) requiring Monin–Obukhov similarity theory.

2.4.1 Vertical flux of momentum and turbulence closure schemes

The exchange of momentum between atmosphere and ocean appears in the Navier–Stokes equations through the part of the momentum stress tensor describing the vertical flux of momentum:

$$(\tau)_{i3} = \rho < u_i w >, \qquad i = 1, 2$$

This nonlinear term couples a wide range of scales of the wave motions, the smallest of which are gravity-capillary waves of the order of 1 cm wavelength, comparable to the viscous sublayer thickness, while the largest ocean surface waves appear as swell of up to 1 km wavelength, comparable to the whole ABL thickness. The smallest scales cannot be generally resolved by numerical models which simulate the larger scale motions. To circumvene this problem a statistical approach is invoked by seeking equations for the mean flow. To this end the velocity components are decomposed into ensemble mean and fluctuating parts $u_i = \overline{u}_i + u_i'$ where u_i' can be thought of as a combination of zero (ensemble) mean random (turbulent) and wave motions (a similar decomposition holds for p).

The averaged Navier–Stokes equations contain new unknown covariances of the form $\overline{u_i u_j}$ and $\overline{u_i w}$, so-called *Reynolds stresses*, arising through the nonlinear advection term [*Reynolds* 1894]. The equations are not closed since the second order covariances can depend on higher-order covariances. Therefore, at some stage, the higher-order covariances have to be parametrized in terms of known lower-order covariances using some turbulence closure assumption. Following *Peixoto and Oort* [1992], we briefly review commonly used methods of parametrizing momentum exchange across the air–sea interface (see also *Large and Pond* [1981, 1982], or *Kagan* [1995]). A compilation of flux measurements can be found in *Geernaert* [1990], and more recently *Yelland and Taylor* [1996]; *Smith et al.* [1996]; *Hasse and Smith* [1997].

At this stage we emphasize that wave effects are not yet included in all these approaches. In Section 2.5 we shall see how the parametrizations can be extended to take the moving wave field into account. Furthermore, there is increasing evidence that the presence of waves, e.g. swell, ubiquitous in the open ocean, may cause the direction of the surface wind stress to depart siginificantly from the wind direction. We shall review these observational findings which most of the commonly used parametrizations cannot account for in Section 2.6.

Gradient-flux approach In analogy to molecular diffusion the turbulent shear stress in the direction of the flow may be expressed by a Fickian type law (cf *Boussinesq* [1870]):

$$\tau = -\rho K_M \frac{\partial \overline{u}}{\partial z} \qquad (2.16)$$

where K_M denotes the eddy diffusion coefficient of momentum or *eddy viscosity*, analogous to the kinematic molecular viscosity ν. Technically, this approach allows the determination of the shear stress (for constant K_M, or for $K_M = K_M(z)$) from measurements of vertical profiles of the mean wind velocity (cf. *Batchelor* [1967] or *Lesieur* [1990]).

Mixing length approach and wind profiles Extending the molecular analogy, *Prandtl* [1925] devised a physical mechanism for the turbulent exchange of momentum by introducing a vertical *mixing length l* wich plays a similar role as the mean free path in kinetic theory. Assuming isotropic turbulence, i.e. $|u'| \approx |w'|$, the shear stress is given by

$$\tau_{xz} = \rho \overline{u'w'} = -\rho l^2 \left|\frac{\partial \overline{u}}{\partial z}\right| \frac{\partial \overline{u}}{\partial z} \tag{2.17}$$

Assuming a uniform surface under a neutrally stratified boundary layer, so that $\tau_{xz} = \tau_0$, we find

$$\left|\frac{\partial \overline{u}}{\partial z}\right| = \frac{1}{l}\sqrt{\frac{|\tau_0|}{\rho}} = \frac{1}{l}\, u_* \tag{2.18}$$

introducing the *friction velocity* u_*. Finally, we assume that the scale of the mixing elements is proportional to the available space, i.e. $l = \kappa z$, where $\kappa \approx 0.4$ is the von Kármán constant (for a more general expression see *Rossby* [1932]). Integration of $|\partial\overline{u}/\partial z|$ with respect to z then leads to the *logarithmic wind profile* for turbulent flows over smooth surfaces:

$$|U(z)| = \frac{1}{\kappa} u_* \ln \frac{z}{z_0} \tag{2.19}$$

The integration constant z_0, called *roughness length*, plays an important role when describing the modification of the logarithmic wind profile by the rough moving sea surface. The concept of mixing length comes with some severe restrictions because turbulence is assumed to be in a state of local equilibrium exluding situations where marked contributions to the eddy energy budget are made by advective or diffusive transport of eddy energy and ignoring the history of such processes, important for wave dynamics (*Kagan* [1995] and *Mastenbroek et al.* [1996]).

Bulk aerodyamical approach This widely used approach in oceanography in combination with ship measurements (e.g. *Hellerman and Rosenstein* [1983]; *Fairall et al.* [1996]; *Yelland and Taylor* [1996]; *Hasse and Smith* [1997]) expresses the surface stress in terms of the *drag coefficient C_D*

$$\tau_0 = -\rho\, C_D\, |\boldsymbol{u}(z)|\boldsymbol{u}(z) \tag{2.20}$$

In particular, for neutrally stable conditions, using the logarithmic wind profile equation (2.19), the dimensionless drag coefficient at a reference level z_r (usually 10 m height) is given by

$$C_D = \frac{\kappa^2}{\ln^2(z_r/z_0)} \tag{2.21}$$

Like the roughness length z_0, the drag coefficient plays an important role in the generation of waves from the wind and is supposed to be sea state dependent.

Dissipation method This so-called $e - \epsilon$ method is based on the consideration of the balance of turbulent kinetic energy (TKE) in terms of the shear production of TKE P and the TKE dissipation ϵ. The fluxes of fluctuating TKE e' and dissipation ϵ' can again be related to the vertical gradient of their mean quantities introducing an eddy viscosity K_M which is now a function of the mean TKE e and the mean TKE dissipation ϵ through $K_M \sim e^2/\epsilon$. Under various assumptions involving steady, horizontally homogeneous flows, the friction velocity u_* is found to be a function of ϵ (see *Large and Pond* [1981, 1982], *Garratt* [1992], *Kagan* [1995], and *Yelland and Taylor* [1996]).

Eddy correlation approach In principle, $\tau = \rho \overline{u'w'}$ is directly estimated using three-dimensional measurements to estimate the vertical momentum fluxes. Although no assumptions as to the nature of transfer processes are needed, this method requires a large amount of data, fast-response instrumentation and is very sensitive to the instrument orientation for measureing the wind components which is a great handicap on ships and buoys.

Higher-order closures Parametrizations of gradient type which are the basis of first-order closure are not able to describe processes affecting the growth, maintenance and decay of turbulence. Therefore, higher-order closure schemes have to be invoked where the components of Reynolds stresses and eddy fluxes of scalar substances are considered as new unknowns with suitable parametrizations of the third-order terms (see e.g. *Davis* [1972]; *Kagan* [1995]; *Mastenbroek et al.* [1996]).

2.5 Wind-over-wave coupling

The air-sea coupling parameters play an important role in wave modelling since they enter the wind input source term (cf. equation (2.15)). However, all these were derived in the absence of waves. In the following we outline different concepts of how to modify the parametrizations in the presence of waves.

The complexities involved in the intimate interplay between the atmosphere and the ocean were clearly formulated by Charnock as early as 1951 [*Charnock* 1951]. *Rogers* [1995] has pointed out the importance of understanding small scale air–sea interactions which are at the origin of large scale interactions, the two being tied together through parameterizations which need to be continually improved. However, apart from wave modelling, for most applications in physical oceanography sea state dependence is neglected as a source of influence of the coupling parameters . This might be one reason for the significant deviations obtained with different schemes for estimating the momentum fluxes [*Blanc* 1983]; [*Large et al.* 1995].

2.5.1 Smooth vs. rough flow

A first approach to include the influence of the rough sea surface is to distinguish between flow over *smooth* and *rough* surfaces (see *Monin and Yaglom* [1971] and *Kraus and Businger* [1994]). These two regimes correspond to the flow in the viscous and the inertial sublayer of the inner layer of the ABL, respectively. Molecular diffusion rates in laminar flows are three orders of magnitude smaller than the turbulent diffusion analogue. The behaviour of the wind profile $U(z)$ and the roughness length z_0 are summarised in Table 2.1. For smooth flows the roughness elements can be considered to lie within the viscous sublayer and have no effect on the turbulent flow. As the surface roughness increases the roughness elements are considered to be larger than the molecular sublayer, affecting the turbulent flow. The surface characteristics are now parameterised in the logarithmic wind profile.

	smooth flow	rough flow
thickness scale $h_0 = \frac{\nu}{u_*}$	$z \ll h_0$	$z \gg h_0$
wind profile	$u(z) = \frac{u_*^2}{\nu} z$	$u(z) = \frac{u_*}{\kappa} \ln \frac{z}{z_0}$
roughness length	$z_0(\text{smooth}) = \frac{\nu}{\kappa u_*}$	$z_0(\text{rough}) = \frac{\alpha u_*^2}{g}$

Table 2.1: Characterisation of aerodynamically smooth and rough flow.

For sea surfaces the transition from smooth to rough flows occurs as the wind increases [*Phillips* 1977]. Waves become steep or break, thus serving as roughness elements that increase the wind stress. The relationship for $z_0(\text{rough})$ in Table 2.1

$$z_0 = \frac{\alpha_{ch} u_*^2}{g} \tag{2.22}$$

is the so-called *Charnock relation* proposed by *Charnock* [1955] (see also *Charnock* [1981]). Although *Monin and Yaglom* [1971] treat the sea surface as a rough rigid wall resulting in a constant α_{ch} of the order of $0.011 < \alpha_{ch} < 0.018$, it has become clear that the roughness length z_0 must depend upon the sea state and so must the Charnock constant α_{ch} (see e.g. *Phillips* [1977], *Geernaert* [1990], *Donelan* [1990], *Donelan and Hui* [1990] and *Donelan et al.* [1993]).

2.5.2 Effects of the moving surface wave field

The impact of the moving wave field on the wave growth rate β was recognized by *Jeffreys* [1925, 1926] and *Miles* [1957, 1959a,b] leading to their theories of wave generation in which the wave growth depends on the instantaneous wave field (quasi-linear theory – in contrast to *Phillips* [1957] theory which is independent of the wave spectrum, cf. Section 2.3.3). Subsequent field experiments (in particular the Bight of Abaco measurements by *Snyder et al.* [1981]) showed order of magnitude agreement between the observed and predicted growth rates from Miles' theory.

Despite its successful implementation in wave prediction models, Miles's theory suffers from some conceptual shortcomings which will need to be improved if additional transfer processes including heat and gas exchanges are to be included into wave models. The main two problems are discussed in the following.

2.5.2.1 Wave-dependent parameters in the growth rate

Waves affect the air flow and the momentum flux $\boldsymbol{\tau}$ at the air–sea interface through their orbital velocity. This leads to a so-called *wave-induced stress* $\boldsymbol{\tau_w}$ in addition to the turbulent stress $\boldsymbol{\tau_{turb}}$

$$\boldsymbol{\tau} = \boldsymbol{\tau_{turb}} + \boldsymbol{\tau_w}$$

The wave-induced stress incurs a back-interaction of the wave field on the air flow, which has to be accounted for in the growth rate, equation (2.15). Although already noticed by *Stewart* [1961] the impact of the wave field on the air-sea coupling parameters such as the drag coefficient, the roughness length, or the Charnock constant, was only explicitly included in models beginning with *Makin* [1987] and *Janssen* [1989], leading to a two-way interaction of the air flow and the wave field. Today, there exist a variety of approaches for the treatment of this problem. Either the roughness length z_0 itself is considered to be explicitly sea-state dependent, or z_0 is expressed in terms of the Charnock relation equation (2.22) introducing a sea-state dependent Charnock constant α_{ch}, or z_0 is related to the drag coefficient C_D through equation (2.21) introducing a sea-state dependent C_D. These parameters are then expressed in terms of the wave spectrum full $F(f,\theta)$, or of quantities incorporating wave spectral properties such as

- the wave age c_{ph}/u_*
- the fraction of the wave-induced stress to the total stress τ_w/τ
- total wave variance $\text{E} = \int F(f,\theta)\text{d}f\text{d}\theta$.
- the Phillips constant α_p parametrizing the level of the equilibrium range of the wave spectrum

The classification of waves according to their wave age is given in Table 2.2. Additional parameters, reflecting the atmospheric stability (z/L with Obukhov length scale L), the gustiness of the wind field (σ_u/U_{10} with r.m.s. of the wind variance σ_u), and the fetch X will not be further discussed here (for a discussion see *Komen et al.* [1994]). Details of the different approaches may be found e.g. in *Kitaigorodskii* [1973]; *Geernaert* [1990]; *Donelan* [1990]; *Smith et al.* [1992]; *Donelan et al.* [1993]; *Makin et al.* [1995]; *Kagan* [1995]; *Komen et al.* [1998]; *Hasse and Smith* [1997].

young windsea	$c_{ph}/u_* \leq 10-20$
old windsea	$c_{ph}/u_* \approx 20-30$
fully developed	$c_{ph}/u_* \approx 30-40$
swell	$c_{ph}/u_* \geq 30-40$

Table 2.2: Classification of wave age.

In the following we focus on the approach implemented in the WAM model, cycle 4, which was proposed by *Janssen* [1989, 1991, 1992]. The method involves a two-way interaction between the air flow and the wave field. Starting from the logarithmic wind profile, equation (2.19), which relates u_* and $U(z)$, the momentum transfer is given by

$$\tau = \left[\frac{\kappa U(z)}{\ln(z/z_0^J)}\right]^2$$

The sea state dependence is introduced through a Charnock relation which, compared to equation (2.22), has a modified Charnock parameter α_{ch}^J which is no longer constant but sea-state dependent:

$$z_0^J = \frac{\alpha_{ch}^J u_*^2}{g}, \quad \text{with} \quad \alpha_{ch}^J = \frac{\tilde{\alpha}_{ch}}{\sqrt{1-\frac{\tau_w}{\tau}}} \tag{2.23}$$

The value of the Charnock constant $\tilde{\alpha}_{ch}$ as given in the literature varies between 0.0185 to reproduce data for old windsea by *Wu* [1980, 1982], 0.0144 (*Garratt* [1977]), 0.035 (*Kitaigorodskii* [1973]), and 0.011 as proposed by *Janssen* [1989] in combination with the modified version α_{ch}^J. Whenever the wave-induced stress τ_w becomes of the order of the total stress τ (which occurs for young wind sea ripples) the Charnock parameter and thus the surface roughness are significantly enhanced yielding an efficient momentum transfer at the air–sea interface.

It is customary to work in terms of the drag coefficient instead of the roughness length due to the measurement techniques implied. Their role and remaining uncertainties in the context of parametrizations needed for large–scale ocean GCMs is discussed in *Hasse and Smith* [1997]. Using equation (2.22) with a modified roughness length, equation (2.23) leads to the modified drag coefficient in terms of the modified Charnock relation and dimensionless height $\mathcal{Z}$:

$$C_D^J(z) = \left[\frac{\kappa}{\ln(\mathcal{Z}/\alpha_{ch}^J)}\right]^2, \quad \text{with} \quad \mathcal{Z} = \frac{g}{u_*^2}\, z \tag{2.24}$$

The sea state dependence of the drag coefficient as well as the validity of the Charnock relation are still subject to controversial discussions. Recent data collected during the HEXOS campaign [*Smith et al.* 1992] are consistent with a wave age dependent parametrization of the Charnock relation [*Komen et al.* 1998]. However, there is considerable scatter in the data. Furthermore, questions remain as to the representativeness of the HEXOS results for open ocean conditions. In addition, an important problem is the representation of the high wavenumber part of the spectrum (e.g. in terms of the wave age) which supports a subtantial part of the stress. *Makin et al.* [1995] investigate how the detailed spectral form contributes to the formation of the sea drag. The question whether the high wavenumber spectral tail is wave age dependent or not is found to be crucial to determine whether the drag coefficient is. As current measurements of the high wavenumber spectrum do not favour any of the two possibilities the problem of a wave age dependent drag is considered to remain an open issue.

Finally, most studies to date consider only pure windsea, ignoring the generally complex wave field in the open ocean. The modulation of the short waves by long swell is expected to add further to the sea state dependence of the parameters [*Kudryavtsev et al.* 1997]; [*Mastenbroek et al.* 1997].

2.5.2.2 Modelling of the turbulent boundary layer

The second conceptual shortcoming with Miles' critical layer theory is that the flow is assumed to be quasi-laminar. The turbulence is not explicitly modelled, but is only invoked to maintain a logarithmic wind profile. Detailed approaches of turbulence modelling using different closure assumptions were recently performed (see e.g. the review in *Belcher and Hunt* [1998], and *Makin and Mastenbroek* [1996]; *Mastenbroek et al.* [1996]) to clarify the limitations of the bulk and mixing length concepts for flows over waves.

Different regimes of time scales between the turbulent eddies and the shear stress within the boundary layer were found which have to be accounted for in the modelling approaches [*Belcher and Hunt* 1993]; [*Makin and Mastenbroek* 1996]. Furthermore, a dependence of the momentum flux on the closure scheme was found [*Mastenbroek et al.* 1996]. The findings might have important consequences for the modelling of exchange of sensible heat at the air–sea interface. As an example, whereas organised wave-induced motions related to the form drag account for the momentum exchange, sensible heat flux is only indirectly determined by the waves through the diffusivity of the turbulence, requiring an adequate modelling of the turbulence above waves [*Weisse and Alvarez* 1997].

2.5.3 Conclusion

Much attention has been payed in recent years to the improvement of the representation of air-sea coupling coefficients for flow over waves, to improve the expression of the growth rate in the wind input source term. Besides the discussion of how to account for the sea state dependence and the wave-induced stress in the parametrizations, there is some evidence that simple eddy viscosity or mixing-length approaches fail to give a detailed description of the underlying physical processes. However, most of these turbulence modelling approaches deal with more or less monochromatic wave fields, neglecting the spectral details encountered in the ocean. Furthermore, the omission of a statistical description neglects the role of the nonlinear interactions among growing wave components which is crucial in the generation and evolution of ocean surface waves.

The wind input source term implemented in the WAM model is based on a modified Miles' approach which rests on simple first order closure assumptions, but nevertheless includes wave-dependent coupling parameters. The wave growth at high wavenumbers is mainly determined by the net effect of wind input and dissipation [*Barzel* 1994], while the growth at low wavenumbers is controlled by the nonlinear interactions. Therefore, model predictions with the WAM are nevertheless considered to give appropriate wave growth rates. However, improving the physics of the input source term would be desirable as it would in turn allow to draw conclusions on the dissipation source term which is still poorly known. In addition the physical mechanisms need to be understood in more detail if heat, water vapour and gas transfer are to be included in the modelling of transfer processes across the wavy air–sea interface.

2.6 Direction of wind and wind stress in the presence of swell

It is customary to estimate the wind stress τ_0 near the sea surface from the wind speed $u(z)$ at height z using the bulk aerodynamical approach, equation (2.20) (Section 2.4)

$$\tau_0 = -\rho C_D |\boldsymbol{u}(z)| \boldsymbol{u}(z)$$

In practise, the drag coefficient C_D might be a function of various environmental parameters, and a number of refinements have been made, taking into account either the effect of stability and heat fluxes or the presence of surface waves (Section 2.5). However, all these refinements focus on the magnitude of the wind stress while assuming its direction to be aligned with the wind speed vector.

2.6.1 In-situ measurements

After *Zemba and Friehe* [1987] and *Geernaert* [1988] found evidence for a departure between wind stress and mean wind direction which they attribute to the effect of heat fluxes, numerous recent publications suggest that surface waves, in particular the long waves, significantly affect the direction of the wind stress (see *Geernaert et al.* [1993], *Dobson et al.* [1994], *Rieder et al.* [1994], *Rieder* [1997], *Rieder and Smith* [1998]).

From the analysis of data from the Surface Waves Processes Program (SWAPP, 1990), *Rieder et al.* [1994] report deviations between the directions of the wind stress and the wind velocity under the influence of swell. Directional wave spectra and direct measurements of the vertical fluxes of momentum and heat were measured simultaneously, the former by means of a surface scanning Doppler radar and the latter using a three-component sonic anemometer. The data point to a dynamic coupling between wind and wave fluctuations at similar frequency bands in the sense that each wind stress spectral component (e.g. the low frequency regime) is aligned more closely with the direction of the wave spectral component at that frequency (e.g. the swell regime). The investigations of the SWAPP data also indicate a complex dependence of the sea surface drag on the wind profile and the windsea and swell components of the sea state [*Rieder* 1997].

The observation of a directional deviation between mean wind and wind stress and its coupling in frequency domain was subsequently confirmed by *Rieder and Smith* [1998] using concurrent wind and wave data gathered during the Marine Boundary Layer Experiment (MBLEX, 1995). The wind stress was broken into three frequency bands in order to distinguish between large-scale motions in the boundary layer ($f < 0.06\,Hz$), windsea and swell motions ($0.06\,Hz < f < 0.16\,Hz$), and high frequency motions in near equilibrium with the wind. In the middle band there was poor correspondence both in the direction and the magnitude between the wind stress and the wind speed. The swell redirected the middle band stress away from the wind, and added significant variability to the drag coefficient due to its disequilibrium with the local wind.

Upon subtracting a wave-correlated stress estimate which appeared to be an effective measure of the wave influences, the residual stress fraction in the mid-frequency band could be realigned with the mean wind and its magnitude modelled by a wind speed dependent drag coefficient. This strongly suggests that the waves were responsible for the discrepancies in the mid-frequency band.

2.6.2 Evidence from ERS-1 scatterometer measurements

The scatterometer onboard the ERS-1 satellite [*ERS-1/2 Wind Scatterometer* WWW] measures the normalized radar backscattering cross-section (NRCS) of short Bragg ripple waves at three different look directions (cf. Section 4.2.4). Taking the NRCS to be a function of the incidence angle, the wind speed and the wind direction, the wind vector can be retrieved by means of empirical wind algorithms (e.g. CMOD4 / ESA [*Stoffelen and Andersen* 1997], CMOD / IFREMER [*IFREMER/CERSAT* 1996]). Although their overall performance is satisfactory, discrepancies remain in the operational wind speed retrievals. These discrepancies are associated with the fact, that other geophysical parameters such as hydrodynamic interactions, atmospheric stability and the presence of long waves affect the NRCS. Current research therefore focusses on more physically based scatterometer models (see e.g. *Barthel and Breivik* [1996]).

In this context a comparison of wind direction retrievals from different algorithms with TAO buoys in the equatorial Pacific and with *NDBC* [WWW] buoys in the mid-latitude Pacific was performed by *Rufenach* [1996, 1998]. An offset of about 10° between scatterometer retrievals and buoy measurements was revealed in the equatorial Pacific, whereas no significant deviation was found at mid-latitudes. The wind directions was found to be systematically shifted towards the mean direction of the swell, suggesting the direction of the windsea to be influenced by the swell.

The hypothesis of the influence of long waves on the wind direction retrieval was simulated by *Essen* [1998] using a composite surface scattering model. The model results revealed a deviation of some 20 ° between the empirical and the composite surface model wind retrieval.

2.6.3 Conclusion

To conclude, we emphasize [*Rieder and Smith* 1998] that the wave coupling approaches presented in the following sections are theoretically and empirically well founded only for collinear winds and waves. However, the ubiquity of swell in the open ocean makes this condition the exception rather than the rule. The treatment of nonlinear atmosphere–wave interactions in the framework of a statistical field theory (cf. Section 2.3.3) could provide a description of the spectral coupling of the wind stress to the wave field.

In Section 7.4.1 we present some evidence that the above described effect could also be observed from ERS-1 SWM spectral retrievals. Thus, the new information from ERS-1/2, including both wave spectral data and scatterometer wind measurements, could aid significantly in collecting more data to address the issue.

3 THE WAVE MODEL WAM

This chapter gives a brief summary of the physics and the implementation of the state-of-the-art global wave prediciton model WAM, in which many of the concepts outlined in Chapter 2 have found their application.

3.1 WAM physics

As a third generation model (as opposed to second generation models, [*SWAMP Group* 1985]), the WAM model introduces no prior assumptions on the shape of the spectrum, but determines the evolution of the spectrum by direct integration of the energy balance equation (2.12) from first principles, based only on the structure of the three source terms [*WAMDI Group* 1988]; [*Günther et al.* 1992]; [*Komen et al.* 1994]; [*WAM* WWW]. On the sphere the transport equation reads

$$\begin{aligned}\frac{\mathrm{D}}{\mathrm{D}t}F &= \frac{\partial}{\partial t}F + \frac{1}{\cos\varphi}\frac{\partial}{\partial\varphi}\left(\dot{\varphi}\cos\varphi\, F\right) + \frac{\partial}{\partial\psi}\left(\dot{\psi}F\right) + \frac{\partial}{\partial\theta}\left(\dot{\theta}F\right) \\ &= S_{in} + S_{nl} + S_{ds}\end{aligned} \tag{3.1}$$

for the two dimensional wave spectrum $F = F(f, \theta; \varphi, \psi, t)$ as a function of frequency f and direction θ (see Appendix B) on a spherical coordinate grid φ, ψ. The source terms on the right hand side of the equation are integrated using an implicit integration scheme (with a time step of 15 minutes in the ECMWF's operational set-up), while the integration of the advection terms on the left hand side is performed using a first-order upwind scheme (with a time step of 30 minutes in the ECMWF's operational set-up). The advection time step is related to the model resolution and must be chosen so as to fulfil the Courant–Friedrichs–Lewy (CFL) criterion (e.g. *Press et al.* [1992]). The source terms have the following properties:

S_{in}: The input source term S_{in} describes the momentum transfer from the wind to the wave field. It is proportional to the wave spectrum. In the WAM's present cycle 4 the wind forcing is based on Miles' critical layer mechanism for laminar flows as adopted by *Snyder et al.* [1981] and modified by *Janssen* [1989, 1991, 1992] to include the effect of a wave induced stress $\boldsymbol{\tau}_w$ (see Section 2.5.2).

S_{nl}: The nonlinear transfer term S_{nl} is given by the so-called direct interaction approximation of the full Boltzmann collision integral (*Hasselmann, S. and Hasselmann, K.* [1985] and *Hasselmann, S. et al.* [1985a]; see also *Young and van Vledder* [1993]) that describes the conservative spectral energy transfer due to resonant weak nonlinear wave-wave interactions [*Hasselmann, K.* 1961, 1963a,b] (see Section 2.3.2).

S_{ds}: The dissipation term S_{ds} is the least well known. The dominant dissipation process is generally regarded as white capping, which involves many scales of breaking waves. However, as a process which is weak-in-the-mean (Section 2.3.4), it follows from general principles [*Hasselmann, K.* 1974] that it can normally be represented as quasi-linear process. The form implemented in WAM cycle 4 is based on a parameterisation explored by *Komen et al.* [1984] and extended by *Janssen* [1991] to account for the wave-induced stress (cf. Section 2.3.4).

3.2 Model set-up and model runs

The three year set of wave spectra between January 1, 1993, and December 31, 1995, at our disposal stem from the operational WAM model runs at *ECMWF* [WWW].

3.2.1 The wind forcing

The initialized analyzed wind field u_{10} at 10 m height of the ECMWF atmospheric general circulation model (AGCM) are used to drive the wave model. The u_{10} winds are inferred from the values at the lowest model level and the surface.

The operational ECMWF model is based on a spectral horizontal representation with a triangular truncation at wavenumber 213 (T213) on a reduced Gaussian grid, corresponding to an effective resolution of roughly 0.8°. The vertical is divided into 31 layers. The numerical advection is performed by means of a semi–Lagrangian scheme at a time step of 15 minutes. This configuration is effective since 1991. The various parametrizations used are summarized in [*ECMWF* 1995].

Besides the AGCM itself, the second important element of the operational set-up is the assimilation scheme. Two main sources of data are available for operational assimilation:

1. Satellite data, disseminated via WMO's global telecommunication system (GTS). Again, these data fall into three main categories:
   - Cloud cleared radiance, humidity and temperature data (SATEM and TOVS) provided by the polar orbiting NOAA satellites [*NESDIS* WWW] which deploy, among others, a high resolution infrared sounder (HIRS), a microwave sounding unit (MSU) and a stratospheric sounding unit (SSU).
   - Cloud track wind (SATOB) data collected by the geostationary meteorological satellites *METEOSAT* [*EUMETSAT* WWW] (Europe), *GOES* [WWW] (USA), and *GMS/HIMAWARI* [WWW] (Japan).
   - ERS-1/2 scatterometer wind data. However, no scatterometer data were assimilated into the ECMWF model before mid-1996.
2. Conventional observations, based on the ECMWF real-time data collection from the Meteorological Archive and Retrieval System (MARS). They comprise, among others, surface observation at land stations, ship and buoy data, and radiosonde and aircraft observations.

The assimilation scheme is a one-dimensonal variational analysis (1D-Var; see e.g. *ECMWF* [1995], *Gibson et al.* [1997] and references therein). The assimilation of SATOB data from geostationary satellites is zonally restricted to 50° N/S. We shall see later (Section 7.4) that large discrepancies occur between ECMWF and ERS-1 scatterometer wind fields south of 50° in the Southern Hemisphere [*Bentamy et al.* 1996]. There is some evidence that these discrepancies can also be inferred from ERS-1 SWM (Section 7.4.2).

3.2.2 The WAM model

The operational wave forecast model WAM, cycle 4, at ECMWF computes ocean wave spectra every 6 hours (corresponding to one assimilation time step) on a global 3° × 3° (since July 1994: 1.5° × 1.5°) latitude-longitude grid.

Since August 1993 ERS-1 altimeter wave height data are routinely being assimilated by ECMWF into the WAM model using an optimal interpolation scheme [*Lionello et al.* 1992, 1995], thereby influencing the first guess wave field through the analysis six hours earlier.

To assess the impact of the assimilation we have re-run the WAM model over a seasonal period June–July–August 1995 in a set-up identical to the operational set-up at ECMWF and using the same initialised analysed wind fields but without assimilation of satellite data. While refering to Chapter 9 for details, we anticipate here that the model runs without assimilation corroborated the statistical analyses of the operational data presented in Chapter 7.

Furthermore, the three month model run was performed using an extended version of the WAM model developed by E. Bauer [*Bauer et al.* 1996a], which also computes the spectral wave age for each frequency / direction bin at each grid point.

3.2.3 Spectral wave age

Spectral wave age as used here contains much more information on the spectral dynamics and the wind forcing than the highly idealized quantity $u_{c_{ph}/*}$ usually referred to, which is meaningful only (monomodal) wind waves. The module computing the spectral wave age was kindly provided by E. Bauer from the PIK. The spectral wave age was introduced by *Bauer et al.* [1996a] in the context of an assimilation scheme of spectral wave data based upon an impulse response (or Green's) function method. For every spectral bin the time of last influence by the wind is determined. To this end two propagation equations are solved for four spectral wind impact variables. Two of these impact variables are needed to infer the correction in the wind field from each modified spectral energy bin. The other two impact variables together enable the computation of an average time interval at each spectral grid point, which has past since the spectral bin last received an appreciable wind input. This yields a two-dimensional wave age spectrum.

We shall later partition the full energy spectrum into its main spectral wave components which can then be adequately expressed by mean quantities. In accordance with this representation, we define the mean spectral wave age of each wave spectral partitioning as the average over all spectral bins belonging to the same system.

3.3 WAM validations

The WAM model now runs routinely at most operational forecasting centres and has been implemented at more than 100 research institutions. It has been extensively validated through case studies and field data including fetch-limited wave growth conditions and extreme storm conditions, and on a statistical basis against buoy data (see the summary in *Komen et al.* [1994]).

Validation of the WAM model using spaceborne data has so far been limited to H_s data derived from satellite altimeters. A comprehensive compilation of WAM validation studies using spaceborne altimeter data from SEASAT (1978), GEOSAT (1985-1989), ERS-1 (1991-1996) and TOPEX/-POSEIDON (since 1992) as well as a global comparison between ERS-1 and TOPEX altimeter significant wave heights is given in *Bauer and Staabs* [1998].

Most validation exercises indicate a good overall agreement between model and observation, but significant differences are nevertheless occasionally found. The discrepancies in individual cases tend to differ from study to study and have mostly been attributed to errors in the forcing wind field or, in some cases, to inadequate model resolution. Small systematic deviations of the model from a larger ensemble of altimeter wave height data have also been partly attributed to differences in the instrument calibrations or in the sensor algorithms, or to differences in the spatial and temporal sampling.

Despite their continuous global coverage, altimeter data suffer from the basic limitation of yielding only significant wave heights. When trying to detect detailed deficiencies in the spectral properties of a wave model, validation studies based on altimeter data alone therefore remain of restricted use [*Lionello et al.* 1992, 1995]; [*Bauer et al.* 1996a]; [*Voorrips et al.* 1996]. The SAR is at present the only instrument able to provide the required detailed two-dimensional spectral data with continuous global coverage. The present study represents the first attempt at a global assessment of the available ERS-1 SWM data and a detailed spectral intercomparison with WAM model data.

4 SATELLITE REMOTE SENSING OF OCEAN SURFACE WAVES

4.1 Satellite oceanography: an overview

The world oceans cover roughly three quarters of the earth's surface. They play an eminent role in the coupled atmosphere–ocean climate system (see e.g. *Houghton et al.* [1996]; *Kondratyev et al.* [1996]) as well as in men's activities, ranging from overseas transport to offshore activities. They therefore need to be investigated and monitored. However, regular measurements of the oceans are inherently difficult. Global and continuous observational coverage can be achieved only through remote sensing from space. The last quarter of this century has witnessed tremendous advances in this field. Today numerous applications of satellite data in all areas of oceanography have emerged, and various new insights are owed to spaceborne measurements (for an overview see *Robinson* [1985], *Stewart* [1985] and more recently *Jones et al.* [1993]). Remote sensing devices relevant for oceanography can be broadly classified into four main categories:

1. *Optical sensors* are sensitive to radiation in the visible wavelength domain and measure the ocean colour and its variation through scattering, absorption and attenuation with wavelength. From this, phytoplankton productivity, suspended solid concentrations and sediment movement can be inferred. Besides biological and dynamical oceanography (in the latter, plankton and suspended particles are considered as passive tracers) the main application is in coastal areas.
2. *Infrared radiometers* rely on near surface infrared emissions and require clear-sky measurement conditions. The main oceanic parameter measured is sea surface temperature (SST), but many related quantities such as surface heat fluxes, deep convection and water mass formation, dynamical features (equatorial waves, mesoscale eddies) and oceanic fronts can also be inferred.
3. *Passive microwave radiometers* are all weather devices in contrast to optical and infrared sensors. The dependency of microwave emissivity on the surface roughness yields information on the surface wind speed in addition to SST. The attenuation of microwaves by rain cells is the basis for quantifying the precipitable water over the ocean. The spectral characteristics of sea ice brightness temperature and the roughness properties enables the detection of sea ice and estimates of its age and thickness.
4. *Active microwave sensors* illuminate the scene by their own source. They are insensitive to cloud and sunlight conditions and are thus all wheather systems which operate day and night. Active microwave sensors are radars which emit short microwave pulses and record the backscattered signals from the surface. The main instruments are radar altimeters (RA),

satellite	*country*	*from*	*until*	*Altimeter*	*Scat*	*SAR*
SKYLAB	USA	25/5/1973	8/2/1974	yes	–	–
GEOS-3	USA	14/4/1975	1/12/1978	yes	–	–
SEASAT	USA	27/6/1978	9/10/1978	yes	yes	yes
SIR-A	NASA	1982	1982	–	–	yes
SIR-B	NASA	1984	1984	–	–	yes
KOSMOS-1870	Russia	7/1987	10/1989	–	–	yes
GEOSAT	USA	1985	1990	yes	–	–
ALMAZ-1	Russia	31/3/1991	17/10/1992	–	–	yes
ERS-1	ESA	16/7/1991	02/06/1996	yes	yes	yes
JERS	Japan	11/2/1992	1998	–	–	yes
TOPEX/POSEIDON	USA/F	8/1992	1998	yes	–	–
SIR-C	NASA	9/4/1994	20/4/1994	–	–	yes
SIR-C	NASA	30/9/1994	11/10/1994	–	–	yes
ERS-2	ESA	21/4/1995	1999	yes	yes	yes
RADARSAT	Canada	4/11/1995	1999	–	–	yes
ADEOS	USA/J/F	4/8/1996	30/6/1997	–	N-Scat	–
ENVISAT-1	ESA	2000	2004	yes	–	ASAR
JASON-1	USA/F	2000	2004	yes	–	–
ALMAZ-2	Russia	2000	2003	yes	yes	yes
METOP-1	EUMETSAT	2001	2004	–	A-Scat	–

Table 4.1: Satellites deploying altimeter, scatterometer or SAR.

wind scatterometers (WNS), and synthetic aperture radars (SAR) (see e.g. *Ulaby et al.* [1986] and *Elachi* [1988]). Table 4.1 lists spacecrafts deploying either a RA, WNS or a SAR. The two European remote sensing satellites ERS-1/2 both deploy all three instruments. *ENVISAT* [WWW] will deploy a RA and a SAR, the WNS being provided through the METOP mission. We shall discuss oceanographic applications in the context of ERS-1 (cf. next section).

The ideal instrument to measure ocean surface waves on a global continuous basis is the SAR. While the RA yields accurate measurements of significant wave heights, the SAR can resolve the two-dimensional spectral details of the local wave field. The first SAR deployed on SEASAT in 1978 demonstrated the feasibility of mapping ocean waves by a SAR [*SEASAT* 1983], despite SEASAT's short life time of three months. ERS-1/2 provide the first set of SAR data of continuous global coverage over a multi-year period. The satellite will be shortly described in the following section. In Section 4.3 we briefly sketch the basic principle of a SAR, following a discussion of the problem of ocean wave imaging by a SAR in Section 4.4. We conclude the chapter by a short description of the state-of-the-art algorithm to retrieve ocean wave spectra from SAR image spectra (Section 4.5) which was used throughout this work.

4.2 The ERS-1 satellite

The objective of the ERS-1 mission was to explore the capabilities of environmental monitoring from space as a forerunner of a new generation of operational earth observation satellites. The instruments on board the ERS-1 gather data that yield valuable information for operational wind and wave field prediction, air-sea interactions, monitoring of coastal areas, observation of the ocean circulation, and for various terrestrial applications.

4.2.1 The ERS-1 orbit

The ERS-1 was launched on July 16, 1991, form Kourou, French Guiana, into a near-polar, elliptical, sun-synchronous orbit. The orbit choise offers many advantages:

- A near polar orbit with an inclination of 98,4° extends to 81.5° N/S, thus allowing large parts of the polar regions to be covered, where in-situ measurements are scarce.
- A sun-synchronous orbit is characterized by an orbit plane which rotates at a frequency of 360° per year. The orientation of the orbit plane is therefore locked to the earth's rotation about the sun. As a consequence, the satellite crosses all latitudes of the part of the globe facing the sun at one and the same local solar time on each pass throughout the year, and each latitude on the backward face of the globe 12 hours later (in local solar time). For ERS-1 this local solar time on the day-side is 10:30 while the satellite is on its descending orbit, and 22:30 on the satellite's ascending orbit on the night-side. The data colltected are thus made up of two samples of distinct uniform solar irradiation. The sun-synchronous orbit is achieved by a precession of the satellite orbit plane. The gravitational field of the non-spherical earth exerts a torque on the satellite's elliptical path. By suitably choosing the orbit parameters, the precession period can be adjusted to the required 0.986° per day.

The ERS-1 mission was divided into 5 phases of different repeat cycles, to satisfy different scientific requirements. The phases are listed in Table A.2.

4.2.2 The ERS-1 payload

The ERS-1 carries a C-band (5.3 GHz) active microwave instrument (AMI) comprising a synthetic aperture radar (SAR) and a wind scatterometer (WNS), as well as a Ku-band (13.8 GHz) radar altimeter (RA) and an along–track scanning radiometer (ATSR).

- The *ERS-1/2 SAR* [WWW] provides high resolution all-weather images over the oceans, polar ice sheets, coastal zones and land. While the SAR can be operated in full swath 100 × 100 km image mode only for a maximum of 12 min per orbit and while in line-of-sight to a ground receiving station, the SAR wave mode (SWM), which records 10 × 5 km imagettes every 200 km along the satellite track is designed for continuous operational purpose over the ocean, providing low bit rate (LBR) information on the sea state at a global quasi–continuous coverage.
- The *ERS-1/2 Wind Scatterometer* [WWW] is operated simultaneously to the SAR wave mode. It consists of three antennas measuring the normalized radar cross section (NRCS) under different looking angles from which the mean surface wind speed and direction over a 50 × 50 km cell can be extracted.
- The *ERS-1/2 Radar Altimeter* [WWW] is a nadir-pointing active microwave sensor designed to measure the time return echoes from ocean and ice surfaces. It provides information of significant wave heights and sea surface height, relevant for studying ocean waves and currents, tides and the surface geoid. Furthermore, various parameters over sea ice and the polar ice sheets can be extracted.
- The ATSR consists of two passive instruments. The four–channel infrared radiometer (IRR) provides high accuracy sea surface temperatures (SST). The two–channel microwave sounder (MWS) measures the vertically integrated atmospheric water vapour and liquid content, that is used for computing the path delay of the RA signal.

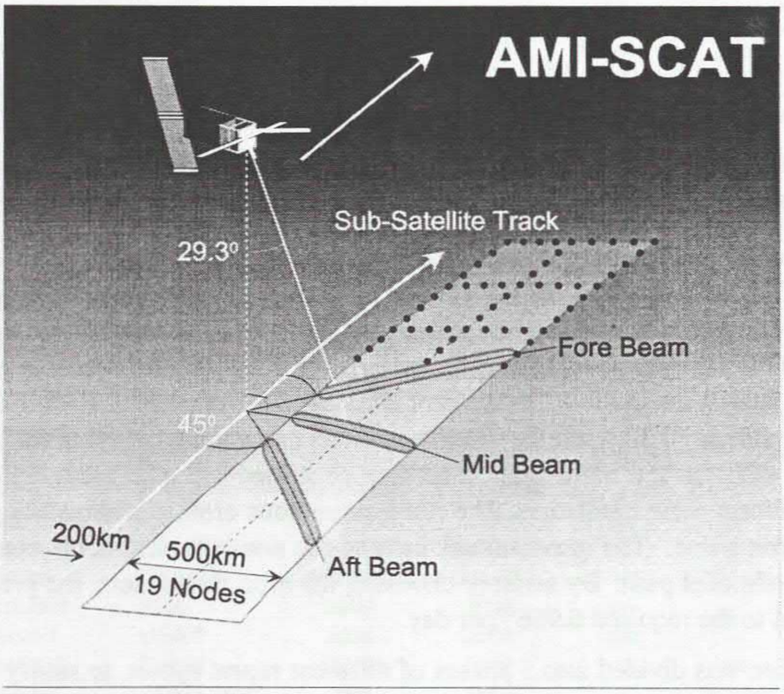

Figure 4.1: Geometry of the ERS-1 Wind Scatterometer.

4.2.3 ERS-1 altimeter–derived wave heights

In Chapter 6 we shall consider significant wave height data derived from the ERS-1 and the TOPEX altimeters for an independent validation of the total energy of SWM–retrieved wave spectra. Satellite borne altimeters are nadir-looking radars which measure the echoes of their emitted microwave pulses from the sea surface. Ocean waves modify the shape of the received pulse form. The following information is embedded in the return pulse shape as a function of time [*ESA* 1992]

- the time delay with respect to the emitted pulse provides a measure of altitude
- the slope at the leading edge of the return echo time series is related to the width of the wave height distribution of reflecting facets, and thus to wave height parameters such as H_s
- the power level of the echo signal depends on small scale surface roughness, and thus on ocean surface wind field parameters

In determining the pulse characteristics, statistical effects (noise) are reduced by averaging over several individual echo curves. The altimeter H_s data used in the present study were obtained from averages over 1-second intervals. A 1-s sample represents a mean over an area given by the diameter of the footprint of a pulse and by the distance overflown by the satellite within 1 s. The footprint increases with wave height from a few km to about 10 km for 10 m significant wave height.

4.2.4 ERS-1 scatterometer wind fields

Various studies in the past have repeatedly confirmed that dicrepancies between modelled and observed wave heights could largely be attributed to incorrect wind forcing [*Komen et al.* 1994]. Thus,

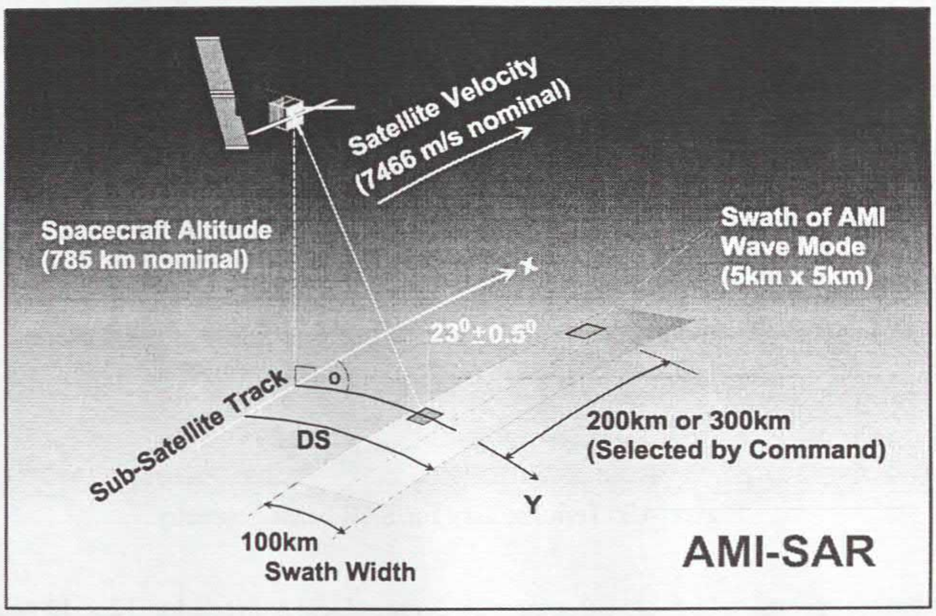

Figure 4.2: Geometry of the ERS-1 SAR wave mode.

any assessment of wave model results has to take this into account as a possible error source. Fortunately, the ERS-1 scatterometer operates simultaneously to the SAR wave mode. Therefore, the wind field is measured simultaneously to the SWM imagette.

The scatterometer's swath is composed of segments of 500 × 500 km extent in azimuth and range direction. Each segment consists of 19 × 19 pixels. As the satellite proceeds along its orbit it measures the NRCS from three different look directions (three antennnae) at 19 range nodes from near range to far range separated by 25 km (Figure 4.1). The SAR wave mode imagettes are interlaced to the scatterometer swath, falling into node 2 for 19.9° and node 4 for 23.5°. Thus, to every SWM imagette, a precisely collocated wind vector can in principle be retrieved [*Chapron et al.* 1995]; [*Kerbaol et al.* 1998], provided both instruments are operational and both the SWM and the wind retrieval algorithms yield reliable results.

For the present study, offline ERS-1 scatterometer wind fields processed at *IFREMER/CERSAT* [1996] (see also *Bentamy et al.* [1996, 1997]) were at our disposal. We shall utilize these wind vector retrievals in Chapter 9. The wind vectors used are those which are closest collocated to the SWM imagette spectrum, i.e. which correspond to the cell that contains the SWM imagette. Furthermore, annual zonal mean ERS-1 scatterometer wind speeds kindly provided by A. Bentamy are shown in Section 7.4.2 in the context of conjectured ECMWF wind field deficiencies.

4.2.5 The ERS-1 SAR wave mode fast delivery product

The operation of the ERS-1 Synthetic Aperture Radar (SAR) in the intermittent sampling *wave mode* provided for the first time global two-dimensional wave spectral data in near real time. In the SAR wave mode (SWM) 10 × 5 km snap shot *imagettes* are recorded every 200 km along the satellite track. The data are stored on board and transmitted once per orbit to the ERS ground stations. This yields a daily coverage of the global wave spectral field (with occasional gaps when the SAR was operated in full swath mode) at an along track resolution comparable with the model resolution, but with a lower cross track resolution of order 1000 – 2000 km. The imagettes are Fast Fourier Transformed to 512 ×

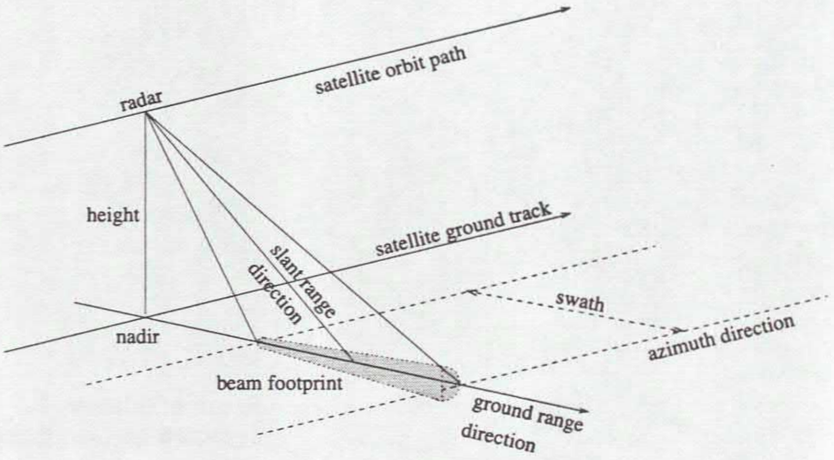

Figure 4.3: Terminology for SAR beam geometry.

512 wavenumber spectra, which are subsequently averaged and converted to 12 × 12 polar wavenumber coordinates (see Table A.1; detailed descriptions are given in *ESA* [1993], *Brooker* [1995] and *Hasselmann, S. et al.* [1998]).

The European Space Research Institute (ESRIN) at Frascati, Italy, distributes the ESA fast delivery product (FDP) in quasi real-time to the major operational forecasting centres. We received the FDP via the United Kindom Meteorological Office (UKMO) at Bracknell (UK) and the Deutscher Wetterdienst (DWD) at Offenbach (FRG).

4.3 The synthetic aperture radar

The synthetic aperture radar is a side–looking instrument which emits short microwave pulses and processes a two-dimensional image from the received complex-valued radar backscatter. The across–track or *range* coordinate of the backscattering facet is infered from the travel time of the pulse from emission to reception, the along–track or *azimuth* coordinate is embedded in the phase history of the signal. A single emitted pulse spreads out into a beam, illuminating a footprint of typically 100 km in range and 4.3 km in azimuth (in case of the ERS-1 SAR).

Across–track / range: Successive pulses are emitted at a pulse repetition frequency $PRF = 1/T$. The period T between two successive pulses has to be larger than the travel time difference between a signal received from near range of the footprint and a signal received from the far range.

A single pulse can be decomposed into a complex-valued envelope $g(\tau)$ which is modulated by a carrier frequency ν_0

$$g(\tau) = \mathrm{e}^{i2\pi\nu_0\tau}$$

τ refers to the temporal pulse width. At the receiver the carrier frequency modulation is removed through a coherent demodulation, resulting in a complex echo signal of a point scatterer at slant range distance R of the form

$$g\left(\tau - 2R/c\right)\,\mathrm{e}^{i4\pi\frac{R}{c}\nu_0}$$

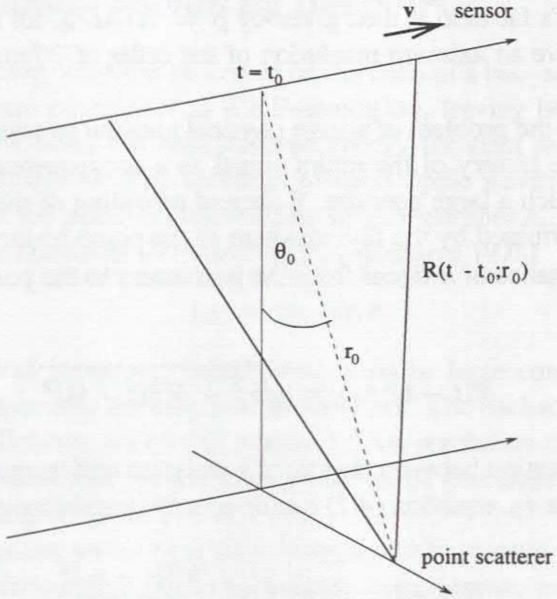

Figure 4.4: SAR signal path geometry.

(antenna pattern, point spread and processor impulse response functions are neglected in this schematic description, see e.g. *Hasselmann, K.* [1980], *Hasselmann, K. et al.* [1985], *Bamler and Schättler* [1993]).

The range resolution ρ_{ra} is determined by the ability of the SAR processor to disciminate between two pulses which are scattered from two range locations separated by ρ_{ra}. It is related to the pulse width τ through

$$\rho_{ra} = \frac{c\tau}{2\sin\theta}$$

where c denotes the speed of light, and θ the signal incidence angle. Thus, in order to achieve a high range resolution the pulse envelope $g(\tau)$ should approach a δ–function. Although this could be satisfied by choosing a $sinc$–type function, short pulses which are to carry sufficiently high energy require prohibitively high transmit power for spaceborne SAR operation. Therefore, long duration phase coded pulses are employed, in which a constant amplitude of bandwidth B_ν (represented through a $rect$–type function) is multiplied by a so-called chirp function

$$g(\tau) \sim \exp\left(i\pi \cdot \mathrm{const} \cdot \tau^2\right) \cdot \mathrm{rect}\left(\frac{\tau \cdot \mathrm{const}}{B_\nu}\right)$$

whose instantaneous phase $\mathrm{d}/\mathrm{d}\tau\, \varphi = \pi \cdot \mathrm{const} \cdot \tau$ increases linearly with time. It can be shown, that this chirp function can be re-compressed to a $sinc$–function through multiplying the complex signal spectrum with its complex conjugate, the so-called matched filter transfer function. This range compression is performed by the SAR processor, yielding the signal variance spectrum.

To summarize, the SAR simulates a short signal pulse required for high range resolution by emitting a broad, linearly frequency modulated chirp pulse which is re-compressed through a matched filter in the SAR processor.

Along–track / azimuth: For a real aperture radar the azimuth resolution of a SAR antenna is determined by the "real" aperture D_R (in the strict sense used in wave optics). The resolution of a ground cell in the antenna's far field is then given by $\rho = R/\lambda D_R$, for a radar signal of wavelength λ. Thus, in order to achieve an azimuth resolution of the order of 20 m, an enormous large antenna would be necessary.

The SAR circumvenes the problem of a large physical antenna by taking advantage of the Doppler shift occuring in the phase history of the return signal as a consequence of the satellite velocity V, to effectively synthesize such a large aperture. Coherent recording of the return signals then yields a much finer resolution determined by the fine structure of the phase history.

Consider the travel distance of a signal from the instrument to the point scatterer at slant range r_0 at time t_0

$$R(t - t_0; r_0) = \sqrt{r_0^2 + V^2(t - t_0)^2} \tag{4.1}$$

Assuming the satellite migration between the signal's emission and its reception $V(t - t_0)$ to be small compared to the slant range r_0, equation (4.1) can be approximated through

$$R(t - t_0; r_0) \approx r_0 + \frac{V^2(t - t_0)^2}{2r_0}$$

The signal path in azimuth then translates into the signal phase $\exp[i\varphi(t - t_0; r_0)]$ via the travel time

$$\varphi(t - t_0; r_0) = 2\pi\nu\tau = \frac{4\pi}{\lambda}\left(r_0 + \frac{V^2}{2r_0}\tau^2\right)$$

where ν, λ denote the signal frequency and wavelength, respectively, related through $c = \lambda\nu$, and $\tau = 2R/c$ is the travel time. Thus, the phase function related to azimuth is a chirp, just like the phase of the pulse envelope, related to range. However, the azimuth chirp is produced by a completely different mechanism. The same form of the azimuth and range chirp are accidental. The instantaneous frequency

$$f_D = \frac{1}{2\pi}\frac{\mathrm{d}}{\mathrm{d}T}\varphi \approx \frac{2}{\lambda}\frac{V^2}{r_0}(t - t_0)$$

is refered to as Doppler frequency and varies linearly with time.

The azimuth chirp is processed in the same way as the range chirp by a matched filter, yielding a signal variance which is localized at the reference frequency of the matched filter. Thus, only those points contribute constructively to the signal variance whose local frequency closely correspond to the reference frequency, whereas points whose local frequency is more distant from the reference frequency interfere destructively. As a result, the matched filter picks out the signal at a certain position for a given reference frequency. Scanning through all reference frequencies of the Doppler spectrum finally yields the full azimuth array. This imposes a second requirement on the PRF: The temporal sampling rate must be at least twice the highest Doppler frequency shift in the return signal, if the Doppler history of each point is to be unambiguously recognisable without aliasing.

Finally, the azimuthal resolution of a SAR is found to be independent of both satellite velocity and slant range distance:

$$\rho_{az} = \frac{D_R}{2}$$

4.4 Imaging of ocean waves by the SAR

The imaging of ocean waves by a SAR is described on the basis of a two–scale model. The short waves are described statistically and are subject to WKB–averaging, leaving behind the long waves on the deterministic scale. To first order the backscattered energy for slant incident microwaves ($20° < \theta < 70°$) is determined by the variance spectrum of short ripple waves (the small scale) which are in resonant interaction with the incoming microwaves of wavenumber k_e, i.e. whose wavenumber k_B fullfill the Bragg resonance condition [*Wright* 1968]; [*Valenzuela* 1978]

$$k_B = 2k_e \sin\theta$$

The tangential plane of local incidence, called facet, must be large comapared to the microwave's wavelength, but small compared to the long wave's curvature. The backscattered energy cross section is an ensemble mean of all facets which fall within a SAR resolution cell and which contribute to the Bragg scattering. Its modulation by the long ocean waves (the large scale), represents the basic mechanism for RAR imaging of waves.

However, imaging of ocean waves by a SAR is produced by mainly *two* mechanisms: the linear RAR (real aperture radar) modulation of the backscatter cross-section, and the orbital motion effects that induce Doppler shifts modifying the phase history of the backscattered signals used to reconstruct the SAR image. The RAR modulation is caused by hydrodynamic interactions between the short backscattering Bragg waves and long waves, and the tilting of the backscattering facets by the long waves (cf. next section). The orbital motion Doppler shifts produce azimuthal displacements of the backscattering elements in the SAR image plane, leading to a redistribution of the apparent backscattering density ("velocity bunching"). If the azimuthal displacements become comparable with a typical ocean wavelength, the image becomes nonlinearly distorted (cf. Section 4.4.2).

4.4.1 Linear RAR modulation

For frozen surfaces, i.e. neglecting surface motion, the imaging process can be described by linear real aperture radar (RAR) modulation theory. In terms of the wavenumber Fourier components $\zeta_{\mathbf{k}}$ of the sea surface elevation at the position $\boldsymbol{x}$

$$\zeta(\boldsymbol{x},t) = \sum_{\boldsymbol{k}} \{\zeta_{\boldsymbol{k}} \exp[\mathrm{i}(\boldsymbol{k}\cdot\boldsymbol{x} - \omega t)] + \text{c.c.}\} \tag{4.2}$$

the Fourier coefficients $I^R_{\boldsymbol{k}}$ of the RAR image intensity modulation $I^R_{\boldsymbol{x}}$, are linearly related to $\zeta_{\boldsymbol{k}}$ through RAR modulation transfer functions (MTF; see e.g. *Plant* [1988])

$$I^R_{\boldsymbol{k}} = T^R_{\boldsymbol{k}}\zeta_{\boldsymbol{k}} + (T^R_{-\boldsymbol{k}}\zeta_{-\boldsymbol{k}})^* \tag{4.3}$$

The variance spectrum of the image intensity modulation $P^R_{\boldsymbol{k}} = 1/2 < I^{R*}_{\boldsymbol{k}} I^R_{\boldsymbol{k}} >$ can then be expressed in terms of the ocean wave spectrum $F_{\mathbf{k}} = < \zeta^*_{\boldsymbol{k}}\zeta_{\boldsymbol{k}} >$ through the linear transform

$$P^R_{\boldsymbol{k}} = \frac{1}{2}\left\{|T^R_{\boldsymbol{k}}|^2 F_{\boldsymbol{k}} + |T^R_{-\boldsymbol{k}}|^2 F_{-\boldsymbol{k}}\right\}. \tag{4.4}$$

The RAR MTF is the sum of a geometrical tilt part $T^{tilt}_{\mathbf{k}}$ and a hydrodynamical part $T^{hyd}_{\mathbf{k}}$:

$$T^R_{\boldsymbol{k}} = T^{tilt}_{\boldsymbol{k}} + T^{hyd}_{\boldsymbol{k}}.$$

- For vertical polarisation as in the case of the ERS-1 SAR the tilt MTF is given by

$$T_{\boldsymbol{k}}^{tilt} = 4\mathrm{i}k_l \cot\theta \left(1+\sin^2\theta\right)^{-1} \qquad \text{for } \theta \leq 60^\circ \tag{4.5}$$

  where θ is the incidence angle (at the centre of imagette) and k_l denotes the component of the incident wavenumber in the radar look direction [*Wright* 1978]; [*Valenzuela* 1978]; [*Alpers et al.* 1981]; [*Monaldo and Lyzenga* 1986].

- For $T_{\mathbf{k}}^{hyd}$ describing the long wave modulation of the short waves we use the theoretical expression

$$T_{\boldsymbol{k}}^{hyd} = 4.5 \frac{\omega - \mathrm{i}\mu}{\omega^2+\mu^2} k\omega \left(\frac{k_y^2}{k^2} + Y_{re} + \mathrm{i}Y_{im}\right) \tag{4.6}$$

  where μ is a relaxation parameter for the Bragg waves which is empirically determined. The MTF was first derived by *Alpers and Hasselmann* [1978] and subsequently extended [*Plant* 1982, *Plant et al.* 1983]; [*Feindt* 1985, *Feindt et al.* 1986] to include a complex feedback factor $Y_{re} + \mathrm{i}Y_{im}$ which depends, among others, on the surface wind (for a detailed discussion see [HH]). However, this expression is still under discussion as no comprehensive models on the wind dependence of the hydrodynamical MTF yet exists and validation of existing approaches are intricate (see e.g. *Hara and Plant* [1994]; *Keller et al.* [1994]; *Schmidt et al.* [1995]).

  In the SAR-to-wave retrieval used in the present study the wind dependency of the MTF is neglected (although it could be easily incorporated into the algorithm). Preliminary results with a wind field dependent expression showed neglectable impact on the retrieval result in the case of ERS-1 SWM (W. Plant, private communication). This agrees with the fact that, first, for spaceborne SARs of high range distance to platform velocity ratio (R/V) the velocity bunching mechanism outreaches the remaining modulation mechanisms, and second, for low incidence angles also the tilt MTF dominates the hydrodynamic MTF [*Alpers et al.* 1981]; [*Hasselmann, K. et al.* 1985]. Only for range travelling waves, $T_{\mathbf{k}}^{hyd}$ becomes on the order of the other transfer functions.

There are further processes which determine the imaging mechanism. In contrast to the tilt and hydrodynamical effects which act on the image intensity $I^R(\boldsymbol{x})$, these act not on $I^R(\boldsymbol{x})$ itself but on its coordinate $\boldsymbol{x}$

$$\boldsymbol{\xi} : \boldsymbol{x} \longmapsto \boldsymbol{x} + \boldsymbol{\xi}(\boldsymbol{x}) \tag{4.7}$$

The two main processes are:

- *the velocity bunching effect:* the wave's orbital motions $u_r(\boldsymbol{x})$ induce Doppler shifts in the phase history of the backscattering signals (cf. the references in the MARSEN review [*Hasselmann, K. et al.* 1985] and *Tucker* [1985]), thus modifying the azimuth coordinate x through the transform

$$\xi_x : x \longmapsto x + \xi_x(\boldsymbol{x}), \qquad \xi_x(\boldsymbol{x}) = \frac{R}{V} u_r(\boldsymbol{x}) \tag{4.8}$$

  The associated MTF reads

$$T_{\boldsymbol{k}}^{vb} = \frac{R}{V}\omega \left(\frac{k_r}{|\boldsymbol{k}|}\sin\theta + i\cos\theta\right) \tag{4.9}$$

- *range bunching:* the variation of the slopes along the long wave's profile induces an error in the registration of the radial (i.e. approximately the range) position of the backscattering element [*Gower* 1983]. The misregistration is proportional to the surface elevation and depends on the incidence angle θ under which the surface elevation is recorded:

$$\xi_y \,:\, y \longmapsto y + \xi_y(\boldsymbol{x}), \qquad \xi_y(\boldsymbol{x}) = \frac{\zeta(\boldsymbol{x})}{\tan\theta} \tag{4.10}$$

The associated MTF reads

$$T^{rb}_{\boldsymbol{k}} = \frac{1}{\tan\theta} \tag{4.11}$$

It should be noted that although ξ_x and ξ_y act on the coordinate domain, i.e. on the position of the backscattering facets, the transfer functions $T^{vb}_{\boldsymbol{k}}$ and $T^{rb}_{\boldsymbol{k}}$ are an attempt to translate the effect of facet displacement ('facet bunching') into an effective modulation of the intensity at a given position (i.e. for fixed facet positions).

However, the MARSEN review has corroborated that in the context of SAR imaging, incorporating $T^{vb}_{\boldsymbol{k}}$ and $T^{rb}_{\boldsymbol{k}}$ into the linear transform equation (4.4) is not a valid approximation. The facet displacements act on the phase of the backscattered signal, thus inducing nonlinear coherence effects in the signal covariance. In the following section we focus on the transform $x \mapsto x + \xi_x$, associated with the wave orbital motion $u_r(\boldsymbol{x})$.

4.4.2 Nonlinear velocity bunching as a composite stochastic process

The velocity bunching effect, was introduced by *Alpers and Rufenach* [1979]; *Swift and Wilson* [1979] in the context of imaging of ocean waves by airborne or spaceborne synthetic aperture radars (SARs). After the basic processes governing the imaging of ocean waves by a SAR were understood and it was recognized that linear RAR imaging could not account for the nonlinearities (see the MARSEN review in *Hasselmann, K. et al.* [1985] and *Tucker* [1985]), methods were sought to extract ocean wave spectra from SAR image spectra.

First simulations of the fully nonlinear velocity bunching mechanism were achieved using Monte Carlo methods [*Alpers* 1983]; [*Alpers et al.* 1986]; [*Brüning et al.* 1990]. This technique, however, requires considerable computing time and does not lend itself readily to an inversion, as required for the construction of a retrieval algorithm.

It was not until the derivation by *Hasselmann, K. and Hasselmann, S.* [1991] of a closed nonlinear spectral integral transform of a wave spectrum into a SAR image spectrum that the inversion problem became tractable. Subsequently, *Krogstad* [1992] showed, that this nonlinear transform could also be derived by means of a characteristic function and its associated G function of a multivariate random vector. This framework allowed straightforward generalizations to include additional processes (see e.g *Bao et al.* [1994], *Krogstad et al.* [1994], *Engen and Johnsen* [1995]).

In the following the spectral wave–to–SAR transform is considered as a multivariate composite stochastic process

$$\boldsymbol{x} \;\overset{\boldsymbol{\xi}}{\longmapsto}\; \boldsymbol{\xi}(\boldsymbol{x}) \;\overset{I^R}{\longmapsto}\; I^R(\boldsymbol{\xi}(\boldsymbol{x}))$$

4.4.2.1 The relation between the characteristic function, the G function and the covariance function

We follow *Krogstad* [1992] to show how the nonlinear integral transform of the SAR image spectrum $P(\boldsymbol{k})$ *[Hasselmann, K. and Hasselmann, S.* 1991] can be expressed as the Fourier transform of a G function through

$$P(\boldsymbol{k}) = \int G(\boldsymbol{x},\boldsymbol{k})\, e^{-i\boldsymbol{x}\cdot\boldsymbol{k}}\, \mathrm{d}x_1 \ldots \mathrm{d}x_n \tag{4.12}$$

(here, $n = 2$) with a generalized covariance function

$$G(\boldsymbol{x},\boldsymbol{k}) = < I^R(\boldsymbol{x}) I^R(\boldsymbol{o})\, e^{i\boldsymbol{k}\cdot[\boldsymbol{\xi}(\boldsymbol{x})-\boldsymbol{\xi}(\boldsymbol{o})]} > \tag{4.13}$$

Consider the multivariate random vector

$$\boldsymbol{X}(\boldsymbol{x}) = [I^R(\boldsymbol{x}), I^R(\boldsymbol{o}), \boldsymbol{\xi}(\boldsymbol{x}), \boldsymbol{\xi}(\boldsymbol{o})] \tag{4.14}$$

The G function can be generally computed from the characteristic function of the multivariate random vector $\boldsymbol{X}$, also called generating function (see e.g. *Johnson et al.* [1994]). The characteristic function Z of $\boldsymbol{X}$ is defined as

$$\begin{aligned} Z(\boldsymbol{K}) &= < e^{i\boldsymbol{K}\cdot\boldsymbol{X}} > \\ &= \int p(X_1,\cdots,X_m)\, e^{i\boldsymbol{K}\cdot\boldsymbol{X}}\, \mathrm{d}X_1 \ldots \mathrm{d}X_m \end{aligned} \tag{4.15}$$

where the second expression denotes the mean in terms of the joint probability density function (pdf) $p(\boldsymbol{X})$. $Z(\boldsymbol{K})$ may thus be interpreted as the Fourier transform of the joint pdf of the multivariate random vector $\boldsymbol{X}$.

Assuming that the characteristic function $Z(\boldsymbol{K})$ can be expanded in a Taylor series, and also that all moments exist, one recovers from the exponential form of $Z(\boldsymbol{K})$ the general relation

$$\left.\frac{\partial^l}{\partial K_{j_1}\cdots\partial K_{j_l}}\right|_{\boldsymbol{K}=\boldsymbol{O}} Z(\boldsymbol{K}) = i^l < X_{j_1}\cdots X_{j_l} > \tag{4.16}$$

Thus, all higher order statistical moments of the distribution of the multivariate random vector $\boldsymbol{X}$ may be obtained as higher order derivatives of $Z(\boldsymbol{K})$.

In particular, the second order partial derivative with respect to K_{j_1}, K_{j_2}, taken at $\boldsymbol{K} = \boldsymbol{O}$ yields the covariance function $< X_{j_1} X_{j_2} >$. Inserting equation (4.14) into equation (4.17), the G function may be identified with the second derivative of $Z(\boldsymbol{K})$ with respect to K_1, K_2, taken at $\boldsymbol{K} = (o, o, \boldsymbol{k}, -\boldsymbol{k})^t$ [*Krogstad* 1992]

$$G(\boldsymbol{x},\boldsymbol{k}) = -\left.\frac{\partial^2}{\partial K_1 \partial K_2}\right|_{\boldsymbol{K}=(o,o,\boldsymbol{k},-\boldsymbol{k})} Z(\boldsymbol{K}) \tag{4.17}$$

The result can be interpreted as follows: The primary RAR modulation process $I^R(\boldsymbol{x})$ is altered through a secondary process which consists in a transform of the variable $\boldsymbol{x} \mapsto \boldsymbol{x} + \boldsymbol{\xi}(\boldsymbol{x})$ of the primary process I^R, thus leading to a redistribution of the image intensity $I^R(\boldsymbol{x})$ through a redistribution of the effective facet density (see e.g. *Hasselmann, K. and Hasselmann, S.* [1991]; *Delignon* [1993]; *Kerbaol* [1997]).

One observes that in the absence of the process $\boldsymbol{\xi}$ equation (4.13) reduces to the two-dimensional Fourier transform of the covariance of I^R, hence the variance spectrum of I^R. The process $\boldsymbol{\xi}$ thus introduces a nonlinearity into the system. It can be understood as a coherent process since it produces interferences in the product. This is also evident from a different perspective: Consider the complex-valued function

$$\tilde{I}(\boldsymbol{y}) = I^R(\boldsymbol{y})\, e^{i\,\boldsymbol{k}\,\cdot\,\boldsymbol{\xi}(\boldsymbol{y})} \tag{4.18}$$

which differs from $I^R(\boldsymbol{y})$ by a phase function. In this form the G function equation (4.13) can be readily recovered by the ensemble mean of the complex scalar products

$$G(\boldsymbol{x},\boldsymbol{k}) = < \tilde{I}(\boldsymbol{x})\, \tilde{I}^*(\boldsymbol{o}) > \tag{4.19}$$

The r.h.s. of equation (4.19) can again be viewed as covariance function of the complex-valued random process $\tilde{I}$. Compared to the usual covariance function it includes an additional phase function of the form $e^{i\,\boldsymbol{k}\cdot\boldsymbol{\xi}(\boldsymbol{x})}$. The complex-valued multivariate random vector now reads $X' = [\,\tilde{I}(\boldsymbol{x}), \tilde{I}(\boldsymbol{o})\,]$. The phase function alters the primary stochastic process. Apparently, this stochastic process cannot be approximated by a random phase approximation. The secondary process $\boldsymbol{\xi}$ introduces a coherence which has to be taken into account and introduces genuine nonlinearities in the transform (see e.g. *Chapron et al.* [1994], *Le Caillec et al.* [1996] and *Schmidt and Bao* [1998]).

4.4.2.2 The characteristic function for a Gaussian random process

Assuming that $\boldsymbol{X}$ is a Gaussian process with mean $\boldsymbol{\mu} = [I_0, I_0, 0, 0]$ and covarianve matrix $\boldsymbol{\Sigma}$, the G function is a function of auto- and cross-covariances of I^R and $\boldsymbol{\xi}$ [*Krogstad* 1992]

$$Z(\boldsymbol{K}) = \exp\left[\, i\,\boldsymbol{K}^t \cdot \boldsymbol{\mu} - \frac{1}{2}\boldsymbol{K}^t\,\boldsymbol{\Sigma}\, t\,\right]$$

$\boldsymbol{\Sigma}$ contains the auto- and cross-covariance functions ρ_{ab} defined in Table 4.2. As both these are functions of the wave spectrum, G is therefore a closed function of $F(\boldsymbol{k})$. T^a, T^b are the modulation transfer functions defined in Section 4.4.1.

For linear real aperture radar imaging the RAR image intensity I^R is linearly related to the sea surface elevation. The same holds for the velocity bunching process. In sum, the auto- and cross-covariances are linear functions of the wave spectrum $F(\boldsymbol{k})$ weighted by the bilinear products of the modulation transfer functions (MTF) $T^{ab}(\boldsymbol{k})$, and are thus determined by the separate linear modulation mechanisms. It is through the coherent products in the generalized covariances which describe the composite process, that the SAR imaging process becomes nonlinear.

The explicit form of the covariance matrix $\boldsymbol{\Sigma}$ can be found in *Krogstad* [1992] (its extension to a process, for which the velocity bunching is two-dimensional, i.e. for which $\xi_y = \zeta(\boldsymbol{x}) / \tan\theta$ where θ dentotes the incidence angle (range bunching) is discussed in *Engen and Johnsen* [1995]). For completeness we give the resulting G function

$$\begin{aligned} G(\boldsymbol{x}, k_x) = {} & e^{-k_x^2[\,\rho_{\xi\xi}(\boldsymbol{O}) - \rho_{\xi\xi}(\boldsymbol{x})\,]} \\ & \times \Big\{ \rho_{II}(\boldsymbol{o}) + \rho_{II}(\boldsymbol{x}) + ik_x \Big[\rho_{I\xi}(\boldsymbol{x}) - \rho_{I\xi}(-\boldsymbol{x}) \Big] \\ & \qquad + k_x^2 \Big[(\rho_{I\xi}(\boldsymbol{o}) - \rho_{I\xi}(\boldsymbol{x}))(\rho_{I\xi}(\boldsymbol{o}) - \rho_{I\xi}(-\boldsymbol{x})) \Big] \Big\} \end{aligned} \tag{4.20}$$

stochastic processes $I^R(\boldsymbol{x})$ and $\boldsymbol{\xi}(\boldsymbol{x})$ are linearly related to ζ

$$I^R(\boldsymbol{x}) \;=\; \sum_{\boldsymbol{k}} \hat{I}^R(\boldsymbol{k})\, e^{i\boldsymbol{k}\cdot\boldsymbol{x}} \qquad\qquad \xi(\boldsymbol{x}) \;=\; \sum_{\boldsymbol{k}} \hat{\xi}(\boldsymbol{k})\; e^{i\boldsymbol{k}\cdot\boldsymbol{x}}$$

$$\Big\downarrow \qquad \zeta(\boldsymbol{x},t) = \sum_{\boldsymbol{k}} \left\{\hat{\zeta}(\boldsymbol{k}) e^{i(\boldsymbol{k}\cdot\boldsymbol{x}-\omega t)} + \text{c.c.}\right\} \qquad \Big\downarrow$$

$$\begin{aligned}\hat{I}^R(\boldsymbol{k}) &= T^R(\boldsymbol{k})\hat{\zeta}(\boldsymbol{k}) \\ &\quad + \left(T^R(-\boldsymbol{k})\hat{\zeta}(-\boldsymbol{k})\right)^*\end{aligned} \qquad\qquad \begin{aligned}\hat{\xi}(\boldsymbol{k}) &= T^{vb}(\boldsymbol{k})\hat{\zeta}(\boldsymbol{k}) \\ &\quad + \left(T^{vb}(-\boldsymbol{k})\hat{\zeta}(-\boldsymbol{k})\right)^*\end{aligned}$$

$\hat{I}^R(\boldsymbol{k})$ and $\hat{\xi}(\boldsymbol{k})$ are linear in $\hat{\zeta}(\boldsymbol{k})$ with transfer functions $T^R(\boldsymbol{k})$, $T^{vb}(\boldsymbol{k})$

auto- and cross-covariances ρ_{II}, $\rho_{I\xi}$, $\rho_{\xi\xi}$ of $\hat{I}^R(\boldsymbol{k})$, $\hat{\xi}(\boldsymbol{k})$

$$\rho_{ab}(\boldsymbol{x}) = < a(\boldsymbol{o})\, b(\boldsymbol{x}) >$$

$$\rho_{ab}(\boldsymbol{x}) = \int P^{ab}(\boldsymbol{k})\, e^{-i\boldsymbol{k}\cdot\boldsymbol{x}}\, \mathrm{d}\boldsymbol{k} \qquad \Big\downarrow \qquad F(\boldsymbol{k}) \;=\; 2 < \hat{\zeta}(\boldsymbol{k})\hat{\zeta}^*(\boldsymbol{k}) >$$

$$P^{ab}(\boldsymbol{k}) = \tfrac{1}{2}\Big\{\, T^a(\boldsymbol{k})T^{b*}(\boldsymbol{k})F(\boldsymbol{k}) \,+\, T^{a*}(-\boldsymbol{k})T^b(-\boldsymbol{k})F(-\boldsymbol{k}) \,\Big\}$$

variance and cross spectra $P^{ab}(\boldsymbol{k})$ are linear in $F(\boldsymbol{k})$

Table 4.2: Relationship between surface elevation and wave spectrum for the separate stochastic processes. a, b label the image intensity I^R and the displacement ξ

Here, $\rho_{II}(o) = \sigma(o) = 1$. The exponential only contains pure auto-covariances of the velocity bunching process. Comparing equation (4.20) with the integrand of the closed integral expression in *Hasselmann, K. and Hasselmann, S.* [1991] we identify $e^{-k_x^2\rho_{\xi\xi}(\boldsymbol{O})}$ with the overall azimuthal cut-off factor $e^{-k_x^2<\xi_x^2>}$ which may be taken outside the integral. The remaining term $e^{k_x^2\rho_{\xi\xi}(\boldsymbol{x})}$ produces higher-order products of the covariance functions and thus of the wave spectrum, rendering the composite process inherently nonlinear.

The exponential cut-off factor describes the azimuthal fall-off of the SAR image spectrum beyond an azimuthal cut-off wavenumber k_x, where $\xi = R/V \cdot u_r$ is the product of the rms orbital (range) velocity u_r and the range-to-platform velocity ratio $\beta = R/V$ (see [HH]). Thus, for large displacements compared with a wavelength, the image is effectively smeared out.

The form of the nonlinear integral mapping implemented in the WASAR algorithm is based on the Taylor series expansion of the nonlinear term $e^{k_x^2\rho_{\xi\xi}(\boldsymbol{x})}$, derived in [HH]. The series consists of terms of higher order products of the auto- and cross-covariance functions ρ_{ab} appearing in Table 4.2 which can be efficiently computed through fast Fourier transforms.

4.4.2.3 Experimental verification of the SAR imaging theory

The imaging theory and nonlinear mapping relation have been verified in a number of field experiments with airborne SARs, such as the Labrador Extreme Waves Experiment (LEWEX, see *Beal* [1991]) and the Synthetic Aperture Radar and X-Band Ocean Nonlinearities - Forschungsplattform Nordsee (SAXON-FPN) campaign (see *Plant and Alpers* [1994]) as well as with spaceborne SARs on board SEASAT (see the special *SEASAT* [1983] issue of the *Journal of Geophysical Research* and *Hasselmann, K. et al.* [1991]), the Space Shuttle Imaging Radar B and C missions (SIR-B/C), (e.g. *Alpers et al.* [1986], *Monaldo and Lyzenga* [1988], *Brüning et al.* [1988], and *SIR-C* [WWW]), and the Grand Banks ERS-1 SAR Wave Spectra Validation Experiment, that included also a validation against airborne SAR's (see *Grand Banks* [1994] and the ALMAZ-1 satellite mission *Wilde et al.* [1994]).

For aircraft SARs, the quasi-linear approximation of the SAR imaging expression, obtained by terminating the Fourier series expansion after the first linear terms, but retaining the nonlinear exponential azimuthal cut-off factor, is often an acceptable approximation (see e.g. *Monaldo and Lyzenga* [1986], *Beal et al.* [1991], *Monaldo and Beal* [1995] and references therein). However, the quasi-linear approximation is unable to account for the nonlinear image distortions inherent in the imaging process for the high range-to-platform velocity ratios typical of satellite SARs (for ERS-1, $R/V = 112$ sec, which is much larger than typical R/V ratios for low flying aircrafts).

4.5 The retrieval algorithm

Subsequent to their derivation of the nonlinear integral transform, [HH] presented an algorithm for inverting the spectral mapping relation. Their retrieval algorithm has since been extended ([HBHH]) by adding an explicit cut-off adjustment term to the cost function and a second iteration loop that successively modifies the first guess input spectrum (see flow chart, Figure 4.5 and Section 4.5.2). The latter extension effectively decouples the retrieval from the original first guess spectrum. In the following we briefly review the main features of the technique. A technical software description of the WASAR algorithm is given in a Technical Report of the DKRZ [*Hasselmann, S. et al.* 1998].

4.5.1 Inversion of the nonlinear transform

The first step of the retrieval algorithm is the inversion of the nonlinear spectral mapping relation for a given first-guess input spectrum by minimizing the following error cost function (inner iteration loop in Figure 4.5)

$$J = \int \left[P(\boldsymbol{k}) - \hat{P}(\boldsymbol{k})\right]^2 \hat{P}(\boldsymbol{k})\,\mathrm{d}\boldsymbol{k} + \mu \int \frac{\left[F(\boldsymbol{k}) - \hat{F}(\boldsymbol{k})\right]^2}{\left\{B + \min\left[F(\boldsymbol{k}), \hat{F}(\boldsymbol{k})\right]\right\}^2}\,\mathrm{d}\boldsymbol{k} + \eta\,\frac{\left(\alpha\lambda_c^2 - \hat{\lambda}_c^2\right)^2}{\max\left\{\lambda_c^4, \hat{\lambda}_c^4\right\}} \tag{4.21}$$

Here, $\hat{F}(\boldsymbol{k})$ denotes the first guess wave spectrum, $F(\boldsymbol{k})$ the best estimate wave spectrum, $\hat{P}(\boldsymbol{k})$ and $\hat{\lambda}_c$ the observed SAR spectrum with associated cut-off length scale, $P(\boldsymbol{k})$ and λ_c the SAR spectrum simulated from the best estimate wave spectrum with associated cut-off length scale, and μ, η are weighting factors. B is a small constant to prevent the denominator from vanishing. α is a free energy-scaling parameter which, applied to the whole spectrum, reduces the error between the observed and the simulated cut-off. For detailed discussion of the numerical inversion scheme we refer to [HBHH] and *Hasselmann, S. et al.* [1998].

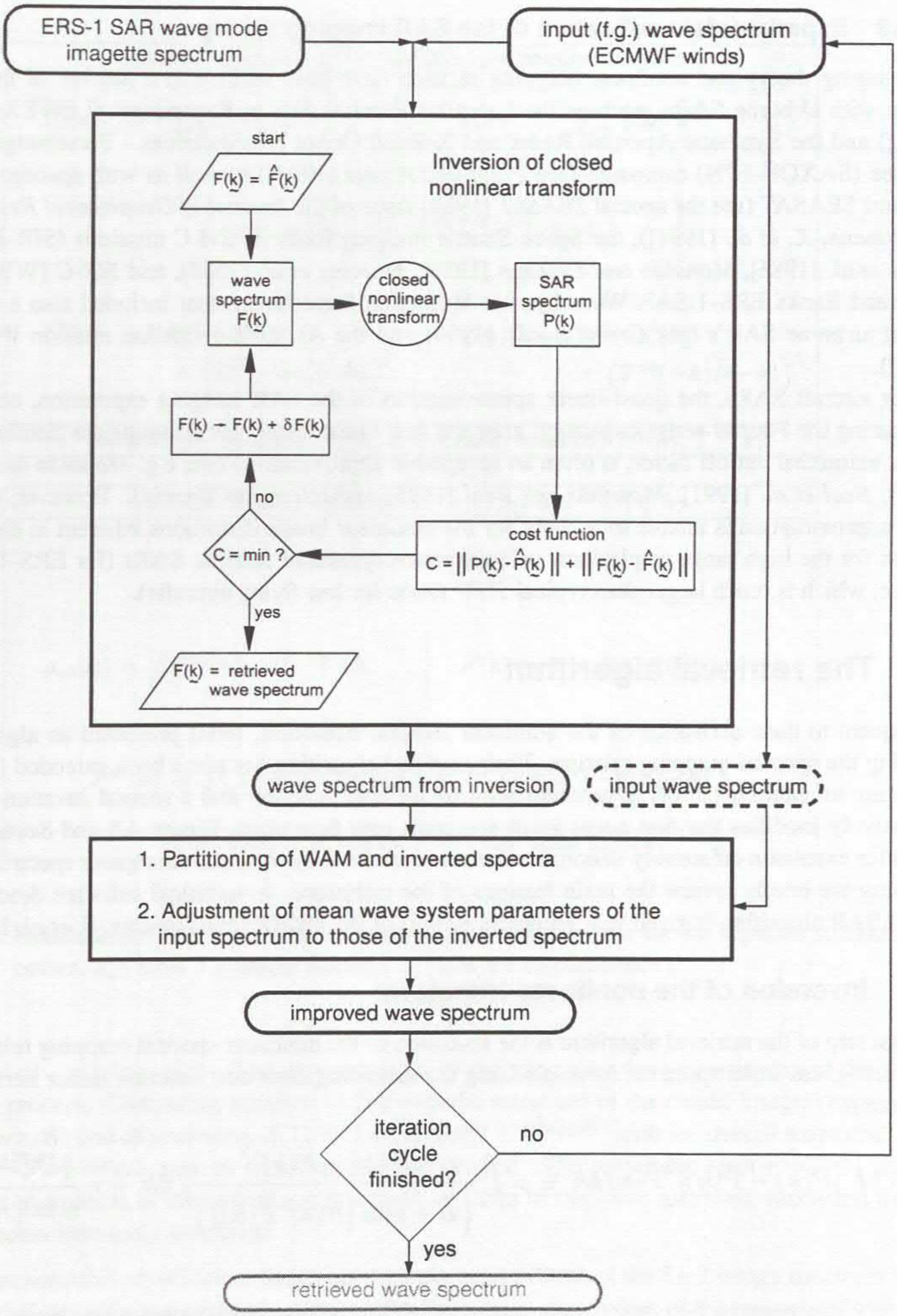

Figure 4.5: Flow chart of the retrieval algorithm showing the inner-loop iterative inversion procedure of the closed nonlinear transform and the outer-loop iterative updating of the input spectrum using a spectral wave partitioning scheme

A first guess is required for two reasons:

- Since the standard SAR product is an image of the instantaneous sea surface, it contains a 180° directional ambiguity. The ambiguity can be resolved only through additional information from a first guess spectrum (cf. Section 5.3 for an assessment of the sensitivity of the retrieval with respect to changes in the first guess).

Alternative techniques to overcome the ambiguity problem have been proposed, which make use of the information on the wave propagation direction contained in successive components of multi–look images [*Atanasov et al.* 1985]; [*Young et al.* 1985]; [*Vachon and Raney* 1991]; [*Rosenthal et al.* 1989]; [*Rosenthal and Ziemer* 1991]; [*Johnsen* 1992]; [*Engen and Johnsen* 1995]; [*Bao and Alpers* 1996]). However, although the feasibility has been demonstrated, the technique has not yet been implemented operationally. Nevertheless, the dissemination of multi–look image cross spectra containing the information of the wave propagation direction is planned as part of the fast delivery product for ENVISAT.

- The nonlinear velocity bunching mechanism smears out the short wave components beyond an azimuthal cut-off wavenumber dependent on the rms orbital velocity. The missing information must again be augmented by a first guess wave spectrum. However, this limitation is partially overcome in [HBHH] by including an explicit penalty term in the cost function for errors in the azimuthal cut-off, which is sensivitive to short waves beyond the cut-off (see Chapter 8 for a validation of the cut-off fitting procedure).

A valuable feature of the SAR spectral retrieval algorithm is the availability of an internal calibration based on the level of the background clutter spectrum. Thus, the retrieved spectra can be calibrated in absolute wave height units without reference to the SAR instrument calibration or measurements of the absolute backscattering cross section (see *Alpers and Hasselmann* [1982] and *Brüning et al.* [1994]).

4.5.2 Spectral partitioning and iterative updating of the input spectrum

Although the overall level of the high wavenumber part of the spectrum is adjusted through the inclusion of an explicit azimuthal cut-off penalty term in the cost function, the inversion method modifies the detailed form of the spectrum only in the main part of the spectrum for which direct SAR spectral information is available. A straightforward inversion of the SAR spectrum therefore normally leads to unrealistic discontinuities in the transition zone near the azimuthal cut-off wavenumber separating the spectral regions with and without direct SAR information [HH].

This difficulty is overcome in the revised algorithm of [HBHH] by introducing a spectral partitioning scheme into the additional iteration loop that updates the input spectrum (cf. Figure 4.5). The iteration consists of repeatedly replacing the input spectrum used for the inversion for the iteration cycle $k + 1$ by the wave spectrum derived from the inversion in the previous iteration cycle k. However, instead of simply replacing the spectra wavenumber by wavenumber, the transfer is implemented via a spectral partitioning scheme (a modified form of the original partitioning algorithm of *Gerling* [1992] – see *Brüning et al.* [1994]; [HBHH]). This effectively extends the available SAR information below the azimuthal cut-off into higher wavenumbers beyond the cut-off. The new input spectrum retains the continuity properties of the original input spectrum, but the scales and propagation directions of the wave systems of the new spectrum are adjusted to the inverted spectrum. For details we refer to [HBHH] and *Hasselmann, S. et al.* [1998].

In the present study, five iterative updates of the input spectrum were carried out. As discussed in [HBHH], the iteration leads to a closer agreement between the observed and simulated SAR spectrum for the first iteration cycles, but then often begins to diverge. We have accordingly selected as the best

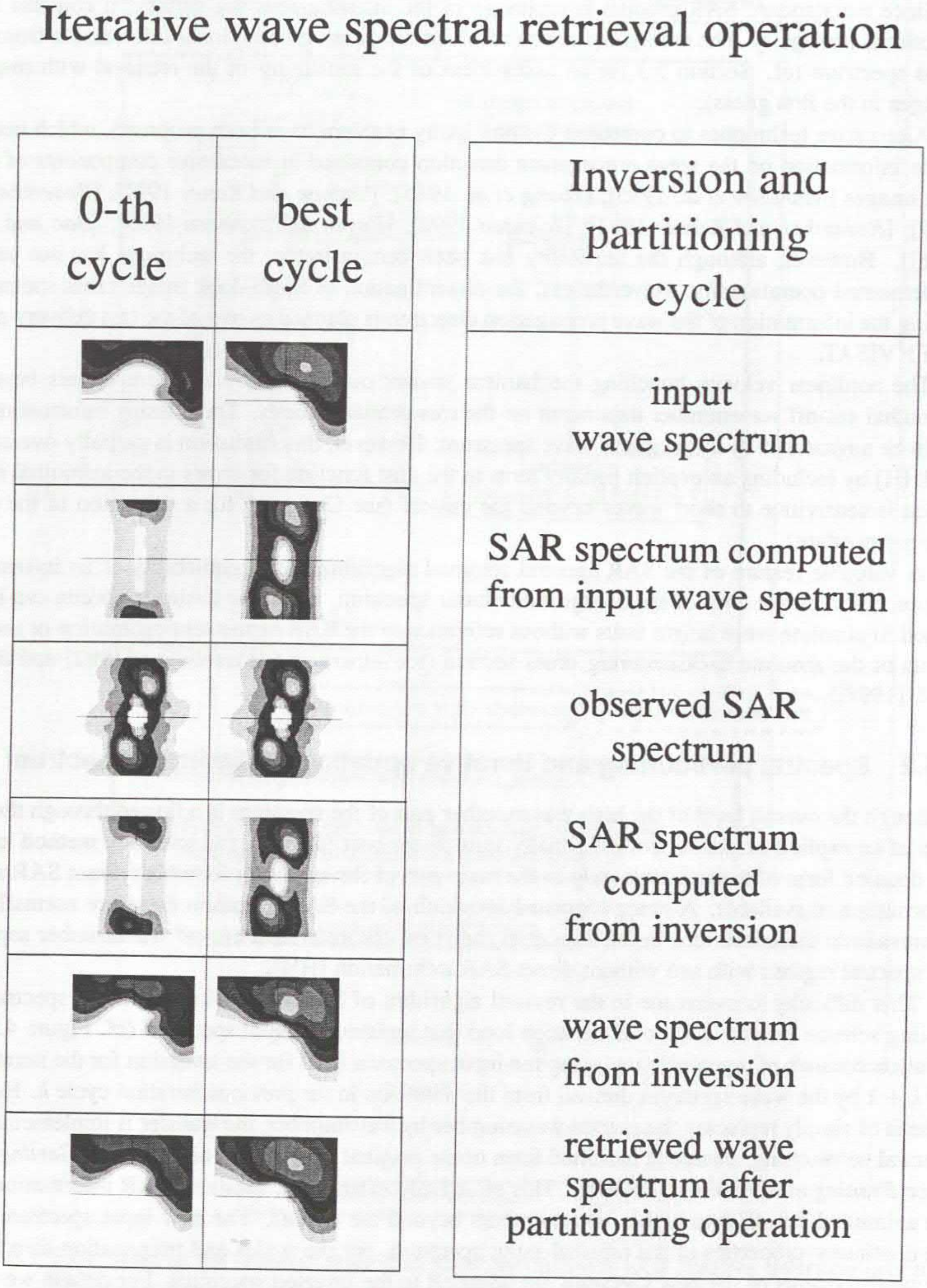

Figure 4.6: Example showing the intermediate steps of the iterative wave spectral retrieval operation on a cartesian 128 × 128 wavenumber grid.

retrieval the solution that yields the smallest dimensionless square error ϵ defined as

$$\epsilon^2 = \frac{\int\int\left[P_{sim}(f,\theta) - P_{obs}(f,\theta)\right]^2 \mathrm{d}f\mathrm{d}\theta}{\sqrt{\int\int P_{sim}^2(f,\theta)\mathrm{d}f\mathrm{d}\theta \cdot \int\int P_{obs}^2(f,\theta)\mathrm{d}f\mathrm{d}\theta}} \tag{4.22}$$

between the SAR spectrum P_{sim} computed from the input wave spectrum and the observed SAR spectrum P_{obs} (cf. [HBHH] and Figure 4.6). An assessment of the iteration procedure will be given in Section 5.2.

We shall occasionally use the spectral pattern correlation

$$\rho^2 = \frac{\int\int P_{sim}(f,\theta)P_{obs}(f,\theta)\mathrm{d}f\mathrm{d}\theta}{\sqrt{\int\int P_{sim}^2(f,\theta)\mathrm{d}f\mathrm{d}\theta \cdot \int\int P_{obs}^2(f,\theta)\mathrm{d}f\mathrm{d}\theta}} \tag{4.23}$$

as an alternative measure to ϵ. We note, however, that ρ is a less stringent measure because two spectra which deviate significantly in absolute level but which can be linearly rescaled bin-by-bin by almost the same rescaling factor have high correlation but also high spectral error. In the present work we have estimated high ρ to occur simultaneously to high ϵ for maximally 5 percent of the data.

5 ASSESSMENT OF THE RETRIEVAL PERFORMANCE

An assessment of the overall performance of the combined ERS-1 SAR wave mode system and retrieval procedure involves several complementary aspects.

1. Data quality. This concerns the quality of the SWM product in terms of signal-to-noise and contamination with non-wave-like features ([HH] and *Brüning et al.* [1994]). Nonlinear image distortions, on the other hand, as an inherent property of the measurement mechanism, are not regarded as a quality reduction of the SWM product.

2. Retrieval fidelity. This refers to the ability of the retrieved wave spectrum to reproduce the observed SAR spectrum. If the SAR spectrum computed from the retrieved wave spectrum via the full nonlinear forward transform agrees closely with the observed wave spectrum, as measured, for example, by the normalized spectral error, the retrieval has high fidelity. This is clearly the first goal of a retrieval algorithm. A retrieval with high fidelity has extracted all the information that is available from the SAR spectrum (see [HH], *Brüning et al.* [1994] and [HBHH]). An assessment of the retrieval fidelity together with the data quality is given in Section 5.1.

3. Retrieval validation. This assesses the degree of agreement of the retrieved spectrum with the true wave spectrum. We pursue two complementary approaches to address this issue.

The first approach presented in Chapter 7 consists of intercomparing the retrievals with model data. A comparison with model data has the advantage that both data sets are available globally for the complete two-dimensional wave spectra and throughout the entire three year analysis period. But the approach naturally raises the question whether model spectra can be regarded as reasonable approximations of the true wave spectra. However, this is a basic shortcoming of all intercomparisons. Normally, it is not possible to regard either of the two data sets of an intercomparison as faithful replica of the true state. All one can do is cross-validate the data in an attempt to gain a synthetic assessment of both data sets, taking into account their individual shortcomings.

The second approach presented in Chapter 6 is a multisensor validation of SWM-retrieved significant wave heights with TOPEX and ERS-1 altimeter data. Unfortunately, although satellite altimeters also provide global continuous coverage, the lack of detailed spectral information limits the value of such validation exercises. Nevertheless, the spectral information provided by the SWM data allows to go beyond a pure validation of H_s.

4. Operational efficiency. Three considerations are relevant for operational efficiency:

1. The number of SWM spectra delivered to the operational forecast centre (in the present case, ECMWF) in quasi real-time time per month, or, equivalently, the percentage of time the end-to-end SWM system was functioning satisfactorily in the operational quasi real-time mode.
2. The percentage of the receipt SWM spectra for which the operational centre was able to provide collocated first guess wave spectra as input for the retrievals. Failure to provide an input spectrum can

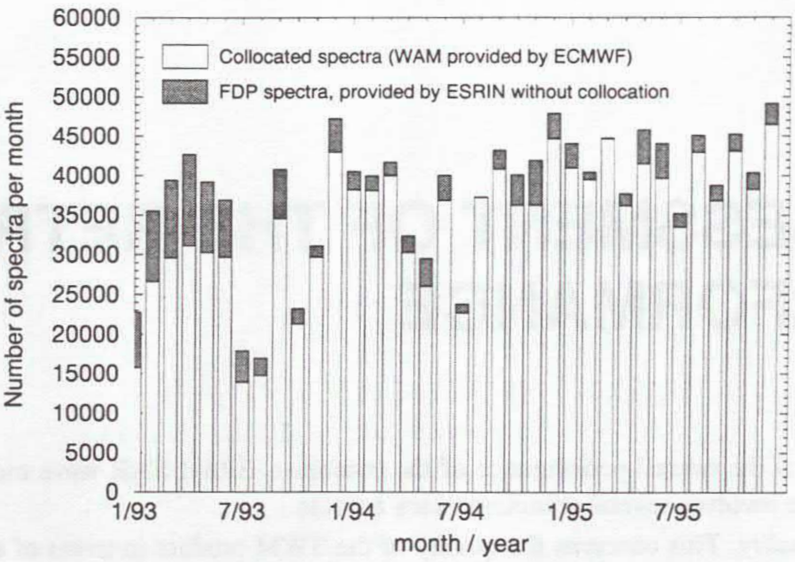

Figure 5.1: Number of monthly available ERS-1 SAR Wave Mode data. SWM spectra that could be collocated with WAM model spectra are represented by the light lower column segments, those for which no first guess model spectra were available by the dark upper segments.

be either due to receival of the SWM product outside the relevant operational time window (which is classed as a failure of the delivery system), or to system interruptions at ECMWF.
3. The computational load of the operational production of global SWM spectral retrievals. At a peak frequency of one SWM spectrum every thirty seconds, it is imperative to keep cpu time low. This requires a trade-off between the number of iterative cycles of the input wave spectrum and cpu time.

We shall consider questions *1.* and *2.* regarding the production reliability in Section 5.1 and the aspect *3.* of computational efficiency in Section 5.2. A sensitivity analysis of the retrieval with respect to the first guess input spectrum is given in Section 5.3 (see also *Heimbach et al.* [1998]).

5.1 Data quality and retrieval fidelity

The three year set of ERS-1 SWM data between January 1993 and December 1995 comprises a total of some 1.2 million wave spectra with an average daily output of 1100 spectra. The number of monthly available SWM spectra is shown in Figure 5.1. The dark column segments indicate the number of fast delivery product (FDP) spectra for which no first guess model spectra were available. The envelope of the FDP columns shows a high value from the outset. A low FDP content was found during the summer seasons 1993 and 1994. For summer 1993 this can be explained by a change in the set-up of the operational wave forecasting facilities; the origin of the second minimum is not clear.

The retrieval process incorporated two quality tests: a data quality test for the input SWM data, and a fidelity test for the retrieval. The input SWM data was rejected if the signal-to-noise ratio of the image spectrum (defined as the ratio of the spectral peak to the clutter noise background) was less than 3 db or if the first guess wave height was below 0.1 m. The retrieved spectra were discarded if the cost function was not reduced to less than half of its initial value. Furthermore, all spectral information beyond 800 m wavelength was excluded. These frequently represent non-wave-like sea surface features like slicks, wind rows etc. [*Brüning et al.* 1994]. Statistical analyses (cf. Chapter 7) indicate that swell of extreme wavelengths beyond 800 m are rare.

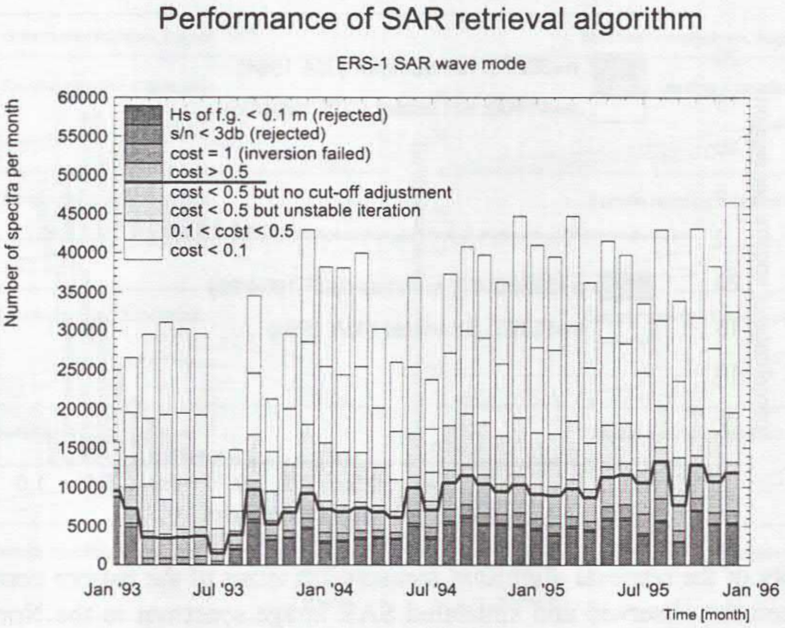

Figure 5.2: Data quality and performance of the retrieval algorithm measured in terms of the cost function reduction factor. Retrievals with a cost function reduction below 0.5 are regarded as reliable. For data of too poor quality no retrieval was attempted (below solid line).

Figure 5.2 shows that with the beginning of the quasi real-time distribution of the FDP through the European Space Research Institute (ESRIN) in February 1993, maximally 2 % of the data showed low signal-to-noise ratios. Another 10% of the data were rejected because the first guess wave height was too low ($H_s < 0.1$ m).

For roughly 85 % of the remaining data, the retrieval algorithm achieved an acceptable performance, with cost function reductions to less than 0.5 of the initial value, for one third a reduction factor of less than 0.1 was achieved. Spectra with a cost function reduction factor lower than 0.5 for which the azimuthal clutter cut-off adjustment or the convergence of the iterative inversion procedure was poor were nevertheless retained in the subsequent analysis, as their fidelity measured in terms of the pattern correlation coefficient was generally still acceptable. The remaining 15% inversions for which the ratio of the final to initial cost could not be reduced below 0.5 generally exhibited relatively low pattern correlations between the simulated and observed SAR spectra and were discarded from the further analysis.

The number of monthly available SWM-retrieved spectra that passed both tests is geographically relatively homogeneous, and varied with the size of the ocean basin from 1500 in the North Atlantic to 5000 in the Tropical Pacific.

The retrieval performance is represented in Figure 5.3 in terms of the distributions of the pattern correlation coefficients for the simulated and observed SAR spectra for the summer 1994 and winter 1994/95 seasons in the Northern and Southern Hemisphere. All distributions show a rather narrow peak around 0.9, indicating that for the major part of the data successful retrievals of high fidelity were achieved. The winter distributions in both hemispheres appear to be peaked towards slightly higher correlations than the summer distributions, suggesting that the retrieval performance is generally higher for high sea states (as may be expected from the generally higher signal-to-noise ratios for higher sea states).

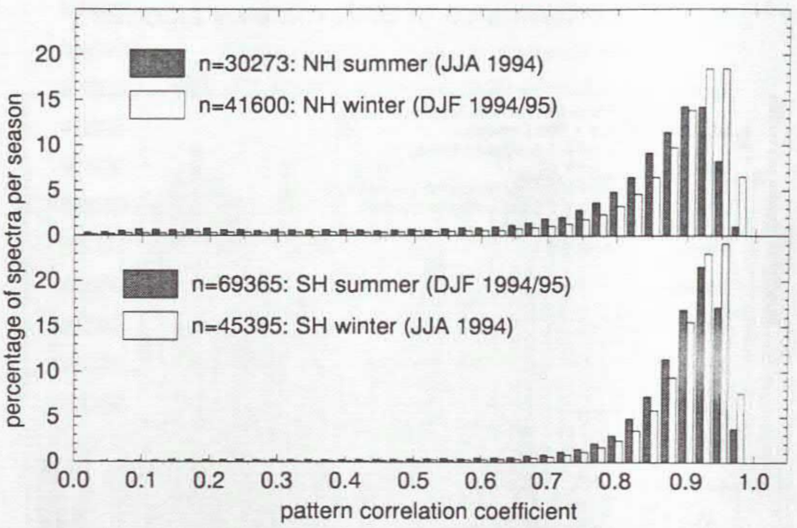

Figure 5.3: Fidelity of the retrieval algorithm measured in terms of the pattern correlation coefficient between the observed and simulated SAR image spectrum in the Northern Hemisphere (top panel) and Southern Hemisphere (bottom panel).

5.2 Iteration procedure

As described in Section 4.5, five iterations of the input wave spectrum were carried out, and the inversion that yielded the smallest error between the observed and simulated SAR spectrum was then selected as the final retrieval. A time series of the monthly distribution of the number of iterations yielding the best retrieval revealed a stable behaviour throughout the three years. Table 5.2 shows the average percentage of spectra for which N iterations of the input spectrum yielded an optimal retrieval. For about 92 % of the retrievals an iteration of the input spectrum yielded an improvement, 75% showing a further improvement for more than one iteration. For operational applications a trade-off must be sought between computing time and the improvement in retrieval with increasing number of iterations. We discuss the trade-off first with respect to the impact on the retrieval fidelity, as expressed by the pattern correlation between the simulated and observed spectrum, and subsequently with respect to actually retrieved wave parameters.

The rate at which the error between the simulated and observed image spectrum decreases with the number of iterations, given the number of iterations N for an optimal retrieval, is illustrated in Figure 5.4a/b, which show the histograms of the pattern correlation for August 1995 Northern and Southern Hemisphere, respectively. The total set of spectra for each hemisphere is divided into five samples $\mathcal{S}_0, \ldots, \mathcal{S}_4$, where $\mathcal{S}_N$ denotes the set of spectra for which the optimal retrieval was achieved after N iterations (the last iteration set $\mathcal{S}_5$ is not considered in this analysis, because it contains also spectra that would have required more than five iterations for an optimal retrieval). All histograms are normalized to unit integral values. The graphs correspond, from bottom to top, to spectra requiring 1, 2 etc. iterations for optimal retrieval, and for each sample $\mathcal{S}_N$ the evolution of the histogram

no. of iterations N	0	1	2	3	4	≥ 5
no. of spectra [%]	8	17	17	15	13	30

Table 5.1: Percentage of spectra for which N iterations yielded an optimal retrieval, $N = 1, \ldots, 5$.

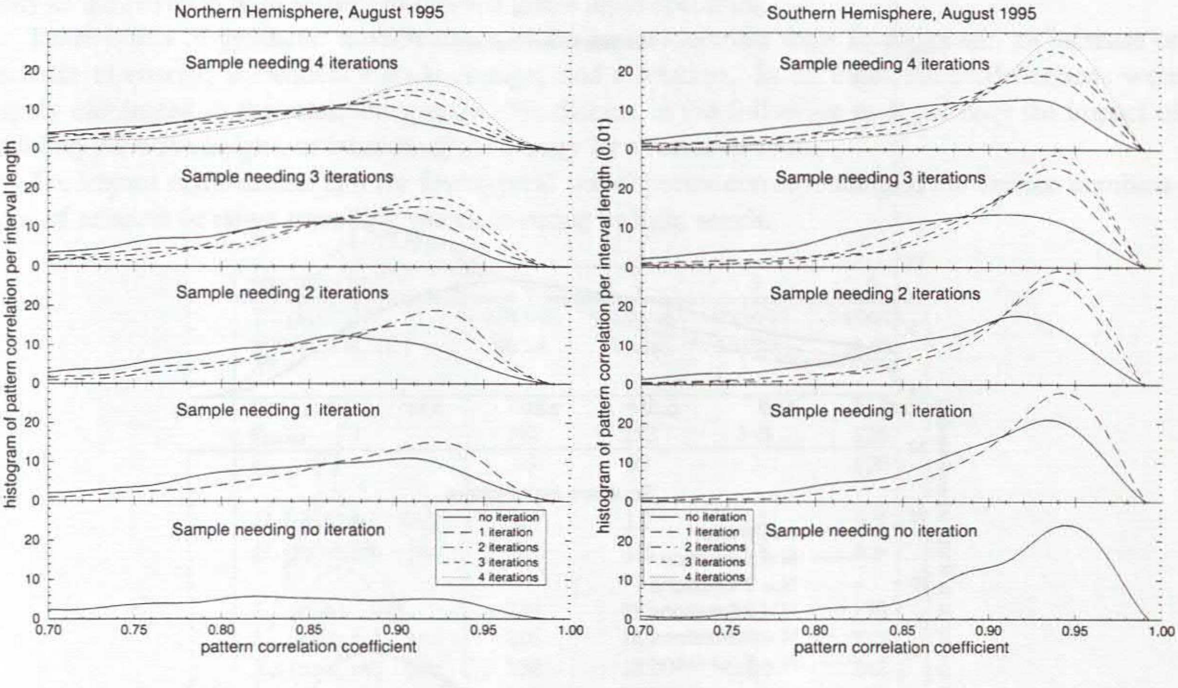

(a) (b)

Figure 5.4: Distribution of pattern correlation in the Northern Hemisphere (a) and Southern Hemisphere (b). The data sets of each panel consist of all spectra for which exactly N iterations produced the optimal retrieval (see Table Table 5.2). The curves within each panel indicate the improvement in pattern correlation with increasing number of iterations.

from iteration to iteration is depicted by $N + 1$ distribution curves. The behaviour is similar in both hemispheres. The largest impact on the retrieval is found in performing the first iteration. The impact of subsequent iterations diminishes with increasing N.

iteration	0th	1st	2nd	3rd	4th	5th
H_s	3.01 m	3.17 m	3.25 m	3.29 m	3.31 m	3.33 m
slope	-	0.993	1.011	1.020	1.028	1.036
correlation	-	0.942	0.897	0.874	0.859	0.846

Table 5.2: Change in mean retrieved H_s and regression parameters with increasing number of iterations for a one month global sample of ERS-1 SWM data (19129 entries).

As an alternative way of assessing the impact of the number of iterations on the retrieval performance, we used the same data sample of August 1995 to carry out a series of retrieval experiments in which the number of input iterations was set at a different fixed number M in each experiment. The best of the M iterations, defined in terms of the dimensionless error, was then taken as the retrieval. For each experiment this yielded a distribution curve of the pattern correlation index, shown in Figure 5.5 for the Northern and Southern Hemisphere. The distributions are qualitatively similar to Figure 5.4. Both results suggest that at least one iteration should be carried out, and that two iterations may represent an acceptable trade-off of retrieval improvement against computing time, the additional improvements beyond $M = 2$ tending to be rather small.

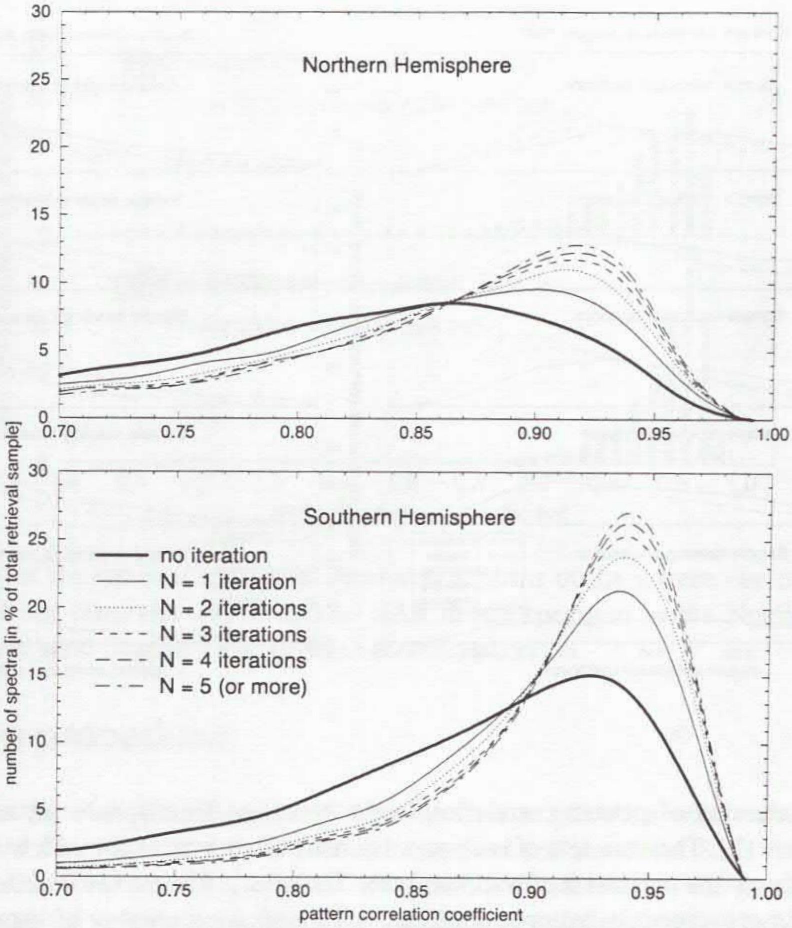

Figure 5.5: Distribution of pattern correlation in the Northern Hemisphere (top panel) and Southern Hemisphere (bottom panel). In contrast to Figure 5.4, each panel is based on the same set. The data set is subjected to a series of retrieval runs, each retrieval differing in the prescribed maximum number of iterations allowed. The retrieval fidelity increases with increasing maximum permitted number of iterations.

3. To assess the impact of the number of iterations not only on the fidelity measure but also on the retrieved wave parameters, a regression was carried out between the significant wave heights H_s of the retrieved spectra with and without iteration of the input spectrum. The regression parameters listed in Table 5.2 confirm that the retrieved wave heights do indeed converge with increasing iteration. The largest change is found as before for the first iteration, but the step from one to two iterations is also non-neglible, supporting the previous conclusion that it appears advisable to carry out at least one, but preferably two iterations.

5.3 Sensitivity of the retrieval with respect to the first guess

Through the inclusion of the deviation between the first guess (f.g.) input spectrum and the inverted spectrum as a (weakly weighted) regularization term in the cost function, the retrieved spectrum tends to be biassed towards the input spectrum. However, the bias is systematically reduced in the HBHH scheme through successive iterations of the first guess input. In this section we investigate the sensitivity of the retrieval with respect to the first guess input spectrum.

Three forms of synthetic modifications of the input spectrum were investigated: an increase or decrease in energy; a frequency scale change; and a rotation. In all cases the modifications were largely eliminated in the retrieved spectra. We discuss in the following in detail only the impact of doubling the wave height, or increasing the energy by a factor of four.

The impact is illustrated first for four typical wave spectra corresponding to the various combinations of azimuth or range travelling waves in strong or light winds.

spectrum no.	1	2	3	4
YY/MM/DD	95/06/02	95/06/06	95/06/07	95/06/08
HH:MM [UTC]	01:28	10:03	07:26	19:07
u_{10} $[m/s]$	19.0	4.0	7.6	20.5
θ_{wind} $[°]$	180	272	345	126
ϕ_{az} $[°]$	10	99	3	126
$H_s(\mathrm{orig,re})$ $[m]$	5.3	1.7	2.3	5.5
$H_s(\mathrm{mod,re})$ $[m]$	5.5	1.6	2.8	5.6
$\lambda_{az}(\mathrm{obs})$ $[m]$	259	191	181	239
$\lambda_{az}(\mathrm{orig,fg})$ $[m]$	266	185	188	259
$\lambda_{az}(\mathrm{orig,re})$ $[m]$	258	187	180	242
$\lambda_{az}(\mathrm{mod,fg})$ $[m]$	299	197	> 400	309
$\lambda_{az}(\mathrm{mod,re})$ $[m]$	259	188	178	242
$n_{iter}(\mathrm{orig})$	5	5	3	2
$n_{iter}(\mathrm{mod})$	5	5	5	5
$\epsilon(\mathrm{orig,fg})$	0.68	0.48	2.46	0.66
$\epsilon(\mathrm{orig,re})$	0.10	0.09	0.17	0.08
$\epsilon(\mathrm{mod,fg})$	0.77	0.41	6.55	0.52
$\epsilon(\mathrm{mod,re})$	0.11	0.09	0.45	0.10

Table 5.3: Characteristic parameters of the retrievals (re) of four ERS-1 SWM spectra, using unmodified (orig) and modified (mod) WAM first guess (fg) spectra.

Figure 5.7 to Figure 5.10 depict the various retrieval steps of the four spectra. In all cases it is apparent that the first inversion already removes most of the artificial error introduced into the modified wave spectra, but the error is suppressed still further in the subsequent iteration of the input spectrum. Table 5.3 summarizes the impact of the retrieval on characteristic wave parameters of the four spectra. In all four cases the significant wave heights retrieved from ERS-1 SWM data using modified WAM f.g. spectra $H_s(\mathrm{mod,re})$ agree closely to those $H_s(\mathrm{orig,re})$ retrieved using the original WAM f.g. spectra. The azimuthal cut-off wavelengths $\lambda_{az}(\,.\,,\mathrm{re})$ could be reliably adjusted to the observed values $\lambda_{az}(\mathrm{obs})$. The figures clearly illustrate the relationship between the cut-off length scale and the high frequency energy content (see e.g. the SAR spectrum simulated from the modified input spectrum in Figure 5.7 and Figure 5.10). While for the original WAM f.g. spectra less than five iterations were often sufficient to find the best estimate, the modified WAM f.g. spectra required all five iterations to adjust to the best solutions. Table 5.3 shows that the initial errors $\epsilon(\,.\,,\mathrm{fg})$ between the observed and simulated SAR spectrum are reduced considerably through the retrieval process.

To assess the sensitivity of the retrieval for a larger ensemble of cases, we have repeated the retrieval using WAM f.g. spectra similarly increased by a factor of four for a one day set of some

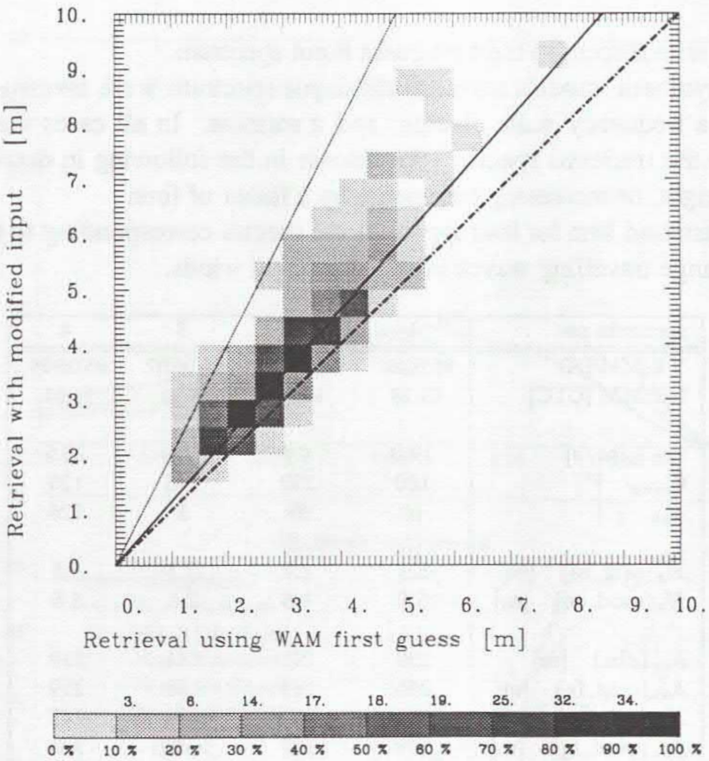

Figure 5.6: Regression between significant wave heights retrieved using the original and modified WAM f.g. input spectra for a one day set of ERS-1 SWM spectra on 95/06/07 (thick solid line). The original vs. modified WAM f.g. regression (thin dotted line) as well as the ideal regression (dot-dashed line) are shown for comparison .

1100 ERS-1 SWM spectra on 95/06/07. For the analysis we have considered only retrievals for which both the original and the modified retrievals yielded an acceptable fidelity level, corresponding to a normalized SAR spectral error ϵ less than 0.3. As can be expected, this eliminated some of the cases that passed the quality test for the original spectra, but not for the modified spectra.

Figure 5.6 shows the regression between the significant wave heights retrieved using the original and modified WAM f.g. input spectra. The regression coefficient is 1.15. Thus, the retrieval reduced the relative error of the modified f.g. wave heights on average by a factor of 6, from 1 to 0.15. The error would have been reduced still further if more iterations of the input spectrum had been carried out. However, typical errors of the first guess wave fields are significantly smaller than the synthetic errors considered here, so that five iterations are normally quite adequate (cf. Section 5.2).

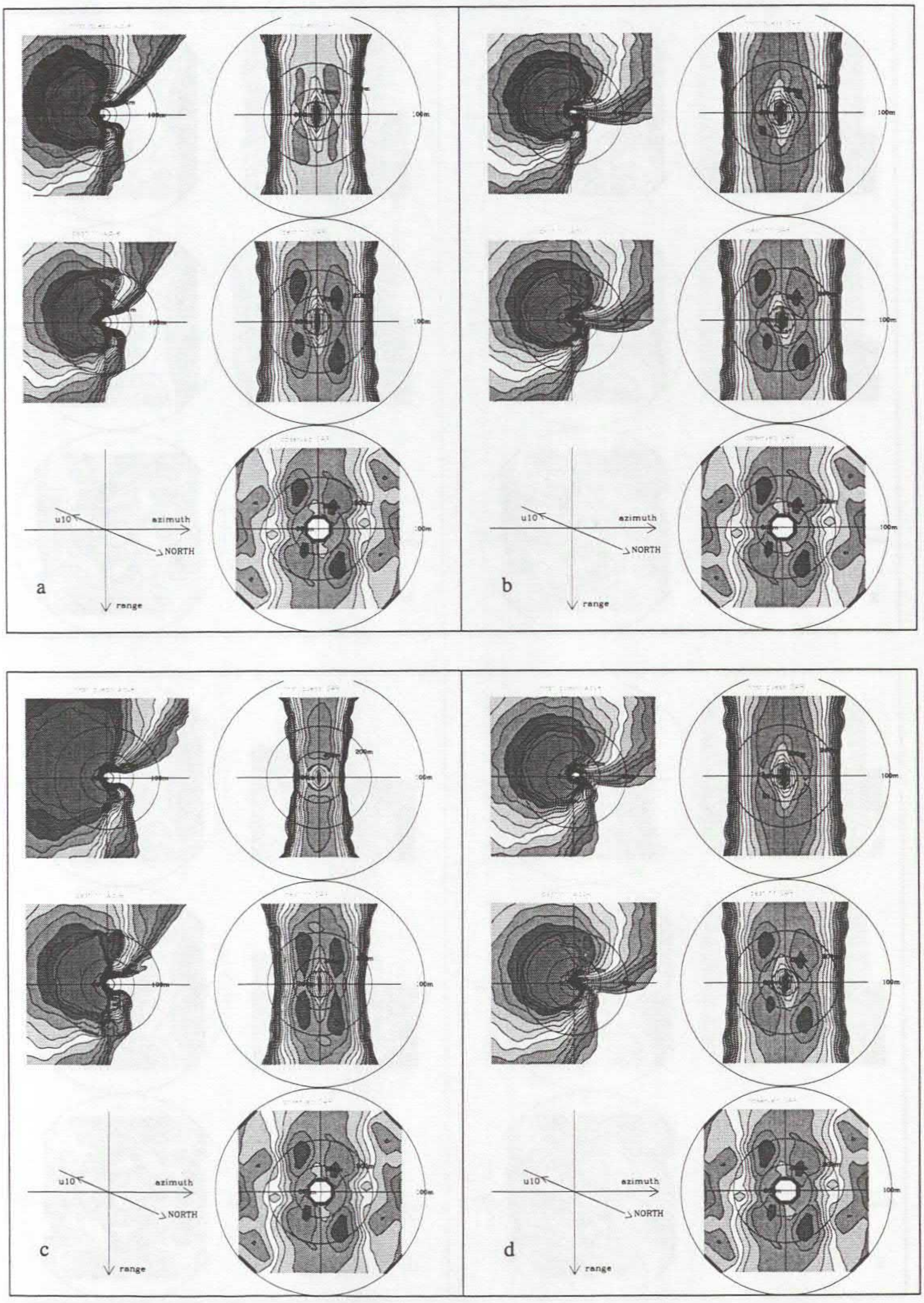

Figure 5.7: Input and retrieved wave spectra with associated SAR spectra for azimuthally travelling waves under strong winds (see figure captions in Table 5.4).

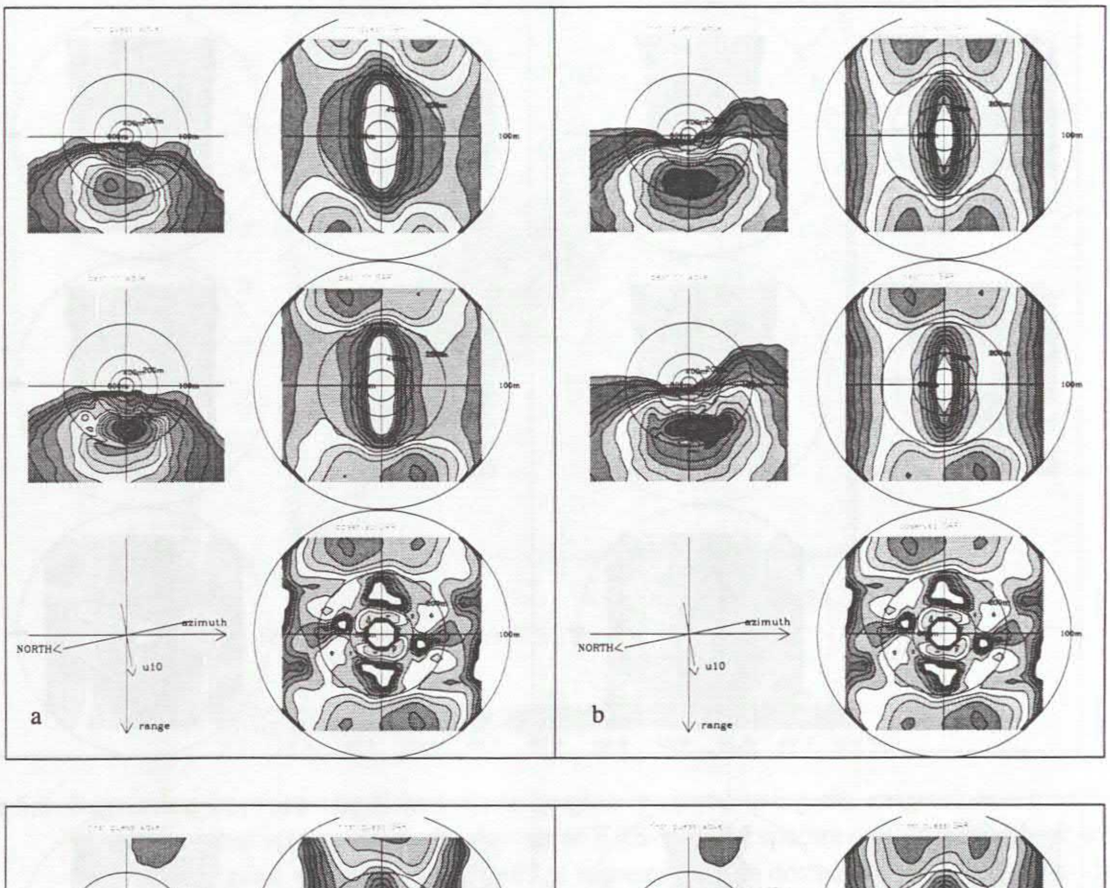

Figure 5.8: Same as Figure 5.7 for range travelling waves under light winds (see figure captions in Table 5.4).

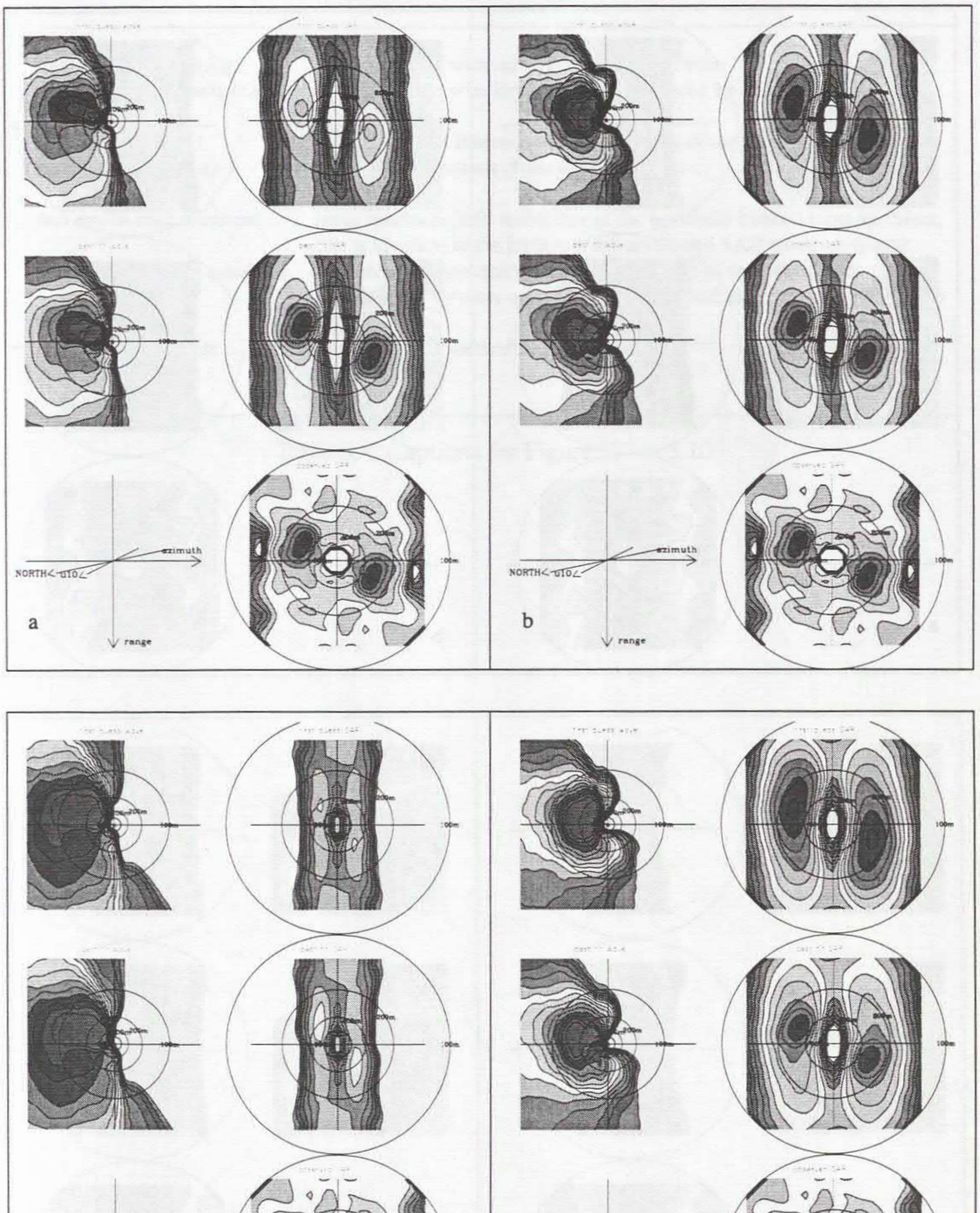

Figure 5.9: Same as Figure 5.7 for azimuthally travelling waves under light winds (see figure captions in Table 5.4).

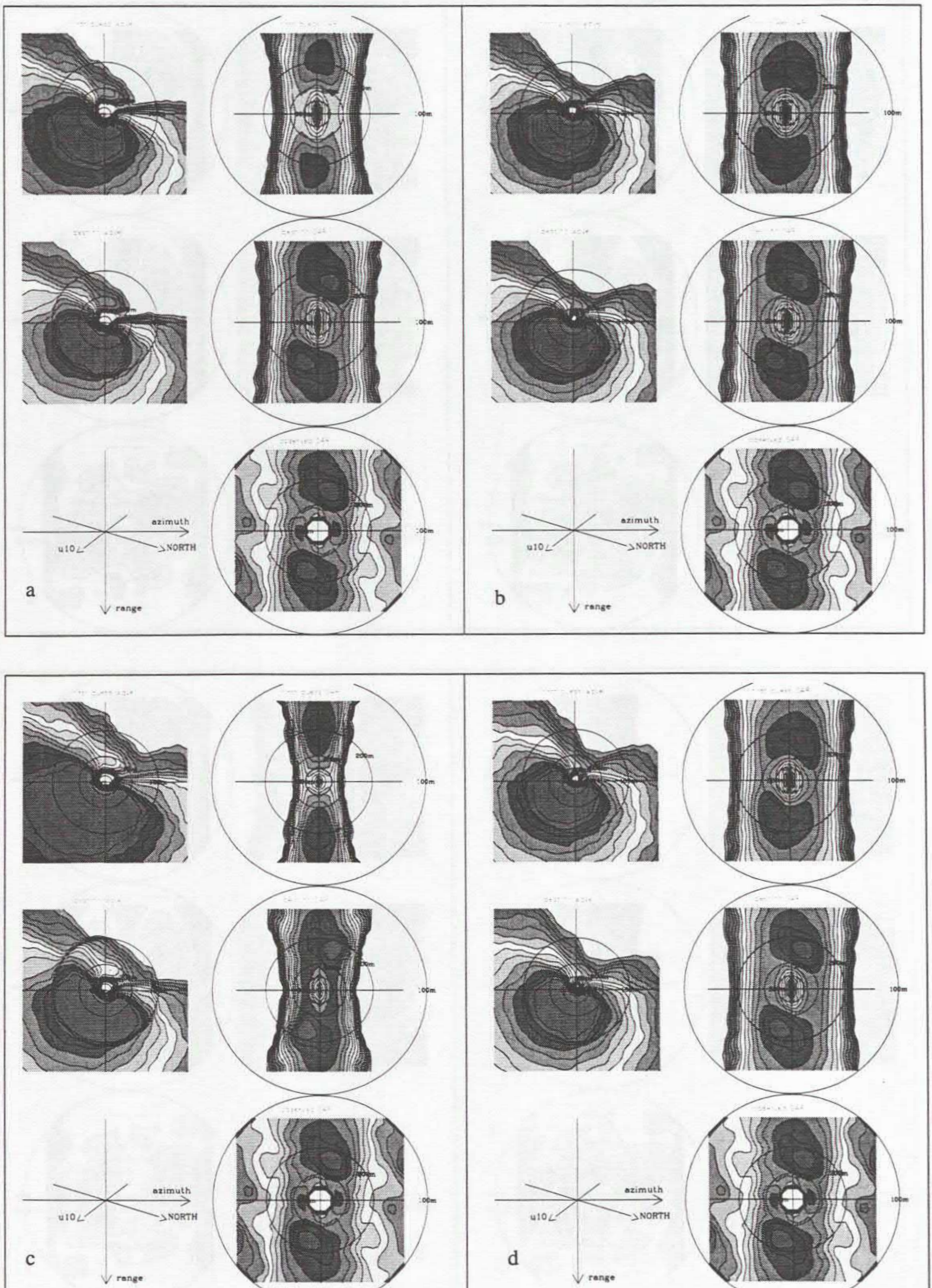

Figure 5.10: Same as Figure 5.7 for near-range travelling waves under strong winds (see figure captions in Table 5.4).

top two quadrants (a,b)	inversion steps with unmodified input spectrum
bottom two quadrants (c,d)	inversion steps with input spectrum increased by a factor four
left quadrants (a,c)	straightforward inversion without iteration of the input spectrum
right quadrants (b,d)	best of five iterations of the input spectrum
first row in each quadrant	input spectrum (left; in the case of the optimally iterated input spectrum, this is identical to the retrieval) and associated SAR spectrum (right)
second row in each quadrant	inverted wave spectrum (prior to application of smoothing and interpolation by wave system partitioning) and associated SAR spectrum
bottom right panel in each quadrant	observed SAR spectrum

Table 5.4: Captions for Figure 5.7 to 5.10

6 VALIDATION OF ERS-1 SWM–RETRIEVED SIGNIFICANT WAVE HEIGHTS USING TOPEX AND ERS-1 ALTIMETER DATA

Spaceborne altimeters provide global homogeneous measurements of significant wave height, $H_s = 4\sqrt{E_{tot}}$. They are thus highly suitable to validate the total energy E_{tot} of the wave height variance spectrum retrieved from the ERS-1 SAR wave mode data. Although limited in scope from a perspective of a detailed validation of spectral properties, the verification of SWM–retrieved wave heights against independent H_s altimeter data is an essential task and complementary to the model intercomparisons to be presented in Chapter 7. Furthermore, it offers some advantages to buoy comparisons, since it yields a global coverage, comprising data of various wind and wave regimes.

In this chapter we validate ERS-1 SWM–retrieved significant wave heights H_s^{swm} using altimeter–derived wave heights from the TOPEX/POSEIDON (H_s^{top}) and from the ERS-1 (H_s^{ers}) (see also *Bauer and Heimbach* [1998]). The comparisons are performed for the period of 1994. At the beginning of this year a revised sensor algorithm for the ERS-1 altimeter was implemented. The altimeter samples are described in Section 6.1.1. The statistical comparison of the collocated data is performed using different widths of the spatial and temporal collocation windows to account for dependencies on space-time variations (Section 6.1.2). Detailed statistical intercomparisons are presented in Section 6.2.

The SWM spectral retrievals offer the possibility to stratify the collocated data into spectrally distinct cases, for example into pure windsea and pure swell samples. This is exploited in Section 6.3 were we investigate discrepancies between H_s^{swm} and H_s^{alt} as a function of the spectral characteristics.

6.1 The data set

6.1.1 Significant wave heights from TOPEX and ERS-1 altimeter data

ERS-1 deploys a Ku–band altimeter (cf. Section 4.2.3). TOPEX/POSEIDON [*T/P at JPL* WWW, *T/P at CNES* WWW] is a joint french–american mission, deploying a Ku–band TOPEX (NASA/JPL) and a C–band POSEIDON (CNES) altimeter. We have used H_s from the Ku–band TOPEX altimeter provided as off-line product by *AVISO* [WWW] (Toulouse, FRANCE), and the ERS-1 altimeter fast delivery (FD ERS) product obtained via *ECMWF* [WWW] (Reading, UK). The 1-second echo averages correspond to footprint sizes of 5 to 10 km in range direction (cf. Section 4.2.3), thus matching the representative area of SWM imagettes.

Data quality In a quality control process a small fraction of the 1-s H_s samples for both satellites were rejected because they were flagged as being over land or had large rms values compared to the 1-s average, indicating disturbances during measurement.

- *Quality of TOPEX data:* Validation studies of H_s^{top} revealed its accuracy to be better than the specified performance goal of 0.5 m or 10% whichever is larger. Comparisons of H_s^{top} with buoy measurements repeatedly confirmed the high quality of H_s^{top} [*Callahan et al.* 1994]; [*Cotton and Carter* 1994]; [*Gower* 1996]. Collocated H_s^{top} and buoy H_s over a range of 0.1 to 8 m (including one case above 12 m) with a temporal separation of less than 37 minutes and a spatial separation of often less than 40 km showed that H_s^{top} is about 5% lower with an rms scatter of 0.3 m [*Gower* 1996].

- *Quality of ERS-1 data:* The FD ERS H_s required additional corrections and quality controls. Comparisons of FD ERS H_s data against buoy measurements and against TOPEX H_s data revealed significant underestimation of FD ERS H_s [*Cotton and Carter* 1994]; [*Queffeulou* 1996]; [*Cotton et al.* 1997]; [*Bauer and Staabs* 1998]. For the FD ERS H_s obtained from January 1994 onward linear correction formulae were determined by D. Cotton (pers. communication) and *Queffeulou* [1996]. In the following we shall apply the correction of *Queffeulou* [1996]

$$H_s^{ers} = 1.11\, H_s^{\text{FD ERS}} + 0.09 \tag{6.1}$$

for all ERS-1 altimeter wave heights. This correction has been extensively verified over a wide range of wave heights between 1 and 10 m.

A further quality control was applied to eliminate spurious data in coastal regions and in very low sea state conditions. Low sea state causes difficulties in determining a smooth average pulse form and may lead to large errors in deriving H_s. These spurious data are identified through large fluctuations between succeeding data points. If the rms fluctuation of 3 consecutive values exceeds 40% of the 3-point mean, these samples are rejected. This empirically determined threshold eliminated less then 1% of the data, but improved the statistical results.

6.1.2 Collocation

Both estimates of H_s from SWM retrievals and from altimeters represent instantaneous measurements of an area of about 50 to 100 km^2. The random measurement uncertainty inherent in the altimeter data is reduced by taking the average of the closest collocated 1-s H_s sample and its immediate temporal neighbors (3-s averages, see above).

The spatial and temporal distances between the two data pairs have to be reasonably small to ensure that both encounter the same geophysical condition. At the same time, the space and time windows should be large enough to obtain a sufficiently large number of collocation events to achieve statistical confidence. Estimates of reasonable collocation windows for open ocean wave conditions are of the order of one hour and 100 km [*Monaldo* 1988]; [*Tournadre and Ezraty* 1990].

In practice, the spatial and temporal distances between collocated data, and the achievable number of collocation events are restricted by specific satellite and instrument properties:

1. The spatial distance between collocated H_s^{swm} and H_s^{ers} data always amounts to about 260 km, being fixed by the geometry of the slant-looking SAR with a 19.9° incidence angle relative to the nadir-looking altimeter. Ideally, i.e. when both instruments are operational, each H_s^{swm} may be collocated to a simultaneously measured H_s^{ers} yielding on the order of 30,000 H_s samples per month.

2. H_s^{swm} can be collocated to H_s^{top} data whenever the ERS-1 and the TOPEX footprint paths cross within reasonable space and time windows. This restricts the number of collocations of H_s^{swm} with H_s^{top} to roughly 1/10 the number of collocations with H_s^{ers}.

3. The differing orbit inclinations impose a further restriction. The ERS-1 is a sun-synchronous near polar orbiting satellite with an inclination of 98.5° (cf. Section 4.2.1). In contrast, the altimetric-oceanographic orbit of the TOPEX with an inclination of 66° is characterized by near orthogonal crossing angles between the ascending and descending paths. Consequently, the TOPEX measurements are most densely distributed near 66° N/S yielding more collocation events in strong westerly wind regions than at low latitudes. ERS-1 has its highest coverage density at high latitudes where no TOPEX data are available. The difference in spatial distributions among the data of the two satellites leads to relatively more frequent measurements of high sea states by the TOPEX and thus higher global mean TOPEX values.

The limitations imposed by these 'exogene' factors prevent the criteria of *Monaldo* [1988] and *Tournadre and Ezraty* [1990] to be met in the strict sense for the ERS-1 altimeter. Henceforth, we adopt a compromise for the ERS-1 altimeter data, setting the space window equal to 260 km (the distance between the nadir and the SWM footprint) and the time window equal to 90 min. Complementary, two samples are devised from the set of TOPEX data, the first containing data which fulfill the collocation criteria in the strict sense, and the second requiring the same collocation distances as those imposed on the ERS-1 altimeter sample. We shall see in Section 6.2.2 that the statistcal parameters of the 'strict' TOPEX sample are in good agreement with those of the 'wide' TOPEX sample. Therefore, we are confident that the 'wide' SWM vs. ERS-1 altimeter collocation is is permissible and yields meaningful statistical results.

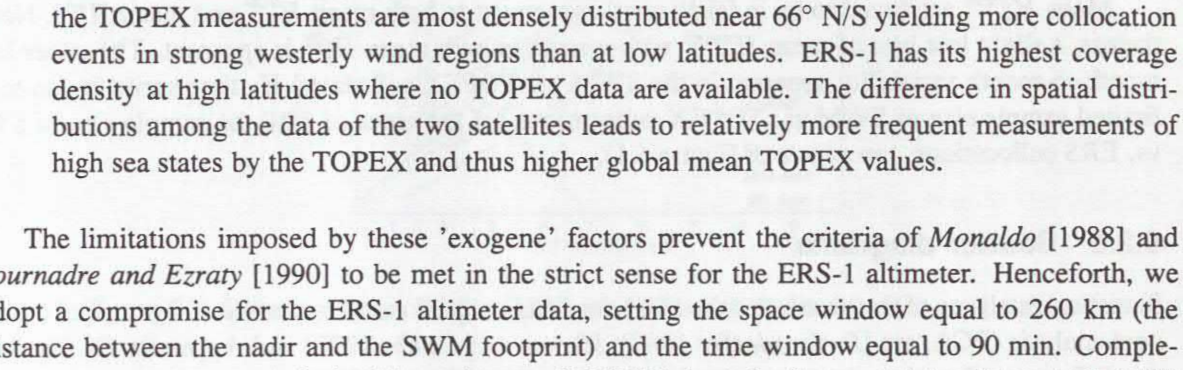

(a) SWM vs. TOPEX altimeter (b) SWM vs. ERS-1 altimeter

Figure 6.1: Upper panels: number of entries of global monthly collocated SWM data to TOPEX (left) and ERS-1 (right) altimeter data. Lower panels: Time series of global monthly mean H_s for SWM (middle curves), WAM (lower curves), and collocated TOPEX (left) and ERS-1 (right) altimeters (upper curves).

6.2 Statistical comparison of H_s data sets

6.2.1 Time series of monthly means and rms

Time series of global monthly mean significant wave heights of H_s retrieved from SAR wave mode spectra are shown in the bottom panels of Figure 6.1 with collocated H_s data from TOPEX (panel a) and from ERS-1 (panel b). Bars refer to the 95 % confidence intervals. Collocated WAM model wave heights are also shown for reference.

Mean H_s^{swm} are found to be in fairly good agreement to both mean H_s^{top} and mean H_s^{ers}. Nevertheless, a slight low bias of mean H_s^{swm} with respect to both mean H_s^{alt} is apparent. The rather large month-to-month variability apparent in the SWM vs. TOPEX collocated H_s time series is due to the limited sample size of SWM vs. TOPEX collocations (of the order of 1/10 the sample size of SWM vs. ERS collocations, top panels of Figure 6.1).

6.2.2 Scatter diagrams

Statistical analyses of the bivariate collocated data sets are performed by means of a principal component analysis (PCA, see [*Preisendorfer* 1988]; [*Bauer and Staabs* 1998] and Appendix C). To assess the different collocation characteristics between the TOPEX vs. SWM and the ERS vs. SWM data sets, two subsets of the TOPEX vs. SWM bivariate data set are investigated. The first subset is defined by a narrow collocation window of 60 km width in space and 60 min in time (Figure 6.2a). This window meets the strict requirements proposed by *Monaldo* [1988] and *Tournadre and Ezraty* [1990]. The second sample is defined by a wide window of 260 km and 90 min (Figure 6.2b). The spatial

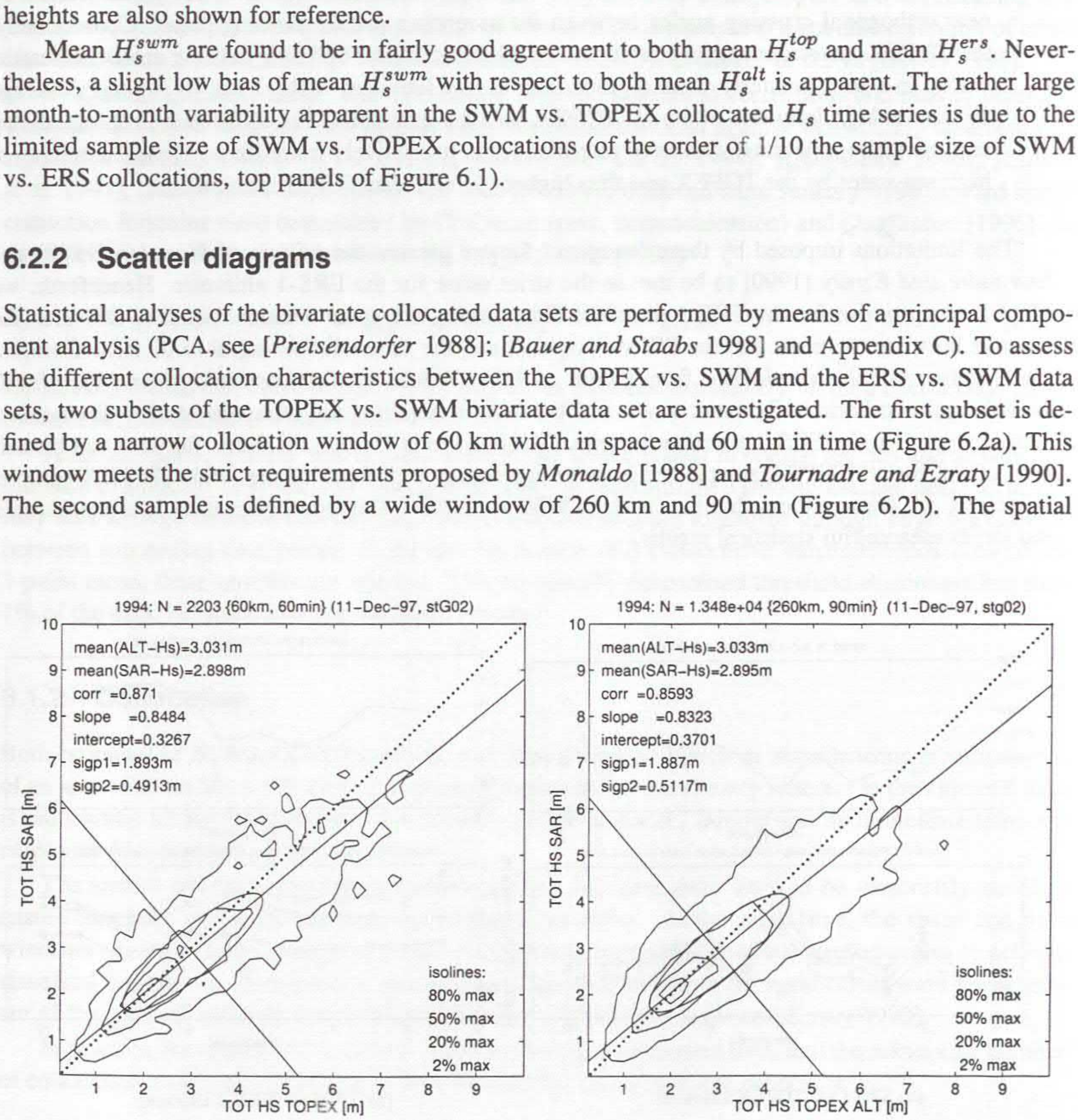

(a) narrow collocation

(b) wide collocation

Figure 6.2: Scatter diagrams of H_s^{swm} vs. H_s^{top} for narrow (panel a) and wide (panel b) collocations. The covariance ellipses are shown together with major and minor principal axes.

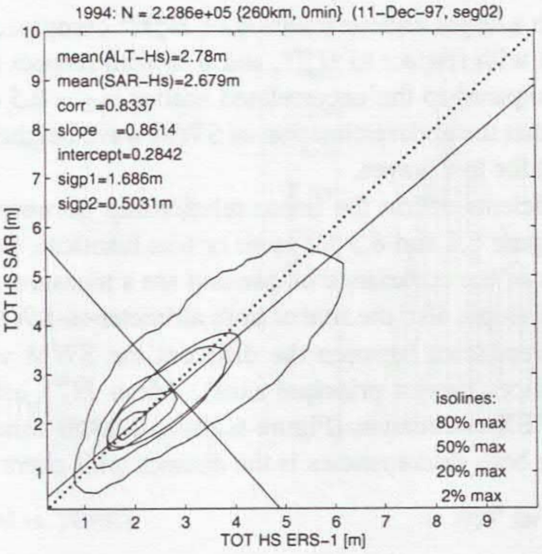

Figure 6.3: Same as Figure 6.2 for H_s^{swm} vs. H_s^{ers} with fixed collocation windows.

limit corresponds to the collocation characteristics of the ERS vs. SWM sample.

The statistical regression parameters between H_s^{swm} and H_s^{top} are summarized in Table 6.1 for the narrow (first column) and the wide (second column) collocation. Although both the collocation characteristics and the sample size of the two TOPEX subsets differ substantially, all statistical regression parameters are in very close agreement. Despite their larger spatial separation, this result gives confidence that wide the ERS vs. SWM collocations as well provide meaningful statistical parameters.

The scatter plot of H_s^{swm} vs. H_s^{ers} is depicted in Figure 6.3. Corresponding statistical parameters are listed in the third row of Table 6.1. Both TOPEX vs. SWM sets and the ERS vs. SWM set show a

	SWM vs. TOP *60 km, 60 min*	*SWM vs. TOP* *260 km, 90 min*	*SWM vs. ERS* *260 km, 0 min*
N	2203	13,339	227,077
$< H_s^{swm} >$ [m]	2.90 ± 0.05	2.90 ± 0.02	2.68 ± 0.01
$< H_s^{alt} >$ [m]	3.03 ± 0.05	3.03 ± 0.02	2.78 ± 0.01
rms dev [m]	0.74	0.77	0.74
r	0.87	0.86	0.83
b_{pca}	0.85	0.83	0.86
a_{pca} [m]	0.33	0.37	0.28
b_{pca}^0	0.94	0.93	0.95
σ_{p1} [m]	1.89	1.89	1.69
σ_{p2} [m]	0.49	0.51	0.50

Table 6.1: Statistical regression parameters inferred from 1994 global SWM–retrieved wave heights H_s^{swm} collocated to H_s^{top} using narrow (first column) and wide (second column) windows, and to H_s^{ers} for fixed collocation distance (third column). The statistical parameters refer to mean H_s with 95% interval $< \, . \, >$, square-root of the variance of deviations *rms dev*, correlation coefficient r, slope b_{pca} and intercept a_{pca} of the major principal axis, slope b_{pca}^0 of the major principal axis tied to the origin, and principal rms deviations σ_{p2} and σ_{p2} along the major and minor axis, respectively (cf. Appendix C).

fairly good agreement with a slight underestimation of H_s^{swm} compared to H_s^{alt} of 10 cm in all three sets, corresponding to 5 % with respect to H_s^{ers}, and 6 % with respect to H_s^{top}. The underestimation appears to be marginal compared to the uncorrelated scatter σ_{p2} = 0.5 m. The slope of the principal component axis indicates that the underestimation of SWM wave heights is more pronounced for high waves and slighty reversed for low waves.

High correlation coefficients affirm the linear relationship between the altimeter and the SWM data sets. The slopes of Figure 6.2 and 6.3 are more or less identical. So are the minor principal axes which represent the widths of the covariance ellipse and are a measure of the rms error. Therefore, in addition to the bias and the slope, also the rms of both altimeter-to-SWM collocations agree.

The only marked discrepancies between the different the SWM vs. altimeter collocations are the mean values and variances (major principal axes). Mean H_s^{top} exceeds mean H_s^{ers} by 25 cm. The variability of the TOPEX collocation (Figure 6.2b) is 1.89 m compared to 1.69 m for the ERS collocation. The reason for both discrepancies is the distinct orbit characteristics between ERS-1 and TOPEX (cf. Section 6.1.2).

6.2.3 Histograms

Bauer and Staabs [1998] have analyzed the quality of altimeter-derived H_s and their homogeneity and potential applicability for long term climatologies. They found that histograms of global H_s fitted well to the generalized normal (GNO) and the generalized extreme value (GEV) distributions [*Hosking* 1990]. Cases for which significant deviations to the these empirical distributions occured, generally revealed deficiencies in the data. Therefore, the empirical distributions were considered to be a valuable means to assess the quality of the observed data.

Figure 6.4a/b, depict the histograms of the SWM and collocated TOPEX significant wave height samples, respectively, for their narrow collocation (60 km, 60 min), together with the GNO (dashed line) and GEV (solid line) distribution curves. Corresponding plots of the histograms of the SWM and collocated ERS significant wave heights are shown in Figure 6.4c/d, respectively.

As expected from the work of *Bauer and Staabs* [1998] the altimeter sets are in good agreement with the empirical curves. The deviations for the TOPEX sample (Figure 6.4a) are most likely due to the limited sample size. The slight overshoot of the histograms compared to the curves at the peak, which is apparent in all four samples, and already noted by *Bauer and Staabs* [1998], remains unexplained.

As a new feature we see that the SWM-retrieved H_s as well are in very close agreement with the empirical distributions. In view of the different mapping regimes of the nonlinear spectral wave-to-SAR transform for low and high sea states this outcome was not obvious. It therefore represents a further confirmation of the good overall performance of the retrieval algorithm.

6.3 Comparison of H_s data sets of windsea and swell

The precision of the satellite observations can be assumed to be independent of observation time and position. Without showing, we state that this is confirmed by the statistical comparison of regional subsets (northern and southern extratropical and tropical regions of the Pacific, Atlantic, and Indian Ocean) and by the analysis of temporal subsets (monthly and seasonal periods).

The differences revealed in the statistical parameters of the various subsets appear to depend on the different sample sizes, the different wave height ranges covered, and/or the different spectral properties of the sea state encountered, for instance the relative contribution of windsea and swell.

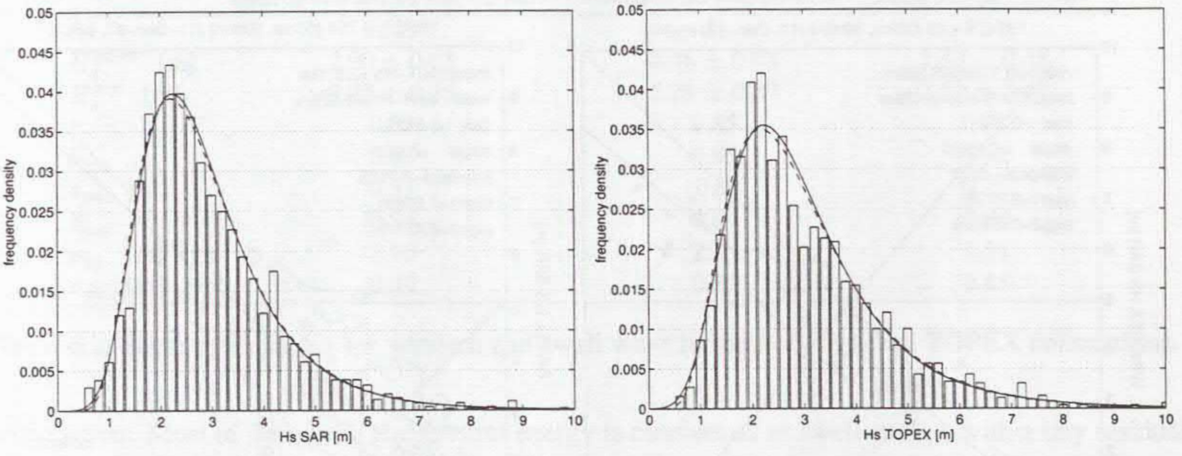

(a) H_s^{swm} for SWM vs. TOPEX (b) H_s^{top} for SWM vs. TOPEX

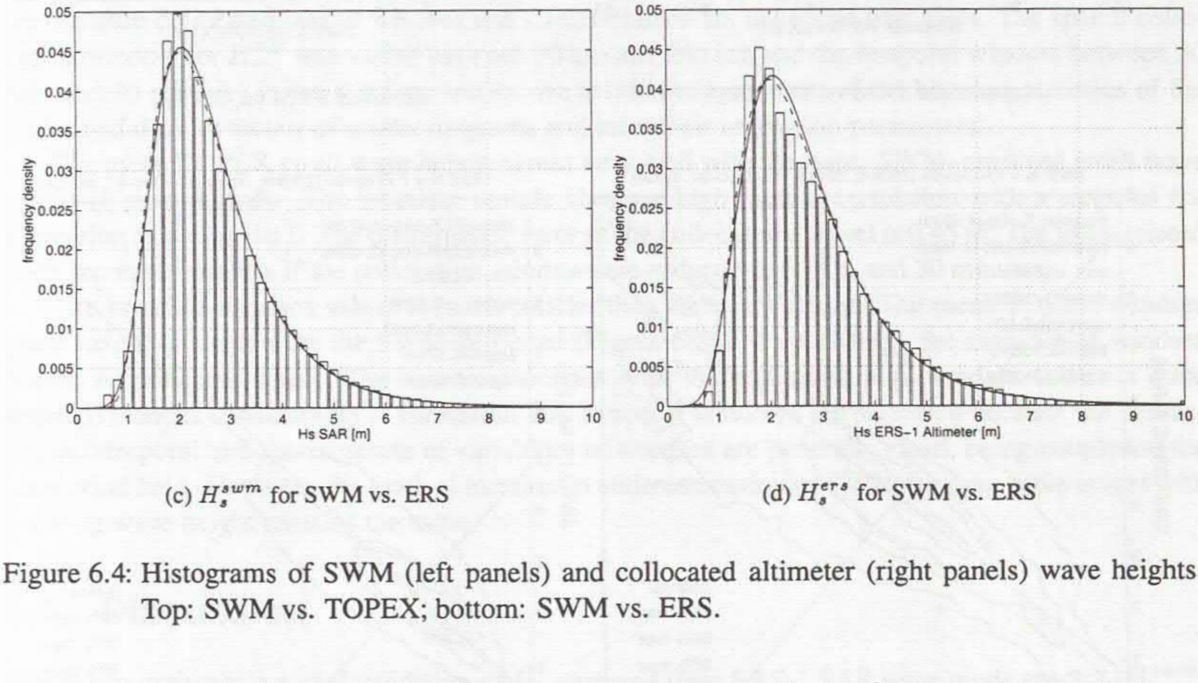

(c) H_s^{swm} for SWM vs. ERS (d) H_s^{ers} for SWM vs. ERS

Figure 6.4: Histograms of SWM (left panels) and collocated altimeter (right panels) wave heights. Top: SWM vs. TOPEX; bottom: SWM vs. ERS.

Some insight into the causes of the differences between H_s^{swm} and H_s^{alt} is expected from a closer investigation of pure windsea and swell samples. This investigation is, among others, motivated by findings that the correspondence between ERS-1 SWM spectral retrievals and WAM model spectra depends on the contributions of windsea and swell (cf. Chapter 7). The measured windsea wave height is smaller than the corresponding modeled wave height. In contrast, the modelled swell wave height is underestimated relative to the observed swell wave height.

To estimate any possible distinct behavior in the H_s^{swm} vs. H_s^{alt} deviations for windsea and swell from total H_s alone, we have extracted two subsets of SWM–retrieved spectra, one representing spectra which only contain a windsea system, the other representing spectra which only contain swell systems. Windsea and swell systems are identified using the spectral partitioning algorithm [HBHH] in conjunction with the local wind vector which in our case is obtained from the ECMWF analysis (cf. Section 4.5). The windsea wave height is determined from the integral over that coherent fraction

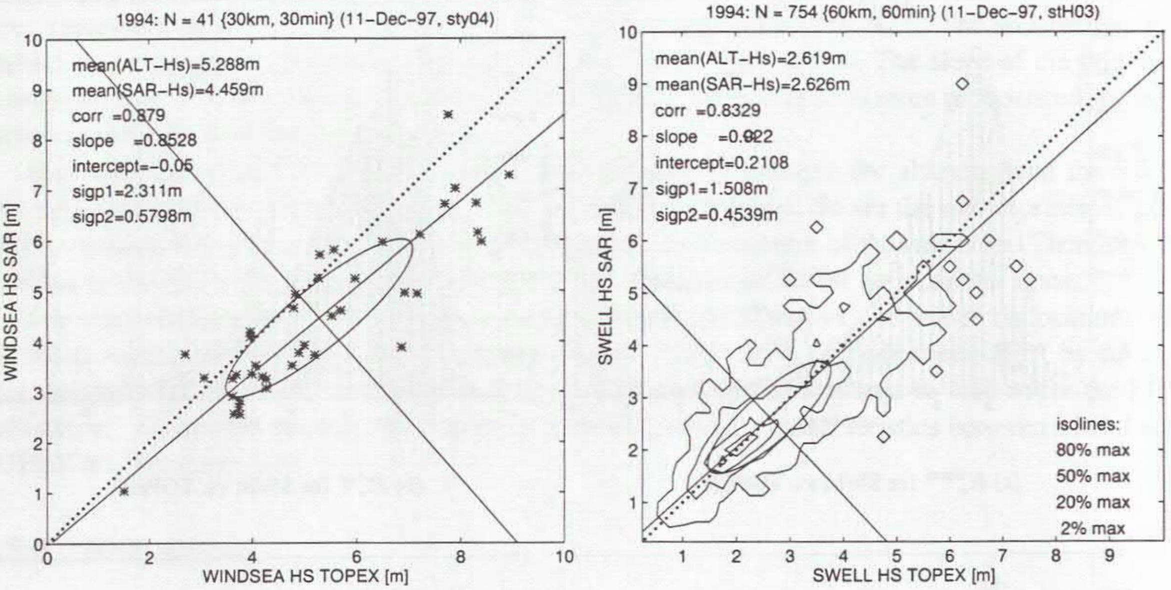

(a) windsea SWM vs. TOPEX

(b) swell SWM vs. TOPEX

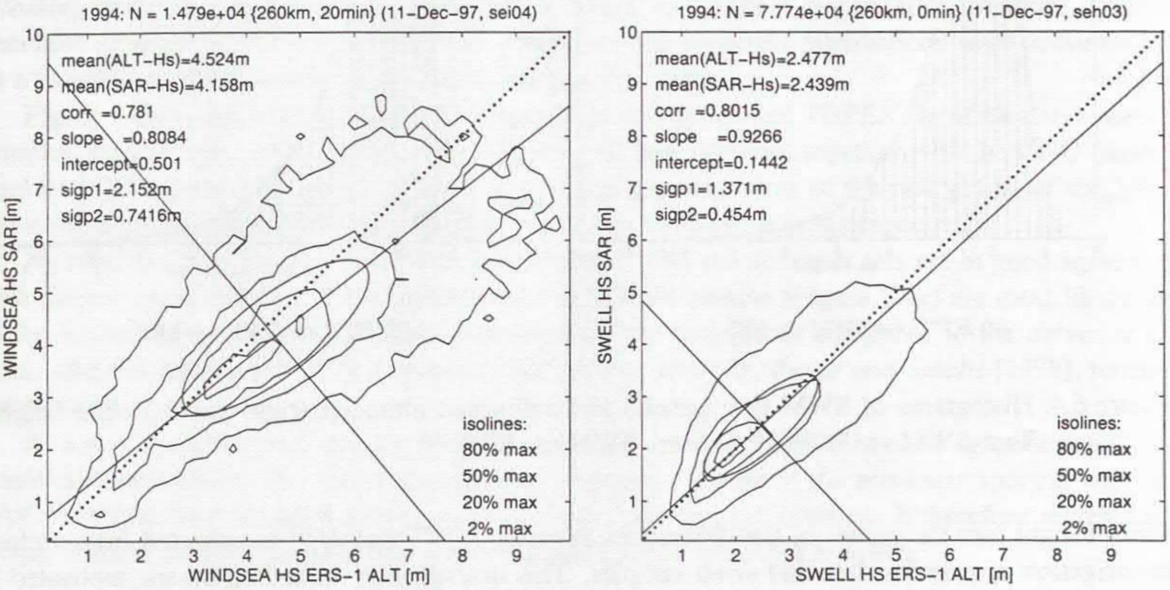

(c) windsea SWM vs. ERS

(d) swell SWM vs. ERS

Figure 6.5: Scatter plots of SWM and collocated altimeter windsea (left panels) and swell (right panels) wave heights. Top: SWM vs. TOPEX; bottom: SWM vs. ERS.

of the spectral wave energy density which is influenced by the local wind. This is the case if the dominant direction of the energy density fraction is aligned with the local wind and the phase speed at the spectral peak is less than 1.3 times the effective wind speed u_{10} in the direction of the wave

	total spectrum 60 km, 60 min	*windsea 60 km, 60 min*	*swell 30 km, 30 min*
N	2203	41	754
H_s^{swm} [m]	2.90 ± 0.05	4.46 ± 0.08	2.63 ± 0.48
H_s^{top} [m]	3.03 ± 0.05	5.29 ± 0.07	2.62 ± 0.48
r	0.87	0.85	0.88
b_{pca}	0.85	0.85	0.92
a_{pca} [m]	0.33	-0.05	0.21
b_{pca}^0	0.94	0.84	0.99
σ_{p1} [m]	1.90	2.31	1.51
σ_{p2} [m]	0.49	0.58	0.45

Table 6.2: Same as Table 6.1 for windsea and swell wave heights of SWM vs. TOPEX collocations.

propagation. Most of the rest of the spectral energy is considered as swell energy, with a tiny residual being attributed to mixed windsea / swell.

The two subsets of SWM-retrieved data and their collocated altimeter data provide good estimates of pure windsea and pure swell wave heights, respectively. As pure windsea occurs relatively seldom we compare collocated sets of windsea and swell obtained for the entire year 1994. The spatial collocation window for H_s^{top} was varied between 30 km and 260 km and the temporal window between 30 min and 90 min. As in the previous section we assess the agreement of the bivariate statistics of the collocated data by means of scatter diagrams and infer their regression parameters.

The mean TOPEX swell wave height agrees very well with the mean SWM–retrieved swell wave height (Figure 6.5b/d). The bivariate sample shows a high mutual correlation with a slope of the regression axis close to 1. The uncorrelated error of the collocated data set is 0.45 m. The uncorrelated error increases slightly if the collocation windows are reduced to 30 km and 30 minutes.

The bivariate windsea subset is much smaller than the swell subset. The mean TOPEX windsea wave height is larger than the SWM–retrieved (Figure 6.5a). In particular, the high SWM windsea waves are underestimated. The scatter associated with the collocated pure windsea subset is quite large. It reduces considerably if the spatial and temporal windows are narrowed because the characteristic temporal and spatial scales of variability of windsea are generally small, being coupled to the local wind field. However, the gradual increase in underestimation of SWM windsea wave height with growing wave height remains the same.

6.4 Discussion

A first comprehensive global validation of H_s retrieved from ERS-1 SAR wave mode spectra (H_s^{swm}) with independently measured H_s from radar altimeters on board the TOPEX (H_s^{top}) and ERS-1 (H_s^{ers}) satellites has been performed. Complementary to the quality assessment and statistical intercomparison with WAM model data of the spectral properties of the SWM–retrievals (cf. Chapter 5 and 7, respectively) this exercise is highly relevant to ascertain more generally their validity. Furthermore, this study adds to the investigation of statistical properties of H_s data measured from different space borne altimeters [*Bauer and Staabs* 1998].

In view of the entirely different data processing schemes applied to the SWM, altimeter and WAM model data the overall agreement is encouraging. In particular, the following conclusions can be drawn:

1. A remarkably high degree of agreement is apparent between H_s^{swm} and H_s^{top} for low to moderate sea states, assessing the reasonable quality of H_s^{swm} for these sea states.

2. Histograms of H_s^{swm} agree well with empirical distribution functions which are believed to provide an accurate representation of global H_s distributions, corroborating the overall good performance of the WASAR algorithm.

3. For high sea states H_s^{swm} are found to be low compared to H_s^{alt}. Suspecting the SWM retrievals to be too tightly bounded to their first-guess, is disproven by the fact that H_s^{swm} also differs increasingly from WAM model wave heights with increasing H_s. The underestimation of H_s^{swm} with respect to H_s^{top} is mainly attributed to the underestimation of SWM windsea retrievals.

4. A scatter of smilar magnitude to the SWM vs. altimeter windsea comparisons was found for the collocations between H_s^{top} and H_s^{ers} [*Bauer and Staabs* 1998]. This shows, that at least part of the measurement uncertainties for high sea states must be attributed to the altimeter measurements. This demonstrates that the SWM data are useful also to assess possible shortcomings of the altimeter data. First, they provide spectral information which are helpful in identifying possible mechanisms for these dicrepancies. Second, they represent a further independent data set which helps to clarify the causes of the scatter among the TOPEX and ERS-1 altimeter data, which otherwise would have to rely solely on localized buoy measurements.

5. Stratification with respect to travel direction of extreme deviations between SWM and altimeter H_s occuring occasionaly, indicated no problem in the retrieval of azimuth travelling waves which might be expected in view of the azimuthal cut-off [*Bauer and Heimbach* 1998]. Although rare, these extreme deviations were found predominantly for range travelling waves in the mid-latitudes during winter. This is a hint of the effect of the hydrodynamical transfer function (cf. Section 4.4.1) which may have to be further improved.

In summary, the applicability of SWM wave height retrievals has been confirmed. Candidate mechanisms for remaining discrepancies were discussed which require closer investigation, e.g. through the use of buoy data. Nevertheless, these discrepancies do not obscure the results of the statistical intercomparisons of SWM-retrieved spectral properties with WAM model data, to be presented in the next chapter. In fact, giving preference to the altimeter data would leave the main features unchanged, if not even pronounce some aspects.

7 GLOBAL INTERCOMPARISON OF ERS-1 SWM RETRIEVALS WITH WAM DATA

Global and regional intercomparisons between the collocated spectral wave parameters retrieved from ERS-1 SWM spectra and computed with the WAM model were carried out for the three year period January 1, 1993, to December 31, 1995 (see also *Heimbach et al.* [1998]). The collocation was performed using the nearest model gridpoint and nearest six hourly model synoptic time to the observation location and time.

7.1 Comparison of integral properties

In a first analysis the data were divided into eight ocean basin regions, namely: the North, Tropical and South Pacific, the North, Tropical and South Atlantic, and the Tropical and South Indian Ocean, with tropical boundaries at 25° N/S. Linear regressions were performed of the collocated data for monthly, seasonal and the full-period data sets (see Appendix C).

Monthly mean H_s Figure 7.1 compares the time series of monthly mean significant wave height in different regions of the Atlantic, Pacific and Indian Ocean retrieved from ERS-1 SWM (dashed curve) and computed by the WAM model (solid curve).

The overall agreement is satisfactory. There is a more pronounced annual cycle in the Northern than in the Southern Hemisphere, the summer wave heights decreasing more strongly to about 1.5 m in the North as compared to 2.5 m in the South. This reflects the higher zonal winds prevailing in the Southern Hemisphere mid-latitudes during summer season, associated with a higher meridional pressure gradient, and the higher abundance of low-pressure wind systems that still prevail in the southern mid-latitude zonal belt during the summer season. In the Northern Hemisphere, the monthly mean H_s are higher (by about 10 %) in the Atlantic than in the Pacific, while the opposite holds for the Southern Hemisphere (20 % higher values in the Pacific than in the Atlantic). The maxima of the South Atlantic winter are also less strongly pronounced than in the other southern and northern basins for the winter seasons. The tropical Atlantic and Pacific show essentially no annual cycle, with monthly mean H_s values fluctuating about 2 m in the tropical Pacific and 1.75 m in the tropical Atlantic. In contrast, the tropical Indian Ocean exhibits a marked seasonal cycle reflecting the monsoons. Pronounced maxima comparable to those in the North Atlantic (although somewhat broader) are found also in the Southern Indian Ocean.

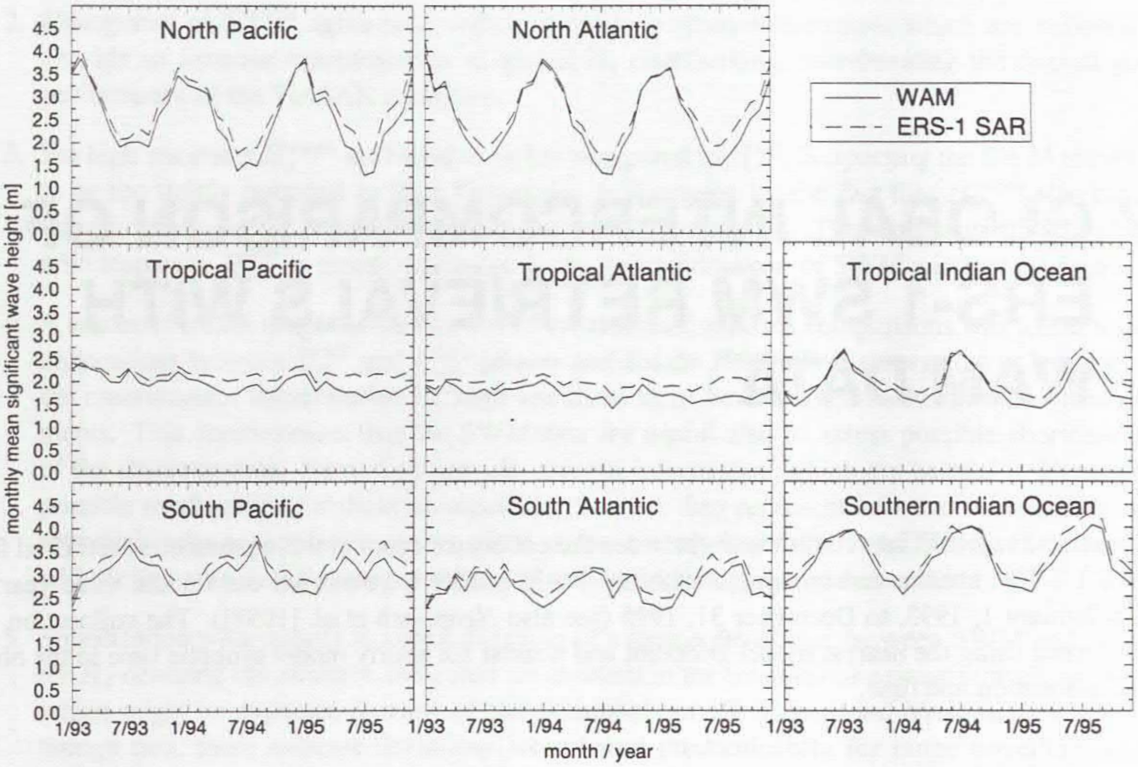

Figure 7.1: Time series of monthly mean significant wave heights between January 1993 and December 1995 for different ocean basins. Dotted curves refer to WAM model values, dashed curves to ERS-1 SWM values.

Bias Despite the satisfactory overall agreement between modelled and retrieved wave heights, a small but systematic underestimation of H_s by the WAM model relative to the ERS-1 SWM data is seen in Figure 7.2 (solid curve). The bias is more pronounced for low sea state summer conditions. A different behaviour for different ocean basins is again apparent. In the Northern Hemisphere, the negative bias shows a pronounced seasonal cycle, with larger values during summer (low sea states) than winter (high sea states). The bias in the tropical Pacific and Atlantic oceans also exhibits a weak seasonal cycle that follows the Northern Hemisphere, in contrast to the bias of the tropical Indian Ocean, which follows the Southern Indian Ocean. The Southern Hemisphere basins, finally, exhibit an approximately constant negative bias without a significant seasonal modulation.

Regression line slope In addition to the bias, a second useful parameter characterizing the statistical relation between modelled and retrieved wave heights is the slope b of the regression line (we have defined the regression line here as passing through the zero point of the axes, for details see Appendix C). Figure 7.3 (solid curve) shows time series of b for the monthly data sets. Values greater (smaller) than 1 represent under(over)-estimated model values compared to observation.

Correlation Time series of monthly correlation coefficients obtained from the regression are shown in Figure 7.4 (solid curve). In the extra-tropical northern and Southern Hemisphere, fairly constant values of the order of 0.8 are found, except for a weak seaonal cycle in the North Pacific, with minima

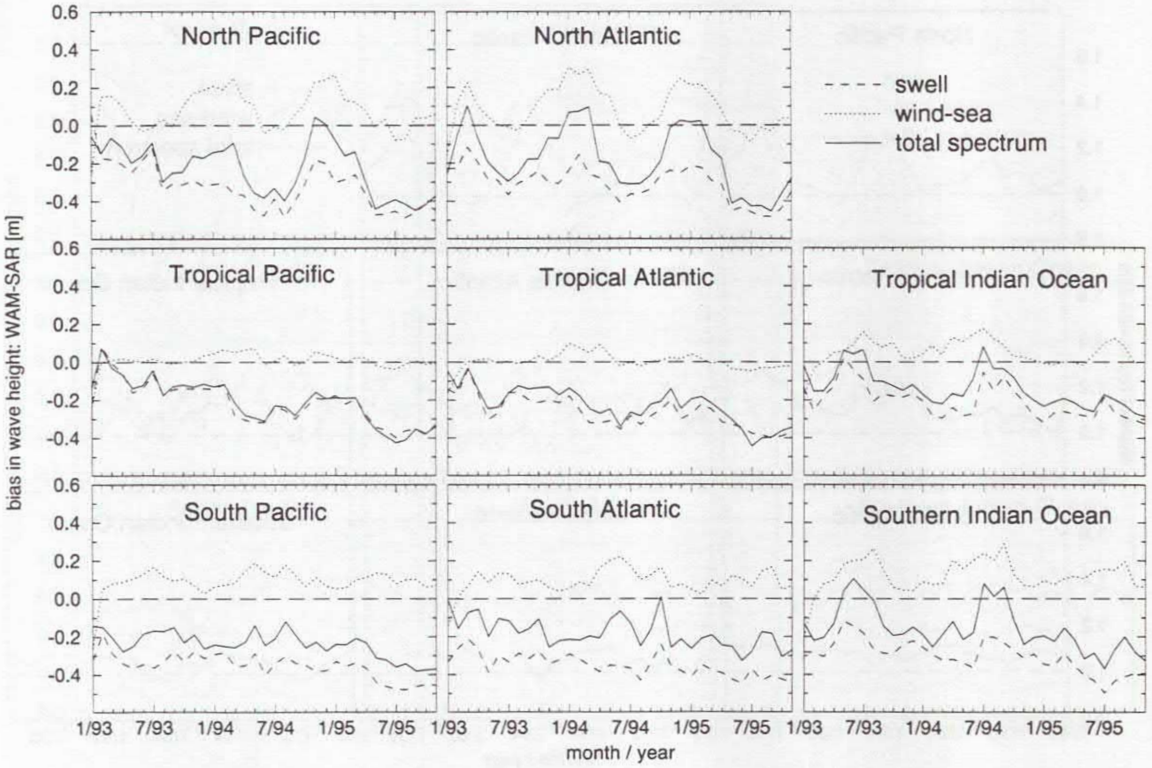

Figure 7.2: Same as Figure 7.1 for the bias between monthly WAM model and ERS-1 SWM significant wave heights (solid line), windsea wave heights (dotted line) and swell wave heights (dashed line).

corresponding to low Northern Hemisphere summer sea states. The tropical Atlantic and Pacific exhibit somewhat lower correlation levels between 0.5 and 0.7. Winds in the tropics are generally low, so that the wave spectra are dominated by swell (see Section 7.2). This suggests that the degree of agreement between model and observation is generally higher for locally generated windseas than for swell that has travelled to the observation location from distant sources. This interpretation will be supported later in Section 7.2 by the correlation time series of partitioned windsea and swell systems.

7.2 Comparison of spectral partitionings

A more detailed intercomparison of modelled and retrieved wave spectra can be obtained by partitioning the spectra into wave systems (cf. Section 4.5; for details of the partitioning system, the method for cross-assigning individual wave systems of the collocated modelled and retrieved wave spectra, and the criteria applied in the discrimination between young and old windsea, mixed windsea/swell and pure swell systems, we refer to [HBHH]). For the present analysis we have included in the windsea category young and old windsea systems (as defined in [HBHH]), while swell refers to "pure" swell. Mixed windsea-swell systems are not included in either category and are also not presented as a separate wave system class, since their contribution to the total wave energy is relatively small.

Figure 7.5 shows as example the global distributions of the modelled and observed average number of swell systems per spectrum for DJF 1993/94. The largest number is found in the tropics, which receive swell from the mid-latitude high wind regimes in both hemispheres as well as locally generated

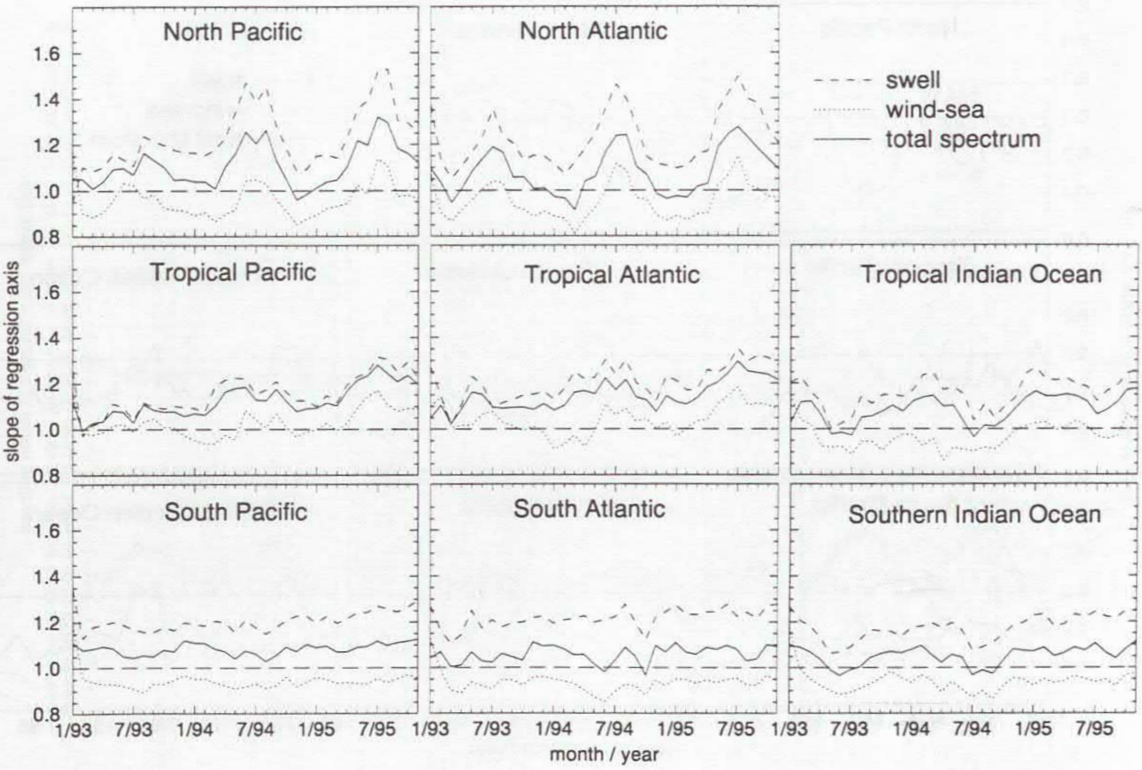

Figure 7.3: Same as Figure 7.1 for the slope of the monthly regression between WAM model and ERS-1 SWM significant wave heights (solid line), windsea wave heights (dotted line) and swell wave heights (dashed line).

swell by the trade winds. The ability of both the model and the SAR system to distinguish between a relatively large number of different wave systems, and the agreement between the simulated and observed distributions of this characteristic structural spectral parameter, is encouraging.

The corresponding distributions for windsea systems are not shown. Theoretically, they should be nearly uniform at a value ≈ 1, since a windsea is always present as soon as a light breeze occurs. However, for the operational WAM model, which was integrated with a resolution of $3^\circ \times 3^\circ$ (later $1.5^\circ \times 1.5^\circ$), such light wind cases, as well as typical windsea situations with changing wind directions, yielded wave systems that were normally classed as mixed windsea-swell systems rather than pure windsea (cf. [HBHH]). The SAR is similarly unable to detect or adequately resolve windsea systems for low to moderate wind speeds because of the azimuthal high wavenumber cut-off (although, as explained above, partially resolved windseas are reconstructed in the retrieval system of [HBHH] using the information on the azimuthal cut-off in combination with the partitioning scheme incorporated in the iterative updating of the input spectrum). The data on windsea systems presented in the following refer therefore only to windseas generated by fairly large, moderate to strong wind fields that produce spectra satisfying the pure young or old windsea criteria of [HBHH].

The time series of the monthly mean swell wave heights H_{sw} (defined as the significant wave height corresponding to the total swell energy summed over all swell systems) are shown in Figure 7.6 for the modelled (dashed curves) and retrieved (long-dashed curves) in different basins of the Atlantic, Pacific and Indian Ocean. Also shown are the simulated and observed monthly mean windsea wave heights H_{ws} (dotted and dot-dashed curves, respectively). The general agreement between model and observation and the distinctive annual cycles are again confirmed.

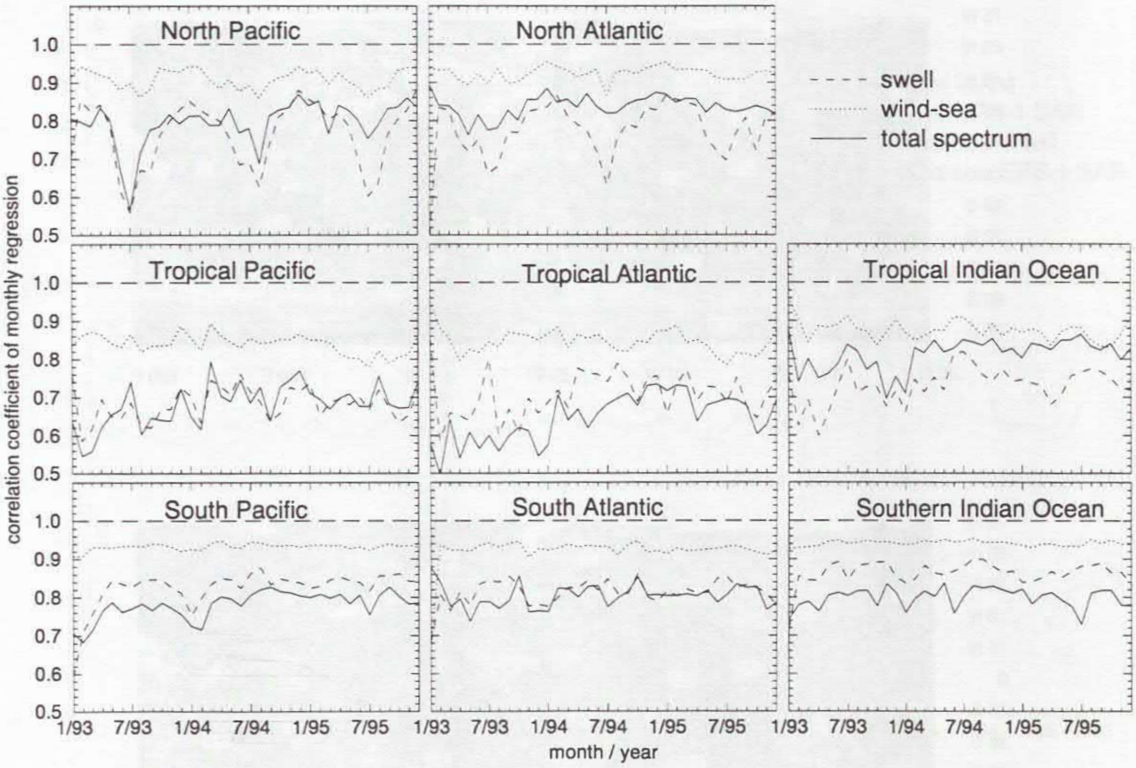

Figure 7.4: Same as Figure 7.1 for the correlation of the monthly regression between WAM model and ERS-1 SWM significant wave heights (solid line), windsea wave heights (dotted line) and swell wave heights (dashed line).

However, a discrimination is now possible with respect to the small systematic deviations noted earlier between the simulated and observed total wave heights. Whereas the WAM windsea tends to be slightly overpredicted by about 10 % relative to the retrieved data, with larger relative deviations for high sea states corresponding to winter conditions, the swell wave heights are systematically underestimated by about 20 to 30 %.

The overestimation of windsea is most pronounced for high monthly mean H_{wi} during winter seasons, whereas the underestimation of swell, especially in the Northern Hemisphere, is seen most clearly for low swell, i.e. during summer. The biases for windsea and swell in the Northern Hemisphere exhibit strong seasonal cycles, whereas in the Southern Hemisphere they remain fairly constant. We note that the swell biases exhibit a slight downward trend that is not present in the windsea biases. The time series of the slope of the monthly regression lines for windsea and swell (Figure 7.3, dotted and dashed curves, respectively) follow the bias curves.

As the magnitudes of the windsea and swell wave heights are of the same order, the different features of the windsea and swell biases cannot be explained simply by a dependence on wave height, but must be attributed to the different spectral and dynamical properties of windsea and swell. We have considered four possible causes for the differences:

1. The hydrodynamic transfer function occurring in the SAR mapping relation is poorly known. The present nonlinear forward mapping uses the theoretical MTF proposed by *Feindt* [1985] without the wind dependent terms (see [HH]). Experiments with a wind dependent MTF showed little influence on the retrieval in the case of ERS-1 SWM spectra [W.R. Plant, private communication]. This is to be expected for spaceborne SARs, for which the velocity bunching mechanism is the dominant

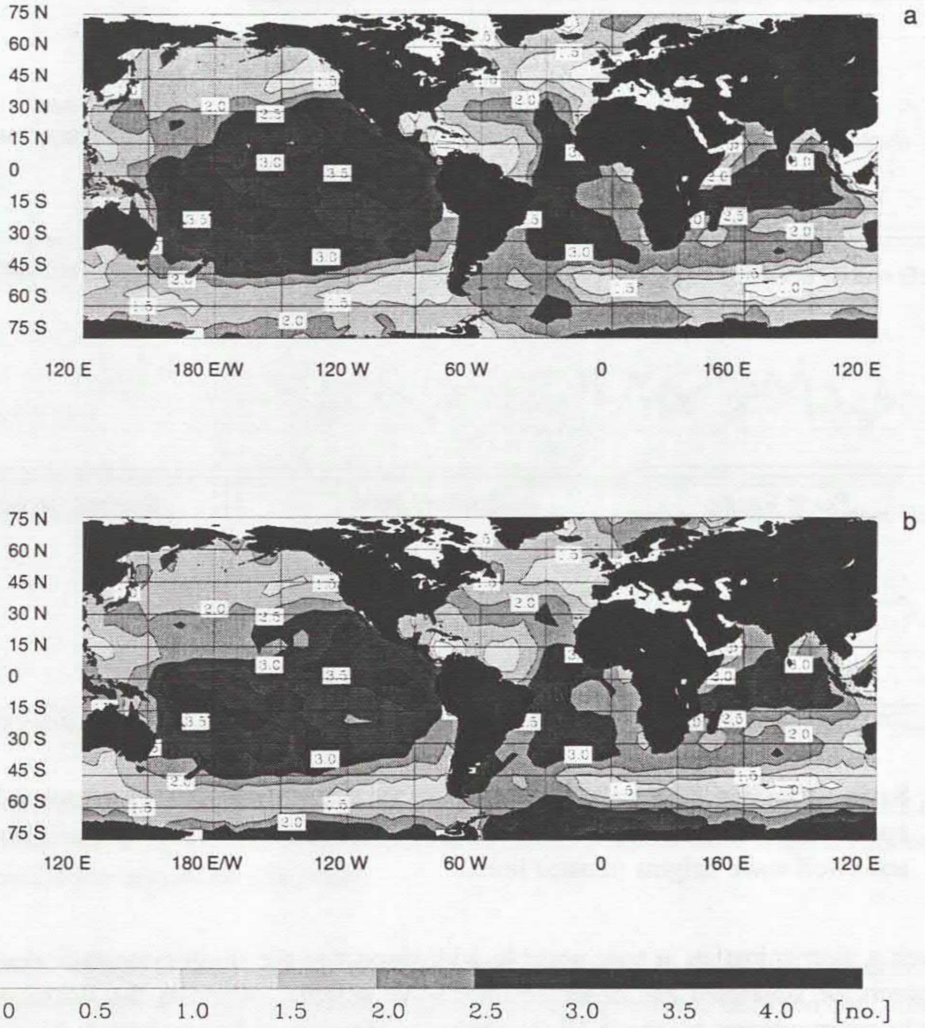

Figure 7.5: Global map of the average number of swell partitionings per spectrum for DJF 1993/94. Top panel: WAM model, bottom panel: ERS-1 SWM.

mapping contribution due to the high R/V ratio (see Figure 6 of *Alpers et al.* [1981]). In the limited domain of linear mapping for range travelling waves, where the RAR MTF becomes important, it contains also a significant contribution from the geometrically well defined tilt modulation MTF. Errors in the hydrodynamic MTF should appear as systematic errors in only a small subset of data representing range travelling waves, rather than in a difference between windsea and swell distributed rather uniformly over all data. Thus the hypothesis of errors in the hydrodyamic MTF causing differences in the statistics of windsea and swell errors appears improbable.

2. Recent results from wave data assimilation exercises in which both the wave field and the generating wind field were updated suggest that in certain areas of the Atlantic and Pacific the ECMWF analysed wind fields produce too strong winds and thus too strong windseas (see e.g. *Bauer et al.* [1996a], *Bauer et al.* [1996b], *Hasselmann, S. et al.* [1997], and *Heimbach et al.* [1996]). However, if this were the only error, an overestimation of the windsea would necessarily lead also to an overestimation of the swell that emerges from the storm region, which is not found. Another source of error must therefore be sought.

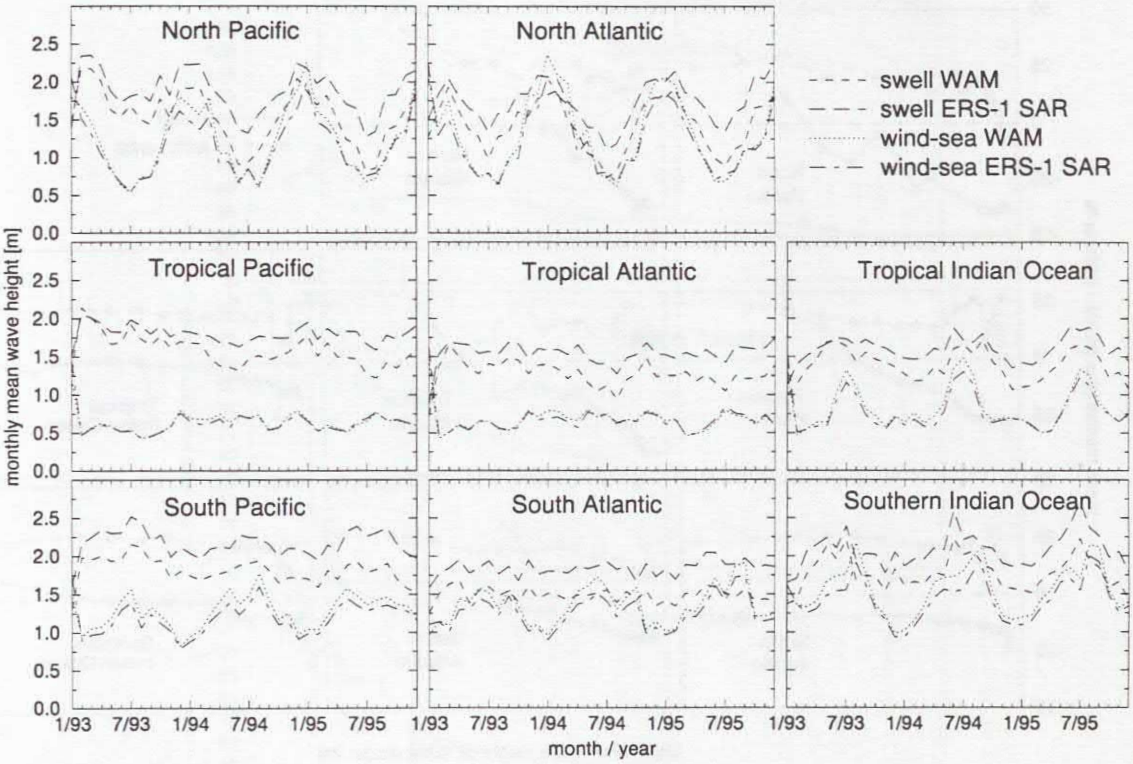

Figure 7.6: Same as Figure Figure 7.1 for the monthly mean windsea and swell wave heights.

3. The combination of an overestimation of the windsea together with an underestimation of swell suggests a possible error in the balance between windsea and swell dissipation. The balance could be modified to conform with the SAR data either by increasing the exponent characterizing the frequency dependence of the dissipation source function, which would decrease the ratio of swell to windsea dissipation, or by increasing the nonlinearity dependence, which would similarly result in a relatively weaker dissiption of long swell, which is characterized by smaller wave slopes.

4. The transition regime between windsea and swell in the area close to but outside the immediate wind generation region, where the wind forcing has already decreased but the nonlinear interactions are still important, plays a critical role in determining the ratio of windsea to swell energy (see e.g. *Snodgrass et al.* [1966], *Hasselmann, S. et al.* [1985a] and *Young et al.* [1987]). It is conceivable that the strongly simplified discrete interaction parametrization of the nonlinear energy transfer implemented in the WAM model is inadequate for a proper representation of this process. Deficiencies in the parametrization of the nonlinear energy transfer may thus be considered as another candidate for explaining the different biases.

We have also considered numerical errors associated with the first-order upwind propagation scheme employed in the WAM model. In developing the WAM model, two schemes where tested: a first-order upwind scheme and a second-order leapfrog scheme (*WAMDI Group* [1988]). While the first-order scheme produced a higher numerical dispersion, a diffusion term had to be introduced in the second-order scheme to supress negative energies occurring in regions of high gradients, which resulted in a comparable effective diffusion. Because of the relatively small differences between the two schemes, the simpler first-order scheme was chosen. A third-order scheme has also been proposed (*Tolman* [1995]). However, numerical errors in the propagation scheme can be excluded in principle as the origin of the spatially and temporally averaged mean global bias in swell energy. Provided

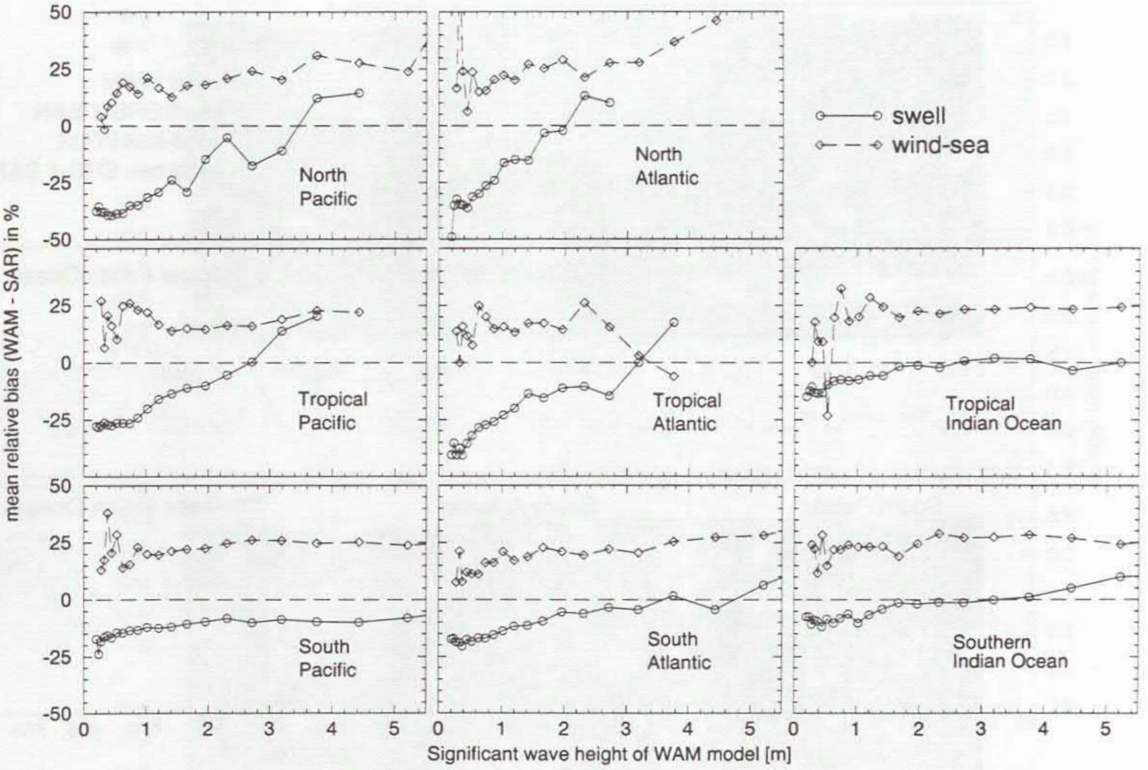

Figure 7.7: Mean relative bias between WAM and ERS-1 SWM as a function of the WAM model wave height for JJA 1994. Solid curves refer to swell, dashed curves to windsea.

the propagation schemes satisfy the standard requirement of energy conservation, all schemes will necessarily yield the same globally averaged swell energy, even though they yield different spatial distributions for individual swell cases.

We regard the third candidate of a too strong damping for low frequency swell as the most likely explanation for the negative swell bias. This is supported by a plot of the relative bias of the WAM wave heights relative to the SAR as a function of wave height for both windsea and swell, shown in Figure 7.7 for the data sample JJA 1994. The windsea graphs show a fairly constant relative bias of 15 to 25 % for waveheights $H_{wi} > 1$ m, except for a slight positive slope in the Northern Hemisphere. In contrast, all swell graphs exhibit a more or less pronounced change in relative bias from negative values at low H_{sw} (-35 % in the NP, NA, TP, TA and -15 % in the SP, SA, SI and TI) to positive values at high H_{sw} (except in the SP, where a -10 % bias remains).

This can be understood by the dependence of swell height on propagation distance. The further a swell system has propagated, the lower its energy level due to geometrical dispersion (and, to a smaller extent, dissipation, cf. *Snodgrass et al.* [1966]). At the same time, if the dissipation is too large, as hypothesized, the further the swell has propagated, the larger the negative bias of the swell relative to the observations. Thus we should expect a direct correlation between the bias and the swell wave height, as seen in Figure 7.7.

The impact of the swell propagation distance on the bias could be demonstrated more directly if the swell propagation distance or, equivalently, swell age were computed by the WAM model. Unfortunately, this is not one of the output quantities of the standard WAM model. However, *Bauer et al.* [1996a]) have developed a WAM model version for their Green function spectral data assimilation scheme which provides this information, and Bauer (personal communication) has kindly made

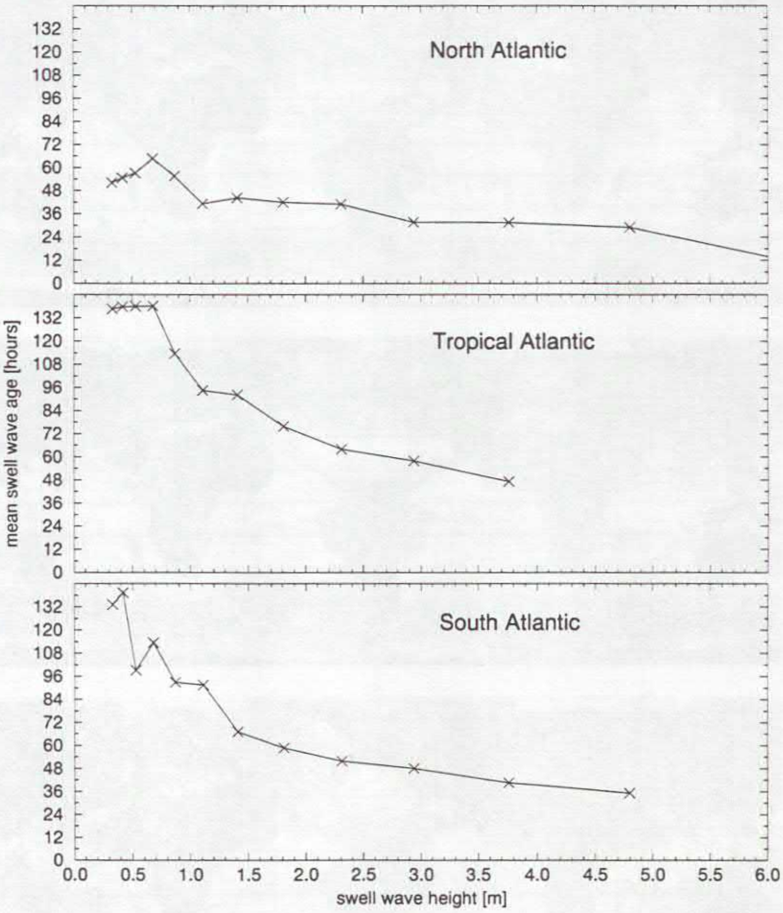

Figure 7.8: Average wave age as function of wave height of individual swell partitionings for a data set in the Atlantic for November 1992

available wave age data in the Atlantic for the period November 1992 with which we could test the assumed correlation between wave age and wave height. (The term wave age is meant here and in the following literally as the elapsed time since the waves last experienced a significant wind input, in contrast to the alternative usage of the term in windsea studies as the ratio of the phase velocity to the wind speed.) A more detailed discussion using spectral wave age for a global seasonal data set will be presented in Chapter 9. Figure 7.8 shows the average wave age over this period as a function of H_s for the North, Tropical and South Atlantic. The plots confirm that low H_s is associated on the average with high wave ages, especially in regions of low wind activity. Thus in the statistical average it appears justified to regard the wave height in Figure 7.7 as a proxy for the wave age.

A remark needs to be made concerning the operational WAM model data. Since August 1993, ERS-1 altimeter wave height data have been assimilated by ECMWF into the WAM model using an optimal interpolation scheme, thereby influencing the first guess wave field through the analysis six hours earlier. The swell wave field is thus continuously updated by the assimilation of new wave height data, thereby reducing the impact of systematic model errors in the propagation of swell over large distances.

However, an investigation of altimeter wave heights suggests that the impact on the first guess data available for the present study is probably rather limited (*Bauer and Staabs* [1998] and *Bauer*

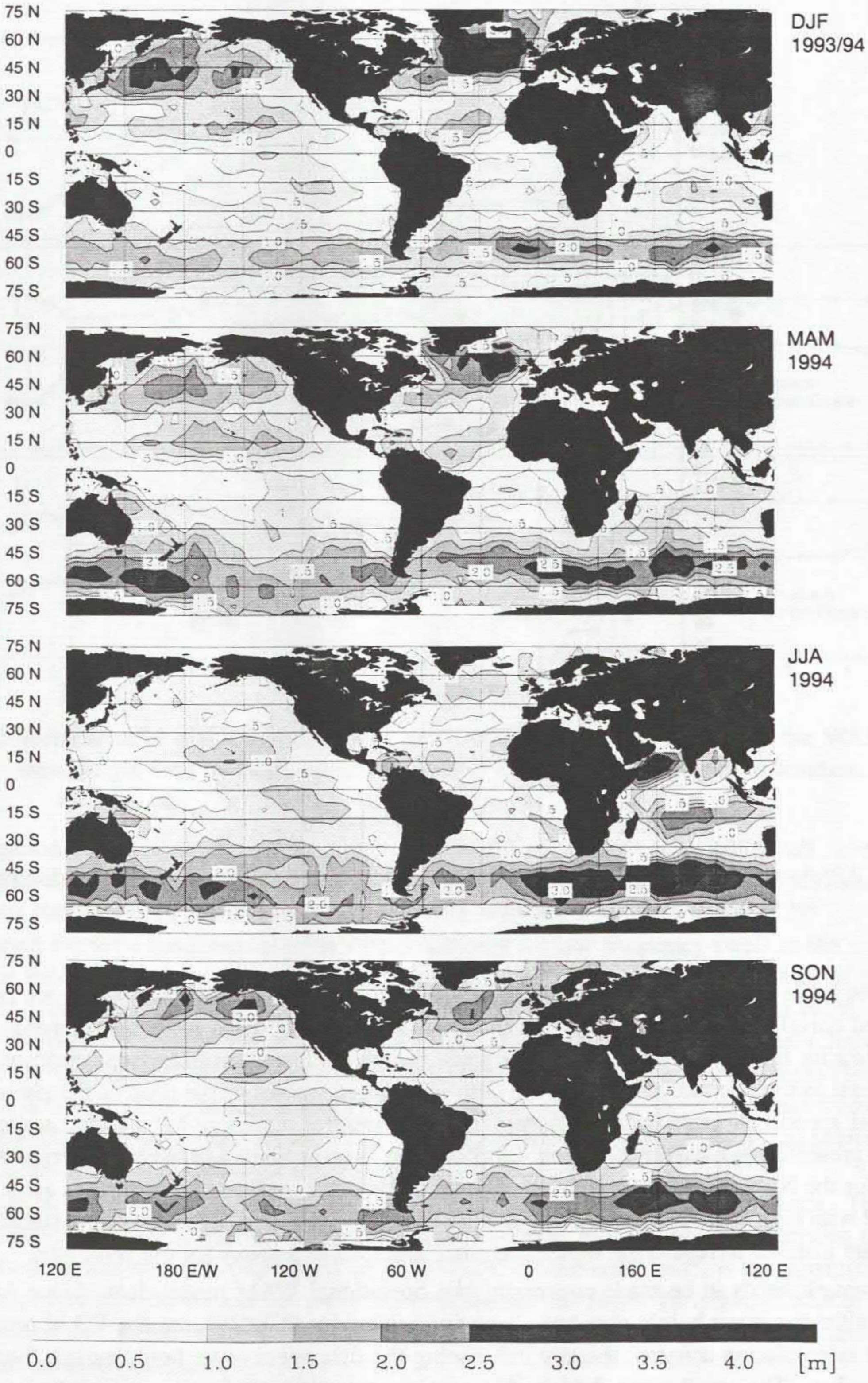

Figure 7.9: Global maps of the seasonal mean windsea wave height for the fours seasons DJF 1993/94 (top panels) to SON 1994 (bottom panels) for the WAM model.

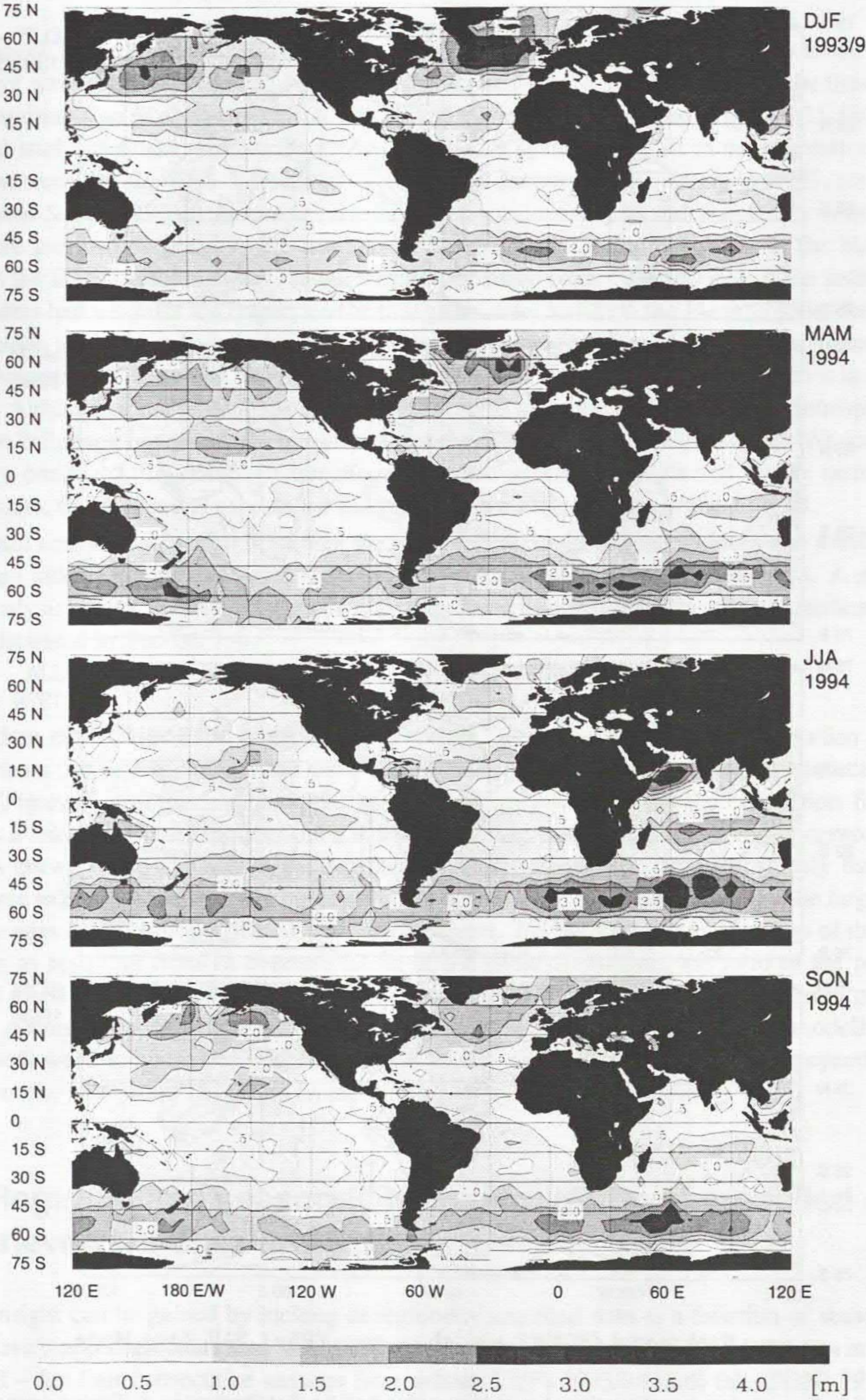

Figure 7.10: Same as Figure 7.9 for the ERS-1 SWM windsea.

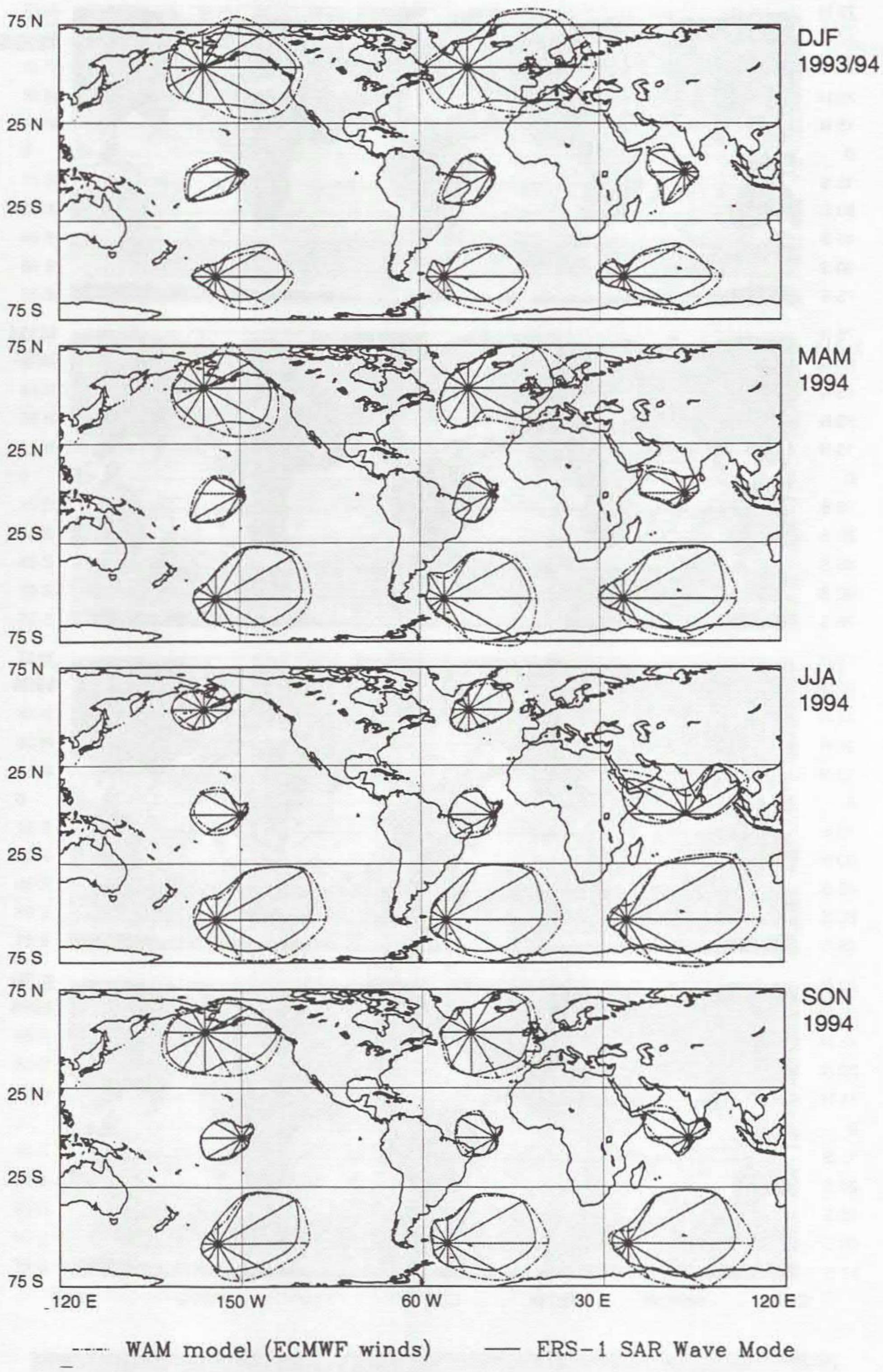

Figure 7.11: Seasonal mean directional windsea wave height distribution in different ocean basins for the fours seasons DJF 1993/94 (top panel) to SON 1994 (bottom panel). Dashed-dotted curves: modelled; solid curves: retrieved from ERS-1 SWM.

and Heimbach [1998]; see also Chapter 6). First, no marked change in the monthly mean significant wave height time series can be seen for the Northern Hemisphere summer 1993, at the time when operational assimilation of altimeter H_s into the WAM model was introduced (Figure 7.1). Furthermore, the careful study of *Bauer and Staabs* [1998] revealed a systematic shift in the monthly mean wave height time series of the ERS-1 altimeter beginning in January 1994 relative to 1993, (see Figure 8 in *Bauer and Staabs* [1998]), the values for 1994 being reduced by as much as 0.6 m in the Northern Hemisphere extra-tropics and in the tropics. This results in a systematic shift in the bias between WAM and the ERS-1 altimeter wave heights in the transition from 1993 to 1994. If the assimilation of altimeter data had a significant impact on the first guess data, a shift in the H_s time series for the WAM towards lower values should have been noticeable both in the summer of 1993, when the assimilation scheme was introduced, and at the end of 1993, when the ERS-1 altimeter algorithm was apparently modified. Although some indication of this effect may be apparent in the Northern Hemisphere extra-tropics, no influence is seen in the tropics, where the swell contribution is largest. We are therefore reasonably confident that, although our model data are undoubtedly affected by the assimilation of altimeter data, the dynamical aspects we discuss later are still apparent in the data set.

We shall confirm in Section 9.3.2 that the main differences between windsea and swell regarding the bias are indeed maintained when switching off the assimilation of altimeter data. A more quantitative analysis of the windsea and swell bias requires a regional and directional statification of the data, as discussed in Section 7.4.

Correlation coefficient for windsea and swell The time series of the correlation coefficient obtained from the regression analysis show another interesting difference between windsea and swell systems (Figure 7.4, dotted and dashed curves, respectively). Whereas the correlation for windsea maintains a fairly constant high level of 0.9, the correlation for swell is lower and undergoes stronger variations between 0.6 and 0.8 in the Northern Hemisphere and in the tropics, only the Southern Hemisphere exhibiting also a fairly constant value of 0.8. This can be explained by the large and variable wave ages (propagation distances) of swell systems. Accepting the interpretation of the observed swell bias as resulting from an overestimation of the swell dissipation, the ratio of the predicted to measured swell energy will be a function of the propagation distance. The large range of propagation distances occurring in the ocean will therefore reduce the correlation between the modelled and observed swell wave heights, and will lead also to variations in the correlation level depending on the season, i.e. the location of the storm areas.

7.3 Regional and seasonal intercomparison of modelled and retrieved windsea and swell

Further insight can be gained by looking at regionally stratified data as a function of season. To this end we have mapped all collocated WAM and SAR wave system data – subdivided again into windsea and swell – for four consecutive seasons from winter (DJF) 1993/94 until fall (SON) 1994 on a 5° × 5° global ocean grid. Figure 7.9/7.10 and Figure 7.12/7.13 show the distributions for the windsea and swell wave heights, respectively, while the associated "directional wave roses" representing the energy-weighted distributions of the wave propagation directions in the different ocean basins are reproduced in Figure 7.11 and 7.14. The directional wave roses were computed as the square root of the mean energy for each 30° angular sector.

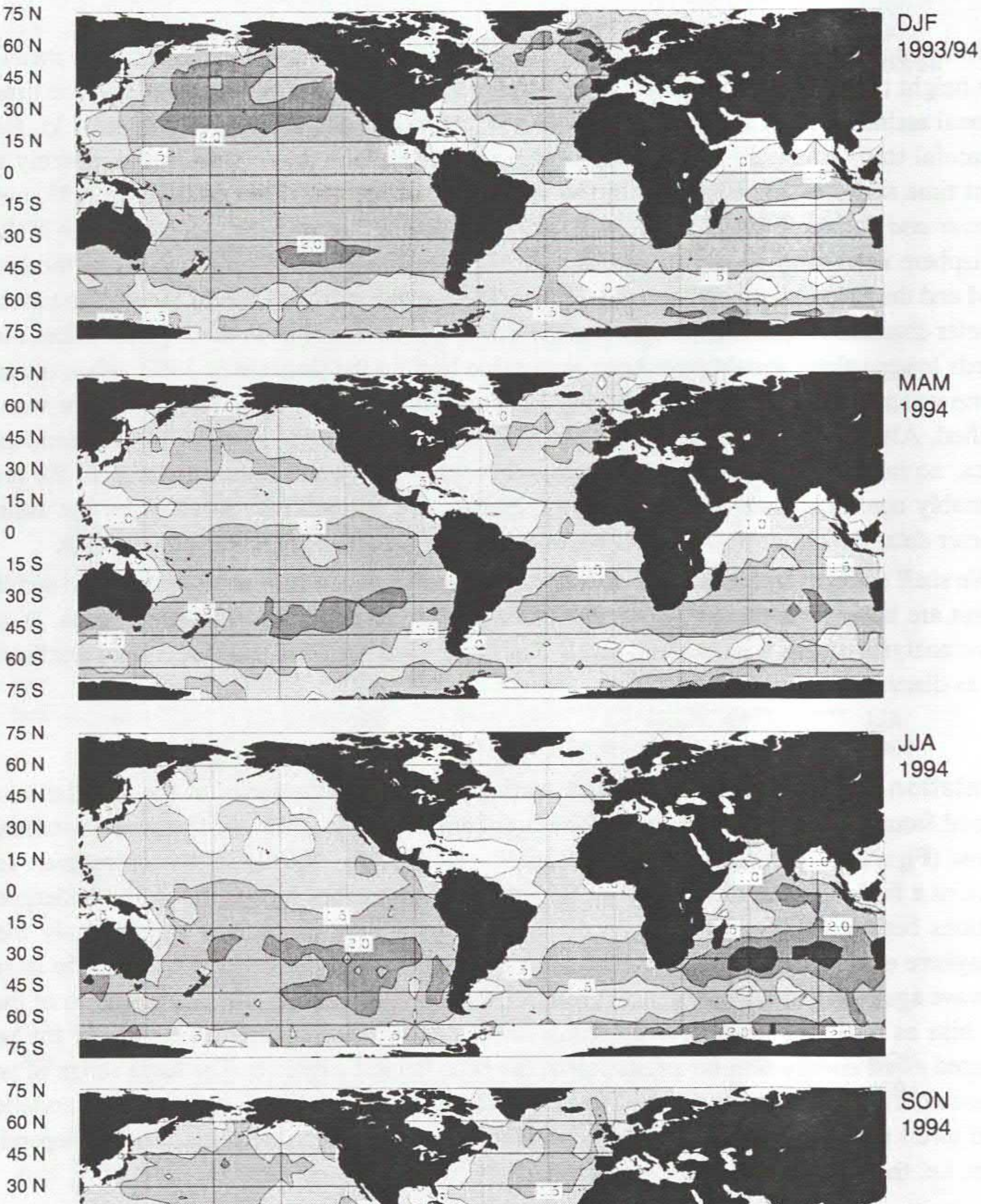

Figure 7.12: Same as Figure 7.9 for the WAM model swell.

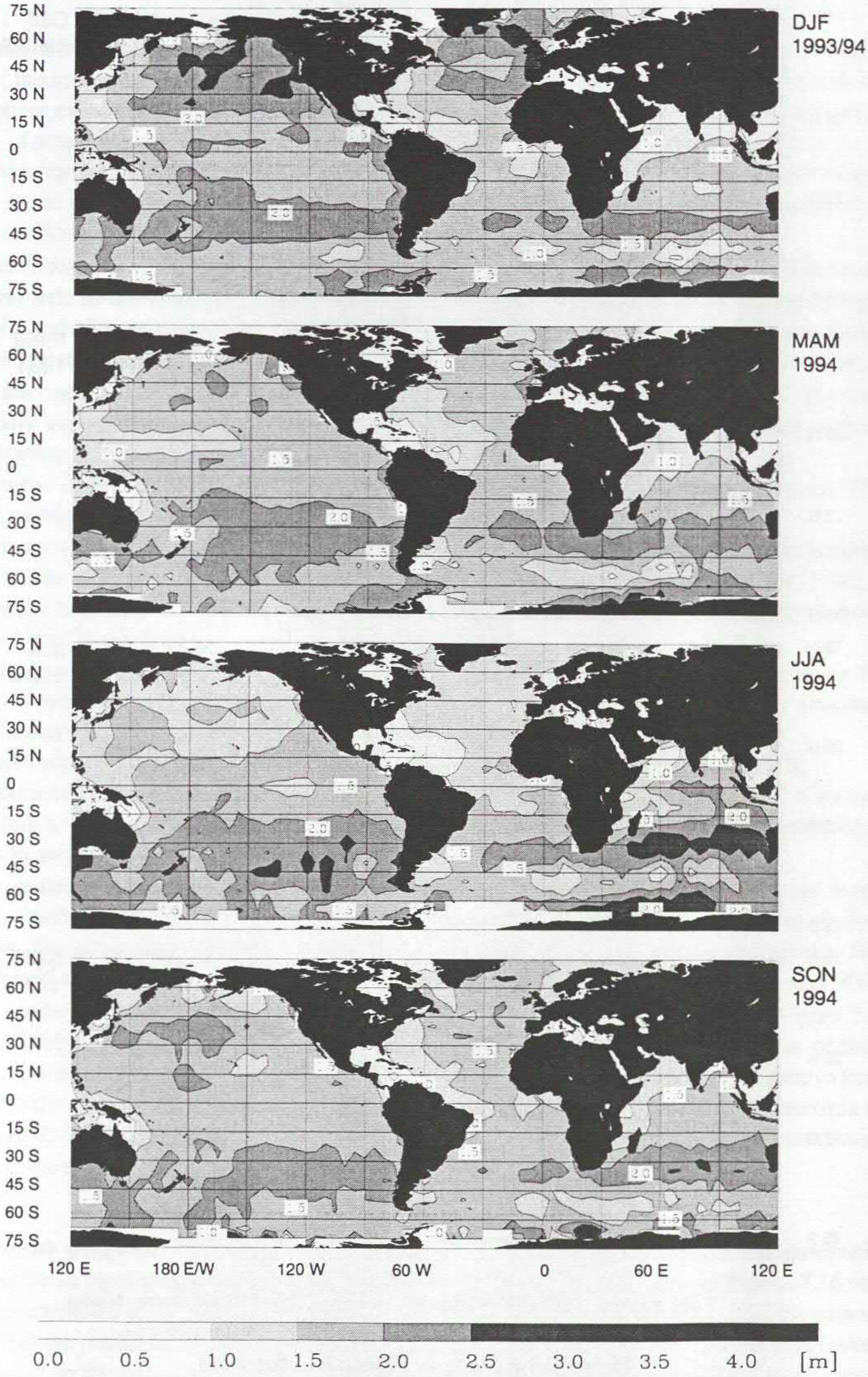

Figure 7.13: Same as Figure 7.9 for the ERS-1 SWM swell.

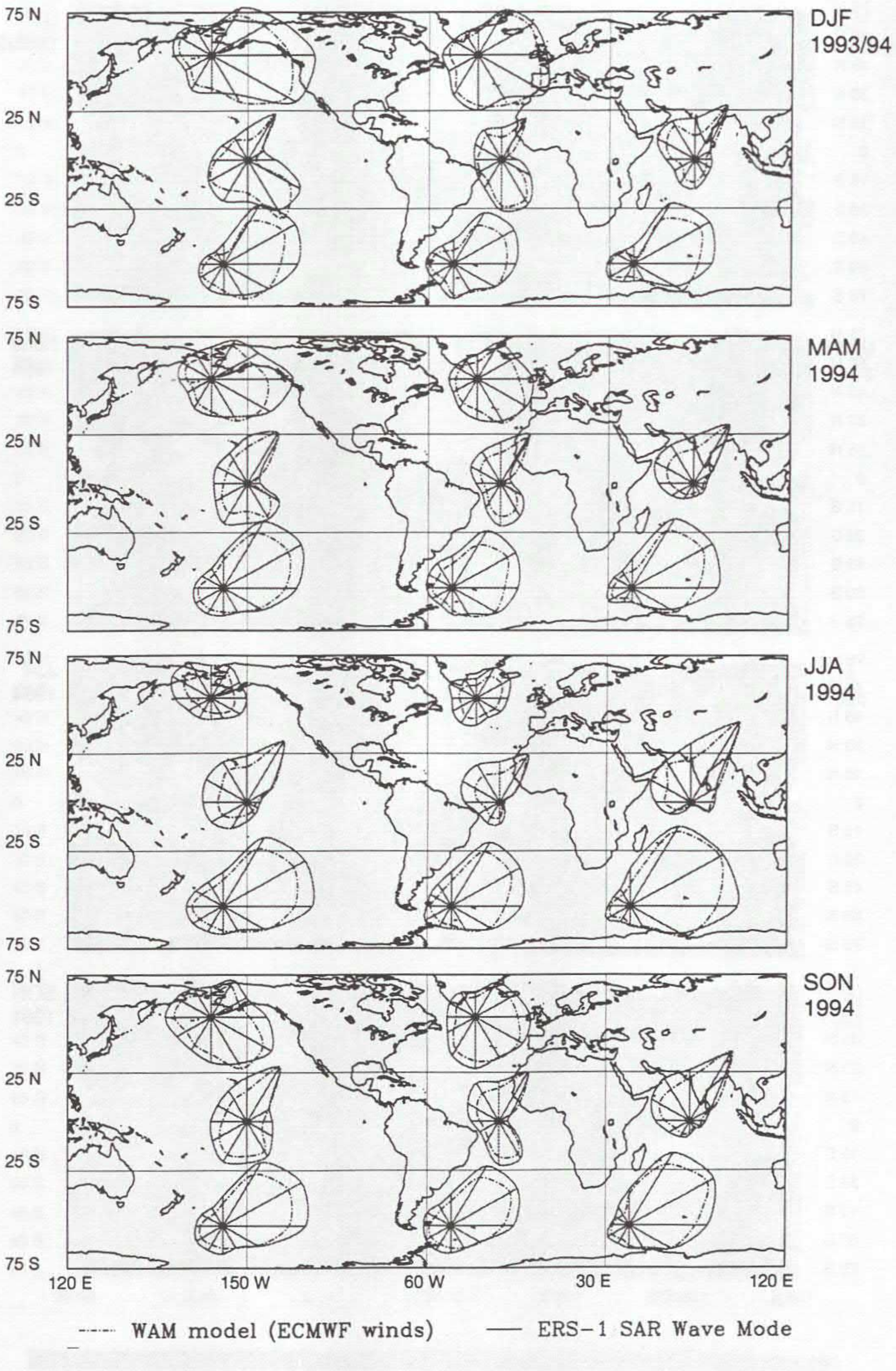

Figure 7.14: Same as Figure 7.11 for swell.

Windsea wave heights The windsea distributions (Figure 7.9 and 7.10) reflect the seasonal properties of the atmospheric circulation (see e.g. *Peixoto and Oort* [1992]). In the Northern and Southern Hemisphere extra-tropics, the windsea wave heights are governed by the mid-latitude westerlies. The regions of strongest windsea activity in DJF (Northern Hemisphere winter) are found in the vicinity of the Aleutian low in the North Pacific and the Islandic low in the North Atlantic. A belt of moderate H_{wi} is found in the Southern Hemisphere mid-latitudes, driven by the summer westerly wind belt around the Antarctic.

In the Southern Hemisphere winter JJA, the highest windseas are found in the mid-latitude westerly wind belt in the Southern Hemisphere. Strong monsoon driven windsea systems propagating to the NE and NW are found also in the Arabian Sea. In the tropics, the dominant wave propagation direction is determined by the easterly trade winds, which are generally stronger in the winter seasons.

An alternative view of the global sea state structure is provided by the latitudinal distribution of the zonally averaged wave heights and directions for windsea (Figure 7.15) and swell (Figure 7.16) The following features can be recognized:

- low wave heights in the seasonally shifting equatorial intertropical convergence zone (ITCZ) due to weak surface easterlies;
- northwestward (in the Southern Hemisphere) to southwestward (in the Northern Hemisphere) propagating waves of moderate wave height in the trade wind regimes on either side of the ITCZ;
- low wave heights in the region of the sub-tropical quasi-permanent high-pressure cells around 30° N/S (the horse latitudes);
- strong windsea systems in the mid-latitude west wind belts, particularly in the roaring fourties, fighting fifties and screeming sixties in the winter Southern Hemisphere; the stronger seasonal cycle in the Northern Hemisphere noted already in the H_{wi} time series is also seen;
- the influence of the easterly winds from the polar high-pressure cells south of 65° S;
- pronounced seasonal differences in zonally averaged swell wave height around 25° N in the Indian Ocean, due to the seasonal monsoon cycle, and below 60° S near the Antarctic, presumably due to changes in sea ice extent.

The seasonal maps and zonal averages of wave heights and directional distributions confirm the previous findings of a generally overestimated windsea by the WAM model relative to the SWM retrievals. The effect is strongest in high sea states occurring in mid-latitudes during winter. However, the modelled windsea is slightly underestimated in the trade wind regions during JJA and SON.

The modelled and retrieved directional distributions in both Figure 7.15/7.16 and Figure 7.11/7.14 are remarkably similar. However, WAM shows a rather more symmetrical distribution of the meridional component about the west-east axis in the Southern Hemisphere extra-tropics, with a maximum directed to the east (90°), whereas the SWM retrieved data are more asymmetric with maxima directed towards ENE (60°). Discrepancies can also be seen in the directional distribution of east to northward travelling waves in the tropical Indian Ocean during the summer monsoon.

Swell wave heights The seasonal maps of swell wave heights and directional distributions are less sensitive to local atmospheric conditions, but the principal features seen in Figure 7.16 can again be largely attributed to the synoptic conditions that produced the windsea that is later transformed into swell. Thus the predominance of eastward and equatorward propagating swell in the mid-latitudes can be explained by the strong westerly cyclones in that belt. The significant meridional swell components in the tropics, characterized by a marked seasonal variation in the directional distribution, presumably also originate in the mid-latitude cyclones. In addition, the tropical distributions exhibit a significant westward component due to the trade winds.

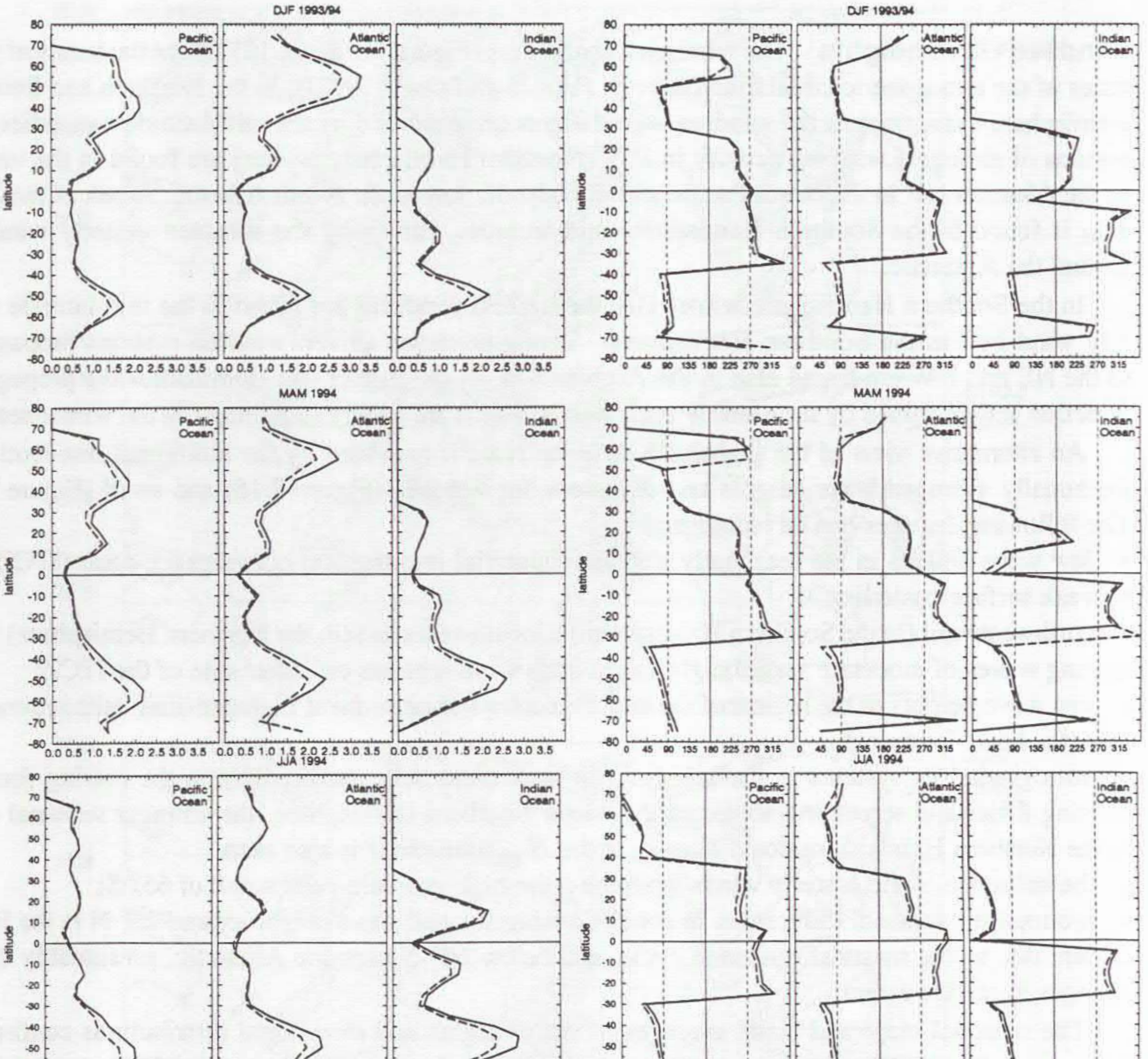

Figure 7.15: Seasonal zonal mean windsea wave heights (left) and directions (right) in the Pacific, Atlantic and Indian Ocean for the four seasons from DJF 1993/94 (top panel) to SON 1994 (bottom panel). Solid curves: modelled; dashed curves: retrieved from SWM.

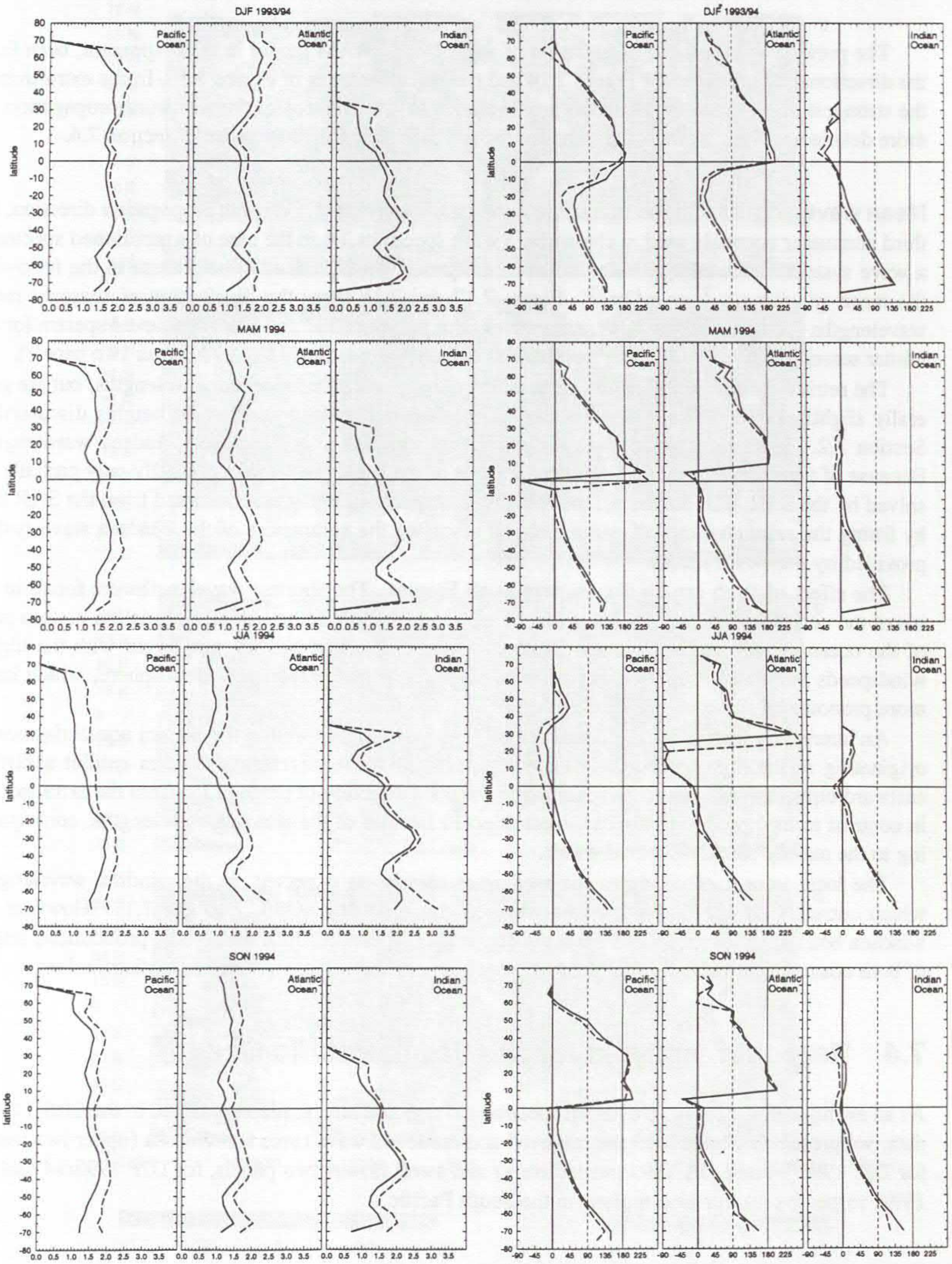

Figure 7.16: Same as Figure 7.15 for swell.

The previously noted underestimation of swell by the WAM model is again apparent, both from the directional distributions of Figure 7.14 and the zonal averages of Figure 7.16. In the extra-tropics the strongest bias is seen for eastward propagating swell, in the tropics for westward propagation. A more detailed analysis of the conditions for the South Pacific Ocean is given in Section 7.4.

Mean wavelengths In addition to the significant wave height and mean propagation direction, the third parameter normally used to charactize a wave spectrum, or, in the case of a partitioned spectrum, a wave system, is the energy weighted mean frequency $\bar{f}$. Eqivalently, we present in the following the mean wavelength $\bar{\lambda} = g/2\pi\bar{f}^2$. Figure 7.17 and 7.18 show the distribution of seasonal mean wavelengths for windsea and swell, respectively, for the modelled and SWM-retrieved spectra for the winter season DJF 1993/94 (upper two panels) and summer season JJA 1994 (lower two panels).

The retrieved swell wavelengths agree rather closely with the modelled wavelengths, but are generally slightly larger. This is consistent with the higher retrieved swell wave heights discussed in Section 7.2. Too much significance should not be attached to the retrieved windsea wavelengths. Because of the azimuthal cut-off, the windsea part of the wave spectrum is normally only partially resolved by the SAR (cf. Chapter 8), the full windsea spectrum being reconstructed from the SAR data by fitting the azimuthal cut-off parameter and rescaling the parameters of the windsea wave system provided by the WAM model.

The effect of fetch can be clearly seen in all Figures. The shortest wavelengths are found in the lee of the continents, in mid-latitudes off the east coasts, the longest wavelengths in the eastern parts of the ocean basins and in the open Southern Ocean. The increase in wavelength with the higher windspeeds in winter is also clearly visible, particularly in the Northern Hemisphere, which has a more pronounced seasonal cycle (see Section 7.1).

An interesting feature is the occurrence of long wavelength swell in the eastern equatorial oceans originating in the high-wind mid-latitude regions: the swell wavelength isolines exhibit a distinct eastward-equatorward slant, corresponding to the main direction of propagation from the extra-tropics, in contrast to the predominantly east-west oriented isolines of the windsea wavelengths, corresponding to the mainly zonally directed winds.

The local impact of windspeed is seen most clearly, as expected, in the windsea wavelengths, which correlate well with the windsea wave heights, cf. Figure 7.9, 7.10 and 7.17. However, for windsea both the windspeed and the fetch are important, as demonstrated by the pronounced impact of both coastal shadowing and the high-wind regions on the windsea wavelength distributions.

7.4 Regional analysis for the South Pacific Ocean

As an example illustrating the detailed spectral and regional information contained in the ERS-1 SWM data, we present in Figure 7.19 the retrieved and modelled wave roses for windsea (upper two panels, for DJF 1993/94 and JJA 1994, respectively) and swell (lower two panels, for DJF 1993/94 and JJA 1994, respectively), for nine regions in the South Pacific.

7.4.1 Directional windsea distributions

The general zonal wind characteristics are reproduced by both the modelled and retrieved data, which show also significant deviations from the mean wind directions that appear as side lobes in the directional distributions.

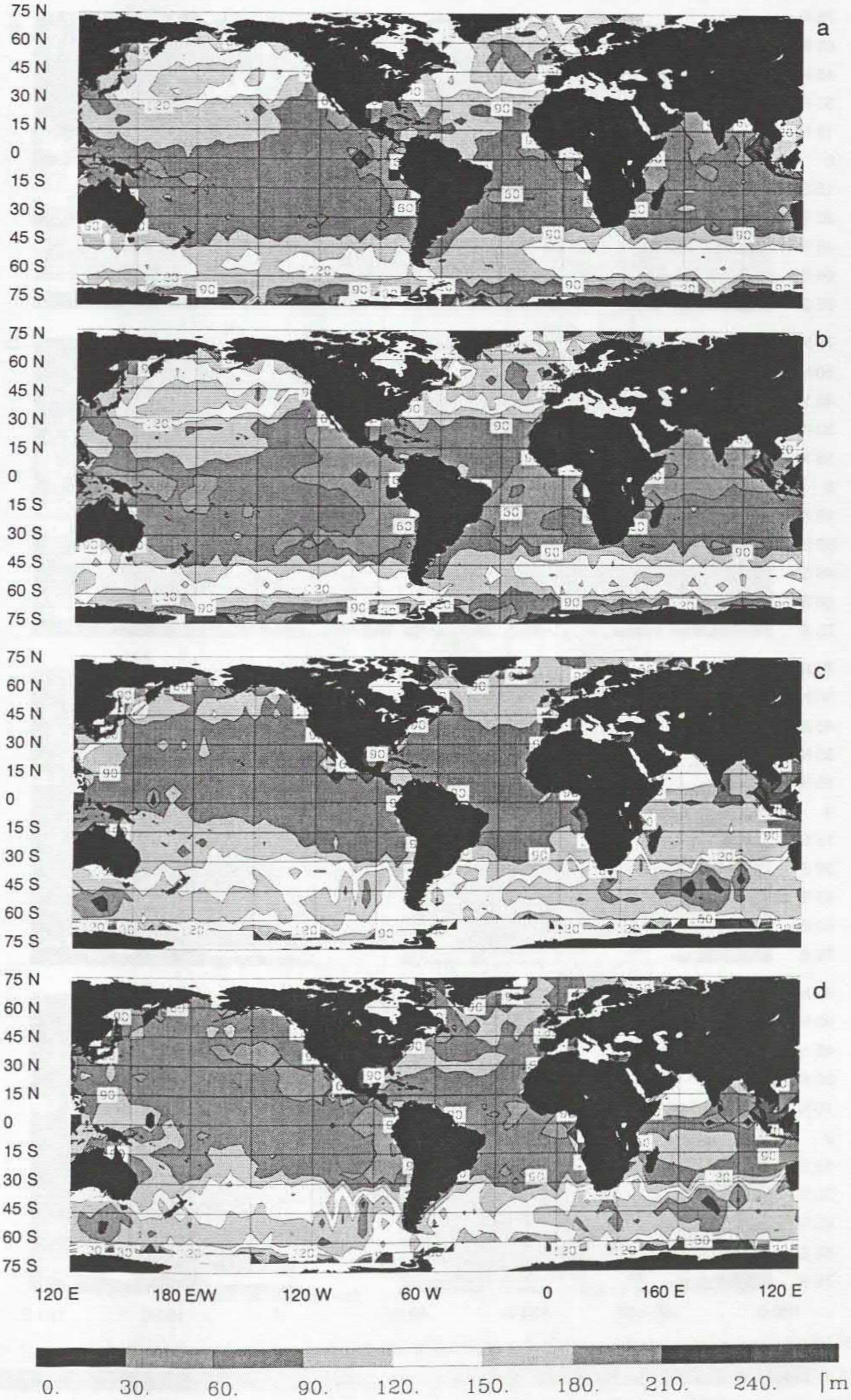

Figure 7.17: Same as Figure 7.9 for the seasonal mean windsea wavelength. From top to bottom: DJF 1993/94 WAM, DJF 1993/94 SWM, JJA 1994 WAM, JJA 1994 SWM.

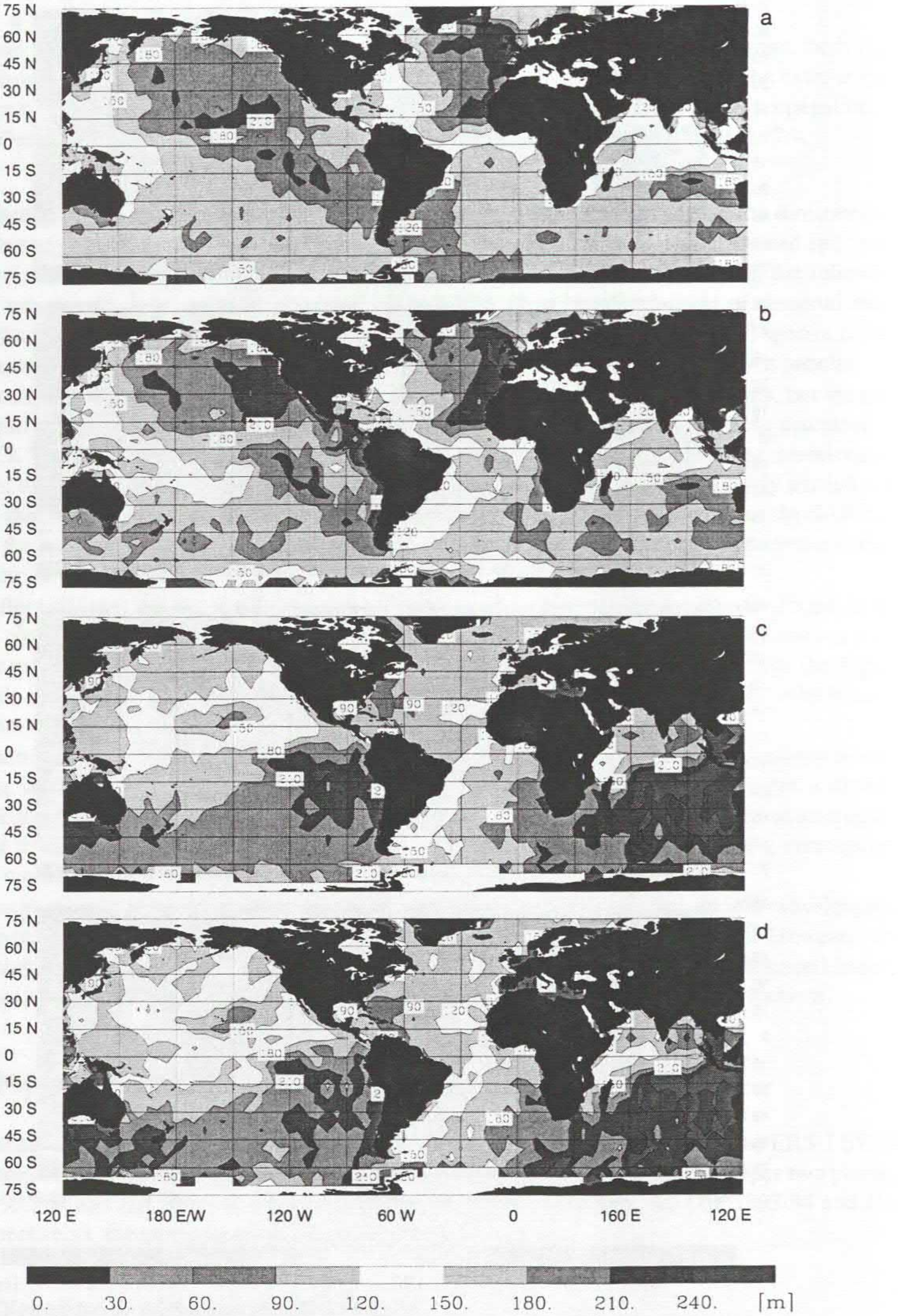

Figure 7.18: Same as Figure Figure 7.17 for swell.

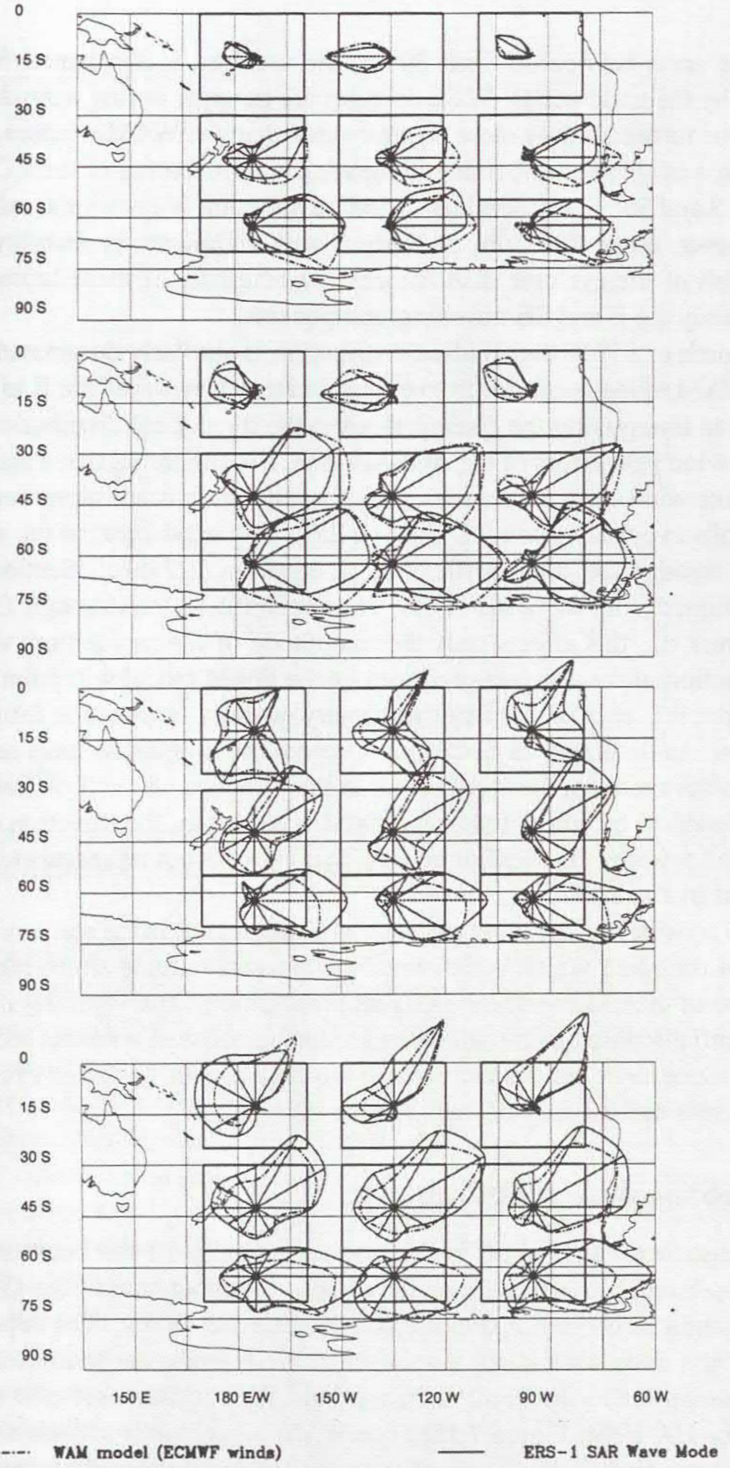

Figure 7.19: Seasonal directional wave height distribution of the windsea and swell in selected areas of the South Pacific for JJA 1994. From top to bottom: WAM windsea, SWM windsea, WAM swell, SWM swell. Dashed-dotted curves: modelled; solid curves: retrieved

In the sample areas between 0° and 30° S, the windsea is dominated by W to NW travelling waves generated by the trade winds. Wave energies are stronger during austral summer. The retrieved windsea tends to be turned slightly more equatorwards than the WAM windsea, particularly for austral winter, suggesting a possible shortcoming in the angular distribution of the ECMWF trade wind field.

Between 30° S and 55° S, the dominant windsea direction is eastwards, reflecting the mid-latitude westerlies. However, other directions also occur with significant probability, for example towards the NW, as a result of the cyclonic disturbances characteristic of these latitudes. The WAM model overestimates mainly the E and SE travelling components.

In the band south of 55° S, the windsea distribution is similarly dominated by eastward travelling waves, and the WAM model again tends to overestimate waves travelling E to SE.

Alternatively to interpreting the discrepancies in the directional distributions in the westerly wind regions as due to wind field errors of the AGCM alone, it is suggested that a misalignment between the wind vector and the wind stress in the presence of swell which is not represented by the WAM model might cause the observed mismatch (cf. Section 2.6). The wind input to the wave is parametrized in the WAM model through the drag coefficient C_D^J, equation (2.24) (cf. Section 2.5.2), thus assuming the wind to be aligned with the wind stress (cf. Section 2.4.1). Although C_D^J is influenced by the wave-induced stress τ_w, this effects only the magnitude of the momentum transfer. Therefore, the WAM model direction of the windsea produced by the WAM model will point towards the main wind direction. However, it is pointed out that the primary quantity responsible for the momentum transfer is the wind stress. As described in Section 2.6, recent measurements have revealed the direction of the wind stress to deviate from the wind vector in the presence of swell. A fraction of the wind stress fluctuation was found to be correlated to the swell wavelength, the direction of this wave-correlated stress being rotated towards the swell direction. This effect is not represented by the WAM model but could be observed by the SAR.

In addition to considering the windsea, such a misalignment in the real world would also affect the mean direction of the swell which is radiated from the mid-latitude storm regions. The swell would keep the signature of the misalignment along its propagation for several days. In fact, the directional distribution of swell discussed in the following section agrees well with this picture. This confirmation is of some importance since the majority of the windsea cannot be directly resolved by the SAR (cf. Section 8.2), whereas the majority of the swell can.

7.4.2 Directional swell distributions

The directional distributions of swell in the tropical latitudinal band between 0° and 30° S are determined by two principal sources: the easterly trades on either side of the ITCZ, producing a broad westward propagating swell sector, and the mid-latitude westerlies. The dependence on fetch leads to an increase of the trade wind swell from East to West, while the southeast travelling waves from the midlatitude westerlies to the South increase from West to East (see also the global distributions of wavelengths for JJA 1994, Figure 7.18). The WAM model tends to underestimate particularly the trade wind swell components. The overestimation of NE-ward propagating swell in the most western sampling area which vanishes in going to the most easterly sampling area might be due to shadowing of some islands that are not resolved in the WAM model but effective in obstructing the propagating swell. With a high island density in the western part of the tropical and South Pacific, the probability of NE-ward propagating swell to hit an island diminishes from west to east.

In the remaining two latitudinal bands South of 30° S, the swell is dominated by the mid-latitude westerlies. The distributions become more isotropic, reflecting the cyclonic character of the generating storms. Nevertheless, clear maxima are found in the NE-ward main directions of radiation. With a

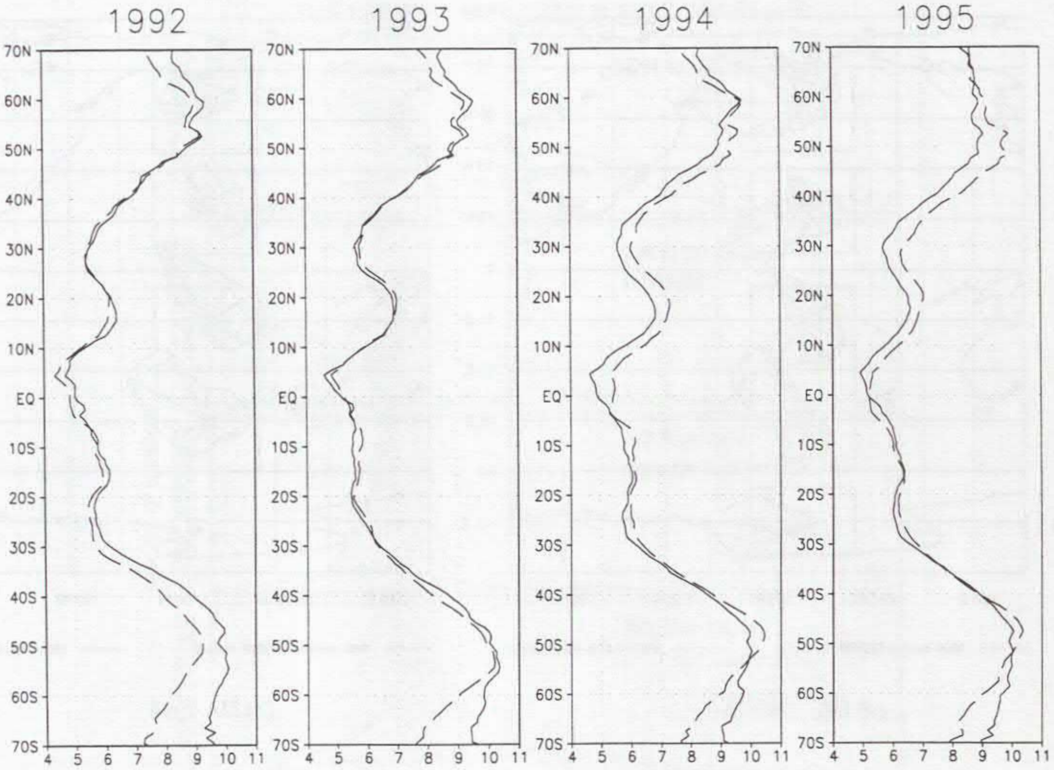

Figure 7.20: Four years of annual zonal mean wind speeds [m/s] from gridded scatterometer (solid line) and ECMWF (dashed line) wind fields. Kindly provided by *Bentamy et al.* [1996].

few exceptions, the WAM model underestimates the swell in all directions.

Particularly noticeable is the underestimation of the E and NE travelling swell south of 55° S. This presumably again points to errors in the wind field. The area is bounded from the South by Antarctic sea ice and thus has rather limited fetch to produce swell with a significant northward component. The existence of such components therefore implies rather strong east to northeastward blowing winds. Katabatic winds could be a candidate, particularly as they are notoriously difficult to capture adequately in global circulation models. However, the predominantly southwesterly component of katabatic winds is not consistent with the easterly propagation direction of the swell.

The claim that the underestimation of eastward propagating swell is due to errors in the wind field implies the ECMWF wind field south of 55° to be too weak, thus reversing the general trend in the remaining areas (cf. last section). In fact, a significant underestimation of the wind would imply that wave systems seen by the SAR are erroneously attributed to swell because the criterion for identifying windsea would fail under such conditions. The actual wind waves would travel significantly faster than the low ECMWF wind speed, thus causing the mis-attribution.

Indeed, *Bentamy et al.* [1996, 1997] have shown the ECMWF wind speeds to be systematically low in the oceans south of 50°S compared to ERS-1 scatterometer winds.. Figure 7.20 kindly provided by A. Bentamy from IFREMER/CERSAT shows annual zonal mean of ECMWF and ERS-1 scatterometer wind speeds for the years 1992 to 1995. Overestimation of the ECMWF wind speed was noticeable during 1994 and 1995, particularly in the northern hemisphere, reaching south to 50°S. However, an abrupt reversal occurs beyond 50°S with an increasing underestimation of the ECMWF wind speed towards the south. One reason for these strong deficiencies in these regions might be the fact, that few routine measurements exist in these regions that could be assimilated into the ECMWF

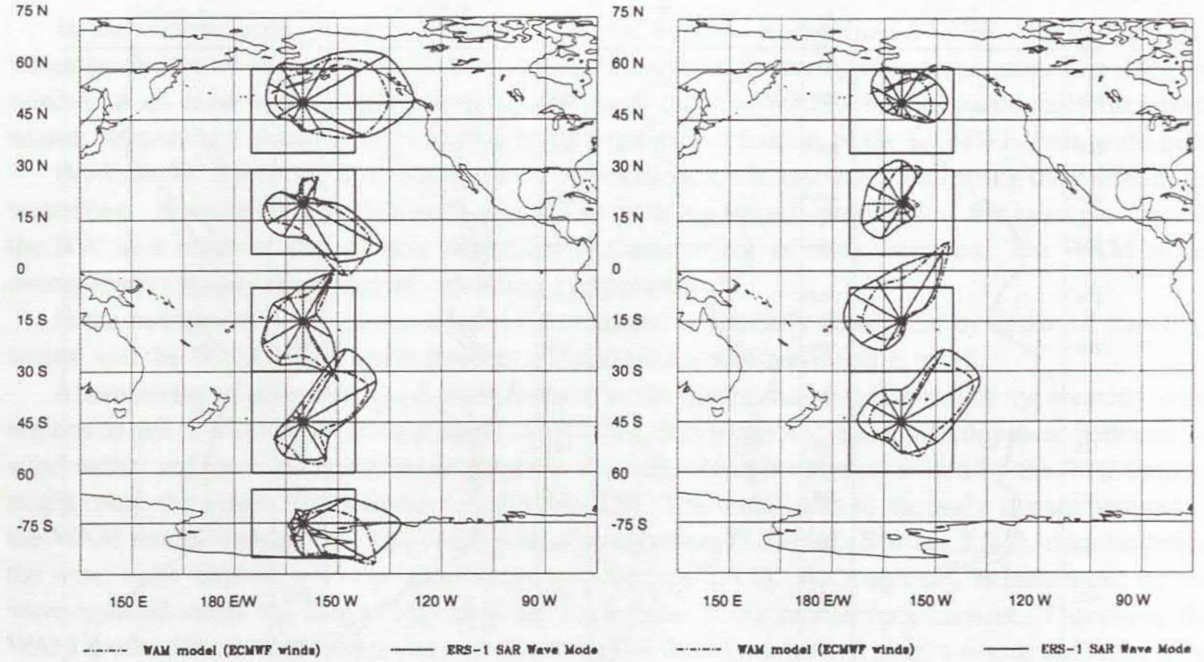

(a) DJF 1993/94 (b) JJA 1994

Figure 7.21: Seasonal directional wave height distribution of the swell in five meridionally distinct boxes of the Pacifc Ocean zonally bounded between 170° E and 150° W. Dashed-dotted curves refer to WAM model values, solid curves to ERS-1 SWM values.

analysis (cf. Section 3.2.1). Assimilation of spaceborne operational weather observations are limited between 50° S N/S [*ECMWF* 1995]. In the northern hemisphere operational land stations can fill the gap, in contrast to the southern hemisphere.

Although our conjecture is supported by ERS-1 scatterometer data, more detailed investigations of statistics from collocated samples are certainly needed to verify this issue.

7.5 North-South distributions through the Pacific

As a further example of the detailed spatial-spectral information provided by the ERS-1 SWM, we have investigated the distribution of wave parameters in five areas along a meridional section of the Pacific for the boreal winter DJF 1993/94 and summer JJA 1994 (Figure 7.21 a,b). The areas are representative of the northern and southern tropics and mid-latitudes, and the Ross Sea in the Antarctic Ocean. Figure 7.21 a,b depicts the polar wave rose plots of the directional distributions for swell, while Figure 7.22 shows the relative distributions of windsea, swell and mixed windsea-swell wave heights.

The directional distributions exhibit considerable structure, with a pronounced seasonal dependence. They can again be explained in terms of the various wind systems characterizing the different latitudinal zones of the Pacific.

As expected, the distribution curves of retrieved swell wave heights (blue dashed curves) are shifted to higher values than the corresponding model distributions, while the opposite holds, although less pronounced, for the windsea curves. A noticeable feature of the distributions (apparent also in the

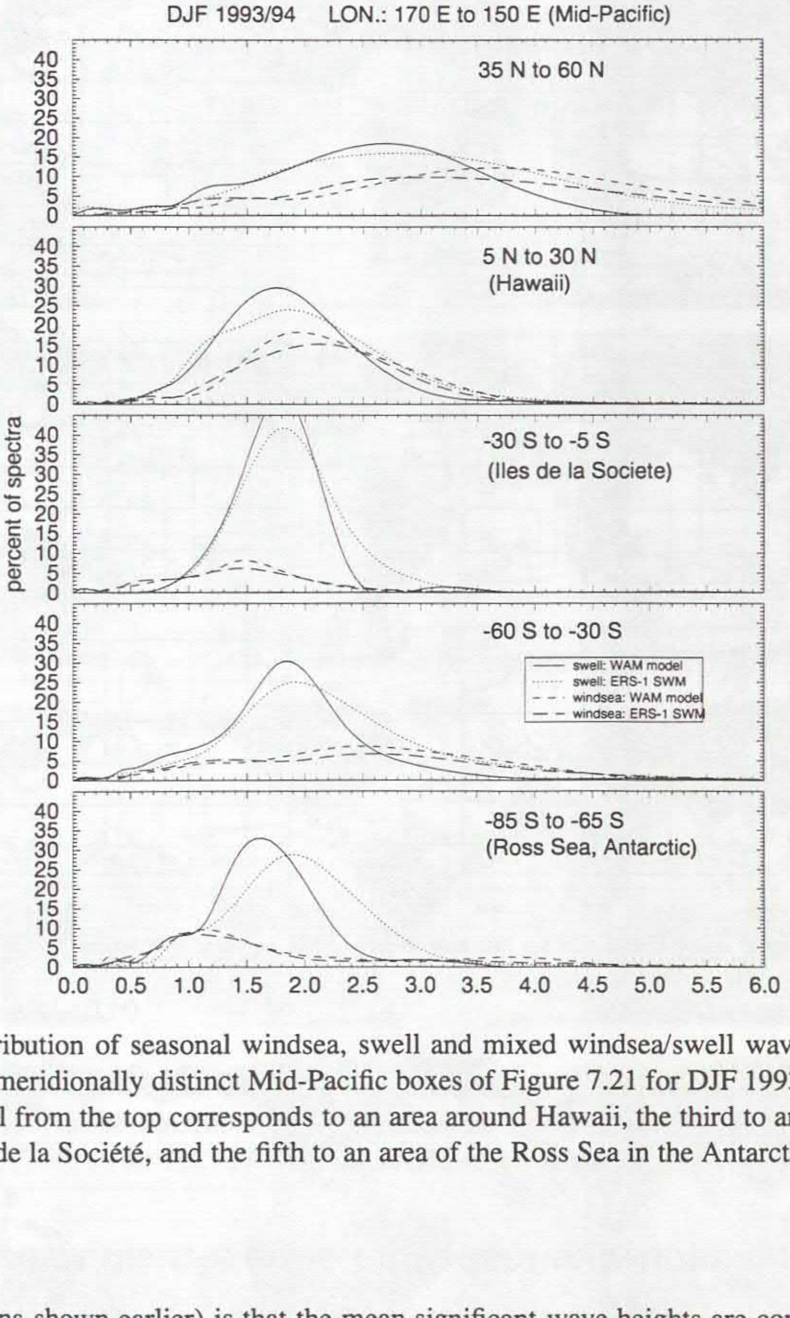

Figure 7.22: Distribution of seasonal windsea, swell and mixed windsea/swell wave heights for the five meridionally distinct Mid-Pacific boxes of Figure 7.21 for DJF 1993/94. The second panel from the top corresponds to an area around Hawaii, the third to an area around the Îles de la Société, and the fifth to an area of the Ross Sea in the Antarctic.

spatial distributions shown earlier) is that the mean significant wave heights are considerably higher for swell than for windsea. This is because a given spectral wave component, although attaining its maximum energy at the end of its relatively short windsea growth period, subsequently propagates through the ocean for a significantly longer period as swell.

We note that while the modelled and retrieved directional distributions for swell are generally consistent with the hypothesis that the WAM model underestimates swell because of a too large swell dissipation, individual features of the polar distributions do not appear to support this interpretation. In particular, the NNE and SSE travelling swell components in Northern Hemisphere and Southern Hemisphere tropics are overestimated by the WAM model. In the next section we analyze this phenomenon in more detail in the spectral domain.

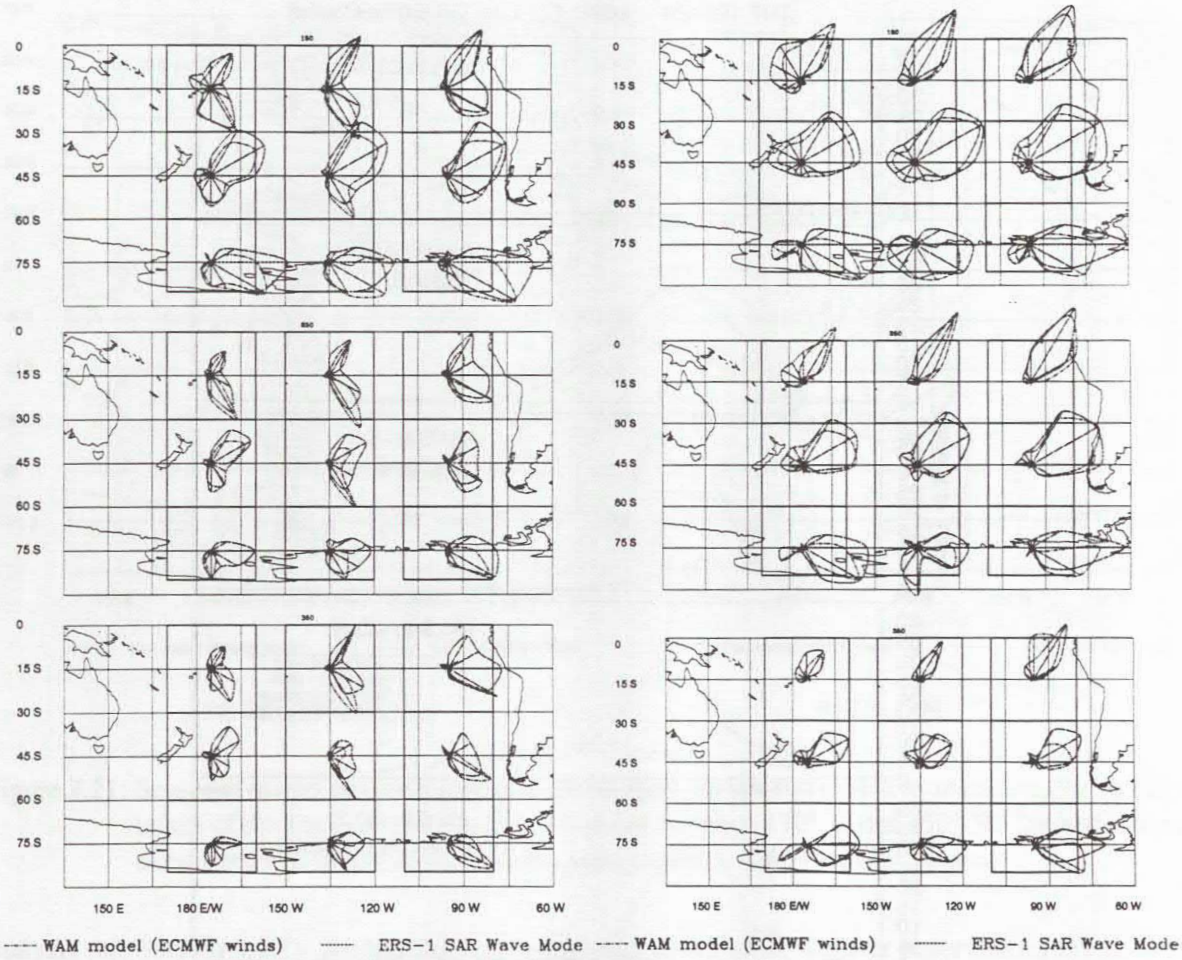

(a) DJF 1993/94 (b) JJA 1994

Figure 7.23: Directional wave height distributions of individual longest-wavelength swell systems in various sampling areas of the South Pacific for different lower wavelength thresholds. Top: $\lambda > 150$ m, middle: $\lambda > 250$ m, bottom: $\lambda > 350$ m.

7.6 Stratification with respect to swell system wavelength

For a clearer insight into the nature of the differences between the modelled and retrieved wave spectra, we need to stratify the partitioned wave systems with respect to wavelength as well as direction. Figure 7.24 shows the global distributions of mean wave height for the same winter and summer seasons DJF 1993/94 (upper two panels for WAM and ERS-1 SWM) and JJA 1994 (lower two panels for WAM and ERS-1 SWM) considered previously, but now only for the longest wavelength swell system in each spectrum. To be included in the statistic, however, the swell wavelength was required to exceed a lower threshold, set in Figure 7.24 at 250 m. Consistent with our general findings for the total swell, the SWM-derived wave heights for these swell systems are again higher than the WAM wave heights. However, in contrast to the maps of the total swell wave height (defined as the rms value of the energy summed over all partitioned swell systems), the distributions for individual long

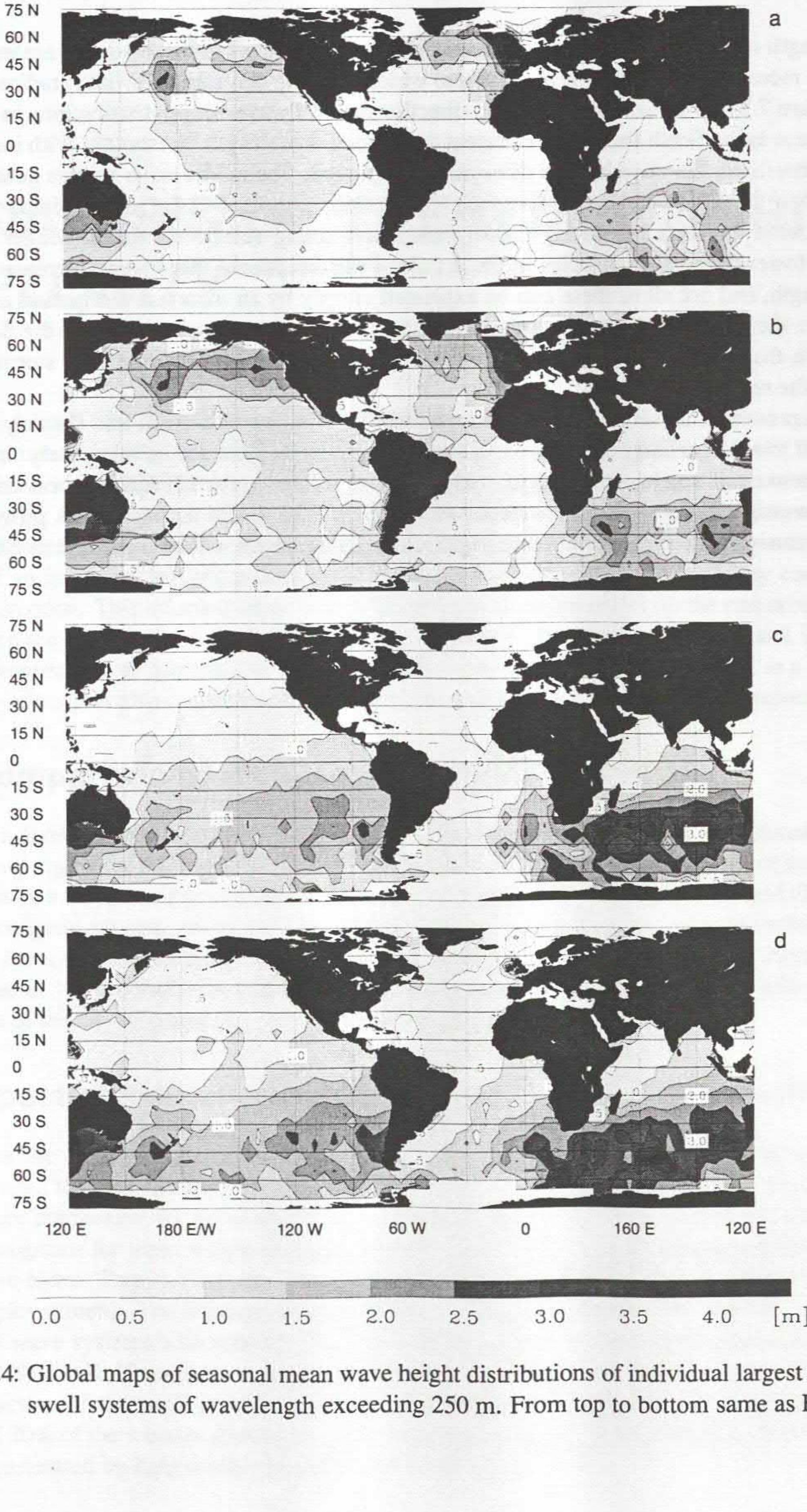

Figure 7.24: Global maps of seasonal mean wave height distributions of individual largest wavelength swell systems of wavelength exceeding 250 m. From top to bottom same as Figure 7.17.

wavelength wave systems are seen to be very similar to the maps of mean swell wavelengths. One can thereby more easily identify the regions into which the long wavelength swell is radiated.

Figure 7.23a/b shows the associated directional swell wave height distributions in different sampling areas in the South Pacific for different lower long-wavelength thresholds. With increasing wavelength threshold, the wave heights diminish, as expected. The model wave heights generally decrease faster than the SWM-retrieved wave heights, as again expected if the underestimation of swell by the model is due to a too strong model dissipation acting selectively on the longer swell components. However, the discrepancies in the details of the directional distribution increase with the swell wavelength, and not all of these can be explained simply by an incorrect dissipation expression. For example, the WAM model predicts significant SE travelling swell components in the Southern Hemisphere in the northern winter, presumably radiating from northern mid-latitude storms, that are not seen in the retrieved swell.

The processes involved in the transformation of windsea into swell and the subsequent propagation of swell over large distances are clearly complex and cannot be adequately analyzed within the framework of a general statistical study. A more refined approach for a process analysis is a detailed investigation of a set of individual events. The ERS SWM measurements provide a valuable comprehensive data base for such investigations. This approach will be presented in Chapter 9.

8 ANALYSIS OF THE R.M.S. ORBITAL VELOCITY

As already pointed out, a basic limitation of SAR ocean wave images is the azimuthal cut-off of the image spectrum caused by the nonlinear velocity bunching mechanism [HH], [HBHH]. The cut-off normally lies within the windsea part of the spectrum and suppresses the direct spectral information provided by the SAR on short to moderate wavelength waves with significant components of propagation in the azimuthal direction. However, the azimuthal cut-off wavenumber also provides a direct measure of an important integral parameter of the wave field: the rms orbital velocity component in the range direction. This information is used in the retrieval algorithm to adjust the rms orbital velocity to reproduce the observed cut-off, thereby partially replacing the missing direct spectral information at high wavenumbers, as discussed in Section 4.5. However, the cut-off wavenumber, as a measure of the orbital velocity, is also useful data in its own right, and will be analyzed in this chapter.

8.1 Comparison of observed vs. simulated cut-off

Figure 8.1a shows scatter diagrams and regression lines for the observed and simulated azimuthal cut-off wavelengths for the boreal winter DJF 1993/94 in the tropics and the Northern and Southern Hemisphere extra-tropics. The observed azimuthal cut-off wavelengths were determined directly from the SAR imagette spectra, while the simulated cut-off wavelengths were inferred, using the same algorithm, from the SAR imagette spectra computed from the retrieved wave spectra. Regression line slopes close to 1 and correlation coefficients of 0.9 and higher in all three data sets indicate that the adjustment of the cut-off parameter in the retrieval algorithm was successful.

8.2 Spectral resolution imposed by the azimuthal cut-off

To estimate the impact of the azimuthal cut-off on the retrieval of windsea and swell systems, we have computed the ratio k_c/k_x of the observed azimuthal cut-off wavenumber to the mean azimuthal wavenumber component for an ensemble of windsea and swell systems. Figure 8.2 shows the resulting histograms for three windsea (top panel) and swell (bottom panel) data sets for the Northern Hemisphere Extra- Tropics (red), the Tropics between 25° N/S (blue) and the Southern Hemisphere Extra-Tropics (green). The medians of the histograms are listed in Table 8.2, together with the percentage of wave systems with ratios k_c/k_x greater than 1, representing waves that can be explicitly imaged by the SAR. The values clearly demonstrate the ability of the ERS-1 SAR to detect a substantial fraction of the swell systems encountered in the ocean, despite the high R/v ratio. A fair fraction of 30% of the windsea systems can also be directly imaged by the SAR, but short wave length windseas generated by light winds can not be seen at all by the SAR.

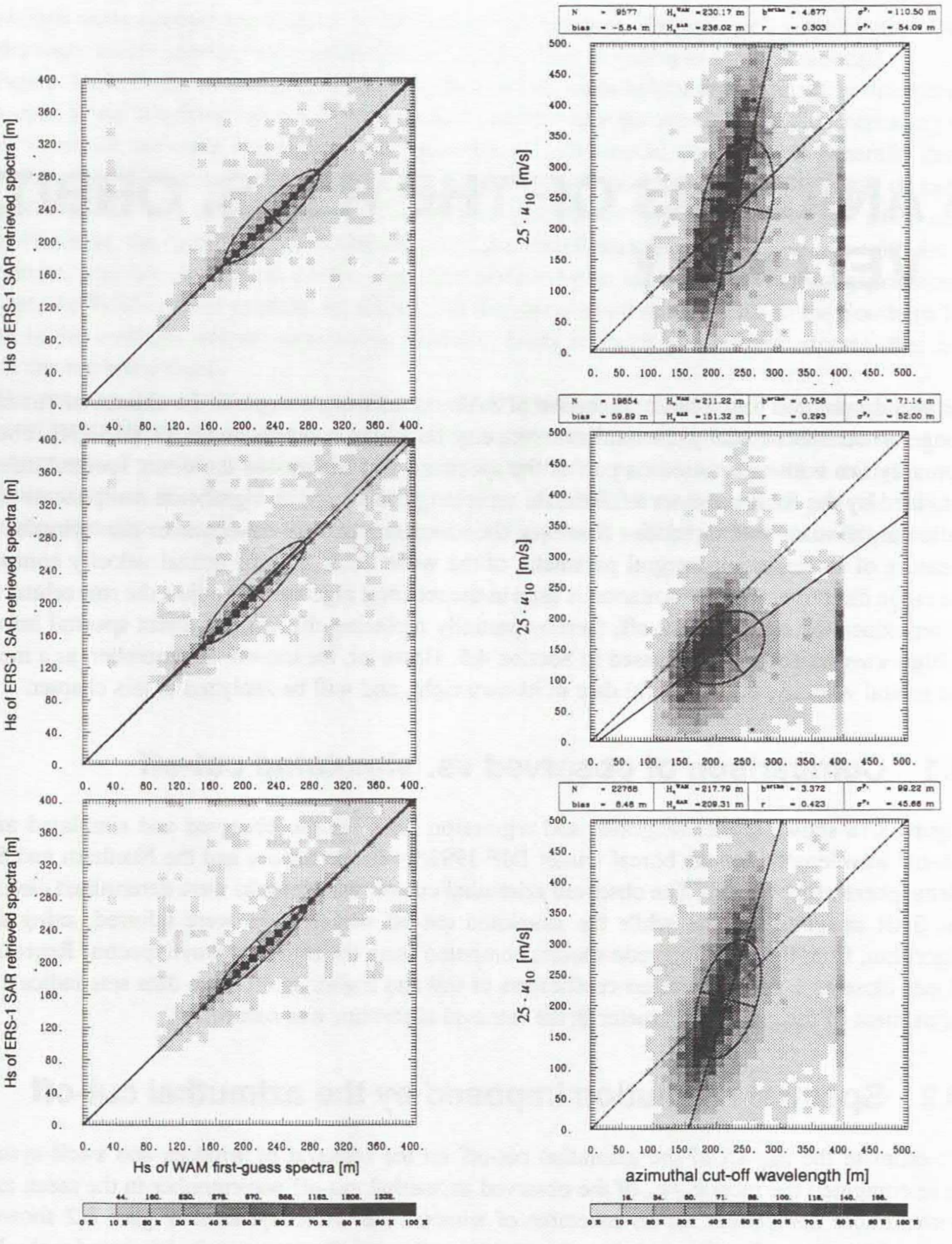

(a) (b)

Figure 8.1: Regression between observed and simulated azimuthal cut-off wavelengths (a), and between observed cut-off and $25 \cdot U_{10}$ (b). Top: NH Extra-Tropics; middle: Tropics; bottom: SH Extra-Tropics.

windsea / swell	*median*	*percent of waves with ratio $k_c/k_x > 1$*
N-Hem.	0.65 / 1.4	34 / 72
Tropics	0.5 / 1.85	28 / 78
S-Hem.	0.65 / 1.5	35 / 74

Table 8.1: Histogram characteristics of ratio of observed azimuthal cut-off wavenumber k_c to mean wavenumber component in the azimuth direction k_x.

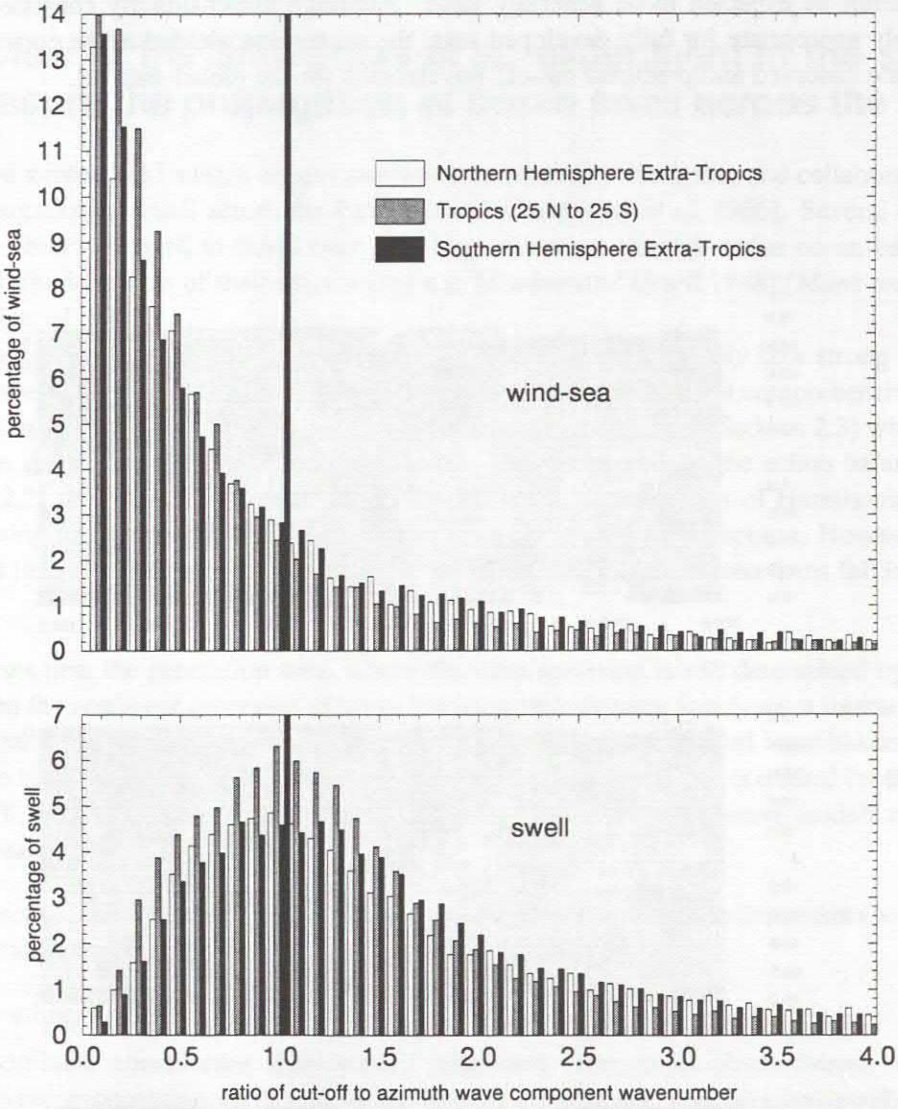

Figure 8.2: Histogram of windsea (top) and swell (bottom) systems with respect to the ratio k_c/k_x of the observed azimuthal cut-off wavenumber to the mean azimuthal wavenumber component. The data for the period DJF 1995/96 were divided into three ensembles for the NH Extra-Tropics (red), the Tropics between 25° N/S (blue) and the SH Extra-Tropics (green).

8.3 Global analysis of the cut-off

A global map of seasonal mean azimuthal cut-off wavelength λ_c for DJF 1995/96 is shown in Figure 8.3. High cut-off wavelengths corresponding to high rms orbital velocities are found, as expected, in the regions of high winds in mid-latitudes. In addition, a pronounced fetch effect is seen. Young windseas have higher energies at shorter wavelengths and therefore higher rms orbital velocities than well developed windseas. Thus the cut-off wavelength is significantly higher in the western parts of the mid-latitude ocean basins and in enclosed or partially enclosed seas such as the Baltic, Mediterranean, Gulf of Mexico and Carribian, the Bering Sea, or the seas south of New Guinea.

In view of the strong dependence of the orbital velocity on fetch a general expression relating λ_c alone to the wind velocity u_{10} at 10m height, for example in the form $\lambda_c = 25\,u_{10}$ [*Chapron et al.* 1995], cannot be expected to be generally valid. Although dimensionally consistent and therefore presumably appropriate for fully developed seas, the expression yielded a low correlation of 0.3-0.4 between the observed and predicted cut-off wavelengths for the global data set.

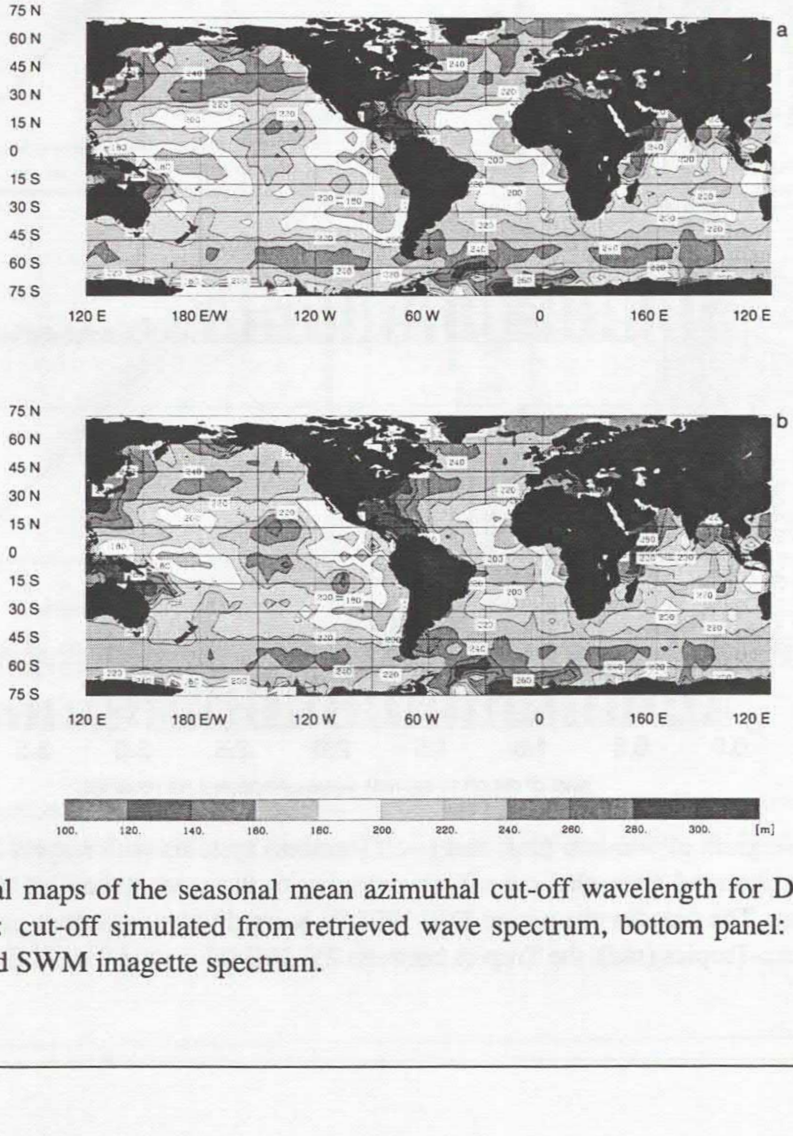

Figure 8.3: Global maps of the seasonal mean azimuthal cut-off wavelength for DJF 1995/96. Top panel: cut-off simulated from retrieved wave spectrum, bottom panel: cut-off from observed SWM imagette spectrum.

9 TRANS-OCEAN PROPAGATION OF SWELL

9.1 Review of the Snodgrass et al. experiment in the sixties to measure the propagation of ocean swell across the Pacific

During austral winter 1963 a large experiment was carried out by Snodgrass and collaborators to measure the propagation of swell across the Pacific ocean [*Snodgrass et al.* 1966]. Several observations indicated the ability of swell to travel over very large distances through entire ocean basins or even beyond the antipodal points of their origins (see e.g. [*Barber and Ursell* 1948];[*Munk and Snodgrass* 1957]; [*Munk et al.* 1963]).

The main goal of the experiment was to describe whether, and possibly how strong and by what mechanism swell was attenuated along its propagation path. At that time a comprehensive theory for resonant nonlinear interactions among ocean waves had just emerged (cf. Section 2.3) which was able to explain the generation of large wavelength swell. The framework of the action balance equation (cf. Section 2.2) permitted to view the propagation of swell as a problem of Hamiltonian dynamics of freely moving particles which propagate along great circle rays on the sphere. However, little was known at that time about the dissipation of ocean swell. The candidate mechanisms fall into two main categories:

1. Processes near the generation area, where the wave spectrum is still determined by the balance between the nonlinear processes of wave breaking and resonant wave–wave interactions. These nonlinear processes continue to be effective immediately after the wind input has ceased (or outside the storm area) but rapidly become weak. This transition regime is critical for the prediciton of swell, and its adequate representation in today's state-of-the-art wave models might still be inadequate.

2. Processes which attenuate freely propagating swell that has left the immediate vicinity of the generation area. They comprise

    - nonlinear resonant interactions among propagating wave groups
    - nonlinear nonresonant short-wave / long-wave interactions [*Hasselmann, K.* 1971] between propagating swell and locally generated windsea (e.g. windsea-swell interactions as the swell crosses the trade wind regions), by which the long waves modulate the short waves, making wave breaking more likely

No theoretical approach to describe wave breaking and short wave – long wave interactions was available in the early 1960's.

PROPAGATION OF OCEAN SWELL ACROSS THE PACIFIC

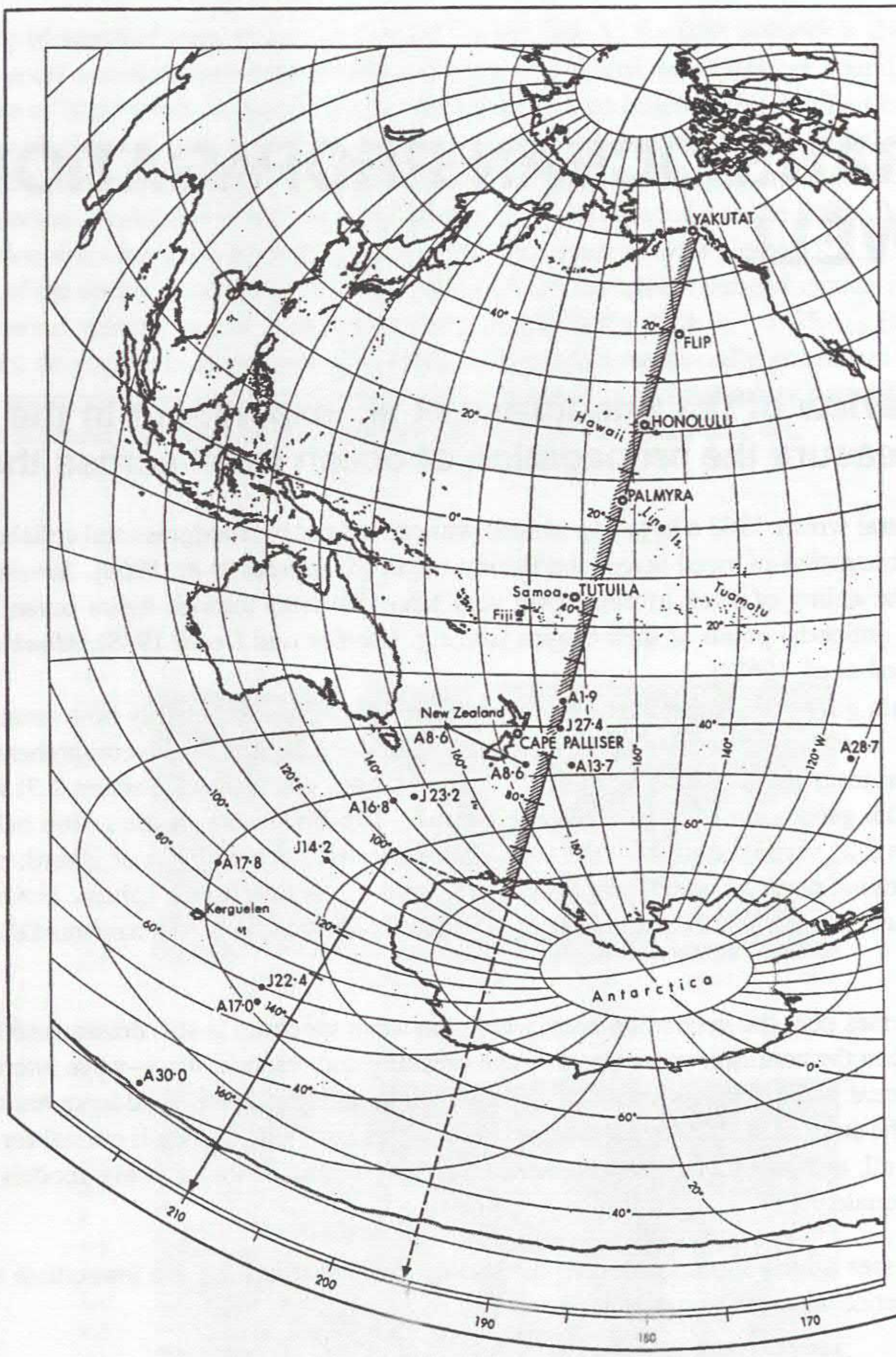

FIGURE 1. Great-circle chart based on Honolulu showing the location of the six wave instruments and of the principal storm sources. The 'reference great-circle' is in the direction 195·5° T from Honolulu; the Tasman window into the Indian Ocean bears 210° T. Distances from Honolulu are in degrees (1° = 60 nautical miles). Each storm is marked by a dot and its fractional date (J27·4 means 27 July, 9·6 h G.M.T.).

Figure 9.1: Taken from *Snodgrass et al.* [1966]

To infer the source of long swell and to estimate its travel time from the measured frequency frequency and directional measurements were essential. The approach of *Snodgrass et al.* [1966] was to concentrate on a great circle in the Pacific along which several wave stations were set up (see Figure 9.1). This reference great circle was chosen at an inclination of 195.5° with respect to Honolulu and connects regions of high storms east of New Zeeland with the coast of Alaska at Yakutat. In addition to originating in the region of abundant generation of long swell during austral winter the distance of this great circle segment is among the longest in the Pacific (135°). Wave stations in the tropical regions (Tutuila, Palmyra and Honolulu) enabled the estimation of the potential influence of the trade winds on the swell. Longer distances could have been achieved by considering the inter–basin propagation of swell generated in the Indian Ocean on a route into the Pacific between Australia and Antarctica. However, these routes are most likely to pass west of New Zealand through the Tasman Sea and are partly obstructed by the Fiji and Lau Islands. (Nevertheless, swell from the Indian Ocean was actually measured in Alaska, more than 180° away).

Snodgrass et al. [1966] were able to detect 12 principal events, five of which were analysed in detail. Their main results can be summarized as follows:

- For waves of wavelengths larger than roughly 280 m (corresponding to frequencies lower than 75 millicycles per second, mps) the swell attenuation was too low to be measured.

- For waves of wavelenghts between roughly 240 m (80 mps) and 280 m (75 mps) a weak attenuation is visible for large events, but again no detectable attenuation for moderate to small events.

- For wavelenghts below roughly 240 m (frequencies beyond 80 mps) waves disappear in the background field and identification of individual events is lost. The interpretation given in *Snodgrass et al.* [1966] is supported by our seasonal statistical analyses (Section 7.3). The mid-latitude storm belt witnesses frequent moderate storm events, particularly during austral winter, which maintain a higher frequency background field of swell. Severe storms occur more seldom, at intervals large compared to the storm duration, producing swell of low frequency which may easily be distinguished from the higher frequency background swell.

- No pronounced attenuation anomaly in the trade wind belt was found. Trade winds thus appear to have no effect on the swell.

- For most of the events shadowing of waves by intervening islands had to be taken into account and complicated the quantitative tracing of the propagation of energy. For some events shadowing was so important that farther stations along the trajectory could hardly record it.

- Finally, there was considerable lack of reproducibility in the attenuation measurements in that individual events differed from each other quite significantly. The findings of *Snodgrass et al.* [1966] therefore have to be considered as indicative rather than definitive.

In the following we re-address the issue of swell propagation over very large distances, however with the very different approach of using ocean wave spectra retrieved from ERS-1 SAR wave mode data. Although satellite data cannot provide continuous time series at specific locations they yield a global quasi-continuous coverage of the ocean enabling various stages of the travelling swell to be observed at various locations and different times.

9.2 Overview of the the present experiment

The period of our analysis extends over the austral summer June–July–August (JJA) 1995, during which the most severe storms are encountered in the Southern Hemisphere extra–tropical storm belt. The so-called 'roaring fourties' and 'fighting fifties' are the main generation areas of long ocean swell.

ERS-1 SAR wave mode data together with collocated WAM model data are at our disposal during this period. However, despite the spectral and directional information thus available to infer great circle paths and travel times, we decided to re-run an extended version of the WAM model which also computes the spectral wave age for each direction–frequency bin at all grid points [*Bauer et al.* 1996a] (cf. Section 3.2.3). These wave age spectra will be seen to add valuably in identifying the source locations of the swell.

The analysis is based on a case study of an extreme storm event in the Pacific, which, due to its basin geometry, supports the largest west–to–east oriented great circle sections. Actually, the reference great circle chosen by *Snodgrass et al.* [1966] represents an ideal choise. Various analyses will be performed to investigate this intra-basin propagation of swell.

Further cases of inter-basin propagating swell were analyzed. They included swell generated in the South Atlantic Ocean which then propagated into the tropical Indian Ocean and reached the coasts of Southeast Asia, as well as swell generated in the Indian Ocean southeast of Madagascar which at an inclination of about 130° to 150° passed between Australia and Antarctica and entered the Pacifc Ocean (either west of New Zealand through the Tasman Sea or east of New Zealand, depending mainly on the latitude and inclination of its source) to reach the Central to North American west coasts. However, as these cases yielded no significant additional insights, we have confined the analysis to the Pacific case as detailed feasibility study.

9.3 Satellite data, model simulations and spectral wave age

The satellite data belong to the set of three years of ERS-1 SAR wave mode spectral retrievals analysed in Chapter 5 and 7. Despite the quasi-continuous operation of the wave mode over the ocean a data gap exists between July 1 – 6, 1995 (further gaps occur on 95/06/25 and 95/07/10).

9.3.1 Model simulation

To avoid any spurious influence of the assimilation of ERS-1 altimeter significant wave heights, we re-ran the WAM model for the period JJA 1995. The set-up and the wind forcing was chosen identical to the operational configuration at ECMWF (see Section 3.2).

Although the re-analysed atmospheric data from the ERA project at ECMWF (see *Gibson et al.* [1997]) are meanwhile available, we chose the original initialised analysed data that are used in the ECMWF operational runs in order to estimate the influence of the assimilation on the statistical wave parameters presented in Chapter 7. Note that the ERA period covers the years 1979 to 1993, thus excluding our period of interest. Note also that the re-analysis should have little impact on the 1995 wind data, since the main aim of the ERA project was to produce a more homogeneous climatology through re-running the ECMWF AGCM (in the coarser T106 horizontal resolution) over a longer period of 25 years with a unique version of the ECMWF model and data assimilation set-up, frozen in its April 1995 configuration.

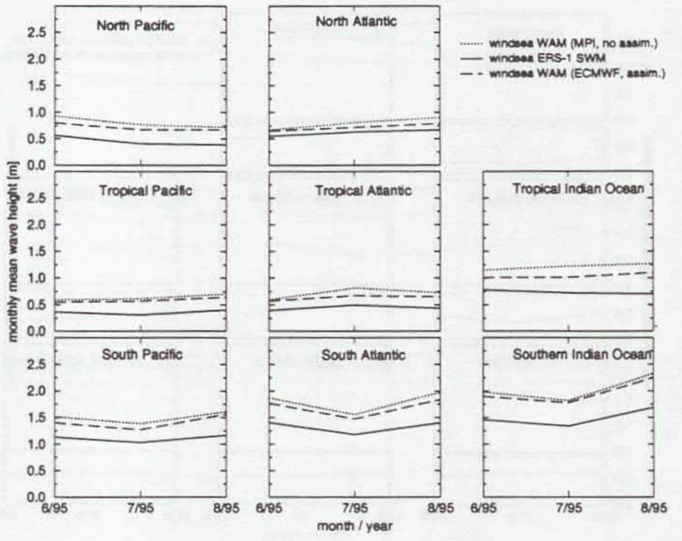

(a) windsea

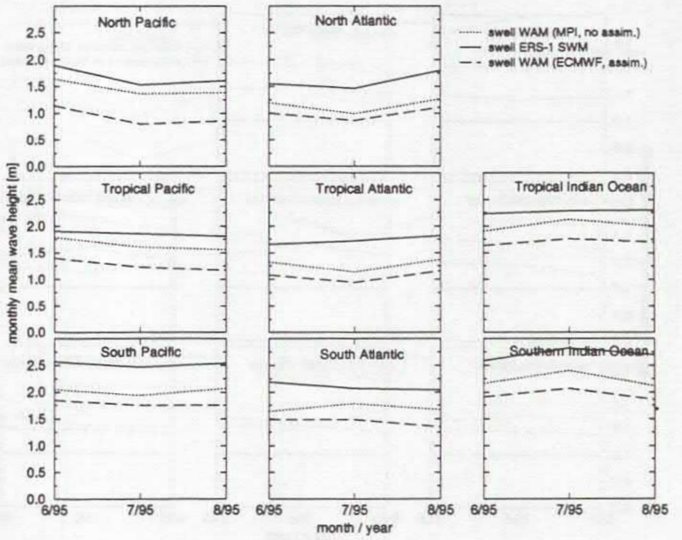

(b) swell

Figure 9.2: Time series of monthly mean windsea (a) and swell (b) wave heights for ERS-1 SWM (solid), WAM with assimilation (long dashed) and WAM without assimilation (dotted) in different ocean basins during JJA 1995.

9.3.2 Intercomparison of model simulations with and without assimilation

As a side exercise we intercompare the ERS-1 SWM retrievals with the model simulations performed at MPI without assimilation of ERS-1 altimeter data and with the operational WAM model runs at ECMWF, which are affected by the assimilation. The results are satisfactory in the sense that they confirm the qualitative conclusions drawn in Chapter 7. Here we focus on the behaviour of windsea and swell which were found in Chapter 7 to behave differently when compared to the ERS-1 SWM.

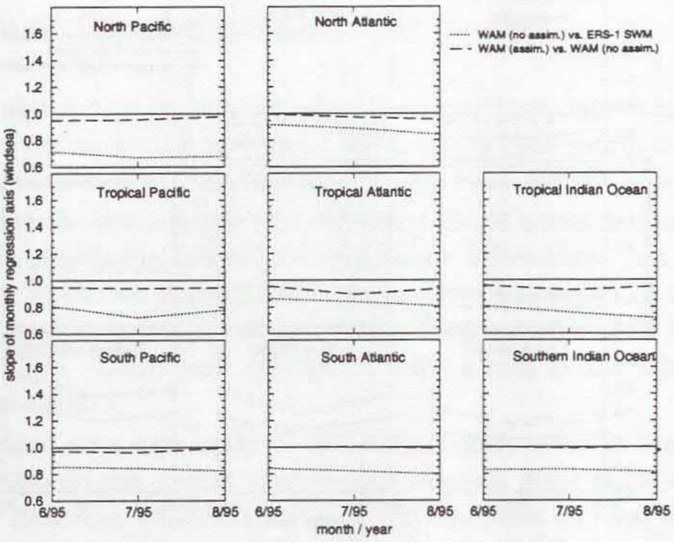

(a) windsea

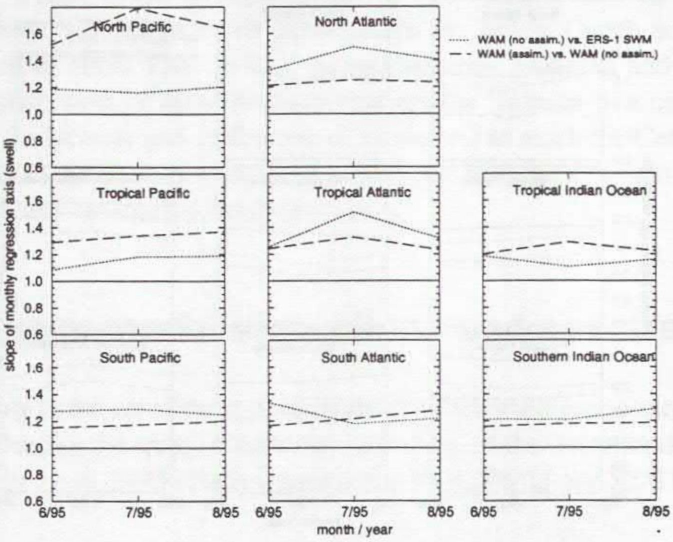

(b) swell

Figure 9.3: Slope of regression axis of wave heights between WAM without assimilation and ERS-1 SWM (dotted), and regression between WAM with and without assimilation (long dashed) for windsea (a) and swell (b).

Figure 9.2 depicts the three month time series (JJA 1995) of monthly mean windsea (a) and swell (b) wave heights in the same eight ocean basins that were considered in Sections 7.1 and 7.2. Solid curves refer to ERS-1 SWM, long-dashed curves to the WAM *with* assimilation and dotted curves to the WAM *without* assimilation. The qualitative findings of an overprediced windsea and an underpredicted swell by the WAM compared to the ERS-1 SWM are confirmed. The assimilation of ERS-1 altimeter significant wave heights only affects the magnitude of these discrepancies.

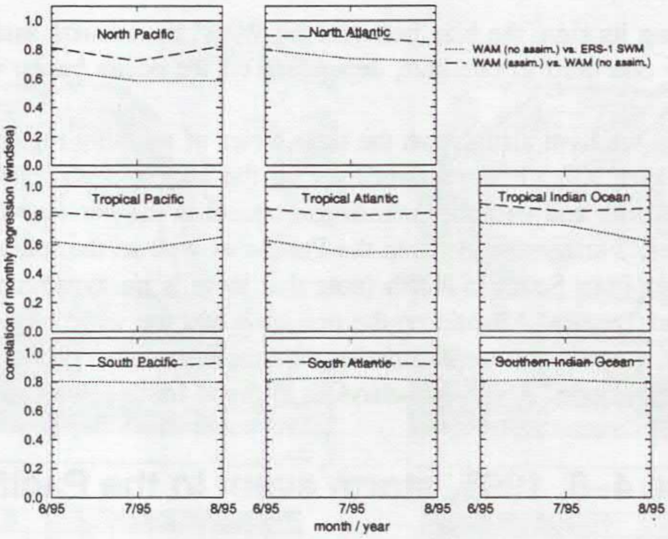

(a) windsea

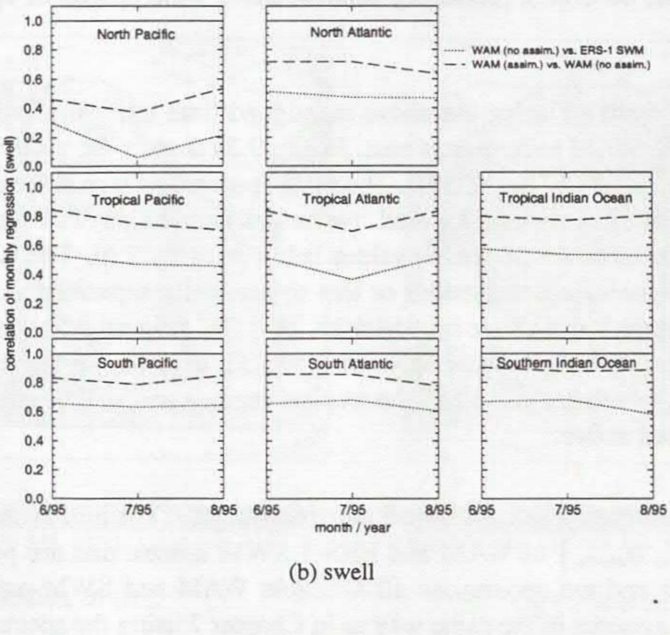

(b) swell

Figure 9.4: Same as Figure 9.3 for the regression correlation coefficient.

As was discussed in Chapter 6 the altimeter data are systematically low-biased since January 1994. As expected, both mean windsea and swell wave heighs of the WAM simulation without assimilation are found to exceed the ECMWF data. However, this effect is only marginal for windsea and more pronounced for swell. This can be readily attributed to the fact that swell covers a much larger area in the ocean than windsea and is more frequently corrected through assimilation than windsea. The optimal interpolation assimilation scheme implemented at ECMWF can only affect the windsea when the satellite passes the storm area at the right time, which is rather unlikely compared to the swell produced by the storm, which may be detected several days later at distant places.

While maintaining its sign, the bias between the WAM model *with* assimilation and the ERS-1 SWM is reduced by one third to one half, depending on the ocean basin, when running the model *without* assimilation.

For completeness we have also drawn the time series of monthly regression slopes (Figure 9.3) and correlations (Figure 9.4). It is noteworthy, that the largest deviations in swell slopes (Figure 9.3a) between WAM with and without assimilation occurs in the Pacific which supports the longest propagation distances. Furthermore, within the Pacific as well as the Indian ocean the deviation in swell slopes increases from South to North (note that there is no dynamical link between the wave field in the South and Tropical Atlantic on the one hand and the wave field in the North Atlantic on the other hand). This supports the conjecture that the longer swell has propagated, the more likely it is influenced by the assimilation. A similar behaviour is found for the swell correlations (Figure 9.4a).

9.4 The June 4–6, 1995, storm event in the Pacific

This case study features a storm event that built up on June 4 in the South Pacific region, southeast of Tasmania (145° E, 60° S). The low pressure system slowly propagated toward east by northeast (165° E, 55° S on 95/06/06, 06 UTC), producing southwesterly wind speeds of up to 20 m/s according to the ECMWF model.

The Pacific wave field During the above mentioned time interval wave heights exceeding 10 m were simulated by the WAM in the storm area. Figure 9.5a depicts the vector field of significant wave heights in the Pacific on 95/06/06, 00 UTC. The most apparent pattern is the pronounced storm centre, where wave heights of 12 m are encountered. Nevertheless, we also draw the reader's attention to the tropics where wave heights are limited to values below roughly 2 m. The wave field in the Northern and Southern Hemispheres are thus more or less dynamically separated at that time. The situation has changed completely 9 days later on 95/06/15, 00 UTC (Figure 9.5b). A northwest-to-southeast oriented ridge supporting wave heights between 2.8 to 3.5 m is visible some 1000 to 2000 km off the American continent, which has perturbed the tropical regions and will be seen to have its origin in the storm event mentioned above.

Selection of dynamically linked swell partitionings The aim in the following is to select a sample $\mathcal{S} = \{\mathcal{S}_{wam}, \mathcal{S}_{swm}\}$ of WAM and ERS-1 SWM spectra that are possibly connected to this storm event. To this end we decompose all available WAM and SWM-retrieved wave spectra into their principal wave systems in the same way as in Chapter 7 using the spectral partitioning algorithm ([HBHH] and Section 4.5). We then construct a grid of great circle rays (see e.g. *WAMDI Group* [1988] for the relevant equations on the sphere) whose origin is in front of the storm centre at 180° E, 45° S. The grid is drawn with an aperture of 100°, with lower azimuth angle of 20°. Now, all swell partitionings are selected whose directions are aligned to within ± 30° with the nearest great circle tangent. The resulting distribution of the sample elements throughout the Pacific is depicted in Figure 9.6 in an azimuthal equidistant projection. The sample of WAM swell systems consists of 2723 spectra, the SWM sample contains 1944 spectra (he spectra were selected regardless of whether the WAM and SWM spectra had mutual collocated spectra or not).

We have also indicated isolines of travel time and distance from the reference origin for a $\lambda = 400$ m swell whose group velocity is accordingly 12.5 m/s. The temporal and spatial increment between two consecutive isolines is is 20 h and 900 km, respectively. The last isoline is at 280 h and 12600 km. The wavelength chosen represents a first guess for the swell we are seeking. This first guess

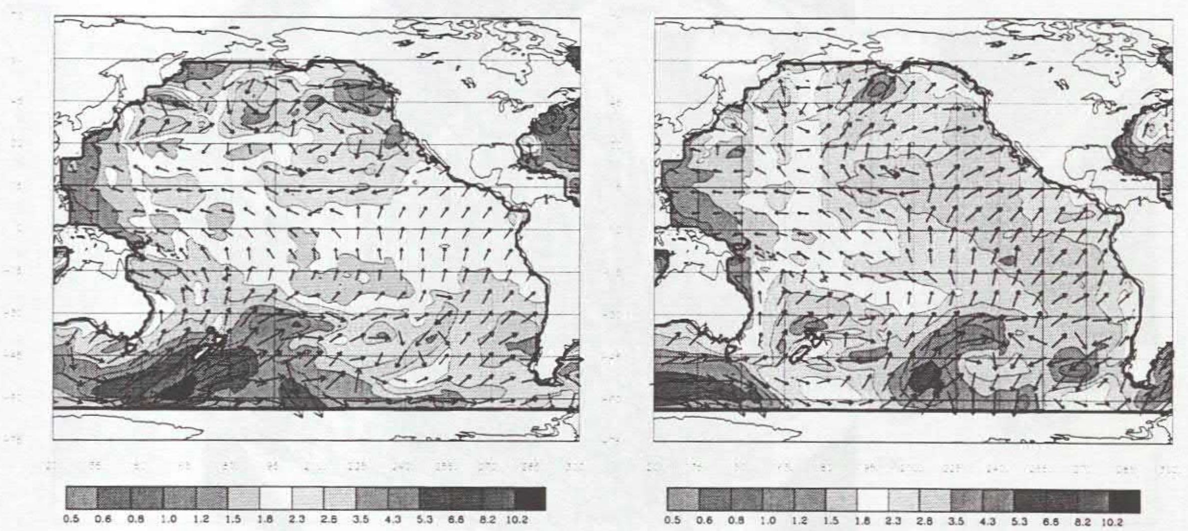

(a) H_s, 95/06/06, 00 UTC (b) H_s, 95/06/15, 00 UTC

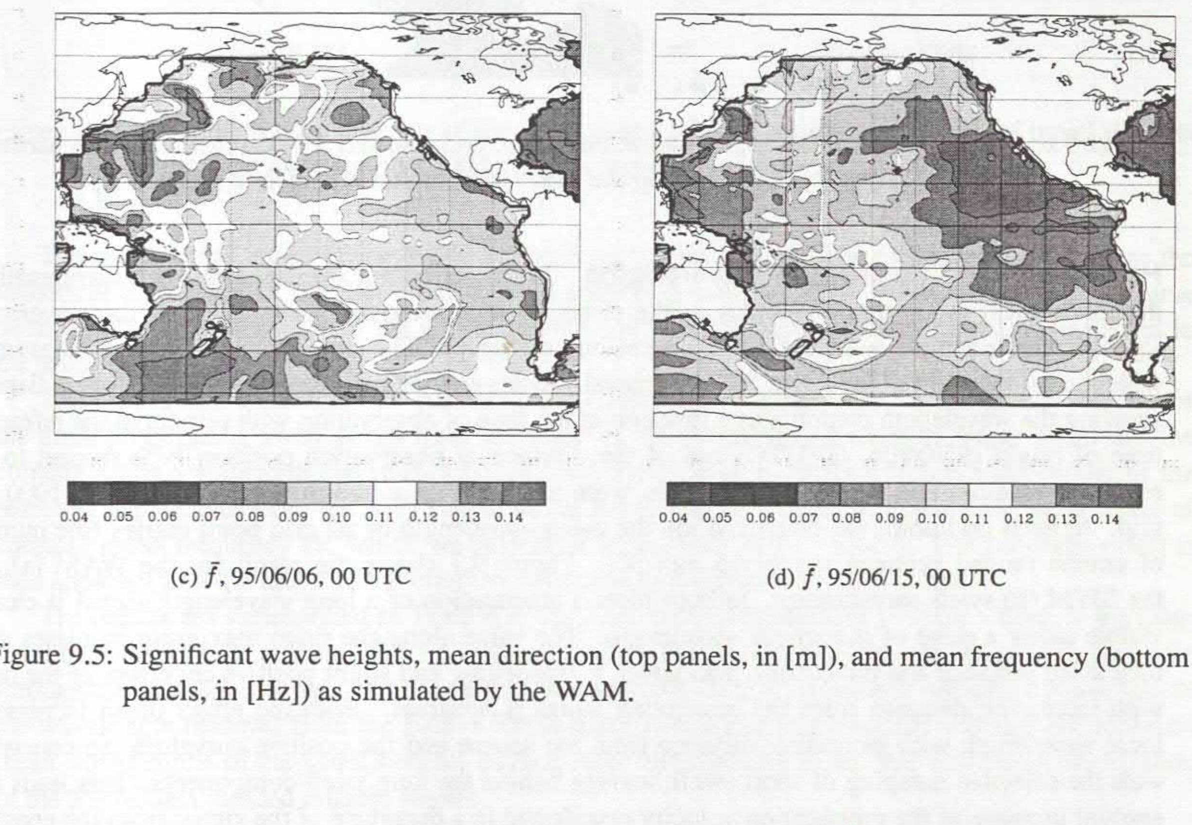

(c) $\bar{f}$, 95/06/06, 00 UTC (d) $\bar{f}$, 95/06/15, 00 UTC

Figure 9.5: Significant wave heights, mean direction (top panels, in [m]), and mean frequency (bottom panels, in [Hz]) as simulated by the WAM.

was obtained by a rough scanning through the selected ERS-1 SWM partitionings. A plot of SWM-retrieved and partitioned wave systems on 95/06/15 shows swell systems of roughly 440 to 480 m wavelength in the desired direction of the propagation grid, which are located on the ridge visible in Figure 9.5. A similar search within the corresponding WAM data set shows swell of roughly 350 to 390 m. However, no use is made of this wavelengths information (or alternatively, the travel time) at this stage.

Figure 9.6: Grid of great circles originating at the storm, and selected SWM-retrieved swell partitionings within two weeks following the storm. (azimuthal equidistant projection)

Hovmüller–type diagram of wavelengths In the following we determine the wavelength of the main swell group that originates in the storm by analyzing the propagation of the wavelength signal from the sample described in the preceeding paragraph. The aim is to obtain a spectral estimate which is independent of the direct SWM retrieval. To this end we construct a Hovmüller–type diagram showing the wavelength contours as a function of the time of observation with respect to the reference time of origin (95/06/06, 00 UTC) and of the distance of observation position with respect to the reference origin. The sample wavelengths were allocated on a two-dimensional 24 h × 1000 km grid. At each grid point we computed the the mean wavelength of all grid point entries (the number of entries ranged between roughly 5 and 30). Figure 9.7 shows the result for the WAM (a) and the SWM (b) swell partitionings. In both plots a propagation of a long wavelength signal is clearly visible along a ridge of maximum wavelength. The value along the ridge maximum increases with increasing distance and travel time. Moreover, a broadening and slight positive curvature of the ridge with increasing distance from the generating storm is apparent. Both the effect of an increase in local wavelength with increasing distance from the source and the positive curvature are consistent with the selective damping of short swell, leaving behind the long swell components. This leads to a gradual increase of the propagation velocity manifested in a departure of the signal from the constant slope, the latter being representative for a constant mean frequency of the wave group. The effect induced by the short swell is further amplified in the present diagrams through the presence of short background swell in the Southern Hemisphere, not related to the storm, but travelling in the direction of the considered signal. This background field "contaminates" especially those grid samples which are situated close to the sources. Again, the damping of the short swell with increasing travel distance contributes to the gradual emergence of the signal of the long swell in the course of propagation.

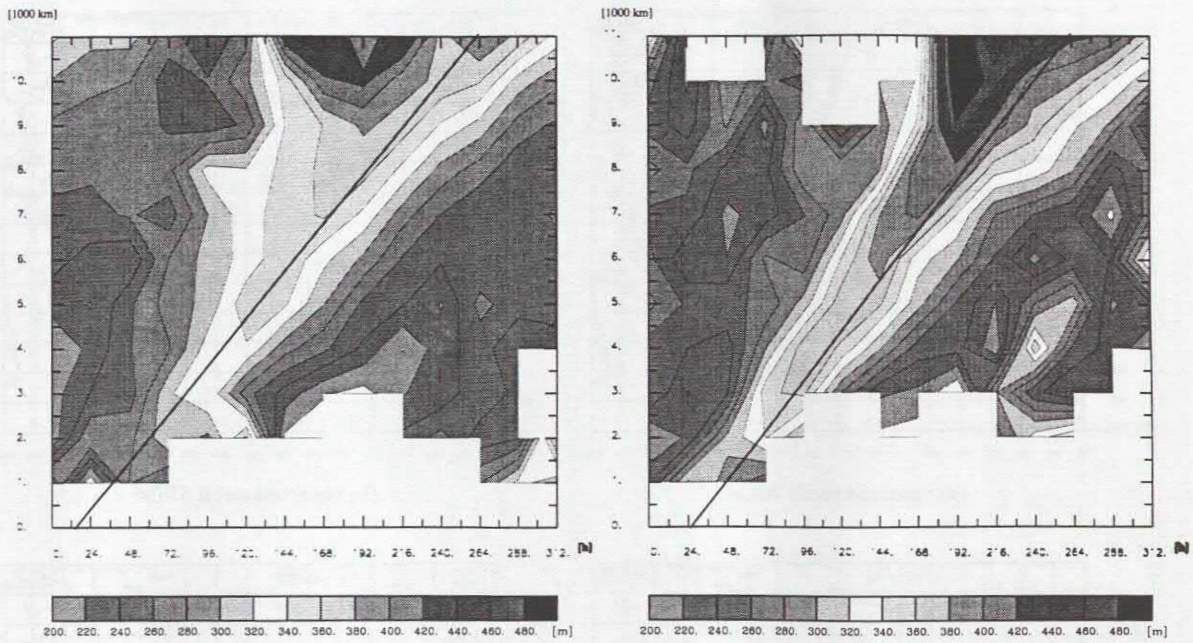

(a) WAM

(b) ERS-1 SWM

Figure 9.7: Hovmüller–type diagram of the propagation of wavelengths as function of travel time (in hours) and distance (in 1000 km) with respect to a reference origin.

The rather broad ridge of the WAM diagram compared to the SWM diagram is attributed to the numerical dispersion of the first order upwind advection scheme of the WAM model. For a coarse directional resolution of 30° of the global operational WAM model this effect cannot be neglected in the study of individual events.

The WAM and ERS-1 SWM contour plots enable the determination of the group velocity of the main propagating swell group from the slope of the maximum wavelength ridge. From this the corresponding wavelength can readily be inferred, yielding an estimate which is independent of the retrieved wavelength from the SWM data. In the following we assume a propagating swell group of constant mean frequency for which we determine its constant group velocity. The curvature effect is then apparent as a deviation of the effective disperion curve from the inferred line.

The results are summarized in Table 9.1. They are in close agreement with the values of the ridge maxima for the WAM and the ERS-1 SWM and confirm the first rough estimates obtained by scanning through the selected sample. As a side effect, we have obtained a simple and successful validation of the wavelength retrieval from the ERS-1 SWM data. The example shows that although the retrieved mean wavelengths of the swell systems deviate quite substantially from their first guess the retrieval of the SWM data yielded reliable results.

	slope (= group velocity)	*wavelength*
WAM (panel a)	12.1 m/s	375 m
ERS-1 SWM (panel b)	13.4 m/s	460 m

Table 9.1: Group velocity and wavelength inferred from main ridges in Figure 9.7

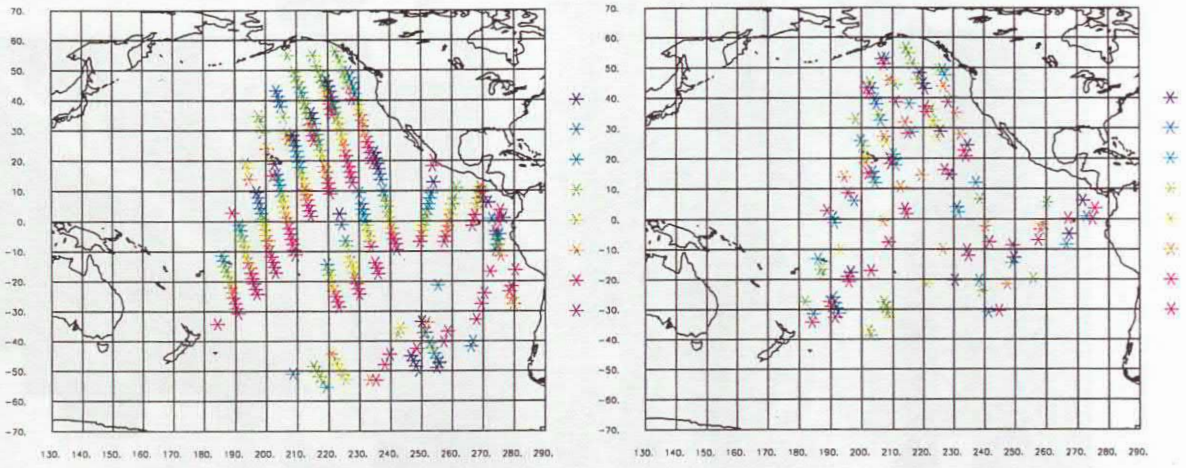

(a) observed swell WAM (b) observed swell SWM

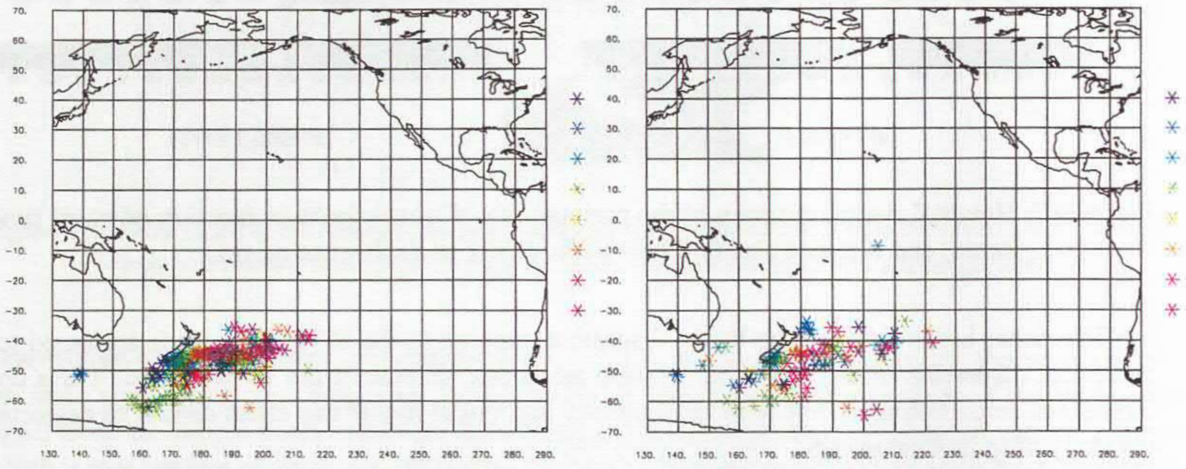

(c) swell origin WAM (d) swell origin SWM

Figure 9.8: Observed (top two panels) and origin (bottom two panels) positions of travelling swell for WAM (a),(c) and SWM (b),(d). Points are divided into 12 h intervals distinguishing times of origin inferred from spectral wave age. Uppermost color: 95/06/04, 00 – 12 UTC, lowermost color: 95/06/07, 12 – 24 UTC.

Ray tracing of swell to its origin using spectral wave age Coming back to our purpose of comparing the swell propagation as simulated by the WAM with the observed propagation we note as a first conclusion that the WAM model significantly underestimates the wavelength of the emerging swell. Possible explanations for this will be given below.

Using the above result concerning the expected WAM and ERS-1 SWM wavelengths we refine the sample $\mathcal{S}$ by discarding all wave systems whose wavelengths fall below 300 m, $\mathcal{S}' = \{s \in \mathcal{S} \,|\, \bar{\lambda}_s \geq 300\,\mathrm{m}\}$. We then compute the swell's great circle rays to their origins in space and time based on the spectral wave age, the position of observation, the observed direction and wavelength. The upper panels in Figure 9.8 depict the observed swell positions which are contained in $\mathcal{S}'$. The lower panels of Figure 9.8 show all source locations whose origins in time fall to within ± 2 days from

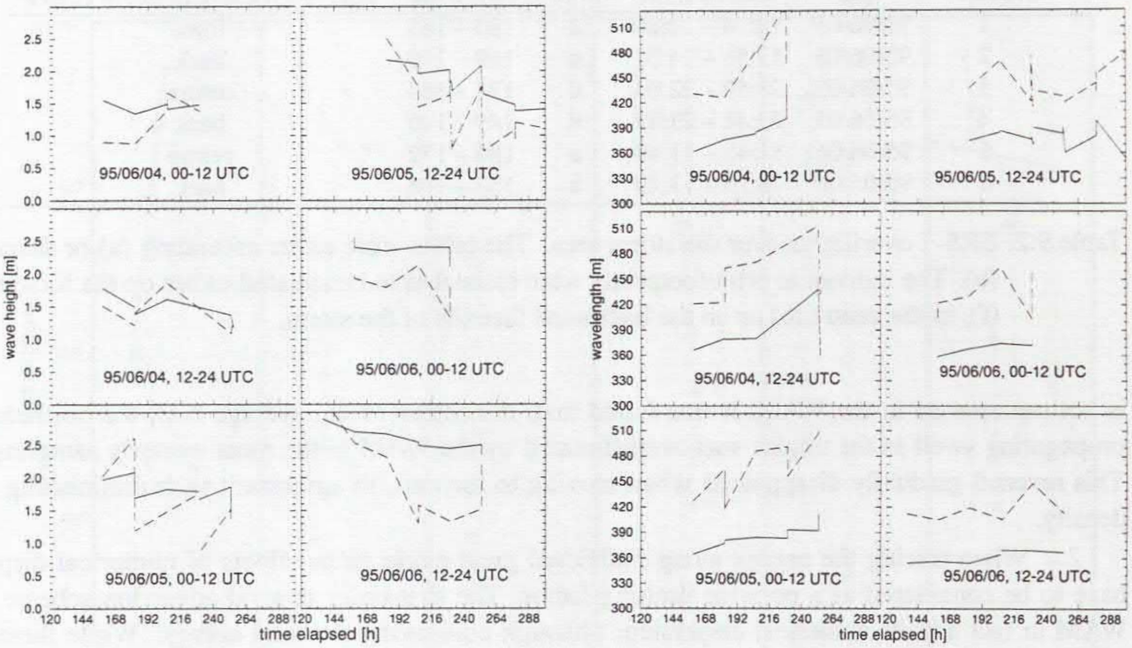

(a) swell wave height

(b) swell wavelength

Figure 9.9: Significant wave heights (a) and mean wavelengths (b) as a function of time with respect to reference origin for WAM (solid curves) and ERS-1 SWM (dashed curves). Different panels refer to different time intervals of swell origin.

the reference time 95/06/06, 00 UTC. The data were subdivided into 8 subsamples, distinguished by different colors, representing 12 h time intervals, the first between 00 – 12 UTC on 95/06/04, the last 12 – 24 UTC on 95/06/07. From the color coding the west-to-east shift of the generation area in the model data (c) is recovered, corresponding to the propagation of the storm centre. The figure clearly demonstrates that the spectral wave age is a very useful quantity to classify the emerging swell.

Time series of swell propagation In a final selection step we consider only model and SWM data which represent collocated pairs in the sample $\mathcal{S}'$. The remaining data were again stratified with respect to their time of origin. Figure 9.9 shows significant wave heights (panel a) and mean wavelengths (panel b) as a function of time with respect to the reference origin. Different subpanels refer to different source times of the swell systems (solid curves: WAM, dashed curves: SWM).

The H_s curves of the SWM data exhibit considerable fluctuations, whereas the WAM H_s remain fairly smooth and at more or less constant overall values. Abrupt "jumps" in the curves stem from data points of more or less successive recordings by the SAR. Several possible sources of the large scatter could be thought of:

1. As *Snodgrass et al.* [1966] have detailed, many islands in the Pacific serve as obstacles to certain trajectories. This hampers the task of a quantitative tracking of swell energy along its propagation path. It could also explain why nearby observations might substantially deviate in energy from each other, by noticing that one trajectory might have been obstructed by an island whereas the other has not. The statistical analyses in Section 7.4.2 suggest that part of this island shadowing

number	*day*	*time interval*	*orbit*	*longitude*	*position relative to storm centre*
1	95/06/05	12:14 – 12:20	a	180 – 165	front
2	95/06/05	13:56 – 14:01	a	149 – 140	back
3	95/06/05	21:59 – 22:04	d	174 – 164	centre
4	95/06/05	23:41 – 23:45	d	149 – 140	back
5	95/06/06	11:45 – 11:49	a	180 – 172	centre
6	95/06/06	13:25 – 13:29	a	158 – 148	back

Table 9.2: ERS-1 overflights over the storm area. The orbits were either ascending (a) or descending (b). The individual orbit footprints were estimated to be situated either on the forward face (f), in the centre (c) or on the backward face (b) of the storm.

is not represented in the WAM. It was found that, in contrast to the average bias, the northeastward propagating swell in the tropics was overestimated by the WAM in the most westerly sampling area. This reversal gradually disappeared when moving to the east, in agreement with diminishing island density.

2. When tracing the energy along individual great circle paths effects of numerical dispersion have to be considered as a possible limiting factor. The first-order upwind advection scheme in the WAM in fact admits numerical dispersion, although conserving the total energy. While these characteristics imply that the effect of numerical dispersion can be neglected when considering statistical properties over larger areas, the tracing of energy along individual rays calls for additional treatment to eliminate this dispersion. One possible approach could be to compute the advection on a rotated model grid in which the numerical dispersion along the selected great circle vanishes.

3. Given the remaining uncertainties in the data selection procedure the time series are still likely to be contaminated by data without dynamical link to the envisaged swell propagation.

4. Inaccurate quantitative SWM wave height as well as wavelength retrievals cannot be ruled out in principle. However, the validation of SWM against altimeter wave heights presented in Chapter 6 reveal a rather high confidence especially in the SWM swell retrievals.

The picture is clearer for the time series of wavelengths (Figure 9.9b). SWM wavelengths range from 420 to 500 m, persistently exceeding WAM wavelengths by 60 to 90 m. This agrees well with the results inferred from the Hovmüller-type diagrams.

We note here that the significant differences between simulated and observed wavelengths, which are a persistent pattern of the propagating swell once it has left the generation area, render the approach of comparing collocated data problematic. In the present case, the SAR sees a swell system that has travelled faster than the WAM by 1.4 m/s. Over a propagation distance of roughly ten days this accumulates to a spatial lag of roughly 1200 km, or, seen from a different perspective, the SWM swell reaches its destination at 10000 km distance about 24 h earlier than the WAM. The collocated data may thus point to different origins in time.

In summary, while the tracking of wave energy is hampered by several processes, the tracking of wavelength provides useful consistent insights. Lower WAM wavelengths suggest that the wind forcing provided by the ECMWF data is too weak compared to the actual wind conditions. This fits well into the picture of strongly underestimated winds in the Southern Hemisphere south of 50°, which we conjectured in the statistical analysis of the South Pacific (Section 7.4.2). Thus, while the validation of the storm event's wind speeds, which we shall attempt next, has to rely on a satellite cross-over just at the appropriate time, the analysis of the wave field which reproduces the impact of the storm over the order of ten days over the large area of the ocean is much more likely to "see the storm".

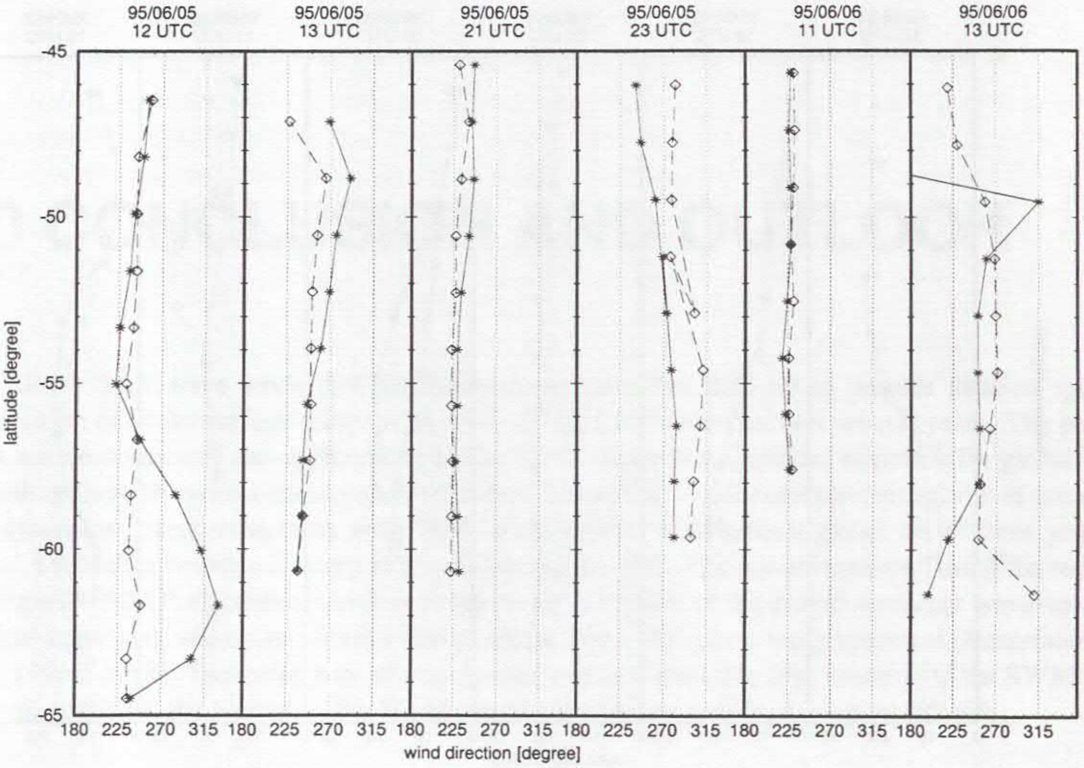

Figure 9.10: Wind direction inferred from the ERS-1 scatterometer (dashed line) and the ECMWF analysis (solid line) along 6 ERS-1 tracks over the storm area.

Analysis of the wind field in the storm region To confirm the hypothesis of a too weak wind forcing provided by the ECMWF analysis we consider the wind vectors retrieved from the ERS-1 wind scatterometer (WNS; cf. Section 4.2.4). We have estimated the storm area to be confined between 140° and 180° East and 45° and 70° South. Between 95/06/05, 0 UTC and 95/06/06, 18:00 UTC this area was overflown six times by ERS-1 (two further overflights occured between 21 and 23 UTC, but the storm had ceased by that time). The orbit characteristics are summarized in Table 9.2.

The wind directions and wind speeds are depicted in Figure 9.10 and 9.11, respectively, as functions of latitude along six ERS-1 tracks over the storm area. Dashed lines refer to ERS-1 scatterometer retrievals, solid lines to ECMWF analyses. According to Table 9.2 only overflights 3 and 5 had footprints passing close to the storm centre. This is confirmed in Figure 9.10 by noting that only these overflights are associated with wind directions of about 225°, i.e. wave propagation directions of 45° corresponding to the mean windsea direction. The other orbits generally exhibit higher angles.

The wind speeds (Figure 9.11) associated with overflight 3 are of the order of 20 m/s for both the WNS retrieval and the ECMWF analysis, the latter being slightly lower by 1 – 2 m/s. Orbit 5 exhibits large deviations, WNS wind speeds reaching extreme values of 29 m/s, one third larger than the ECMWF analysis. This is a clear evidence that the ECMWF analysis could not resolve peak values of the storm.

We note that for moderate wind speeds up to 20 m/s encountered during the remaining overflights 1, 2, 4 and 6 the picture is less clear. About half of the time the ECMWF analysis is slighty overestimated compared to the WNS winds, while half of the time the the opposite holds. However, none of these cases reaches values beyond 22 m/s, in contrast, to orbit 5, confirming that these overflights only passed close to the storm without hitting its centre.

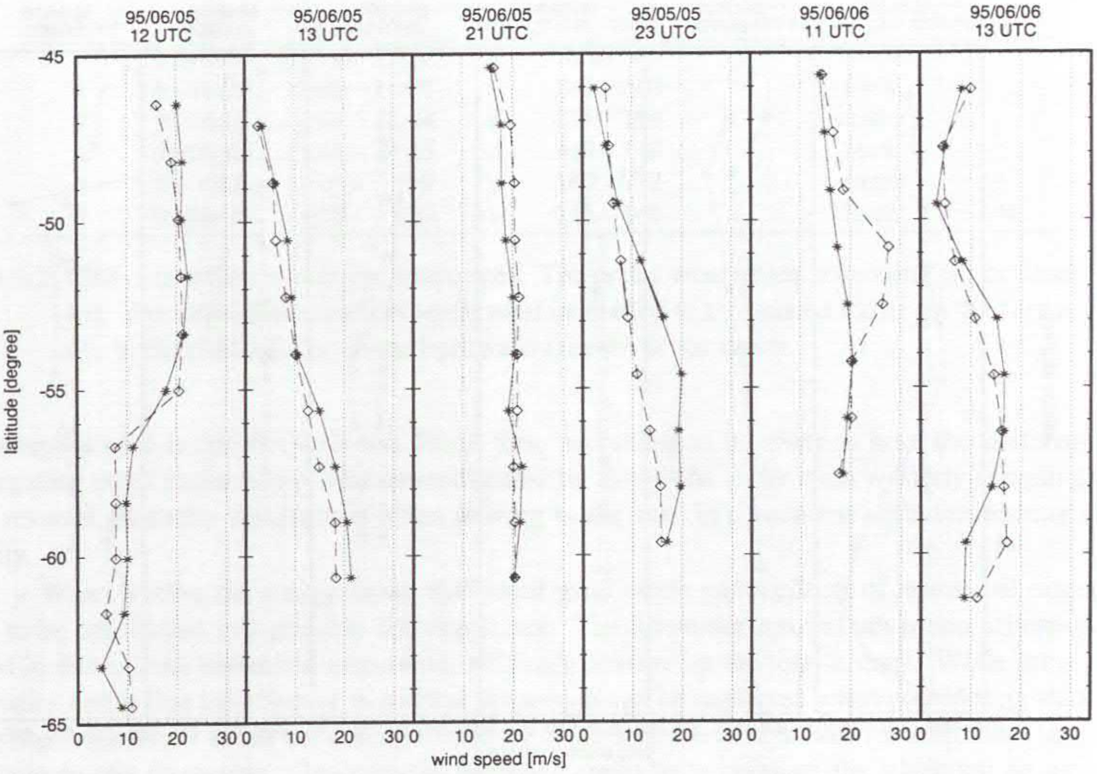

Figure 9.11: Same as Figure 9.10 for the wind speed

10 CONCLUSION AND OUTLOOK

The ERS-1 SAR wave mode (SWM) data represent the first data set to provide detailed spectral information of ocean surface waves with continuous global coverage over several years. The present work has demonstrated the applicability of the SWM ocean wave spectral retrievals for global wave modelling through various quality and performance analyses, validation exercises as well as statistical and dynamical intercomparisons with WAM model data. It features a global set of three years of ERS-1 SWM data between January 1993 and December 1995. These were retrieved using the recently developed WASAR algorithm which is based on the inversion of the closed nonlinear wave–to–SAR spectral transform, and on an iterative improvement of the first guess input spectrum [*Hasselmann, S. et al.* 1996a, 1998]. Two categories of conclusions can be drawn, the first referring to the SWM wave spectral retrievals, the second to the WAM model simulations and the driving wind fields.

10.1 Assessment of the ERS-1 SWM spectral retrievals

The different aspects of

- the SWM raw data quality,
- the fidelity of the ocean wave spectral retrieval algorithm WASAR, and its sensitivity with respect to the first guess input spectrum,
- the validation of significant wave heights by means of independent data provided by the TOPEX and ERS-1 altimeters,
- the analyses of the azimuthal cut-off length scales and their implication for the effective resolution of ocean waves

taken together yield a first comprehensive assesment of the value and applicability of the data, and their possible shortcomings. It is recommended that the analysis techniques developed here be carried out in the future at operational data analysis or forecasting centres. The following conclusions can be drawn:

1. Approximately 75% of the available SWM data yielded successful retrievals. This net return factor represented the product of two quality tests. About 12 % of the SWM data were rejected for data quality reasons related to too low signal-to-noise ratios or contaminations such as slicks or wind rows. The retrieval fidelity (defined in terms of the level of agreement between the observed SAR spectrum and the SAR spectrum computed from the retrieved wave spectrum) was accepted for roughly 85 % of the SWM data that passed the first test.

2. Iteration of the first-guess spectrum used as input for the inversion was found to have a significant positive impact on the fidelity of the retrievals. Tests with different numbers of iteration cycles suggest that one or preferably two iterations may represent a reasonable compromise in operational applications between computing costs and retrieval fidelity. For the present study we carried out five iterations and chose as the retrieval the inversion with the highest fidelity.

3. Sensitivity studies using modified first guess input spectra in the retrieval procedure showed only a weak residual dependence of the retrieved wave spectrum upon the first guess. The retrieval is largely decoupled from the input spectrum, particularly with the introduction of an iterative modification of the input spectrum in the improved algorithm of [HBHH]. The availability of cross spectra through ENVISAT in the near future will enable an ambiguity removal directly from the observed data (e.g. *Engen and Johnsen* [1995]). This information will make the SAR wave mode retrievals still less dependent on the first guess information.

   Nevertheless, the estimation of the high frequency part of the spectrum beyond the azimuthal cut-off still needs consideration. It is argued that, particularly for operational and data assimilation purposes, the use of a first guess from a wave model represents the best way to extract the high frequency energy content of the observed SAR spectrum through adjustment of the azimuthal cut-off. Alternative methods have been proposed by *Mastenbroek and de Valk* [1997], who estimate the windsea part of the spectrum by means of a parametrized spectrum. The wind vector is provided by the interlaced ERS-1 scatterometer measurement. However, this highly simplified "wave model" is unlikely to capture the complexity of open ocean windseas.

4. The overall agreement between SWM–retrieved and TOPEX and ERS-1 altimeter–derived H_s for the global collocated data pairs of 1994 is encouraging. So is the fact, that histograms of SWM-retrieved H_s fit well to a class of empirical distribution functions which were repeatedly confirmed to accurately reproduce global wave height distributions. This can be considered as a further confirmation of the overall retrieval performance under various SAR mapping regimes.

   The spectral information provided by the SWM-retrievals enabled a stratification of the collocated data pairs into subsets of pure windsea and pure swell cases. Deviations in the regression parameters could thus be partly related to spectral properties. SWM and altimeter–derived swell wave heights were in very good agreement. SWM–retrieved windsea wave heights were found to be underestimated. Several potential sources for the windsea discrepancy were envisaged, but no single reason could be isolated. Nevertheless, the following issues are suggested and merit closer inspection:

   - It might be suspected that the dependence of the windsea first guess spectrum prevails for large deviations between the WAM and the actual windsea. However, since the SWM wave heights were generally found to deviate also from the WAM wave heights, the first guess dependence can only occasionaly account for these deviations.
   - A stratification of the data also with respect to direction would reveal whether discrepancies occur more likely for the (very different) SAR mapping regimes of azimuth or range travelling waves. While the former is subject to the image smearing (cut-off) the latter might be affected by the more uncertain hydrodynamical MTF. First investigations suggest the deviations to occur more likely for range travelling waves. This may be a starting point for further investigations of the hydrodynamical MTF and its wind dependence. The rather low cotribution of azimuth travelling waves to the deficiencies indicates an overall good performance of the azimuthal cut-off adjustment of the retrieval algorithm.

- The scatter of the SWM vs. altimeter regression of pure windsea wave heights is comparable in magnitude to the scatter between TOPEX and ERS-1 altimeter wave height comparisons. The remaining uncertainties for high sea states, therefore, have to be, at least partly, attributed to uncertainties in the altimeter measurements. The present validation exercise can thus be viewed more as a cross-validation among all three instruments than as a pure validation against a calibrated reference data set. The SWM data may be further helpful in identifying deficiencies in altimeter–derived wave heights, for example, with respect to possibly incompletely understood return pulse shapes for complex sea states.

5. A different validation strategy addressing the SWM–retrieved wavelength of individual wave systems was presented in the context of dynamical analyses of individual swell propagation. The method consisted in tracking a signal along its propagation over larger distances using ERS-1 SWM data. In our case the signal was given by a propagating wave group of large wavelength. From a Hovmüller–type diagram the propagation (=group) velocity and thus the mean wavelength was inferred. This could then be compared with the locally retrieved wavelength from the SWM. In order to be detected as a propagating signal, the wavelength needed to be higher than the level of background swell wavelengths, which was found to be on the order of 200 m in the Pacific during austral winter. For the case study presented here, the validation was successful.

10.2 Assessment of the WAM model and the ECMWF wind fields

In the statistical investigations, the SWM retrieved data were analyzed together with the corresponding data computed with the ECMWF WAM model. The data were sub-divided into windsea and swell constituents, and were presented in the form of time series for different ocean basins, global maps for different seasons, and polar "wave rose" plots of directional energy distributions. In addition, results were presented for the dominant long-wavelength swell components and for the cut-off wavelengths of the SWM spectra (providing a measure of the rms orbital velocity). Dynamical comparisons for individual propagating swell were performed. The corresponding WAM spectra were re-computed for a three month period JJA 1995 to exclude the effect of assimilation of ERS-1 altimeter data. As a side exercise the impact of the assimilation on the statistical parameters could be assessed. Furthermore, the spectral wave age of *Bauer et al.* [1996a] was included in the model computations.

In evaluating the WAM model simulations, different effects from different superimposed processes need to be considered:

- errors in individual source functions
- errors in the balance between different source functions and in the nonlinear energy transfer
- errors in the large scale propagation
- errors in the wind field
- for operationally produced wave data, the impact of assimilating altimeter H_s

To distinguish between these processes, statistical as well as dynamical comparisons are needed, the former assessing obvious sources of deficiencies, the latter studying in detail the causes, or testing hypotheses suggested through the statistical analyses.

In the discussion of the intercomparison results, it was assumed that the retrieved spectra represented the "truth": all discrepancies between the retrieved and modelled data were attributed to the model. This assumption will need to be scrutinized more carefully as further data become available, but for the present state of knowledge it appears a reasonable assumption: it would be difficult to expain the various types of discrepancies for windsea and swell, different ocean regions and different propagation directions, in terms of a common error source in the SAR retrievals. The deviations between SWM and altimeter–derived windsea wave heights, discussed in Chapter 6, have no influence on the qualitative features of an underestimated WAM windsea. In fact, should the altimeter proove to be closer to the truth, this feature would be even more pronounced.

The retrieved and modelled data both confirm on a global scale the complexity of the spatial, temporal and spectral distributions of ocean wave energy. In view of this complexity, the general structural agreement between the modelled and retrieved spectra is encouraging. It has been demonstrated that this cannot be attributed to the use of a first-guess model spectrum in the retrieval algorithm.

The availability of global spectral data has made possible a more detailed analysis of the performance of the WAM model than has previously been feasible. Although the statistical analysis using the ECMWF WAM model data limits a quantitative assessment of the identified dynamical effects due to the continual assimilation of observed altimeter data in the ECMWF operational model, subsequent comparison with WAM model results without assimilation confirmed all qualitative conclusions as to the different behaviour of windsea and swell. These conclusions are summarized as follows:

1. The time series and regression parameters of significant wave height indicated a good overall agreement between modelled and retrieved spectra, with a small but systematic underestimation of H_s by the WAM model in all ocean basins.

2. The decomposition of the wave energy into windsea and swell components revealed that the net wave height underestimation by the model is due to an underprediction of the swell components by 20 to 30 %, the windsea being slightly overpredicted on average by about 10%. This holds with few exceptions throughout the three year period and for all ocean basins and seasons.

3. The relative windsea overprediction was found to be fairly constant, but slightly higher for high sea states in the mid-latitude winters, suggesting that either the wind dependence of the WAM input source term should be slightly reduced, or that the analyzed wind fields used to drive the model are too strong. The latter suggestion is in agreement with other findings of too strong ECMWF winds compared to ERS-1 scatterometer winds in the regions below latitudes of roughly 50° N/S [*Bentamy et al.* 1996, 1997]. A further confirmation comes from recent data assimilation studies [*Bauer et al.* 1996a]; [*Hasselmann, S. et al.* 1997]; [*Bauer et al.* 1997] in which wind field corrections were inferred from corrected wave fields. However, although these studies revealed the ECMWF winds to be too strong, they were based on single-case studies, thus needing confirmation from a larger representative ensemble.

   The storm event in the South Pacific featured in our case study prooved to be underestimated by the ECMWF wind analysis compared to ERS-1 scatterometer data. This again agrees with findings of *Bentamy et al.* [1996, 1997] who showed that beyond 50° S ECMWF wind fields fall off drastically compared to ERS-1 scatterometer winds. It supports the explanation of weak east to northeastward propagating WAM model swell in the statistical intercomparison in the Southern Pacific to be due to severely underestimated forcing wind fields.

4. In contrast to the fairly constant relative windsea bias, the negative swell bias increases in relative magnitude with decreasing swell wave height. We interpret this as reflecting a dependence

of the swell underprediction on the wave age, larger wave ages being associated statistically with smaller wave heights (wave age refers here literally to the travel time of the swell since emerging from the windsea generation region). A model error with this characteristic may be explained by a dissipation source term which is too large for low frequencies or not sufficiently nonlinear. Another possible explanation is an inadequate representation of the nonlinear transition from windsea to swell in the strongly simplified discrete interaction parametrization. However, this would not readily explain the increase of the swell error with decreasing wave height.

5. On average, modelled wavelengths were generally found to be in close agreement with the retrieved wavelengths. However, the dynamical study revealed that severely over- or underestimated wind fields also have an impact on the modelled wavelength. If, on average, the windsea energy is overestimated, but the swell wavelength is correctly represented, this indicates that the nonlinear windsea-swell transition process might not be adequately represented by the present parametrization of the Boltzmann integral. In conjunction with the preceeding point, it thus appears that that both effects of swell dissipation and nonlinear windsea-to-swell transition seem to influence the model performance.

6. Most of the temporal and spatial features of the wave field distributions could be explained by the general properties of the seasonally varying global wind system. The data for both windsea and swell exhibited a pronounced fetch dependence extending across entire ocean basins. This information is valuable for determining the transition of a growing windsea to a fully developed state, for which little data is otherwise available. Intercomparisons of retrieved and modelled fetch dependences suggest no systematic errors of the WAM model in this respect. Global maps of mean swell wavelengths and the wave heights of long swell, together with polar "wave rose" distributions of wave propagation directions, were useful in identifying the radiation emanating from the mid-latitude storm areas into distant regions.

7. Some discrepancies between modelled and retrieved swell data were detected in the radiation of long swell from the northern into the southern hemisphere, which appeared to be more effective in the model than observed. Again, definitive conclusions have to take the wind field into account. As was seen in the ECMWF vs. ERS-1 WNS wind comparisons (Figure 7.20), the ECMWF winds were more strongly overestimated with respect to the WNS in the northern hemisphere for the year 1994. This seems to have significantly altered also the overall level of swell energy.

8. The directional distributions of windsea and swell energies in different seasons were helpful in identifying evidences for deficiencies in the representation of the momentum transfer in current parametrizations. In fact, the direction of the observed windsea was found to deviate from the modelled windsea and thus from the wind vector. It was rotated towards the background swell travelling to within ± 90° in the wind direction. Also the swell direction was slighty rotated, which is to be expected as a consequence of the rotated windsea source. Thus, the wave field seems to carry a signature of the misalignment between the wind direction and the wind stress, recently observed by several workers (cf. Section 2.6). The modelling of the friction velocity u_* as collinear with u_{10} may thus have to be revisited.

9. The spectral wave age introduced by *Bauer et al.* [1996a] has proven to be valuable for the tracking of propagating swell. It enabled swell emerging from an individual storm event, and observed throughout the Pacific over a ten day period, to be traced back to the storm centre. The

dynamic comparisons, however, suffered from several handicaps which limited the quantitative tracking of swell energy along individual great circle rays. Among these were shadowing of swell propagation by intervening small islands, and numerical dispersion of WAM's propagation scheme which has to taken into account for individual propagation paths. Nevertheless, the wavelength yielded useful insights and enabled a comparison of the observed and the simulated dispersion relation for wave groups. A slight curvature of the dispersion curve within the Hovmüller-type diagram could be detected which is attributed to the selective damping of high frequency components within the propagating wave groups. The curvature may proove to be a useful information, complementary to the mean overall slope of the dispersion curve. A more detailed analysis of such dispersion curves derived from model and observational data might provide an alternative method to investigate wave damping as a function of wave frequency.

10.3 Perspectives

With the development of improved coupled ocean-atmosphere-wave models (see, for example, *Weisse and Alvarez* [1997]) and the continued increase in computing power, an accurate representation of the transfer processes across the moving air-sea interface is becoming increasingly more important. Wave models such as the WAM are an important tool for learning more about these transfer processes. Not only are these processes unavoidably affected by the waves, but the waves can also be considered as a several-day history of the interaction processes, stored the signature which the momentum transfer has imparted to the wave field, and which the wave field then advects away. An incorrect representation of these processes can therefore be much more easily identified from wave measurements than e.g. from wind measurements.

Inverse modelling tools such as the adjoint technique are currently being developed, which enable a dynamic consistent assimilation of data, or a dynamic consistent optimisation of model parameters from observations [*Komen et al.* 1994]; [*Barzel* 1994]; [*Hersbach* 1997a,b]; [*Giering and Kaminski* 1998]. These techniques are expected to yield further insights into the model performance, and to further resolve the different aspects of source function or wind field deficiencies.

Of course, reliable wave measurements are a necessary prerequisite for detecting and properly interpreting the above mentioned signatures and deficiencies. Every effort should thus be made to provide such data. Global satellite data from the SAR wave mode are also very valuable for generating long term wave spectral wave climatologies.

The statistical and dynamical analyses presented here enabled the identification of a number of discrepancies between the ERS-1 SWM and the WAM model data, pointing to various features and possible shortcomings of the WAM model or the forcing wind fields, which are worthy of investigation. In addition, more investigations are needed of a larger ensemble of individual wave events to resolve the complex interplay between the basic dynamical processes. For such detailed studies, the ERS-1/2 SWM system has provided and is still producing a unique global data base which will be hopefully continued and enhanced through the launch of ENVISAT scheduled for the year 2000.

A ERS-1 ORBIT, INSTRUMENT AND DATA SPECIFICATIONS

start	17 July 1991
altitude (nadir)	782 to 785 km polar orbit (sun-synchronous)
inclination	98.52°
orbit period	about 100 min ($\cong$ 14.3 orbits per day)
platform velocity	7455 m/sec
incidence angle	until 6/95: 19.9° at centre of imagette (right looking) after 6/95: 23.5°
antenna size	1 m (range) × 10 m (azimuth)
polarization	linear vertical (VV)
radar Bragg frequency	5.3 GHz, C band (5.6 cm)
imagette size	10 km (range) × 5 km (azimuth)
no. of pixels	600 (range) × 320 (azimuth)
pixel spacing	20 m (range) × 16 m (azimuth)
daily coverage	about 1100 spectra per day on average
product spacing	200 km along track (every 30 seconds)
cross-track resolution	1000 – 2000 km (depending on repeat cycle)
spectral grid	12 wavenumbers in logarithmic spacing corresp. to wavelengths between 100 m and 1000 m 12 directional sectors of 15° width (between 0° and 180°, anti-clockwise relative to azimuth)
intensity	8 bit (0 to 255) relative to maximum
number of looks	3 look incoherent averaging of single-look amplitude
SAR integration time	1.8 sec
R/v ratio	112 sec (R: distance SAR – target, v: platform velocity in orbit)

Table A.1: Some ERS-1 satellite and SAR instrument specifications

	start	end	repeat cycle	orbits per cycle	purpose
Phase A	91/07/14	91/12/10	3 days	43	commissioning
Phase B	91/12/14	92/04/01	3 days	43	ice
Phase C	92/04/14	93/12/21	35 days	501	multidisciplinary
Phase D	93/12/24	94/04/10	3 days	43	ice
Phase E	94/04/10	94/09/28	168 days	2408	geodetic
Phase F	94/09/28	95/03/21	168 days	2408	geodetic
Phase G	95/03/21	end	35 days	501	multidisciplinary

Table A.2: ERS-1 mission phases and repeat cycles; the satellite was switched off in June 1996 but is parked in orbit in a "sleeping" mode

B THE ERS-1 SAR WAVE MODE, WAM, AND COST FUNCTION GRIDS

Three different cartesian wavenumber, polar wavenumber or frequency/direction grids are involved in the retrieval process [*Hasselmann, S. et al.* 1998]:

- *The ERS-1 SAR wave mode grid* (k, θ)*:* The SWM spectra of the FDP are given on a polar wavenumber grid on a semi-disc and are composed of twelve 15° angular sectors between 0° and 180° running counter-clockwise relative to the satellite flight direction (azimuth) and $N_{swm} = 12$ wavenumbers corresponding to wavelengths between 100 m and 1000 m on a logarithmic scale:

$$k_{j+1} = 10^{1/(N_{swm}-1)} \cdot k_j \quad j = 1, \ldots, N_{swm} \quad \text{with } k_1 = \frac{2\pi}{100}\mathrm{m}^{-1}.$$

- *The WAM model grid* (f, θ)*:* The first guess WAM and the retrieved wave spectra are defined on a polar frequency/direction grid composed of 12 30° angular sectors between 0° and 360°, running clockwise relative to North, and $N_{wam} = 25$ frequencies corresponding to logarithmically spaced wavelengths between 9 m and 895 m, or frequencies:

$$f_{j+1} = 1.1 \cdot f_j, \quad j = 1, \ldots, N_{wam} \quad \text{with } f_1 = 0.04177\,\mathrm{Hz}$$

- *The cost function grid* (k_x, k_y)*:* Both the observed SWM image spectrum and the first guess wave spectrum are interpolated to a $N_{cart} \times N_{cart}$ cartesian wavenumber grid with $N_{cart} = 128$ and

$$k_x(j),\ k_y(j) = j \cdot \Delta k, \quad \text{with } -\frac{N_{cart}}{2} < j \le \frac{N_{cart}}{2} \text{ and } \Delta k = \frac{2\pi}{32}\,\mathrm{m}^{-1},$$

on which all computations (nonlinear mapping, cost function, etc.) are performed.

To properly account for the spectral smoothing incurred through the processing of the SWM imagette to the low-resolution polar wavenumber grid of the SWM FDP imagette spectrum, a smoothing filter is introduced whenever a SAR image spectrum is computed from a model spectrum. The filter is obtained by transforming the computed SAR image spectrum from the fine cartesian grid (k_x, k_y) to the coarse polar grid (k, θ) and subsequently interpolating back to the (k_x, k_y) grid, yielding a net smoothing of the simulated high-resolution SAR spectrum analogous to the treatment of the FDP [*Hasselmann, S. et al.* 1996a].

C THE REGRESSION ANALYSIS

In standard regression analysis, a straight line $y(x) = mx + a$ is drawn through a scatter plot of data pairs (x_i, y_i) with slope m and y-axis intercept a chosen such that the sum of the square differences $\sum_i (y_i - y(x_i))^2$ is minimized. Instead of this asymmetric definition of the square error in terms of the ordinate errors, we have fitted our regression line

$$y_i = b_{pca} x_i + a_{pca}$$

by minimizing the sum of the orthogonal distances of the data points from the regression line. The extreme values of this quantity yield the major and minor axes of the covariance ellipse. The method is not only symmetric with respect to an interchange of x and y but is also invariant with respect to rotations in the x, y-plane [*Preisendorfer* 1988]; [*Bauer et al.* 1992]; [*Bauer and Staabs* 1998]. The slope b_{pca} is given by

$$b_{pca} = \tan\phi, \quad \text{where} \quad \tan 2\phi = \frac{< 2xy >}{< x^2 > - < y^2 >},$$

and $< . >$ denotes the average over the data ensemble. The angle ϕ as defined above is actually not invariant with respect to an interchange of x and y, which yields $\phi \rightarrow \phi + 90°$. The correct solution yielding the major rather than the minor ellipse axis can be determined by comparing the square errors for the two solutions.

The principal components are defined by the first and second eigenvalue of the data covariance matrix The eigenvalues $\sigma^2_{p1,p2}$ are equivalent to the variances along the major and the minor principal axes, respectively. The principal variances $\sigma^2_{p1}, \sigma^2_{p2}$ are given by

$$\left.\begin{matrix}\sigma^2_{p1}\\ \sigma^2_{p2}\end{matrix}\right\} = \frac{1}{2}\left\{(s_{xx} + s_{yy}) \pm \left[(s_{xx} - s_{yy})^2 + 4s^2_{xy}\right]^{\frac{1}{2}}\right\} \tag{C.1}$$

where s_{xx}, s_{yy} and s_{xy} denote the variances of x, y and the covariance of x and y, respectively. The ratio σ_{p1}/σ_{p2} may be interpreted as a measure of the signal-to-noise ratio.

The use of two regression parameters a_{pca} and b_{pca}, however, makes it more cumbersome to intercompare the effective calibration of two data sets. We have therefore restricted the regression line in our analyses of Chapter 7 to pass through the origin, $a_{pca} = 0$. Comparisons with adjustable intercepts have shown that these in fact have little influence. In contrast, both regressions with adjustable and fixed intercepts are shown in Chapter 6 as the differences were more pronounced. The origin of this discrepancies is attributed to some residual nonlinearity in the bivariate data set.

The only exception to our orthogonal regression approach is in the scatter diagram of Figure 5.6 comparing the retrievals for a modified and non-modified input spectrum. Here we resorted to the standard non-symmetrical regression analysis, as this yielded a more realistic line passing through the maxima of the distribution.

D ABBREVIATIONS AND ACRONYMS

ABL	atmospheric boundary layer
ADEOS	Advanced Earth Observing Satellite
AMI	active microwave instrument
ATSR	along–track scanning radiometer
CEOS	Committee on Earth Observation Satellites
CERSAT	Centre ERS d'Archivage et de Traitement, Plouzané, France
CFL	Courant Hilbert Lewy stability criterion
CNES	Centre National d'Etudes Spatiales (France)
COARE	Coupled Ocean–Atmosphere Experiment
DFD	Deutsches Fernerkundungs-Datenzentrum, Oberpfaffenhofen, Germany
DJF	December – January – February
DKRZ	Deutsches Klimarechenzentrum, Hamburg, Germany
DLR	Deutsches Zentrum für Luft– und Raumfahrt, Oberpfaffenhofen, Germany
DWD	Deutscher Wetterdienst, Offenbach, Germany
ECMWF	European Centre for Medium–Range Weather Forecasts, Reading, UK
ERA	ECMWF Re-Analysis project
ERS-1	European Remote Sensing satellite
ESA	European Space Agency
ESRIN	European Space Research Institute, Frascati, Italy
ESTEC	European Space Research and Technology Centre, Noordwijk, NL
FDP	fast delivery product
FPN	Forschungsplattform Nordsee
GCM	general circulation model
GKSS	Gesellschaft für Kernenergie in Schiffbau und Schiffahrt, Geesthacht, Germany
GOES	Geostationary Operational Envirnonmental Satellite
GTS	global telecommunication system
HEXMAX	Humidity Exchange over the sea Main Experiment
HEXOS	Humidity Exchange over the Sea Experiment
IFM	Institut für Meereskunde der Universität Hamburg, Germany
IFREMER	Institut Français de Recherche pour l'Eploitation de la Mer, Brest, France
ITCZ	inter–tropical convergence zone
JERS	Japanes Earth Resource Satellite
JJA	June – July – August

JONSWAP	Joint North Sea Wave Project
JPL	Jet Propulsion Laboratory, Pasadena (USA)
KNMI	Koninklijk Nederlands Meteorologisch Instituut, De Bilt, NL
LBR	low bit rate
LEWEX	Labrador Sea Waves Extreme Waves Experiment
MAM	March – April – May
MARS	Meteorological Archive and Retrieval System
MARSEN	Marine Remote Sensing project
MBLEX	Marine Boundary Layer Experiment
MPI	Max-Planck-Institut für Meteorologie, Hamburg, Germany
NASA	National Aeronautics and Space Administration
NASDA	National Space Development Agency of Japan
NDBC	National Data Buoy Center
NESDIS	National Environmental Satellite, Data and Information Service
NH	Northern Hemisphere
NOAA	National Oceanographic and Atmospheric Administration
NRCS	normalized radar backscattering cross-section
NSCAT	NASDA scattering measurement device
NWP	numerical wheather prediciton
PBL	planetary boundary layer
PCA	principal component analysis
PIK	Potsdam-Institut für Klimafolgenforschung, Potsdam, Germany
RADAR	radiowave detecting and ranging
RAR	real aperture radar
RSMAS	Rosenstiel School of Marine and Atmospheric Science, Miami, USA
SAR	synthetic aperture radar
SAXON	Synthetic Aperture Radar and X-Band Ocean Nonlinearities
SH	Southern Hemisphere
SON	September – October – November
SWADE	Surface Wave Dynamics Experiment
SWAMP	Sea Wave Modeling Project
SWAPP	Surface Waves and Processes Program
SWM	ERS-1 SAR Wave Mode
TAO	Tropical Ocean Atmosphere moored buoy array
TKE	turbulent kinetic energy
TOGA	Tropical Ocean Global Atmosphere program
UKMO	United Kindom Meteorological Office, Bracknell, UK
UWA / UWI	user wave / wind product
WAM	wave model
WAMDI	wave model develpment and implementation group
WASA	wa and storms in the North Atlantic
WASAR	ocean wave retrieval from SAR image spectra
WBL	wave boundary layer
WKB	Wentzel, Kramers, Brillouin approximation
WMO	World Meteorological Organization, Geneva, CH
WNS	wind scatterometer

E DICTIONARY OF SOME TECHNICAL TERMS

action	Wirkung
azimuth	Koordinate längs der Flugrichtung
bias	Differenz zweier Mittelwerte
boundary layer	Grenzschicht
bouyancy	Auftrieb
current	Strom
drag coefficient	Reibungsbeiwert
duration	Windwirkdauer
eddy	Wirbel
fetch	Windwirklänge
first guess input spectrum	Eingangsspektrum erster Schätzung
gust	Bö
inviscid fluid	ideales (reibungsfreies) Fluid
irrotational	wirbelfrei
flow	Strömung
flux	Fluß
momentum	Impuls
orbit	Umlaufbahn
range	Koordinate quer zur Flugrichtung
remote sensing	Fernerkundung
roughness length	Rauhigkeitslänge
spaceborne	satellitengestützt
spectral partitioning	spektrale Zerlegung, spektrales Teilsystem
swell	Dünung
synthetic aperture radar	Radar mit synthetischer Apertur
viscosity	Zähigkeit
wind sea	Windsee
wind stress	Windschubspannung

DANKSAGUNG

Besonderer Dank gilt Klaus Hasselmann für die Überlassung des Themas, seine umfangreiche Betreuung und sein Vertrauen. Äußerst motivierend waren sein eigener Einsatz und seine Flexibilität, trotz häufiger Arbeitsüberlastung stets Zeit für Gespräche zu finden. Die von ihm vorgelegte Denkgeschwindigkeit führten zuweilen zu Selbstzweifeln bei dem Betreuten, welche jedoch dank der bereitwillige Beantwortung zahlloser Fragen durch den Betreuer begrenzt blieben.

Ebenso danke ich Susanne Hasselmann für die offene und herzliche Zusammenarbeit. Dank ihrer beharrlichen Anleitung habe ich viel über den Umgang mit umfangreichen Programmen und Daten gelernt. Die zahlreichen Diskussionen fachlicher Art, aber auch die Gespräche über Vieles was uns bewegt, waren mir sehr wertvoll.

Eva Bauer vom PIK danke ich für die gute und freundschaftliche, auch über größere Distanzen hinweg effiziente Zusammenarbeit sowie die zahlreichen Diskussionen. Nicht nur die "B"s, auch das Rheinland dominierte zeitweilig die Seegangsgruppe: Mit Georg Barzel verbindet mich eine Zeit offener und freundschaftlicher Zusammenarbeit. Er war mir u.a. ein wertvoller Gesprächspartner für Fachliches und Vieles darüber hinaus. Ebenso danke ich Renate Brokopf für ihre herzliche und vielfache Unterstützung, ihre stete Geduld bei der Einarbeitung in die Software und bei der Lösung zahlreicher Probleme. Christian Bennefeld und Maurice Toporek danke ich für die lockere und dennoch effiziente Zusammenarbeit. Susanne Lehner vom DFD/DLR danke ich für ihre engagierte Unterstützung bei vielen spannenden und ereignisreichen Konferenzen.

Am Institut wurde die Zeit versüßt durch die Freundschaft von Victor Ocaña, Marisa Montoya und Ulrich Kilian. Mit Axel Timmermann habe ich mich in vielen schönen Gesprächen verloren (cf. die Kefir-Gänge). Für ihre Motivation, gemeinsam den Blick über den eigenen Tellerrand zu wagen, danke ich Thomas Kaminski, Christian Eckert und Marco Giorgetta.

Björn Hansen vom EZMW danke ich für die Extraktion umfangreicher Satelliten- und Modelldaten. Ebensolches gilt für Klaus Arpe vom MPI für die Beschaffung von Windfeldern sowie für Christoph Staabs vom IfM für die Bereitstellung von Altimeter- und Scatterometerdaten. Marion Grunert und Norbert Noreiks gilt mein Dank für ihre vielfältige und unkomplizierte Hilfe bei der Anfertigung von Graphiken, sowie Carola Kauhs für die Beschaffung ausgefallener Literatur. Dank auch dem Beratungsteam des DKRZ für die Hilfe bei Software-Problemen und den Mitarbeiterinnen und Mitarbeitern des MPI für das außergewöhnlich gute Arbeitsklima.

Ich danke Werner Alpers vom IfM für seine Bereitschaft, das Zweitgutachten für diese Arbeit anzufertigen.

Nicht unerheblichen Beitrag zur Weckung meiner wissenschaftlicher Neugier haben u.a. Helga Teichmann, Fritz Zilliken und Günther Knackstedt geleistet.

Frauke Molter-Bock danke ich für ihre Liebe und die vielen wundervollen Erlebnisse und Entdeckungen, die wir gemeinsam unternommen haben.

Diese Arbeit wäre nicht entstanden ohne den Einsatz meiner Mutter, der mit den Attributen mutig und liebevoll nur andeutungsweise beschrieben werden kann.

Bibliography

Alpers, W. [1983], 'Monte Carlo simulations for studying the relationship between ocean wave and synthetic aperture radar image spectra', *J. Geophys. Res.* **88**, 1745–1759.

Alpers, W. and K. Hasselmann [1978], 'The two–frequency microwave technique for measuring ocean–wave spectra from an airplane or satellite', *Bound. Layer Meteorol.* **13**, 215–230.

Alpers, W. and K. Hasselmann [1982], 'Spectral signal-to-clutter and thermal noise properties of ocean wave imaging synthetic aperture radars', *Int. J. Remote Sensing* **3**, 423–446.

Alpers, W. and C.L. Rufenach [1979], 'The effect of orbital motions on synthetic aperture radar imaging of ocean waves', *IEEE Trans. Antennas Propag.* **AP-27**, 685–690.

Alpers, W., C. Brüning and K. Richter [1986], 'Comparison of simulated and measured synthetic aperture radar image spectra with buoy-derived ocean wave spectra during the Shuttle Imaging Radar-B mission', *IEEE Trans. Geosci. Remote Sensing* **24**, 559–566.

Alpers, W., D.B. Ross and C.L. Rufenach [1981], 'On the detectability of ocean surface waves by real and synthetic aperture radar', *J. Geophys. Res.* **86**, 6481–6498.

Atanasov, V., W. Rosenthal and F. Ziemer [1985], 'Removal of ambiguity of ambiguity of two-dimensional power spectra obtained by processing ship radar images of ocean waves', *J. Geophys. Res.* **C90**, 1061–1067.

Backus, G.E. [1962], 'The effect of the earth's rotation on the propagation of ocean waves over long distances', *Deep Sea Res.* **9**, 185–197.

Bacon, S. and D.J.T. Carter [1991], 'Wave climate changes in the North Atlantic and North Sea', *Int. J. Climatol.* **11**, 545–558.

Bamler, R. and B. Schättler [1993], SAR Geocoding: data and systems, *in* G. Schreier, ed., 'SAR data aquisition and image formation', Herbert Wichmann Verlag, Karlsruhe (Germany), pp. 53–102.

Bao, M. and W. Alpers [1996], 'On the cross spectrum between single-look synthetic aperture radar images of ocean waves', *IEEE Trans. Geosci. Remote Sensing*. submitted.

Bao, M., C. Brüning and W. Alpers [1994], A generalized nonlinear ocean wave – SAR spectral integral transform and its application of ERS-1 SAR ocean wave imaging, *in* 'Proceedings of the Second ERS-1 Symposium', Hamburg (Germany), Vol. ESA SP - 361, ESA Publications Division, ESTEC, Noordwijk (NL), pp. 219–224.

Barber, B.F. and F. Ursell [1948], 'The generation and propagation of ocean waves and swell; I. Wave periods and velocities', *Philos. Trans. R. Soc. Lond. A* **240**, 527–560.

Barthel, K. and Ø. Breivik [1996], A physical scatterometer model function with input from a wave model, Research Report , University of Bergen, Bergen (Norway).

Barzel, G. [1994], Optimierung eines Seegangsmodells mit der adjungierten Methode, Ph.D. thesis, Universität Hamburg, Germany, MPI für Meteorologie, Examensarbeit Nr. 26.

Batchelor, G.K. [1967], *An introduction to fluid mechanics*, Cambridge University Press, Cambdridge (UK), 615 pp.

Bauer, E. and P. Heimbach [1998], 'Annual validation of significant wave heights from ERS-1 synthetic aperture radar wave mode spectra using TOPEX/POSEIDON and ERS-1 altimeter data', *J. Geophys. Res.* submitted.

Bauer, E. and C. Staabs [1998], 'Statistical properties of global significant wave heights and their use for validation', *J. Geophys. Res.* **C103**, 1153–1166.

Bauer, E., S. Hasselmann, K. Hasselmann and H. C. Graber [1992], 'Validation and assimilation of Seasat altimeter wave heights using the WAM wave model', *J. Geophys. Res.* **C97**, 12671–1268.

Bauer, E., K. Hasselman, I.R. Young and S. Hasselmann [1996a], 'Assimilation of wave data into the wave model WAM using an impulse response function', *J. Geophys. Res.* **C101**, 3801–3816.

Bauer, E., S. Hasselmann and K. Hasselmann [1996b], An operational wave forecast system using wind and wave data, *in* 'Proceedings of the Second ERS Applications Workshop', London (UK), Vol. ESA SP - 383, ESA Publications Division, ESTEC, Noordwijk (NL), pp. 309–312.

Bauer, E., S. Hasselmann, P. Lionello and K. Hasselmann [1997], Comparison of assimilation results from an optimal interpolation and the Green's function method using ERS-1 SAR wave mode spectra, *in* 'Proceedings of the 3rd ERS Symposium', Florence (I), Vol. ESA SP-414, Vol. 3, ESA Publications Division, ESTEC, Noordwijk (NL).

Bauer, E., M. Stolley and H. von Storch [1998], 'On the response of surface waves to accelerating the wind forcing', *J. Phys. Oceanogr.* submitted.

Beal, R.C., ed. [1991], *Directional ocean wave spectra.*, The Johns Hopkins University Press, Baltimore (USA).

Beal, R.C., T.W. Gerling, F.M. Monaldo and D.G. Tilley [1991], 'Measuring ocean waves from space', *Int. J. Remote Sensing* **12**, 1713–1722.

Belcher, S.E. and J.C.R. Hunt [1993], 'Turbulent flow over slowly moving waves', *J. Fluid Mech.* **251**, 109–148.

Belcher, S.E. and J.C.R. Hunt [1998], 'Turbulent flow over hills and waves', *Annu. Rev. Fluid Mech.* **30**, 507–538.

Bentamy, A., N. Grima, Y. Quilfen, V. Harscoat, C. Maroni and S. Pouliquen [1996], An atlas of surface wind from ERS-1 scatterometer measurements 1991 – 1996, Technical Report , IFREMER/CERSAT, IFREMER, DRO/OS, BP 71, 29280 Plouzané, France.

Bentamy, A., N. Grima, Y. Quilfen, V. Harscoat, C. Maroni and S. Pouliquen [1997], Wind climatology from ERS-1 scatterometer, *in* 'Proceedings of the 3rd ERS Symposium', Florence (I), Vol. ESA SP-414, Vol. 3, ESA Publications Division, ESTEC, Noordwijk (NL), pp. 1181–1186.

Blanc, T.V. [1983], 'An error analysis of profile flux, stability and roughness length measurements made in the marine atmospheric poundary layer', *Bound. Layer Meteorol.* **26**, 243–267.

Boussinesq, J. [1870], 'Essai théorique sur les lois trouvées expérimentalement par M. Bazin pour l'écoulement uniforme de l'eau dans les canaux découverts', *Comptes Rendus Acad. Sci. Paris* **71**, 389–393.

Bouws, E., D. Jannink and G.J. Komen [1996], 'The increasing wave height in the North Atlantic Ocean', *Bull. Am. Met. Soc.* **77**, 2275–2277.

Breivik, L.-A., B. Haugse, H. Johnsen, H. E. Krogstad and M. Reistad [1995], Evaluation of SAR wave products, Research Report 2, The Norwegian Meteorological Institute (DNMI), Oslo (Norway).

Breivik, L.-A., M. Reistad, H. Schyberg, J. Sunde, H.E. Krogstad and H. Johnsen [1997], 'Assimilation of ERS SAR wave spectra in an operational wave model', *J. Geophys. Res.* submitted.

Bretherton, F.P. and C.J.R. Garrett [1969], 'Wavetrains in inhomogeneous moving media', *Proc. R. Soc. Lond. A* **302**, 529–554.

Brooker, G. [1995], *ERS-1/2 UWA processing algorithm specification. Version 2.0*, European Space Research and Technology Centre (ESTEC), Noordwijk (NL).

Brüning, C., W. Alpers, L.F. Zambresky and D.G. Tilley [1988], 'Validation of a SAR ocean wave imaging theory by the Shuttle Imaging Radar-B experiment over the North Sea', *J. Geophys. Res.* **93**, 15403–15425.

Brüning, C., W. Alpers and K. Hasselmann [1990], 'Monte-Carlo simulation studies of the nonlinear imaging of a two-dimensional surface wave field by a synthetic aperture radar', *Int. J. Remote Sensing* **90**, 1695–1727.

Brüning, C., S. Hasselmann, K. Hasselmann, S. Lehner and T.W. Gerling [1993], On the extraction of ocean wave spectra from ERS-1 SAR Wave Mode image spectra, *in* 'Proceedings of the First ERS-1 Symposium', Cannes (France), Vol. ESA SP - 359, ESA Publications Division, ESTEC, Noordwijk (NL), pp. 747–752.

Brüning, C., S. Hasselmann, K. Hasselmann, S. Lehner and T.W. Gerling [1994], 'A first evaluation of ERS-1 synthetic aperture radar Wave Mode data.', *Global Atmos. Ocean System* **2**, 61–98.

Callahan, P.S., C.S. Morris and S.V. Hsiao [1994], 'Comparison of TOPEX/POSEIDON σ_0 and significant wave height distributions to GEOSAT', *J. Geophys. Res.* **C99**, 25015–25024.

Chapron, B., R. Garello, V. Kerbaol and J.M. Lefevre [1994], Nonlinear theory of ocean–SAR transformation and statistical analysis of ERS-1 SAR wave mode imagettes, *in* 'Proceedings of the 2nd ERS-1 Symposium', Hamburg (Germany), Vol. ESA SP - 361, ESA Publications Division, ESTEC, Noordwijk (NL), pp. 247–250.

Chapron, B., T. Elfouhaily and V. Kerbaol [1995], Calibration and validation of ERS Wave Mode products, Document DRO/OS/95-02, IFREMER, IFREMER, DRO/OS, BP 71, 29280 Plouzané, France.

Charnock, H. [1951], 'Meteorology – Energy transfer between the atmosphere and the ocean', *Science Progress* **153**, 80–95.

Charnock, H. [1955], 'Wind stress on a water surface', *Q. J. R. Met. Soc.* **81**, 639–640.

Charnock, H. [1981], Air–sea interaction, *in* B.A. Warren and C. Wunsch, eds, 'Evolution of Physical Oceanography', The MIT Press, Cambridge, MA (USA), pp. 482–503.

Cotton, P.D. and D.J.T. Carter [1994], 'Cross calibration of TOPEX, ERS-1, and GEOSAT wave heights', *J. Geophys. Res.* **C99**, 25025–25033.

Cotton, P.D., P.G. Challenor and D.J.T. Carter [1997], An assessment of the accuracy and reliability of GEOSAT, ERS-1, ERS-2 and TOPEX altimeter measurements of significant wave height and wind speed, *in* 'Proceedings of CEOS Wind and Wave Validation Workshop', ESTEC, Noordwijk (NL), Vol. ESA WPP-147, ESA Publications Division, ESTEC, Noordwijk (NL), pp. 81–93.

Davis, R.E. [1972], 'On prediction of the turbulent flow over a wavy boundary', *J. Fluid Mech.* **52**, 287.

Delignon, Y. [1993], Etude statistique d'images radar de la surface de la mer, Ph.D. thesis, Université de Rennes 1, N° d'ordre 1019.

Dobson, F.D., S.D. Smith and R.J. Anderson [1994], 'Measuring the relationship between wind stress and sea state in the open ocean in the presence of swell', *Atmosphere–Ocean* **32**, 237–256.

Donelan, M.A. [1990], Air-sea interaction, *in* B. Le Méhauté and D.M. Hanes, eds, '*The Sea*: Ocean Engineering Science', John Wiley, New York (USA), pp. 239–292.

Donelan, M.A. and W.H. Hui [1990], Mechanics of ocean surface waves, *in* G.L. Geernaert and W.L. Plant, eds, 'Surface Waves and Fluxes, Vol. 1', Kluwer Academic Publishers, Dordrecht (NL), pp. 209–246.

Donelan, M.A., F.W. Dobson, S.D. Smith and R.J. Anderson [1993], 'On the dependence of sea surface roughness on wave development', *J. Fluid Mech.* **52**, 287–???

ECMWF [1995], User Guide to ECMWF Products. Edition 2.1, Meteorological Bulletin M3.2, ECMWF, Reading (UK).

Elachi, C. [1988], *Spaceborne radar remote sensing: applications and tehniques*, IEEE Press, New York (USA), 255 pp.

Engen, G. and H. Johnsen [1995], 'SAR ocean wave inversion using image cross spectra', *IEEE Trans. Geosci. Remote Sensing* **33**, 1047–1056.

ESA [1992], ERS-1 System, Technical Report ESA SP - 1146, European Space Agency (ESA), ESA Publications Division, ESTEC, Noordwijk (NL).

ESA [1993], ERS User Handbook, Technical Report ESA SP - 1148, Revision 1, European Space Agency (ESA), ESA Publications Division, ESTEC, Noordwijk (NL).

ESA [1996], Application Achievements of ERS-1, Technical Report ESA SP-1176/II, European Space Agency (ESA), ESA Publications Division, ESTEC, Noordwijk (NL).

Essen, H.-H. [1998], 'Theoretical investigation of the impact of long surface waves on empirical ERS-1/2 scatterometer models', *Int. J. Remote Sensing*. submitted.

Fairall, C.W., E.F. Bradley, D.P. Rogers, J.B. Edson and G.S. Young [1996], 'Bulk parameterization of air-sea fluxes for Tropical Ocean Coupled Ocean Atmosphere Response Experiment', *J. Geophys. Res.* **C101**, 3747–3764.

Feindt, F. [1985], Radar–Rückstreuexperimente am Wind-Wellen-Kanal bei sauberer und filmbedeckter Wasseroberfläche im X–Band (9.8 GHz), Ph.D. thesis, Universität Hamburg, Germany, Hamburger Geophysikalische Einzelschriften, Reihe A, Heft 75.

Feindt, F., J. Schröter and W. Alpers [1986], 'Measurement of the ocean wave – radar modulation transfer function at 35 GHz from a sea-based platform in the North Sea', *J. Geophys. Res.* **C91**, 9701–9708.

Fradon, B. [1997], Modélisation numérique de l'état de la mer: comparaison des performances et des limites d'un modèle de deuxième génération et d'un modèle de troixième génération dans le cadre de l'expérience SEMAPHORE, Ph.D. thesis, Université de Paris VII, .

Garratt, J.R. [1977], 'Review of drag coefficients over oceans and continents', *Mon. Weather Rev.* **105**, 915–929.

Garratt, J.R. [1992], *The atmospheric boundary layer*, Cambridge University Press, Cambridge (UK), 316 pp.

Geernaert, G.L. [1988], 'Measurement of the angle between the wind vector and wind stress vector in the surface layer over the North Sea', *J. Geophys. Res.* **C93**, 8215–8220.

Geernaert, G.L. [1990], Bulk parameterizations for the wind stress heat fluxes, *in* G.L. Geernaert and W.L. Plant, eds, 'Surface Waves and Fluxes, Vol. 1', Kluwer Academic Publishers, Dordrecht (NL), pp. 91–172.

Geernaert, G.L., F. Hansen, M. Courtney and T. Herbers [1993], 'Directional attributes if the ocean surface wind stress vector', *J. Geophys. Res.* **C98**, 16571–16582.

Gelci, R., H. Cazalé and J. Vassal [1957], 'Prévision de la houle. La méthode des densités spectroangulaires', *Bull. Infor. Comité Central Océanogr. d'Etudes des Côtes* **9**, 416–435.

Gerling, T.W. [1992], 'Partitioning sequences and arrays of directional wave spectra into component wave systems', *J. Atmos. Ocean. Techn.* **9**, 444–458.

Gibson, J.K., P. Kållberg, S. Uppala, A. Hernandez, A. Nomura and E. Serrano [1997], ECMWF Re-Analysis Project: ERA description, ERA Project Report Series 1, ECMWF, Reading (UK).

Giering, R. and T. Kaminski [1998], 'Recipes for adjoint code construction', *ACM Transactions on Mathematical Software* , . in press; also available as MPI Report No. 212.

Gower, J.F.R. [1983], '"Layover" in satellite radar images of ocean waves', *J. Geophys. Res.* **C88**, 7719–7720.

Gower, J.F.R. [1996], 'Intercalibration of wave and wind data from TOPEX/POSEIDON and moored buoys off the west coast of Canada', *J. Geophys. Res.* **C101**, 3817–3829.

Graber, H.C., R.E. Jensen and V.J. Cardone [1995], Sensitivity of wave model predictions on spatial and temporal resolution of the wind field, *in* 'Proc. 4th Int. Workshop on Wave Hindcasting and Forecasting', Banff, Alberta (Canada), Environment Canada, p. .

Grand Banks [1994], 'The Grand Banks ERS-1 SAR Wave Spectra Validation Experiment', *Atmosphere-Ocean* **32**, 3–256. Special issue.

Günther, H., S. Hasselmann and P.A.E.M. Janssen [1992], WAModel Cycle 4, Technical Report 4, Deutsches Klimarechenzentrum (DKRZ), Hamburg (Germany).

Hammack, J.L. and D.M. Henderson [1993], 'Resonant interactions among surface water waves', *Annu. Rev. Fluid Mech.* **25**, 55–97.

Hara, T. and W.R. Plant [1994], 'Hydrodynamic modulation of short wind-wave spectra by long waves and its measurement using microwave backscatter', *J. Geophys. Res.* **C99**, 9767–9784.

Hasse, L. and S.D. Smith [1997], 'Local sea surface wind, wind stress, and sensible and latent heat fluxes', *J. Climate* **10**, 2711–2724.

Hasselmann, K. [1960], 'Grundgleichungen der Seegangsvorhersage', *Schiffstechnik* **7**, 191–195.

Hasselmann, K. [1961], 'On the non-linear energy transfer in a gravity wave spectrum. Part 1: General theory', *J. Fluid Mech.* **12**, 481–500.

Hasselmann, K. [1963a], 'On the non-linear energy transfer in a gravity wave spectrum. Part 2: Conservation theorems; wave-particle analogy; irreversibility', *J. Fluid Mech.* **15**, 273–281.

Hasselmann, K. [1963b], 'On the non-linear energy transfer in a gravity wave spectrum. Part 3: Evaluation of the energy flux and swell-sea interaction for a Neumann spectrum', *J. Fluid Mech.* **15**, 385–398.

Hasselmann, K. [1966], 'Feynman diagrams and interaction rules of wave-wave scattering processes', *Rev. Geophys.* **4**, 1–32.

Hasselmann, K. [1967], 'Nonlinear interactions treated by the methods of theoretical physics (with application to the generation of waves by the wind)', *Proc. R. Soc. Lond. A* **299**, 77–100.

Hasselmann, K. [1968], Weak-interaction theory of ocean waves, *in* 'Basic developments in fluid dynamics', Vol. 2, Academic Press, New York (USA), pp. 117–182.

Hasselmann, K. [1971], 'On the mass and momentum transfer between short gravity waves and larger-scale motions', *J. Fluid Mech.* **50**, 189–205.

Hasselmann, K. [1974], 'On the spectral dissipation of ocean waves due to white capping', *Bound. Layer Meteorol.* **6**, 107–127.

Hasselmann, K. [1980], 'A simple algorithm for the direct extraction of the two-dimensional surface image spectrum from the return signal of a synthetic aperture radar', *IEEE Trans. Geosci. Remote Sensing* **1**, 219–240.

Hasselmann, K. [1991], Epilogue: Waves, dreams, and visions, *in* R.Beal, ed., 'Directional ocean wave spectra', Baltimore (USA), The Johns Hopkins University Press, pp. 205–208.

Hasselmann, K. and J.I. Collins [1968], 'Spectral dissipation of finite–depth gravity waves due to turbulent bottom friction', *J. Marine Res.* **26**, 1–12.

Hasselmann, K. and Hasselmann, S. [1991], 'On the nonlinear mapping of an ocean wave spectrum into a synthetic aperture radar image spectrum and its inversion', *J. Geophys. Res.* **C96**, 10713–10729.

Hasselmann, K., T.P. Barnett, E. Bouws, H. Carlson, D.E. Cartwright, K. Enke, J.A. Ewing, H. Gienapp, D.E. Hasselmann, P. Kruseman, A. Meerburg, P. Müller, D.J. Olbers, K. Richter, W. Sell and H. Walden [1973], 'Measurements of Wind-Wave Growth and Swell Decay during the Joint North Sea Wave Project (JONSWAP)', *Dtsch. Hydrogr. Z.* **12**, 1–95.

Hasselmann, K., R.K. Raney, W.J. Plant, W. Alpers, R.A. Shuchman, D.R. Lyzenga, C.L. Rufenach and M.J. Tucker (MARSEN Group) [1985], 'Theory of synthetic aperture radar ocean imaging. A MARSEN view', *J. Geophys. Res.* **C90**, 4659–4686.

Hasselmann, K., S. Hasselmann, C. Brüning and A. Speidel [1991], Interpretation and application of SAR wave image spectra in wave models, *in* R.Beal, ed., 'Directional ocean wave spectra', Baltimore (USA), The Johns Hopkins University Press, pp. 117–124.

Hasselmann, S. and Hasselmann, K. [1985], 'Computations and parameterisations of the nonlinear energy transfer in a gravity wave spectrum. Part I: A new method for efficient computations of the exact nonlinear energy transfer integral', *J. Phys. Oceanogr.* **14**, 1369–1377.

Hasselmann, S., K. Hasselmann, J.H. Allender and T.P. Barnett [1985a], 'Computations and parameterisations of the nonlinear energy transfer in a gravity wave spectrum. Part II: Parameterisations of the nonlinear energy transfer for application in wave models', *J. Phys. Oceanogr.* **14**, 1378–1391.

Hasselmann, S., C. Brüning and P. Lionello [1994], Towards a generalized optimal interpolation method for the assimilation of ERS-1 SAR retrieved wave spectra in a wave model, *in* 'Proceedings of the Second ERS-1 Symposium', Hamburg (Germany), Vol. ESA SP - 361, pp. 21–25.

Hasselmann, S., C. Brüning, K. Hasselmann and P. Heimbach [1996a], 'An improved algorithm for the retrieval of ocean wave spectra from SAR image spectra', *J. Geophys. Res.* **C101**, 16615–16629.

Hasselmann, S., P. Lionello and K. Hasselmann [1997], 'An optimal interpolation assimilation scheme for wave data', *J. Geophys. Res.* **C101**, 16615–16629.

Hasselmann, S., P. Heimbach and C. Bennefeld [1998], The WASAR algorithm for retrieving ocean wave spectra from SAR image spectra, Technical Report 14, Deutsches Klimarechenzentrum (DKRZ), Hamburg (Germany).

Heimbach, P., S. Hasselmann, C. Brüning and K. Hasselmann [1996], Application of wave spectral retrievals from ERS-1 SAR Wave Mode data for improved wind and wave field analyses, *in* 'Proceedings of the 2nd ERS Applications Workshop', London (UK), Vol. ESA SP-383, ESA Publications Division, ESTEC, Noordwijk (NL), pp. 303–308.

Heimbach, P., S. Hasselmann and K. Hasselmann [1998], 'Statistical analysis and intercomparison of WAM model data with global ERS-1 SAR Wave Mode spectral retrievals over three years', *J. Geophys. Res.* **C103**, 7931–7978.

Hellerman, S. and M. Rosenstein [1983], 'Normal monthly wind stress over the world ocean with error estimates', *J. Phys. Oceanogr.* **13**, 1093–1104.

Hersbach, H. [1997a], 'Application of the adjoint of the WAM model to inverse wave modelling', *J. Geophys. Res.* , . in press; also available as KNMI Scientific report 97-04.

Hersbach, H. [1997b], The adjoint of the WAM model, Scientific report 97-01, KNMI, De Bilt (NL).

Hosking, J.R.M. [1990], 'L-moments: Analysis and estimation of distributions using linear combinations of order statistics', *J. R. Statist. Soc. B* **52**, 105–124.

Houghton, J.T., L.G. Meira Filho, B.A. Challender, N. Harris, A. Kattenberg and K. Maskell [1996], *Climate Change 1995. The Science of Climate Change. The Second IPCC Assessment Report*, Cambridge University Press, Cambridge (UK), 572 pp.

IFREMER/CERSAT [1996], ERS-1 off-line wind scatterometer products, User Manual C2–MUT–W–01–IF, Version 2.0, IFREMER, Plouzané, France.

Jähne, B. and E.C. Monahan, eds [1995], *Air-Water Gas Transfer*, AEON Verlag & Studio, Hanau (Germany).

Janssen, P.A.E.M. [1989], 'Wave-induced stress and the drag of the air flow over sea waves', *J. Phys. Oceanogr.* **19**, 745–754.

Janssen, P.A.E.M. [1991], 'Quasi-linear theory of wind-wave generation applied to wave forecasting', *J. Phys. Oceanogr.* **21**, 1631–1391.

Janssen, P.A.E.M. [1992], 'Experimental evidence of the effect of surface waves on the airflow', *J. Phys. Oceanogr.* **22**, 1600–1604.

Janssen, P.A.E.M. and P. Viterbo [1996], 'Ocean waves and the atmospheric climate', *J. Climate* **9**, 1269–1287.

Janssen, P.A.E.M., B. Hansen and J. Bidlot [1996], Verification of the ECMWF wave forecasting system against buoy and Altimeter data, ECMWF Technical Memorandum 229, ECMWF, Reading (UK).

Jeffreys, H. [1925], 'On the formation of water waves by wind', *Proc. R. Soc. Lond. A* **107**, 189–206.

Jeffreys, H. [1926], 'On the formation of waves by wind II', *Proc. R. Soc. Lond. A* **110**, 341–347.

Johnsen, H. [1992], 'Multi-look versus single-look processing of synthetic aperture radar images with respect to ocean wave spectra estimation', *Int. J. Remote Sensing* **13**, 1627–1643.

Johnson, N.L., S. Kotz and N. Balakrishnan [1994], *Continuous univariate distributions*, Vol. 1, 2nd edn., John Wiley & Sons, New York (USA).

Jones, I.S.F., Y. Sugimori and R.W. Stewart [1993], *Satellite remote sensing of the oceanic environment*, Seibutsu Kenkyusha, Tokyo (JP), 528 pp.

Kagan, B.A. [1995], *Ocean–Atmosphere Interaction and Climate Modelling*, Cambridge University Press, Cambridge (UK), 377 pp.

Keller, W.C., W.J. Plant, R.A. Petit, Jr. and E.A. Terray [1994], 'Microwave backscatter from the sea: modulation of received power and Doppler bandwidth by long waves', *J. Geophys. Res.* **C99**, 9751–9766.

Kerbaol, V. [1997], Analyse spectrale et statistique vent-vague des images radar à ouverture synthétique. Application aux données des satellites ERS-1/2, Ph.D. thesis, Université de Rennes 1, N° d'ordre 1892.

Kerbaol, V. and B. Chapron [1996], Calibration and validation of ERS-1/2 wave mode products, ESA Contract Report PO NO 160709, IFREMER, IFREMER, DRO/OS, BP 71, 29280 Plouzané, France.

Kerbaol, V., B. Chapron and P.W. Vachon [1998], 'Analysis of ERS-1/2 synthetic aperture radar wave mode imagettes', *J. Geophys. Res.* **C103**, 7833–7846.

Kinsman, B. [1965], *Wind waves – their generation and propagation on the ocean surface*, Prentice–Hall, Englewood Cliffs, N.J. (USA), 676 pp.

Kitaigorodskii, S.A. [1973], *The Physics of Air-Sea Interaction*, (Tranlation from the Russian original, Leningrad 1970), Israel Program for Scientific Translations, Jerusalem (Israel), 237 pp.

Komen, G.J., S. Hasselmann and K. Hasselmann [1984], 'On the existence of a fully developed wind-sea spectrum', *J. Phys. Oceanogr.* **14**, 1271–1285.

Komen, G.J., L. Cavaleri, M. Donelan, K. Hasselmann, S. Hasselmann and P.A.E.M. Janssen [1994], *Dynamics and modelling of ocean waves*, Cambridge University Press, Cambridge (UK), 560 pp.

Komen, G., P.A.E.M. Janssen, V.K. Makin and W. Oost [1998], 'On the sea state dependence of the Charnock parameter', *Global Atmos. Ocean System* , in press.

Kondratyev, K.Ya., A.A. Buznikov and O.M. Pokrovsky [1996], *Global change and remote sensing*, John Wiley & Sons, Chichester (UK), 370 pp.

Kraus, E.B. and J.A. Businger [1994], *Atmosphere–Ocean Interaction. 2nd Edition*, Oxford University Press, New York (USA), 362 pp.

Krogstad, H.E. [1992], 'A simple derivation of Hasselmann's nonlinear ocean-synthetic aperture radar transform', *J. Geophys. Res.* **C97**, 2421–2425.

Krogstad, H.E. [1994], The speckle spectrum of the ERS-1 wave mode product, Report STF10 A94008, SINTEF Industrial Mathematics, Trondheim (Norway).

Krogstad, H.E., O. Samset and P.W. Vachon [1994], 'Generalization of the non-linear ocean-SAR transform and a simplified SAR inversion algorithm', *Atmosphere–Ocean* **32**, 61–82.

Kudryavtsev, V.N., C. Mastenbroek and V.K. Makin [1997], 'Modulation of wind ripples by long surface waves via the air flow: a feedback mechanism', *Bound. Layer Meteorol.* **83**, 99–116.

Kushnir, Y., V.J. Cardone, J. G. Greenwood and M.A. Cane [1997], 'The recent increase in North Atlantic wave heights', *J. Climate* **10**, 2107–2113.

Large, W.G. and S. Pond [1981], 'Open ocean momentum flux measurements in moderate to strong winds', *J. Phys. Oceanogr.* **11**, 324–336.

Large, W.G. and S. Pond [1982], 'Sensible and latent heat flux measurements over the ocean', *J. Phys. Oceanogr.* **12**, 464–482.

Large, W.G., J. Morzel and G.B. Crawford [1995], 'Accounting for surface wave distortion of the marine wind profile in low-level ocean storm wind measurements', *J. Phys. Oceanogr.* **25**, 2959–2971.

Le Caillec, J.M., R. Garello and B. Chapron [1996], 'Two dimensional bispectral estimates from ocean SAR images', *Nonlin. Proc. Geophys.* **3**, 196–215.

LeBlond, P.H. and L.A. Mysak [1978], *Waves in the Ocean*, Elsevier, New York (USA), 560 pp.

Lehner, S., T. Bruns and K. Hasselmann [1996], Test of a new onboard ship routeing system, *in* 'Proceedings of the Second ERS Applications Workshop', London (UK), Vol. ESA SP-383, ESA Publications Division, ESTEC, Noordwijk (NL), pp. 297–301.

Lesieur, M. [1990], *Turbulence in Fluids*, Kluwer Academic Publishers, Dordrecht (NL), 412 pp.

Lighthill, J. [1978], *Waves in Fluids*, Cambridge University Press, Cambdridge (UK), 504 pp.

Lionello, P., H. Günther and P.A.E.M. Janssen [1992], 'Assimilation of altimeter data in a global third generation wave model', *J. Geophys. Res.* **C97**, 14453–14474.

Lionello, P., H. Günther and B. Hansen [1995], 'A sequential assimilation scheme applied to global wave analysis and prediction', *J. Marine Systems* **6**, 87–107.

Makin, V.K. [1987], 'Wavelike momentum fluxes in boundary layer above sea waves', *Oceanology* **27**, 128–132.

Makin, V.K. and C. Mastenbroek [1996], 'Impact of waves on air-sea exchange of sensible heat and momentum', *Bound. Layer Meteorol.* **79**, 279–300.

Makin, V.K., V.N. Kudryavtsev and C. Mastenbroek [1995], 'Drag of the sea surface', *Bound. Layer Meteorol.* **73**, 159–182.

Mastenbroek, C. and C.F. de Valk [1997], A new algorithm for the retrieval of wave spectra from the ERS SAR, *in* 'Proceedings of CEOS Wind and Wave Validation Workshop', ESTEC, Noordwijk (NL), Vol. ESA WPP-147, ESA Publications Division, ESTEC, Noordwijk (NL), pp. 57–60.

Mastenbroek, C., G. Burgers and P.A.E.M. Janssen [1993], 'The dynamical coupling of a wave model and a storm surge model through the atmospheric boundary layer', *J. Phys. Oceanogr.* **23**, 1856–1866.

Mastenbroek, C., V.K. Makin, M.H. Garat and J.P. Giovanangelli [1996], 'Experimental evidence of the rapid distortion of turbulence in the air flow over water waves', *J. Fluid Mech.* **318**, 273–302.

Mastenbroek, C., V.K. Makin and V.N. Kudryavtsev [1997], 'The growth of long water waves due to the interaction with short waves via the atmospheric boundary layer', *Bound. Layer Meteorol.*.

Melville, W.K. [1996], 'The role of surface-wave breaking in air-sea interaction', *Annu. Rev. Fluid Mech.* **28**, 279–321.

Miles, J. [1957], 'On the generation of surface waves by shear flows', *J. Fluid Mech.* **3**, 185–204.

Miles, J. [1959a], 'On the generation of surface waves by shear flows. Part 2', *J. Fluid Mech.* **6**, 568–582.

Miles, J. [1959b], 'On the generation of surface waves by shear flows. Part 3', *J. Fluid Mech.* **6**, 583–598.

Miles, J. [1960], 'On the generation of surface waves by turbulent shear flows', *J. Fluid Mech.* **7**, 469–478.

Miles, J. [1961], 'On the stability of heterogeneous shear flows', *J. Fluid Mech.* **10**, 496–508.

Miles, J. [1962], 'On the generation of surface waves by shear flows. Part 4', *J. Fluid Mech.* **13**, 433–438.

Miles, J. [1967], 'On the generation of surface waves by shear flows. Part 5', *J. Fluid Mech.* **30**, 163–175.

Mitsuyasu, H., R. Nakayama and T. Komori [1971], Observations of the wind and the waves in Hakata Bay, Rep. Res. Inst. Appl. Mech. 19, Kyushu University, Kyushu (Japan).

Monaldo, F.M. [1988], 'Expected differences between buoy and radar altimeter estimates of wind speed and significant wave height and their implications on buoy-altimeter comparisons', *J. Geophys. Res.* **C93**, 2285–2302.

Monaldo, F.M. and R.C. Beal [1995], 'Real-time observations of Southern Ocean wave fields from the Shuttle Imaging Radar', *IEEE Trans. Geosci. Remote Sensing* **33**, 942–949.

Monaldo, F.M. and D.R. Lyzenga [1986], 'On the estimation of wave slope- and height variance spectra from SAR imagery', *IEEE Trans. Geosci. Remote Sensing* **24**, 543–551.

Monaldo, F.M. and D.R. Lyzenga [1988], 'Comparison of shuttle imaging radar–B ocean wave spectra with linear model predictions based on aircraft measurements', *J. Geophys. Res.* **93**, 374–388.

Monin, A.S. and A.M. Yaglom [1971], *Statistical Fluid Mechanics*, MIT Press, Cambridge, MA (USA), 769 pp.

Munk, W.H. and F.E. Snodgrass [1957], 'Measurements of southern swell at Guadalupe Islands', *Deep Sea Res.* **4**, 272–286.

Munk, W.H., G.R. Miller, F.E. Snodgrass and N.F. Barber [1963], ' ', *Philos. Trans. R. Soc. Lond. A* **255**, 505–584.

Pedlosky, J. [1987], *Geophysical Fluid Dynamics (2nd ed.)*, Springer-Verlag, New York (USA), 710 pp.

Peixoto, J.P. and A.H. Oort [1992], *The Physics of Climate*, The American Institute of Physics, New York (USA), 520 pp.

Phillips, O.M. [1957], 'On the generation of waves by turbulent wind', *J. Fluid Mech.* **2**, 417–445.

Phillips, O.M. [1960], 'On the dynamics of unsteady gravity waves of finite amplitude. Part I: The elementary interactions.', *J. Fluid Mech.* **9**, 193–217.

Phillips, O.M. [1977], *The Dynamics of the Upper Ocean*, 2nd edn., Cambridge University Press, Cambridge (UK), pp.

Phillips, O.M. [1981], 'Wave interactions – the evolution of an idea', *J. Fluid Mech.* **106**, 215–227.

Pierson, W.J., G. Neumann and R.W. James [1955], Practical methods for observing and forecasting ocean waves by means of wave spectra and statistic, Technical Report H.O. Pub. No. 603, U.S. Navy, U.S. Hydrographic Office Publication, La Jolla, California (USA).

Plant, W.J. [1982], 'A relationship between wind stress and wave slope', *J. Geophys. Res.* **C87**, 1961–1967.

Plant, W.J. [1988], The modulation transfer function: Concept and application, *in* G.J. Komen and W.A. Oost, ed., 'Scattering from modulated wind waves', Kluwer Academic Publishers, Dordrecht (NL), p. .

Plant, W.J. and W. Alpers [1994], 'An introduction to SAXON-FPN', *J. Geophys. Res.* **C99**, 9699–9703.

Plant, W.J., W.C. Keller and A. Cross [1983], 'Parametric dependence of ocean wave radar modulation transfer functions', *J. Geophys. Res.* **C88**, 9747–9756.

Prandtl, Z.A. [1925], 'Bericht über Untersuchungen zur ausgebildeten Turbulenz', *Z. Angew. Math. Mech.* **5**, 136–169.

Preisendorfer, R.P. [1988], *Principal Component Analysis*, Elsevier, New York (USA), 422p.

Press, W.H., S.A. Teukolsky, W.T. Vetterling and B.P. Flannery [1992], *Numerical Recipes*, Cambridge University Press, Cambdridge (UK), 963 pp.

Queffeulou, P. [1996], Significant wave height and backscatter coefficient at ERS-1/2 and TOPEX/POSEIDON ground track crossing points – Fast Delivery Product, ESA contract final report ESA contract no. 143189, IFREMER, IFREMER, DRO/OS, BP 71, 29280 Plouzané, France.

Reynolds, O. [1894], 'On the dynamical theory of turbulent incompressible viscous fluids and the determination of the criterion', *Philos. Trans. R. Soc. Lond. A* **186**, 123–161.

Rieder, K.F. [1997], 'Analysis of sea-surface drag parameterizations in open ocean conditions', *Bound. Layer Meteorol.* **83**, 355–377.

Rieder, K.F. and J. A. Smith [1998], 'Removing wave effects from the wind stress vector', *J. Geophys. Res.* **C103**, 1363–1374.

Rieder, K.F., J.A. Smith and R.A. Weller [1994], 'Observed directional characteristics of the wind, wind stress and surface waves on the open ocean', *J. Geophys. Res.* **C99**, 22589–22596.

Robinson, I.S. [1985], *Satellite Oceanography*, Ellis Horwood Ltd., Chichester, UK, 455 pp.

Rogers, D.P. [1995], 'Air–sea interaction: Connecting the ocean and the atmosphere', *Rev. Geophys.* **33**, Suppl.

Rosenthal, W. and F. Ziemer [1991], Removal of 180° ambiguity in SAR images of ocean waves, *in* R.C. Beal, ed., 'Directional Ocean Wave Spectra', Johns Hopkins University Press, Baltimore (USA), pp. 125–127.

Rosenthal, W., F. Ziemer, R.K. Raney and P. Vachon [1989], Removal of 180° ambiguity in SAR images of ocean waves, *in* 'IGARSS'89', Vancouver, B.C. (CA), IEEE Press, Piscataway, N.J., USA.

Rossby, C.G. [1932], A generalization of the theory of mixing length with application to atmospheric and oceanic turbulence, Meteorol. Pap. 1, Mass. Inst. Technol., MIT, Cambridge, Massachusetts, USA.

Rufenach, C. [1998], 'Comparison of four ERS-1 scatterometer wind retrieval algorithms with buoy measurements', *J. Atmos. Ocean. Techn.* **15**, 304–313.

Rufenach, C. [1996], An offset between scatterometer directional anisotropy and wind direction across the equatorial Pacific Ocean, *in* 'IGARSS'96', Lincoln, Nebraska (USA), IEEE Press, Piscataway, N.J., USA, pp. 814–816.

Schmidt, A. and M. Bao [1998], 'The modulation of radar backscatter by long ocean waves: A quadratically nonlinear process?', *J. Geophys. Res.* **C103**, 5551–5562.

Schmidt, A., V. Wismann, R. Romeiser and W. Alpers [1995], 'Simultaneous measurements of the ocean wave radar modulation transfer function at L, C, and X bands from the research platform Nordsee', *J. Geophys. Res.* **C100**, 8815–8827.

SEASAT [1983], 'Special issue on SEASAT', *J. Geophys. Res.* **88**, .

Sell, W. and K. Hasselmann [1972], Computations of the nonlinear energy transfer for JONSWAP and empirical wind-wave spectra, Rep. of the Institute of Geophysics , University of Hamburg, .

Smith, S.D., R.J. Anderson, W.A. Oost, C. Kraan, N.Maat, J. DeCosmo, K.B. Katsaros, K.L. Davidson, K. Bumke, L. Hasse and H.M. Chadwick [1992], 'Sea surface wind stress and drag coefficients: The HEXOS results', *Bound. Layer Meteorol.* **60**, 109–142.

Smith, S.D., C.W. Fairall, G.L. Geernaert and L. Hasse [1996], 'Air–sea fluxes: 25 years of progress', *Bound. Layer Meteorol.* **78**, 247–290.

Snodgrass, F.E., G.W. Groves, K. Hasselmann, G.R. Miller, W.H. Munk and W.H. Powers [1966], 'Propagation of ocean swell across the Pacific', *Philos. Trans. R. Soc. Lond. A* **249**, 431–497.

Snyder, R.L. and C.S. Cox [1966], 'A field study of the wind generation of ocean waves', *J. Marine Res.* **24**, 141–178.

Snyder, R.L., F.W. Dobson, J.A. Elliott and R.B. Long [1981], 'Array measurements of atmospheric pressure fluctuations above surface gravity waves', *J. Fluid Mech.* **102**, 1–59.

Snyder, R.L., W.C. Thacker, K. Hasselmann, S. Hasselmann and B. Barzel [1993], 'Implementation of an efficient scheme for calculating nonlinear transfer from wave–wave interactions', *J. Geophys. Res.* **C98**, 14507–14525.

Stewart, R.H. [1985], *Methods of satellite oceanography*, University of California Press, Berkeley and Los Angeles (USA), 360 pp.

Stewart, R.W. [1961], 'The wave drag of wind over water', *J. Fluid Mech.* **10**, 189–194.

Stoffelen, A. and D. Andersen [1997], 'Scatterometer data interpretation: Estimation and validation of the transfer function CMOD4', *J. Geophys. Res.* **C102**, 5767–5780.

Sverdrup, H.U. and W.H. Munk [1947], Wind, sea, and swell: Theory of relations for forecasting, Scripps Institution of Oceanography New Series, No. 303 H.O. Pub. No. 601 / Technical Report No. 1, U.S. Navy, U.S. Hydrographic Office Publication, La Jolla, California (USA).

SWAMP Group [1985], *Ocean Wave Modeling*, Plenum Press, New York (USA), 256 pp.

Swift, C.F. and L.R. Wilson [1979], 'Synthetic aperture radar imaging of moving ocean waves', *IEEE Trans. Antennas Propag.* **AP-27**, 725–729.

Tolman, H.L. [1995], On the selection of propagation schemes for a spectral wind-wave model, Office Note 411, NWS/NCEP, La Jolla, California (USA).

Tournadre, J. and R. Ezraty [1990], 'Local climatology of wind and sea state by means of satellite radar altimeter measurements', *J. Geophys. Res.* **C95**, 18255–18268.

Tucker, M.J. [1985], 'The imaging of waves by satellite synthetic aperture radar: the effect of surface motion', *Int. J. Remote Sensing* **6**, 1059–1074.

Turner, J.S. [1973], *Buoyancy effects in fluids*, Cambridge University Press, Cambdridge (UK), 367 pp.

Ulaby, F.T., R.K. Moore and A.K. Fung [1986], *Microwave Remote Sensing*, Artech House, Dedham, Mass. (USA). 3 Vols.

Vachon, P.W. and R.K. Raney [1991], 'Resolution of the ocean wave propagation direction in SAR imagery', *IEEE Trans. Geosci. Remote Sensing* **29**, 105–112.

Valenzuela, G.R. [1978], 'Theories for the interaction of electromagnetic and ocean waves – a review', *Bound. Layer Meteorol.* **13**, 61–85.

von Storch, H., J. Guddal, K.A. Iden T. Jonson, J. Perlwitz, M. Reistad, J. de Ronde, H. Schmidt and E. Zorita [1993], Changing statistics of storms in the North Atlantic?, Report 116, MPI für Meteorologie, Hamburg (Germany).

Voorrips, A.C. and C. de Valk [1997], 'A comparison of two operational wave assimilation methods', *Global Atmos. Ocean System.* submitted.

Voorrips, A.C., V.K. Makin and S. Hasselmann [1996], 'Assimilation of wave spectra from pitch-and-roll buoys in a North Sea wave model', *J. Geophys. Res.* submitted.

WAMDI Group [1988], 'The WAM model - a third generation ocean wave prediction model', *J. Phys. Oceanogr.* **18**, 1775–1810.

WASA Group [1995], The WASA project: Changing storm and wave climate in the Northeast Atlantic and adjacent seas?, *in* 'Proc. 4th Int. Workshop on Wave Hindcasting and Forecasting', Banff, Alberta (Canada), Environment Canada, pp. 31–44.

WASA Group [1998], 'Changing waves and storms in the Northeast Atlantic?', *Bull. Am. Met. Soc.* submitted; also available as GKSS Report No. 97/E/46.

Weber, S. L., H. von Storch, P. Viterbo and L. Zambresky [1993], 'Coupling an ocean wave model to an atmospheric general circulation model', *Climate Dyn.* **9**, 63–69.

Weisse, R. and E.F. Alvarez [1997], The European Coupled Atmosphere Wave Ocean Model ECAWOM, Report 116, MPI für Meteorologie, Hamburg (Germany).

Whitham, G.B. [1964], 'A general approach to linear and non-linear dispersive waves using a Lagrangian', *J. Fluid Mech.* **22**, 273–283.

Wilde, A., C. Brüning, W. Alpers, V. Etkin, K. Litovchenko, A. Ivanov and V. Zajtsev [1994], Comparison of ocean wave imaging by ERS-1 and ALMAZ-1 synthetic aperture radar, *in* 'Proceedings of the Second ERS-1 Symposium', Hamburg (Germany), Vol. ESA SP - 361, ESA Publications Division, ESTEC, Noordwijk (NL), pp. 239–245.

Willebrand, J. [1975], 'Energy transport in a nonlinear and inhomogeneous random gravity field', *J. Fluid Mech.* **70**, 113–126.

Wright, J.W. [1968], 'A new model for sea clutter', *IEEE Trans. Antennas Propag.* **AP-16**, 217–223.

Wright, J.W. [1978], 'Detection of ocean waves by microwave radar: The modulation of short gravity–capillary waves', *Bound. Layer Meteorol.* **13**, 87–105.

Wu, J. [1980], 'Wind stress coefficients over sea surface near neutral conditions – a revisit', *J. Phys. Oceanogr.* **10**, 727–740.

Wu, J. [1982], 'Wind stress coefficients over sea surface from breeze to hurricane', *J. Geophys. Res.* **C87**, 9704–9706.

Yelland, M. and P.K. Taylor [1996], 'Wind stress measurements from the open ocean', *J. Phys. Oceanogr.* **26**, 541–558.

Young, I.R., W. Rosenthal and F. Ziemer [1985], 'A Three-Dimensional Analysis of Marine Radar Images for the Determination of Ocean Wave Directionality and Surface Currents', *J. Geophys. Res.* **C90**, 1049–1059.

Young, I.R., S. Hasselmann and K. Hasselmann [1987], 'Computations of the response of a wave spectrum to a sudden change in wind direction', *J. Phys. Oceanogr.* **17**, 1317–1338.

Young, I.R. and G.P. van Vledder [1993], 'A review of the central role of nonlinear interactions in wind-wave evolution', *Philos. Trans. R. Soc. Lond. A* **342**, 505–524.

Zakharov, V.E., V.S. L'vov and G. Falkovich [1992], *Kolmogorov Spectra of Turbulence I: Wave Turbulence*, Springer Verlag, Berlin (Germany), 264 pp.

Zemba, J. and C.A. Friehe [1987], 'The marine atmospheric boundary layer jet in the coastal ocean dynamical experiment', *J. Geophys. Res.* **C92**, 1589–1496.

AVISO [WWW],
`http://192.134.216.41/.`

CERSAT [WWW],
`http://www.ifremer.fr/cersat/.`

DKRZ [WWW],
`http://www.dkrz.de/.`

ECMWF [WWW],
`http://www.ecmwf.int/.`

ENVISAT [WWW],
`http://envisat.estec.esa.nl/.`

ERS-1 [WWW],
`http://earth1.esrin.esa.it:8888/dl/eeo3.html.`

ERS-1/2 Radar Altimeter [WWW],
`http://earth1.esrin.esa.it:8888/eeo/fr/eeo4.63/eeo4.64.`

ERS-1/2 SAR [WWW],
`http://earth1.esrin.esa.it:8888/eeo/fr/eeo4.63/eeo4.128.`

ERS-1/2 Wind Scatterometer [WWW],
`http://earth1.esrin.esa.it:8888/eeo/fr/eeo4.63/eeo4.144.`

ESA [WWW],
`http://www.esa.int/.`

EUMETSAT [WWW],
`http://www.eumetsat.de/.`

GMS/HIMAWARI [WWW],
`http://yyy.tksc.nasda.go.jp/Home/This/This-e/gms_e.html.`

GOES [WWW],
`http://ww2010.atmos.uiuc.edu/()/guides/rs/sat/goes/home.rxml.`

NDBC [WWW],
`http://seabord.ndbc.noaa.go/.`

NESDIS [WWW],
`http://ns.noaa.gov/NESDIS/NESDIS_Home.html.`

SIR-C [WWW],
`http://southport.jpl.nasa.gov/sir-c/.`

T/P at CNES [WWW],
`http://www-projet.cst.cnes.fr:8060/topex/Mission.html.`

T/P at JPL [WWW],
`http://topex-www.jpl.nasa.gov/.`

WAM [WWW],
`http://www.dkrz.de/forschung/reports/report4/wamh-1.html.`

WASAR [WWW],
`http://www.dkrz.de/forschung/reports/.`

ISSN 0938-5177